Università degli Studi di Torino
Doctoral School of the University of Torino
PhD Programme in Chemical and Materials Sciences 33rd Cycle

The role of dissolved organic matter in surface-water photochemistry: Photoreactions with water contaminants, photoreactivity inhibition, and effects of climate change.

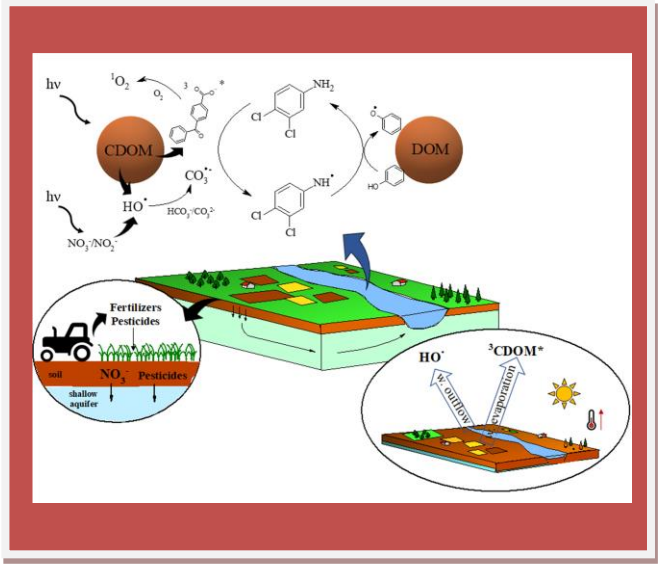

Luca Carena

Supervisor:
Prof. Davide Vione

Abstract

In this work, the role of the excited triplet states of CDOM (^{3}CDOM*) in photodegradation of pollutants taking place in surface waters was (re)examined. In particular, the triplet state of benzophenone-4-carboxylate (^{3}CBBP*) was used as proxy compound of ^{3}CDOM*. A new protocol allowed for the determination of the second-order rate constants of the reactions between ^{3}CBBP* and water contaminants (i.e., ibuprofen, acetaminophen, atrazine and clofibric acid). The experimental results suggested that ^{3}CBBP* is more suitable as ^{3}CDOM* proxy than other compounds used in previous works, such as most notably the triplet state of anthraquinone-2-sulfonate (^{3}AQ2S*). Modeling of photochemical fate of the investigated contaminants showed that when ^{3}CDOM* = ^{3}CBBP* their lifetimes are higher than those predicted by the model when ^{3}CDOM* = ^{3}AQ2S*. However, photochemistry of ^{3}CDOM* would be still dominant in water bodies (especially deep) with high DOM content, regardless of the proxy molecule adopted in the model.

^{3}CBBP*-induced degradation of clofibric acid and N-containing compounds, such as (chloro)anilines and paroxetine, was found to be inhibited in the presence of phenol, which acts as antioxidant by reducing back the partially oxidized intermediates to the parent molecules. The same back-reduction effect was observed when the (chloro)anilines are photodegraded by $CO_3^{\bullet-}$ radicals. Based on these findings, a first general statement for the back-reduction effect was proposed by describing the process in terms of the Marcus electron-transfer Theory.

Finally, in the context of climate change, the effects of the Big Dry, that occurred in the first decade of the 21st century, on the Lower Lakes (SE Australia) photochemistry was investigated. Modeling results showed that

^{3}CDOM* photoreactions increased during that hydrological drought, while $HO^\bullet$ and $CO_3^{\bullet-}$ radicals concentration did not significantly change.

In contrast, photochemical modeling of rivers in the Piedmont region (NW Italy) showed that, in the same decade, the photochemistry of $HO^\bullet$ and $CO_3^{\bullet-}$ radicals increased during water scarcity, while that of ^{3}CDOM* was unchanged. This mainly because of nitrate pollution of groundwaters due to anthropogenic activities. In this scenario, the photochemical self-decontamination potential of Piedmontese rivers from agrochemicals was assessed as well.

Table of Contents

Acknowledgements

Compagnia di San Paolo (Torino, Italy) is gratefully acknowledged for the financial support of the PhD fellowship. The PhD periods abroad at University of Jyväskylä (Department of Biological and Environmental Science, Jyväskylä - Finland) and at Jožef Stefan Institute (Department of Environmental Sciences, Ljubljana – Slovenia) were financially supported by the Erasmus+ Traineeship programme and the bilateral cooperation agreement between Italy and Slovenia (project BI-IT-18-20-005: *Photochemical fate and treatment of pharmaceutical contaminants in drinking water*), respectively.

Special thanks to Prof. Davide Vione for being tutor and mentor during (and before) the PhD.

All the coauthors of the papers on which this work is based are gratefully acknowledged.

Finally, many thanks to Prof. Anssi V. Vähätalo and Prof. Tina Kosjek for their supervision during the time spent at University of Jyväskylä and Jozef Stefan Institute, respectively, as well as for reviewing this work together with Prof. Marco Minella.

Chapter 1

Photochemistry of sunlit surface waters: A brief introduction

List of abbreviations:

AQY = Apparent Quantum Yield
CDOM = Chromophoric Dissolved Organic Matter
DOM = Dissolved Organic Matter
ISC = Inter-System Crossing
PPRIs = Photochemically Produced Reactive Intermediates
ROS = Reactive Oxygen Species
TPs = Transformation Products

Photochemical reactions taking place in sunlit surface waters are environmentally important processes, which support life trough photosynthesis (Schlesinger and Bernhardt, 2013) and account for the abiotic phototransformation of substances (Fenner et al., 2013; Vähätalo, 2009). As 'sunlit surface water' one usually means the photic zone of a water body such as a lake, a river or the ocean, where the incident solar-photons energy can be converted into thermal or chemical energy after it is absorbed by chemical species.

In surface waters, the main absorbing species for wavelengths < 450-500 nm is the chromophoric dissolved organic matter (CDOM), which is a ubiquitous water component (Nelson and Siegel, 2013) deriving from the biotic and abiotic degradation of plant litter in soil (allochthonous CDOM) and/or from *in situ* phototransformation of smaller organic compounds (autochthonous CDOM) (Berto et al., 2018; Osburn et al., 2019; Wershaw, 2004). Upon sunlight absorption, CDOM is able to act as photosensitizer by producing reactive transient species (Vione et al., 2014), called Photochemically Produced Reactive Intermediates (PPRIs). CDOM is also phototransformed upon sunlight absorption, undergoing degradation into smaller organic compounds (Clark et al., 2019; Gonsior et al., 2014; Varanasi et al., 2018) and photomineralization (Koehler et al., 2014). However, these photoreactions are minor pathways for CDOM, because most of the absorbed solar-photons energy (probability of ~95-98%) is released as heat (Nelson and Siegel, 2013; Vähätalo, 2009).

The main PPRIs in inland surface waters include the well-known reactive oxygen species (ROS), such as singlet oxygen ($^1O_2$, $^1\Delta_g$ as molecular electronic configuration), superoxide radical anion ($O_2^{\bullet-}$), hydrogen peroxide (H_2O_2) and hydroxyl radical ($HO^\bullet$). Another important subset of the whole PPRIs pool is represented by the excited triplet states of CDOM ($^3CDOM^*$)

and the carbonate radicals ($CO_3^{\bullet-}$). Soon after PPRIs are produced, they are scavenged mostly by reactions with naturally occurring compounds, such as DOM (not necessarily chromophoric; Westerhoff et al., 2007; Yan et al., 2019) in the case of $HO^{\bullet}$ and $CO_3^{\bullet-}$. As secondary but environmentally very important processes, PPRIs can also react with xenobiotic substances (Remucal, 2014; Vione et al., 2014). The fast production and scavenging rates of PPRIs make their lifetime very low (from a few to some tens microseconds; Schmitt et al., 2017; Sharpless, 2012; Vione et al., 2014) and ensure that their concentration is in steady-state conditions, often ranging in the interval 10^{-18}-10^{-13} mol L^{-1} as far as $HO^{\bullet}$, $CO_3^{\bullet-}$, $^3CDOM^*$ and $^1O_2$ are concerned (Carena et al., 2017; McCabe and Arnold, 2016; Timko et al., 2014; Vione et al., 2014; Xu et al., 2020; Zeng and Arnold, 2013).

The PPRIs photoproduction efficiency by CDOM is expressed as an apparent quantum yield (AQY), which represents the moles of produced reactive intermediates per mole of photons absorbed by CDOM. The term 'apparent' refers to the complex, multi-step mechanism that leads to the production of the reactive transient (Sharpless and Blough, 2014). The AQYs of $HO^{\bullet}$ formation by CDOM usually range between 10^{-5}-10^{-4} (Carena et al., 2017; Cawley et al., 2014; De Laurentiis et al., 2013a; McCabe and Arnold, 2016; Xu et al., 2020), while those for $^3CDOM^*$ and $^1O_2$ are ~10^{-3}-10^{-2} (Carena et al., 2017; De Laurentiis et al., 2013a, 2012b; McCabe and Arnold, 2018; Mckay et al., 2017; McNeill and Canonica, 2016; Paul et al., 2004; Schmitt et al., 2017; Zhou et al., 2019). Therefore, the production of $^3CDOM^*$ and $^1O_2$ is favored over that of $HO^{\bullet}$ when CDOM absorbs sunlight.

The formation mechanism of $HO^{\bullet}$ radicals by CDOM is not yet well understood but two main pathways have been identified, namely a H_2O_2-dependent mechanism and a H_2O_2-independent one. Briefly, the former

process would start with the photoproduction of superoxide radicals ($O_2^{\bullet-}$) upon photoinduced charge-transfer interactions within CDOM (Sharpless and Blough, 2014). In particular, a phenolic component of CDOM (PhOH) absorbs sunlight and undergoes oxidation to the corresponding phenoxy radical ($PhO^{\bullet}$). At the same time, a DOM quinone is reduced to a semiquinone radical forming a charge-transfer couple of the type $CDOM^{\bullet+/-}$ (Garg et al., 2011; Ma et al., 2020; Zhang et al., 2012). The semiquinone can then reduce dissolved oxygen to $O_2^{\bullet-}$ (Zhang et al., 2012; Zhang and Blough, 2016), which would partially back-react with $PhO^{\bullet}$ to give again PhOH and O_2 (Ma et al., 2020). Note that superoxide can be also formed upon photoinduced ligand-to-metal charge transfers in Fe(III)-DOM complexes (Garg et al., 2020, 2018; Xing et al., 2019). The AQY of $O_2^{\bullet-}$ formation by irradiated CDOM is ~10^{-3} (Ma et al., 2020). The remaining fraction of $O_2^{\bullet-}$ (~25%; Ma et al., 2020) undergoes dismutation to H_2O_2 through three main pathways: self-disproportionation, DOM-catalyzed and metal-catalyzed (Cu, Mn and Fe) dismutation (Fujii and Otani, 2017; Garg et al., 2007; Goldstone and Voelker, 2000; Heller and Croot, 2010; Ma et al., 2019). In inland waters, the DOM-catalyzed dismutation should prevail over the other reactions (Ma et al., 2019), but the relative roles of the different processes would vary with the DOM type (Fujii and Otani, 2017). Overall, the H_2O_2 formation AQYs by irradiated DOM samples are ~10^{-4} (Zhang et al., 2012). The H_2O_2 thus generated would be partially reduced to $HO^{\bullet}$ by Fe(II)-DOM complexes and semiquinones (Sanchez-Cruz et al., 2014; Xiao et al., 2020). Note that the produced H_2O_2 can undergo direct photolysis as well, forming two moles of $HO^{\bullet}$ per mole of reaction (O'Sullivan et al., 2005). Because of the involvement of Fe and H_2O_2, this $HO^{\bullet}$ formation mechanism is often referred to as a Fenton-like process (Vione et al., 2014; Xiao et al., 2020).

Interestingly, a similar mechanism could be operational in the case of $HO^{\bullet}$ formation in the absence of light (Minella et al., 2015; Page et al., 2012), where the presence of reduced Fe-DOM complexes and semiquinones can trigger the production of $O_2^{\bullet-}$ upon their interaction with dissolved oxygen (Xiao et al., 2020; Xie et al., 2020; Zeng et al., 2020). Furthermore, extracellular $O_2^{\bullet-}$ can be biologically produced as well and it would react with DOM, producing $HO^{\bullet}$ radicals that are able to degrade DOM itself (Vähätalo et al., 2020; Zhang et al., 2016).

In contrast, the H_2O_2-independent mechanism of $HO^{\bullet}$ production by irradiated CDOM is much less known. A possible contribution of water oxidation by a (small) fraction of produced ^{3}CDOM* may be involved (Bedini et al., 2012; Sur et al., 2011), and the production of non-free $HO^{\bullet}$ radicals has been observed during CDOM irradiation (Page et al., 2011). Additionally, this H_2O_2-independent process would be favored in low-molecular-weight CDOM samples, where the formation of triplet states would not be inhibited by internal charge-transfer interactions and energy dissipation by internal conversion (Vione et al., 2014). Another possible H_2O_2-independent source of $HO^{\bullet}$ is the photolysis of polyhydroxylated intermediates, which are formed upon photoinduced degradation of CDOM (Gonsior et al., 2014; Sun et al., 2015).

Finally, a further formation pathway for $HO^{\bullet}$ in sunlit surface waters is the photolysis of nitrate and nitrite (Mack and Bolton, 1999). The latter processes play an important role in the overall production of $HO^{\bullet}$ radicals when the CDOM content is low. In those conditions, the UVB and UVA components of the solar spectrum can be efficiently absorbed by NO_3^- and NO_2^-, respectively, which form $HO^{\bullet}$ with respective quantum yields of $\sim 1\times10^{-2}$ for nitrate and $\sim(2.5\text{-}6.5)\times10^{-2}$ for nitrite (the latter is wavelength-dependent;

Mack and Bolton, 1999). However, because UVB and UVA photons are efficiently absorbed by nitrate, nitrite as well as CDOM, their attenuation in the water column is strong (Häder et al., 2015; Sommaruga et al., 1999). Therefore, the photochemistry of nitrate and nitrite can be significant only in the uppermost layers or in shallow water columns (Vione et al., 2014).

The production of $HO^{\bullet}$ triggers the formation of $CO_3^{\bullet-}$ radicals upon oxidation of bicarbonate and carbonate (Buxton et al., 1988; Vione et al., 2014; Wojnárovits et al., 2020). Although CO_3^{2-} is more reactive with $HO^{\bullet}$ than HCO_3^- (Buxton et al., 1988), their relative roles in the overall $CO_3^{\bullet-}$ production process strongly depend on the water pH (Vione et al., 2014). Moreover, CO_3^{2-} can also be oxidized by ^{3}CDOM*, which increases the importance of carbonate in $CO_3^{\bullet-}$ formation (Canonica et al., 2005). The ^{3}CDOM* + CO_3^{2-} reaction can account for ~10% of the whole photogeneration of $CO_3^{\bullet-}$ at pH > 9.5 (Carena and Vione, 2016; Yan et al., 2019). Finally, a contribution of similar importance can possibly be given by the reaction between peroxynitrite ($ONOO^-$, which is formed upon nitrate photolysis; Huang et al., 2018; Mack and Bolton, 1999) and dissolved CO_2 at pH < 7.8 (Carena and Vione, 2016). Because CDOM does not produce $CO_3^{\bullet-}$ by direct light absorption, but rather through the formation of $HO^{\bullet}$ and ^{3}CDOM*, it is often considered as an indirect source of carbonate radicals.

The production of ^{3}CDOM* follows light absorption by CDOM, which gets excited to singlet states (^{1}CDOM*) from which inter-system crossing (ISC) can take place to produce the triplet states (McNeill and Canonica, 2016). This very general description of the process will be resumed and addressed in more detail in the introduction of Chapter 2. As said before, the ^{3}CDOM* formation AQYs are ~10^{-3}-10^{-2} and decrease with increasing wavelength (Marchisio et al., 2015). Interestingly, similar AQYs values and wavelength-dependent

behavior have been found for $^1O_2$ (Erickson et al., 2018; Mostafa and Rosario-Ortiz, 2013; Partanen et al., 2020; Paul et al., 2004), because the main dissipation pathway of ^{3}CDOM* in oxygenated waters is the triplet-to-triplet energy transfer with dissolved O_2 (the ground state of which has a molecular electronic configuration of the type $^3\Sigma_g^-$; McNeill and Canonica, 2016). The reaction involving ^{3}CDOM* + O_2 is the main process forming singlet oxygen in sunlit surface waters (Vione et al., 2014). However, these ~10^{-3}-10^{-2} AQY values would account for only a fraction of the $^1O_2$ pool produced by CDOM, because they only refer to $^1O_2$ that is free in solution. In addition to that, higher $^1O_2$ formation AQYs have been observed in the inner hydrophobic cores of CDOM (Appiani and McNeill, 2015).

As far as the scavenging reactions of the PPRIs in surface freshwater are concerned, DOM is the main scavenger of both $HO^\bullet$ and $CO_3^{\bullet-}$ (Brezonik and Fulkerson-Brekken, 1998; Page et al., 2014; Vione et al., 2006; Yan et al., 2019). Because $HO^\bullet$ is more reactive and less selective than $CO_3^{\bullet-}$, the rate constants of the reaction $HO^\bullet$ + DOM range between (1.2-3.3)×10^4 L mg_C^{-1} s^{-1} (Westerhoff et al., 2007), while those of $CO_3^{\bullet-}$ + DOM range between (0.2-2.8)×10^2 L mg_C^{-1} s^{-1} (Canonica et al., 2005; Yan et al., 2019). The rationale for the reported ranges is that the actual rate constant depends on the DOM type. For this reason, the steady-state concentration of $CO_3^{\bullet-}$ is often higher than that of $HO^\bullet$ at low DOM concentration (Vione et al., 2014; Wojnárovits et al., 2020). Furthermore, minor $HO^\bullet$ scavenging pathways are the oxidation of bicarbonate and carbonate to $CO_3^{\bullet-}$ and the oxidation of nitrite to $^\bullet NO_2$ (Buxton et al., 1988). In addition, the reaction of $HO^\bullet$ with Br^- is important in brackish and sea waters (Vione et al., 2014). As previously said, ^{3}CDOM* is mainly quenched by dissolved oxygen (McNeill and Canonica, 2016), while $^1O_2$ is mostly quenched by collision with the water molecules (Wilkinson et

al., 1995). Scheme 1.1 summarizes the production and scavenging processes of the PPRIs that take place in inland surface waters.

As a consequence of all the reactions described above, $HO^{\bullet}$ photochemistry is favored in shallow waters that are at the same time nitrate/nitrite-rich and DOM-poor. In such conditions, the production of $CO_3^{\bullet-}$ can also be significant if water is enough alkaline and its pH is high enough. In contrast, the production of $^3CDOM^*/^1O_2$ is significant in (C)DOM rich waters. Moreover, because CDOM efficiently absorbs radiation in the visible range of the solar spectrum, the however limited amount of photochemistry that takes place in the deep layers of the photic zones is mostly accounted for by $^3CDOM^*$ and (for peculiarly reactive substrates) $^1O_2$ (Vione et al., 2014).

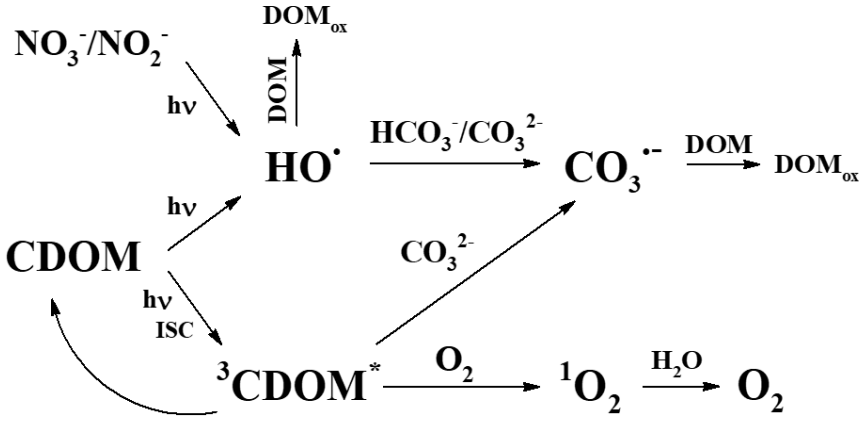

Scheme 1.1 Simplified reaction scheme showing the main photoproduction and scavenging pathways of the main PPRIs in sunlit surface waters. 'DOM_{ox}' generally refers to DOM oxidation by hydroxyl and carbonate radicals.

In the overall process of PPRIs scavenging the reactions between PPRIs and water pollutants play a minor role, because the contaminants' concentrations

are much lower compared to those of the naturally occurring scavengers (Petrie et al., 2015; Topaz et al., 2020). However, reactions with contaminants are extremely important processes in the context of the self-decontamination potential of water bodies (Fenner et al., 2013). Indeed, the presence in the aquatic environments of contaminants of emerging concern and, more in general, of xenobiotic compounds such as pharmaceuticals and personal care products (PPCPs), pesticides and micro-/nano-plastics is a worldwide problem (Ebele et al., 2017; Schwarzenbach et al., 2010, 2006). Photoreactions between PPRIs and water contaminants theoretically act as naturally-occurring self-decontamination processes, which go under the name of indirect photochemistry.

The $HO^{\bullet}$ radicals and $^{3}CDOM^{*}$ are often the PPRIs that play the more important roles in the indirect photodegradation of several water pollutants (Avetta et al., 2016; Remucal, 2014; Tixier et al., 2003; Vione et al., 2010), although some classes of compounds significantly react with $CO_3^{\bullet-}$ (e.g., anilines and sulfonamides; Huang and Mabury, 2000; Wojnárovits et al., 2020) or with singlet oxygen (e.g., chlorophenolates, amino acids and some sulfonamides; Ge et al., 2019; Maddigapu et al., 2011; Remucal and McNeill, 2011). Therefore, PPRIs-induced photodegradation is a potentially important decontamination pathway that can transform pollutants into smaller, more hydrophilic and (often) less harmful molecules. Besides indirect photochemistry, direct photolysis is another important dissipation route for many pollutants that are able to absorb solar radiation (Baena-Nogueras et al., 2017; Bonvin et al., 2013; Carena et al., 2020; Jin et al., 2017; Marchetti et al., 2013). Indeed, we speak of direct photolysis when the absorbed photon energy excites the molecule to an upper electronic state, from which phototransformation can occur *via*, e.g., bond photolysis, photoionization, and photohydrolysis (Katagi, 2018; Luo et al., 2018).

Unfortunately, the described reactions have two potential caveats that are the possible generation of transformation products (TPs) that may be more toxic than the parent compound, and the inhibition of photodegradation by some water components. The former issue has been observed in different cases such as, for instance, during the photodegradation of carbamazepine (De Laurentiis et al., 2012a; Vogna et al., 2004), phenylurea herbicides (Halladja et al., 2007), hydroxylated polybrominated diphenyl ethers (Erickson et al., 2012), and triclosan (Buth et al., 2010), and it poses a high risk for the environment. As far as the second problem is concerned, (C)DOM can inhibit the direct photolysis of pollutants through light screening (Remucal, 2014), and it can inhibit as well some indirect photoreactions by *(i)* scavenging $HO^{\bullet}$ and $CO_3^{\bullet-}$ radicals (Brezonik and Fulkerson-Brekken, 1998; Vione et al., 2006; Yan et al., 2019) and *(ii)* reducing back to the parent compound the partially oxidized contaminants (Canonica and Laubscher, 2008; Wenk and Canonica, 2012). The latter process has been found to take place during the ^{3}CDOM*-induced photoreactions, thanks to the antioxidant (phenolic) moieties of DOM (Canonica and Laubscher, 2008; Leresche et al., 2016; Walpen et al., 2016; Wenk et al., 2011; Wenk and Canonica, 2012).

In the context of the environmental fate of a given contaminant, it is thus important to assess: *(i)* its reactivity with the different PPRIs in terms of second-order reaction rate constants; *(ii)* its direct photolysis quantum yield; *(iii)* the extent by which its photodegradation is inhibited by DOM in the aquatic environment; *(iv)* the nature (and, if possible, the concentrations) of the produced TPs, and *(v)* the potential toxic effects of the latter (Vione and Carena, 2020). At the same time, one needs to know the photochemical features of a water body. Note that (C)DOM plays a key role in most of these points. With this approach, one can assess the photochemical fate of the

compound(s) of interest in surface waters or, from another point of view, the decontamination potential of surface waters from the contaminant(s).

Goals of the work

This work aims at improving the current knowledge about the role of CDOM in surface-water photochemistry, in terms of photoreactivity with water contaminants, of photoreactivity inhibition, and of the decontamination potential of water bodies from pollutants. In particular, Chapter 2 will address the (re)determination of the second-order rate constants of the reactions induced by ^{3}CDOM*, by using the triplet state of an aromatic ketone (benzophenone-4-carboxylate) as a ^{3}CDOM* proxy. The choice of this molecule was made on the basis of the observed spectral and energetic properties of CDOM/^{3}CDOM* (McNeill and Canonica, 2016; Sharpless and Blough, 2014), as well as on the evidence that the triplet states of quinones (previously used to simulate ^{3}CDOM*) can overestimate the reactivity of ^{3}CDOM* (Avetta et al., 2016). The inhibition of the photodegradation of water pollutants (anilines) due to back-reduction processes carried out by phenolic compounds, representative of the antioxidant DOM moieties, was then investigated in the case of both ^{3}CDOM*- and $CO_3^{\bullet-}$-induced reactions (Chapter 3). A first application of the Marcus' electron-transfer theory to the back-reduction process allowed us to get insight into the thermodynamics and the kinetics of the process (Chapter 3). Finally, the decontamination potential of water bodies by pollutants was assessed in different regions of the world, which also allowed for the investigation of some case studies into how climate change and anthropogenic activities can affect the photochemistry of surface waters (Chapter 4). Chapter 5 is finally devoted to conclusions.

Chapter 2

Re-examination of the importance of the excited triplet states of CDOM (^{3}CDOM*) in the photodegradation of water contaminants: using the triplet state of 4-carboxybenzophenone as proxy for ^{3}CDOM*

Based on the results reported in the following published papers:

- **Carena, L.**, Puscasu, C.G., Comis, S., Sarakha, M., Vione, D., **2019**. Environmental photodegradation of emerging contaminants: A re-examination of the importance of triplet-sensitised processes, based on the use of 4-carboxybenzophenone as proxy for the chromophoric dissolved organic matter. *Chemosphere* 237, 124476. https://doi.org/10.1016/j.chemosphere.2019.124476
- Minella, M., Rapa, L., **Carena, L.**, Pazzi, M., Maurino, V., Minero, C., Brigante, M., Vione, D., **2018**. An experimental methodology to measure the reaction rate constants of processes sensitised by the triplet state of 4-carboxybenzophenone as a proxy of the triplet states of chromophoric dissolved organic matter, under steady-state irradiation conditions. *Environ. Sci. Process. Impacts* 20, 1007–1019. https://doi.org/10.1039/c8em00155c

List of abbreviations:

APAP = acetaminophen

AQ2S = anthraquinone-2-sulfonate

ATZ = atrazine

CBBP = benzophenone-4-carboxylate

CDOM = chromophoric dissolved organic matter

CLO = clofibric acid

IBP = ibuprofen

2.1 Introduction

DOM is a complex mixture of diverse organic compounds, the majority of which consists of humic substances that primarily originate from terrestrial plant litter after biotic and abiotic transformation in soil (Wershaw, 2004). The analysis of DOM with several techniques, including ^{13}C-NMR and electron spin resonance (ESR) spectroscopies, as well as Fourier-transform ion cyclotron resonance mass spectrometry (FT-ICR MS) indicate that DOM contains (lignin-like) substituted phenols, ketones, aldehydes, quinones, carboxylic acids as well as carboxyl-rich alicyclic molecules, saturated and unsaturated hydrocarbons, carbohydrates, and nitrogenous material (Berg et al., 2019; Nebbioso and Piccolo, 2013; Niu et al., 2018; Sulzberger and Durisch-Kaiser, 2009; Vähätalo, 2009).

Because of soil runoff and leaching, DOM reaches ground- and surface waters (Lipczynska-Kochany, 2018), where it can undergo further transformations. For instance, photochemical reactions in sunlit surface waters can trigger the breakdown of (C)DOM humic substances into smaller organic molecules (Clark et al., 2019). Notably, these transformations affect the optical and photochemical properties of CDOM (Berg et al., 2019; Garg et al., 2011; Loiselle et al., 2012; Niu et al., 2014) and they also affect the global carbon cycling (Koehler et al., 2014; Sulzberger and Arey, 2016). Besides photochemical reactions, DOM can be significantly transformed by both biotic (Vähätalo et al., 2010) and abiotic (Xiao et al., 2020) reactions in the absence of light, although with lower breakdown rates (Vähätalo, 2009).

The main DOM pool in surface waters derives from soil (allochthonous source), and it consists of large, aromatic humic substances (Niu et al., 2018) that can be degraded into smaller compounds (Clark et al., 2019). However, the additional production of autochthonous, humic-like DOM can be induced

by photochemical reactions that involve biogenic proteinaceous material in water bodies (Berto et al., 2018, 2016; Bianco et al., 2014). This process is very interesting because at a first stage it operates through the oligomerization of small molecules (Berto et al., 2018; Loiselle et al., 2012), which runs counter to DOM mineralization and produces humic-like material with peculiar photochemical properties (De Laurentiis et al., 2013a, 2012b).

Among thousands of CDOM components, aromatic ketones/aldehydes, quinones and (lignin-like) hydroxy-/methoxy-substituted phenols seem to be the main actors in determining the optical and photochemical properties of CDOM (Bianca et al., 2020; Sharpless and Blough, 2014). For instance, the light-absorption spectrum of CDOM monotonically decreases from UV to visible wavelengths as an exponential function, the absorbance-decay rate of which (called 'spectral slope') is lower (0.010-0.014 nm^{-1}) for large, highly aromatic CDOM fractions. Interestingly, the presence of Fe can also significantly decrease the spectral slope, presumably through formation of charge-transfer complexes with organic ligands (Xiao et al., 2020). In contrast, smaller CDOM with fewer conjugated electronic systems shows higher values of spectral slope (> 0.020 nm^{-1}) (Sharpless and Blough, 2014). There has been and there is still debate, as to whether the exponential decay of the absorbance can be satisfactorily accounted for by the mere convolution of the absorption spectra of compounds that are electronically independent from their chemical surrounding. This view is named the 'superposition model'. As an alternative, a 'charge-transfer interaction model' (also 'CT interaction model') might potentially account for several photochemical properties of CDOM. This model is based on electron (charge) transfer between a donor (which absorbs light and undergoes "photoionization") and an acceptor (an oxidizing compound), both occurring within CDOM (Sharpless and Blough, 2014). Candidate donors are phenolic compounds (Zhang et al., 2014), while

potential acceptors can be both/either quinones and/or (aromatic) ketones/aldehydes (Sharpless and Blough, 2014). Upon light absorption, the excited states of phenols (PhOH) are oxidized by electron acceptors that occur in their chemical surrounding, forming charge-separated species ($PhO^{\bullet}$ + $CDOM^{\bullet-}$). The increase in the spectral slope with the decrease of *(i)* CDOM size; *(ii)* the content of aromatic ketones and aldehydes due to reduction by $NaBH_4$, and *(iii)* the solution pH, theoretically corroborate the CT interaction model (Schendorf et al., 2019; Sharpless and Blough, 2014). However, some recently published results have questioned the actual occurrence of charge-transfer processes in CDOM (McKay et al., 2018).

Both the absorption of light by single chromophores within CDOM ('superposition model') and the occurrence of CT processes ('CT interaction model') could be operational at the same time, and be responsible of the formation of different PPRIs. For instance, the photoproduction of the superoxide radical anion ($O_2^{\bullet-}$) upon CDOM light absorption has been proposed to occur through the formation of $CDOM^{\bullet+/-}$ species; of these, the negatively-charged part can reduce dissolved O_2 to $O_2^{\bullet-}$, while the positively-charged one is able to oxidize $O_2^{\bullet-}$ back to O_2 or to produce organic peroxides (Ma et al., 2020). The photoproduction rate of $O_2^{\bullet-}$ (as well as that of hydrogen peroxide, of which superoxide is a precursor via disproportionation) has been found to increase with the phenolic content within DOM (Zhang et al., 2014). In contrast, no significant variations have been observed upon reduction of Suwannee River humic and fulvic acids with $NaBH_4$ (Zhang et al., 2012), suggesting that: *(i)* excited-state phenols and ground-state quinones are good candidates as, respectively, donors and acceptors in CT processes, and *(ii)* aromatic ketones and aldehydes do not play a significant role in $O_2^{\bullet-}$ photoproduction, because they are irreversibly reduced to alcohols by $NaBH_4$.

This finding is corroborated by the higher one-electron reduction potentials of ground-state quinones (~ -0.3 V vs. SHE) compared to ground-state aromatic ketones/aldehydes (~ -1 V vs. SHE) (McNeill and Canonica, 2016). Therefore, excited-state phenols are more prone to reduce ground-state quinones compared to ground-state ketones/aldehydes, thereby producing a CT couple of the type $CDOM^{\bullet+/-}$, made up of phenoxy radical / semiquinone. (However, this process has been recently questioned, suggesting that quinones participate only in low-energy CT transitions (Del Vecchio et al., 2017).) Furthermore, the formation of $O_2^{\bullet-}$ and H_2O_2 by the reaction between semiquinones and O_2 can lead to the production of $HO^{\bullet}$ radicals through Fenton-like processes (Page et al., 2012; Xiao et al., 2020). Consequently, CT processes among excited-state phenols and ground-state quinones may be partially responsible of the observed photoproduction of $HO^{\bullet}$ and (indirectly) $CO_3^{\bullet-}$ radicals by CDOM.

In contrast, aromatic ketones/aldehydes are more likely to account for the photoproduction of $^3CDOM^*$, and of $^1O_2$ as a consequence (Sharpless and Blough, 2014; Zhou et al., 2019). Indeed, the energy of the excited triplet states of the aromatic ketones/aldehydes occurring in CDOM ranges between 250-310 kJ mol^{-1} (corresponding to near-UV wavelengths), while that of the excited triplet states of quinones ranges between 200-250 kJ mol^{-1} (corresponding to visible wavelengths) (McNeill and Canonica, 2016). In the UV region, light absorption by CDOM and the apparent quantum yields of ^3CDOM formation are higher than those measured under visible light (Marchisio et al., 2015; Sharpless and Blough, 2014; Zhou et al., 2019), thereby suggesting that photon absorption by aromatic ketones/aldehydes (as per the superposition model) and the subsequent formation of the relevant excited-triplet states is favored over that of quinones. Therefore, the triplet-state energy of aromatic ketones/aldehydes would make them more prone to

be ^{3}CDOM* photosensitizers than quinones. Coherently, findings reported in a recently published work show that triplet states of aromatic ketones/aldehydes with energy > 250 kJ mol^{-1} account for ~70% of the total pool of ^{3}CDOM* in Pony Lake fulvic acids (PLFA) and effluent organic matter (EfOM). In contrast, the corresponding fraction is almost halved in the case of Suwannee River natural organic matter (SRNOM), which is characterized by a higher content of phenols and quinones (Zhou et al., 2019). The remaining part of ^{3}CDOM* (triplet energy < 250 kJ mol^{-1}) is mainly due to triplet quinones. Furthermore, the ^{3}CDOM* formation quantum yields of PLFA and EfOM are 2-3 fold higher than those observed for SRNOM (Zhou et al., 2019).

Besides the molecular energy, the one-electron reduction potential of the excited triplet states would be a key factor supporting aromatic ketones/aldehydes against quinones, with respect to ^{3}CDOM* photoproduction. Indeed, the proposed interval of reduction potentials of average ^{3}CDOM* ($E^o_{^3CDOM*/CDOM^{\bullet-}}$ ~ 1.4-1.9 V vs. SHE; Canonica et al., 2000) overlaps with that of the excited triplet states of aromatic ketones, such as 4-carboxybenzophenone, acetophenone, benzophenone, and 3-methoxyacetophenone. Conversely, the same is not true for triplet quinones that are too strong oxidants to be part of average ^{3}CDOM* (McNeill and Canonica, 2016).

Despite the previous issues, quinones have been used as CDOM proxy molecules to assess the reactivity of water pollutants with ^{3}CDOM*. For example, the photochemistry of the excited state of anthraquinone-2-sulfonate (^{3}AQ2S*) has been widely investigated (Bedini et al., 2012; Maddigapu et al., 2010; Maurino et al., 2008). Because of the large amount of information about the photochemistry and photophysics of AQ2S, ^{3}AQ2S* was used to estimate the second-order rate constants of the reactions between ^{3}CDOM* and water

contaminants (Avetta et al., 2016, 2014; Carena et al., 2017; De Laurentiis et al., 2012a; Marchetti et al., 2013; Vione et al., 2011). These reactions often occur through electron-transfer (or hydrogen atom-transfer) processes from the xenobiotic to ^{3}CDOM* (McNeill and Canonica, 2016), and their kinetics depends on the reduction potential difference between the species involved (Canonica et al., 2000). However, the case of naproxen has shown that the use of ^{3}AQ2S* as ^{3}CDOM* proxy can cause an overestimation of the photoreactivity of xenobiotics towards ^{3}CDOM* (Avetta et al., 2016).

In the present work, the photoreactivity of four water contaminants (ibuprofen, acetaminophen, clofibric acid and atrazine) towards ^{3}CDOM* was investigated by using the triplet state of benzophenone-4-carboxylate (^{3}CBBP*) as ^{3}CDOM* proxy. The choice of CBBP is based on the issues described above, and especially on the fact that triplet aromatic ketones are more representative of ^{3}CDOM* than triplet quinones. Furthermore, the photochemical fate of these xenobiotics in surface waters was re-assessed in the light of new findings, allowing us to better quantify the role of ^{3}CDOM* in the overall photodegradation of the relevant contaminants in the aquatic environment.

2.2 Materials and Methods

2.2.1 Reagents and solutions preparation

Ibuprofen sodium salt (IBP, purity grade 98%), acetaminophen (APAP, BioXtra, > 99%), clofibric acid (CLO, 97%), atrazine (ATZ, Pestanal® analytical standard, 98.8%), 4-carboxybenzophenone (CBBP, 99%), 2-nitrobenzaldehyde (2NBA, 98%), H_3PO_4 (85%), NaOH (98%) and phenol (99%) were purchased from Sigma-Aldrich. Gradient-grade methanol for HPLC analysis was from VWR Chemicals BDH®.

Aqueous solutions were prepared using ultra-pure water, obtained from a Millipore Milli-Q system (resistivity > 18MΩ cm, organic carbon < 2 ppb). The acidic stock solution of CBBP (pKa ~4.5; NIST, 2004) was prepared monthly and adjusted to pH 7.0 with NaOH 1 mol L^{-1}, to keep the compound in the deprotonated form. The concentration of stock CBBP was 100 µmol L^{-1}. Because of low water solubility (~35 mg L^{-1}; Lewis et al., 2016), the stock solution of ATZ was prepared by adding an aliquot of solid ATZ in water (~1 L), followed by magnetic stirring for ~60 h in the dark to avoid any light-induced degradation. The solution was then filtered on a 0.45 µm pore size polyamide filter (Sartorius) and adjusted to pH 7 with NaOH 0.1 mol L^{-1}. The concentration of the filtered solution was measured by HPLC-DAD (*vide infra*) against methanol/water standards. This solution was stable for all the experiments with ATZ, which took ~2.5 weeks. In the cases of IBP (pK_a ~4.4; NIST, 2004), APAP (pK_a ~9.5; Jones et al., 2002), CLO (pK_a ~3.2; Lewis et al., 2016) and 2NBA the solutions were prepared weekly by direct weighting, thanks to their higher water solubility than ATZ. All the stock solutions were kept refrigerated (~5 °C) in the dark when not used. Finally, the solutions for

the irradiation experiments were adjusted to pH 7 with NaOH 0.1 mol L^{-1} and used the same day they were prepared. Note that IBP and CLO were in their carboxylate forms when irradiated. The pH measurements were performed with a combined glass electrode connected to a Metrohm 602 pH meter, calibrated daily with standard buffers at pH = 4.01, 7.00 and 10.00 (Fluka).

2.2.2 Determination of the second-order rate constant of the reaction between each water contaminant and ^{3}CBBP*

A new protocol aimed at determining the second-order rate constants of the ^{3}CBBP*-induced degradation of water pollutants has been recently developed (Minella et al., 2018). In this work, such a protocol was used to assess the rate constant of the reaction ^{3}CBBP* + S, with S = IBP, APAP, CLO and ATZ.
The method consists in experiments of steady irradiation (UVA light) of aqueous solutions containing CBBP (70 μmol L^{-1}) as photosensitizer, and different concentrations of the investigated contaminant S ($[S]$) (Minella et al., 2018). Upon UVA-light absorption, CBBP reaches its lowest-energy excited singlet state, which undergoes inter-system crossing (ISC) producing the excited triplet state ^{3}CBBP*. The quantum yield of this process ($\Phi_{(^3CBBP^*)}$) is close to unity, making CBBP an effective triplet-photosensitizer (Marciniak et al., 1994). ^{3}CBBP* can undergo two main deactivation pathways, namely *(i)* thermal decay, with rate constant $k'_d = 6\times10^5$ s^{-1} (Minella et al., 2018), and *(ii)* reaction with S. The former is due to collision/reaction with the surrounding molecules and, in particular, 68% of ^{3}CBBP* reacts with dissolved triplet O_2 through triplet-to-triplet energy transfer. The remaining fraction of ^{3}CBBP* (32%) is likely deactivated by internal conversion. Note that collision with O_2 produces singlet oxygen ($^1O_2$) with yield S_Δ = 0.46

(Minella et al., 2018). Under common experimental conditions (*vide infra*), thermal deactivation prevails over reaction with S. The latter usually occurs through (proton-coupled) electron transfer, producing the oxidized forms of S (S_{ox}) and the ketyl radical of CBBP ($CBBP^{\bullet-}$) (Canonica et al., 2000; Heeb and Peters, 2006). Finally, $CBBP^{\bullet-}$ produces again ground-state CBBP by reducing dissolved dioxygen to the superoxide radical anion ($O_2^{\bullet-}$), but $CBBP^{\bullet-}$ may undergo further transformations as well. Scheme 2.2.1 shows these reaction pathways that are at the basis of the kinetic model, from which the second-order rate constant of the reaction ^{3}CBBP* + S (i.e., $k_{(^3CBBP^*+S)}$) was derived.

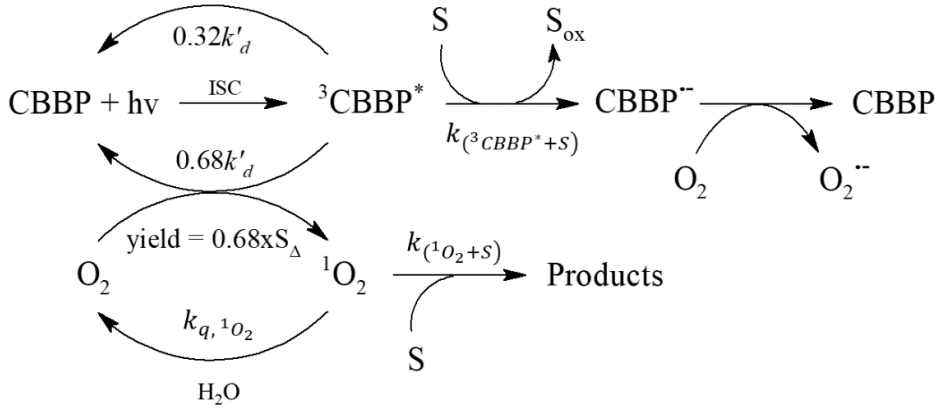

Scheme 2.2.1 Possible reaction pathways taking place in the irradiated solutions.

The net transformation rate of S (R_S) is accounted for by the reactions ^{3}CBBP* + S (with rate $R_{(^3CBBP^*+S)}$) and $^1O_2$ + S (with rate $R_{(^1O_2+S)}$ and second-order rate constant $k_{(^1O_2+S)}$) (Eq. 2.2.1). Here, S direct photolysis and hydrolysis are not considered (no obvious degradation of IBP, APAP, ATZ and CLO by direct photolysis and/or hydrolysis was observed, *vide infra*), but they should be included as part of R_S if the investigated compound is unstable towards these reactions.

$$R_S = R_{(^3CBBP^*+S)} + R_{(^1O_2+S)}$$
$$= [S] \times \left(k_{(^3CBBP^*+S)}[^3CBBP^*] + k_{(^1O_2+S)}[^1O_2]\right) \quad \text{(Eq. 2.2.1)}$$

Steady-state conditions for both $[^3CBBP^*]$ (Eq. 2.2.2) and $[^1O_2]$ (Eq. 2.2.3) were provided by: *(i)* steady irradiation; *(ii)* quite high concentration of CBBP; *(iii)* partitioning of dioxygen between the irradiated solution and the headspace of the glass cell; *(iv)* regeneration of the CBBP ground-state after ^{3}CBBP* quenching; *(v)* continuous formation of $^1O_2$ upon CBBP irradiation, and *(vi)* fast quenching of $^1O_2$ by water.

$$[^3CBBP^*] = \frac{\Phi_{(^3CBBP^*)} \times P_{a,CBBP}}{k_{(^3CBBP^*+S)} \times [S] + k_d'} \quad \text{(Eq. 2.2.2)}$$

$$[^1O_2] = [^3CBBP^*] \times \frac{0.68 \times S_\Delta \times k_d'}{k_{(^1O_2+S)} \times [S] + k_{q,^1O_2}} \quad \text{(Eq. 2.2.3)}$$

$P_{a,CBBP}$ is the rate of photon absorption (E L^{-1} s^{-1}) by CBBP (*vide infra* for its calculation), while $k_{q,^1O_2}$ = 2.5×10^5 s^{-1} is the quenching rate constant of singlet oxygen due to collisions with water molecules (Wilkinson et al., 1995). The remaining parameters were defined above. For low values of $[S]$, the thermal deactivation of both ^{3}CBBP* and $^1O_2$ prevails over their quenching by S, and thus $k_{(^3CBBP^*+S)} \times [S] + k_d' \approx k_d'$ and $k_{(^1O_2+S)} \times [S] + k_{q,^1O_2} \approx k_{q,^1O_2}$. For instance, when $[S]$ = 20 µmol L^{-1}, if $k_{(^3CBBP^*+S)}$ = 5×10^9 L mol^{-1} s^{-1} and $k_{(^1O_2+S)}$ = 1×10^8 L mol^{-1} s^{-1}, quenching by S accounts for ~14% and ~8% of the overall deactivation of ^{3}CBBP* and $^1O_2$, respectively. Therefore,

because the experimental uncertainty is usually 15-20%, one can conclude that quenching by S can be negligible.

Under these assumptions, by substituting Eqs. 2.2.2 and 2.2.3 in Eq. 2.2.1, one gets:

$$R_S = [S] \times P_{a,CBBP} \times \left(\frac{k_{(^3CBBP^*+S)}}{k_d'} + \frac{k_{(^1O_2+S)} \times 0.68 \times S_\Delta}{k_{q,^1O_2}} \right) \quad \text{(Eq. 2.2.4)}$$

The plot of R_S *vs.* $[S]$ would be thus a straight line with slope m (s^{-1}):

$$m = P_{a,CBBP} \times \left(\frac{k_{(^3CBBP^*+S)}}{k_d'} + \frac{k_{(^1O_2+S)} \times 0.68 \times S_\Delta}{k_{q,^1O_2}} \right) \quad \text{(Eq.2.2.5)}$$

If $k_{(^1O_2+S)}$ is known, the rate constant $k_{(^3CBBP^*+S)}$ can be obtained by rearranging Eq. 2.2.5 as follows (Minella et al., 2018):

$$k_{(^3CBBP^*+S)} = k_d' \times \left(\frac{m}{P_{a,CBBP}} - \frac{k_{(^1O_2+S)} \times 0.68 \times S_\Delta}{k_{q,^1O_2}} \right) \quad \text{(Eq. 2.2.6)}$$

2.2.3 Irradiation Experiments

Aqueous solutions (5 mL, pH 7) containing CBBP (70 µmol L^{-1}) and the investigated compound S (i.e., S = IBP, APAP, CLO or ATZ) were put in Pyrex glass cells (4.0 cm diameter, 2.4 cm height) and irradiated under a 18W Philips TL-D UVA lamp, with emission maximum at 369 nm. The UV irradiance on top of the solutions was measured with an irradiance meter by CO.FO.ME.GRA. (Milan, Italy), and it was = 40.5 ± 2.5 W m^{-2}. During

irradiation, the water temperature was ~30 °C. Fig.2.2.1 shows a schematic of the irradiation set-up. At scheduled times the glass cells were withdrawn from the irradiation system, and the solutions were analyzed for the quantification of S by means of HPLC-DAD (*vide infra*). Samples were analyzed after a few hours from their collection.

Direct photolysis experiments (i.e., irradiation of aqueous solutions containing only S) and dark runs (as before for CBBP + S, but with the glass cells wrapped with double aluminum foil) were carried out under the same irradiation conditions.

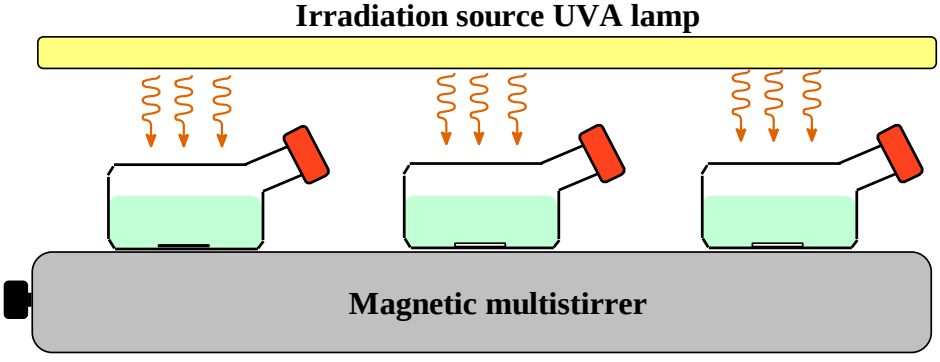

Fig.2.2.1 Schematic of the irradiation system used for the experiments.

The temporal profiles of S concentration ($[S]$) showed pseudo-first order kinetic behavior, as $[S] = [S]_0 \times e^{-k\prime \times t}$, where $[S]_0$ is the initial concentration of S (from ~3 to ~100 μmol L^{-1}, *vide infra* for further details), k' is the pseudo-first order rate constant of S photodegradation, and t is the irradiation time. After computing k' from the data fit of $[S]$ *vs.* t, the initial S degradation rate was calculated as $R_S = k' \times [S]_0$.

2.2.4 Actinometric measurements

2-Nitrobenzaldehyde (2NBA) was used as chemical actinometer to assess the actual spectral photon flux density (units of E L^{-1} s^{-1} nm^{-1}) occurring in the irradiated solutions (Kuhn et al., 2004; Willett and Hites, 2000). 2NBA has been successfully used in previous works as chemical actinometer, in both aqueous solutions and to study ice photochemistry (Allen et al., 2000; Galbavy et al., 2010; Marchisio et al., 2015; Rowland and Grannas, 2011). The fast photoisomerization of 2NBA into 2-nitrosobenzoate under UV irradiation (Allen et al., 2000; Xiang et al., 2009) allows for computing the absorbed spectral light dose, by measuring the photodegradation rate of 2NBA itself.
The emission spectrum of the lamp was taken with an Ocean Optics USB 2000 CCD spectrophotometer, and corrected for the transmittance of the Pyrex window of the irradiation cells. Take $i°(\lambda)$ as the spectral light dose emitted by the lamp. The units of $i°(\lambda)$ can be arbitrary, but they are however proportional to the photon count. $i°(\lambda)$ does not equal the actual spectral photon flux density occurring in the irradiated solution, which is $p°(\lambda)$ (E L^{-1} s^{-1} nm^{-1}). This happens because photons, during their way from the lamp to the bulk solution, undergo scattering processes at the interfaces air-glass, air-water, and water-glass. Moreover, when a photon reaches the bottom of the solution (water-glass interface) it can be reflected backward, passing through the bulk solution again and triggering photochemical reactions. Consequently, one has $p°(\lambda) = \theta \times i°(\lambda)$, where θ is a correction parameter that implicitly considers all the scattering/back-reflection phenomena. Although θ might theoretically be wavelength-dependent, here it was considered as a spectral constant.

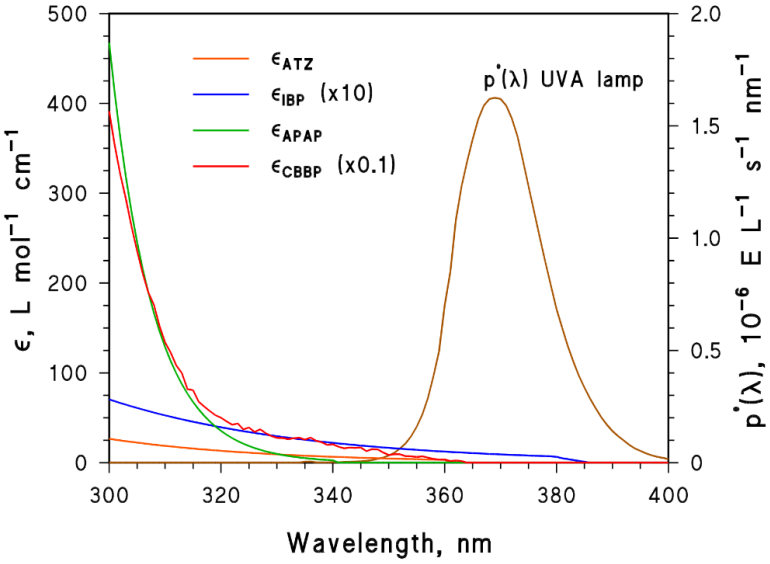

Fig.2.2.2 *Left Y-axis*: molar absorption coefficients of ATZ, IBP, APAP and CBBP. The data for CLO are not shown because the compound does not absorb light with λ > 300 nm. *Right Y-axis*: actinometric spectral photon flux density $p°(\lambda)$ of the used 18W Philips TL-D UVA lamp.

To assess θ, one has to measure both the depletion rate of 2NBA (R_{2NBA}) from the experimental photodegradation profile, and the apparent rate of photon absorption by 2NBA ($P_{a,2NBA}$, units of $i°(\lambda) \times$ nm; Eq. 2.2.7). It should be pointed out that R_{2NBA} has to be measured from the depletion profile of 2NBA until 30% of degradation (Marchisio et al., 2015). For a degradation extent > 30%, the solution composition is too different compared to the beginning of the experiment, which makes the used kinetic model unsuitable for accurate actinometry. Indeed, 2-nitrosobenzoate (the product of 2NBA photoisomerization) is able to absorb UV radiation and, as a consequence of this inner-filter effect, to slow down the rate of 2NBA photodegradation.

$$P_{a,2NBA} = \int_{\lambda} i°(\lambda) \times [1 - 10^{-b \times \varepsilon_{2NBA}(\lambda) \times [2NBA]}] d\lambda \qquad \text{(Eq. 2.2.7)}$$

In Eq. 2.2.7, $\varepsilon_{2NBA}(\lambda)$ is the molar absorption coefficient (L mol^{-1} cm^{-1}) of 2NBA, b = 0.4 cm is the optical path of radiation inside the irradiated aqueous solutions within the glass cells (5 mL volume), and $[2NBA]$ = 100 μmol L^{-1} is the initial concentration of 2NBA. Note that the adopted $[2NBA]$ is suitable to assess an average value of $p°(\lambda)$ in the solution bulk: higher values of $[2NBA]$ (such as 0.1 mol L^{-1}) would in fact lead to complete light extinction in the upper layer of the irradiated solution, thereby leading to a $p°(\lambda)$ spectrum that would be representative of this part only (Galbavy et al., 2010). Because $R_{2NBA} = \Phi_{2NBA} \times \theta \times P_{a,2NBA}$, where Φ_{2NBA} = 0.4 is the direct photolysis quantum yield of 2NBA (Allen et al., 2000), one has:

$$\theta = \frac{R_{2NBA}}{\Phi_{2NBA} \times P_{a,2NBA}} = \frac{R_{2NBA}}{\Phi_{2NBA} \times \int_{\lambda} i°(\lambda) \times [1 - 10^{-b \times \varepsilon_{2NBA}(\lambda) \times [2NBA]}] d\lambda} \quad \text{(Eq. 2.2.8)}$$

Fig.2.2.2 shows the actinometric $p°(\lambda)$ spectrum that is relevant to the conditions of the irradiation experiments of IBP, APAP, CLO and ATZ. The overall photon flux density (the area under the $p°(\lambda)$ curve in Fig.2.2.2) was (3.21±0.15)×10^{-5} E L^{-1} s^{-1}.

2.2.5 High-Pressure Liquid Chromatography - Diode Array Detection (HPLC-DAD) analysis

The HPLC-DAD instrument used for compounds quantification was a VWR-Hitachi LaChrom Elite chromatograph, equipped with L-2200 autosampler (injection volume 60 μL), L-2130 quaternary pump for low-pressure gradients, Duratec vacuum degasser, L-2300 column oven (set at 40 °C), and L-2455 photodiode array detector. The column was a VWR LiChroCART

125-4 Cartridge (125mm×4mm), packed with LiChrospher 100 RP-18 (5µm as particle diameter).

A mixture of (A) water acidified at pH ~2.8 with H_3PO_4 and (B) methanol was used as eluent for analysis, at a flow rate of 1.0 mL min^{-1}. The chromatographic conditions for the different compounds, retention times (t_r) and quantification wavelengths (λ_q) were as follows (the column dead time was 1.5 min):

1. IBP + CBBP. Isocratic elution: 37.5% A and 62.5% B. IBP: t_r = 4.0 min and λ_q = 220 nm. CBBP: 11.3 min and 262 nm.
2. APAP + CBBP. Gradient elution: 10% B for 4 min, up to 70% B in 1.5 min, keep for 4 min, down to 10% B in 2 min, keep for 4.5 min. APAP: t_r = 4.8 min and λ_q = 245 nm. CBBP: 9.9 min and 262 nm.
3. CLO + CBBP. Gradient elution: 30% B for 4 min, up to 55% B in 0.1 min, keep for 10.9 min, down to 30% B in 0.1 min, keep for 1.9 min. CLO: t_r = 12.8 min and λ_q = 227 nm. CBBP: 12.1 min and 262 nm.
4. ATZ + CBBP. Isocratic elution: 60% A and 40% B. ATZ: t_r = 19.8 min and λ_q = 220 nm. CBBP: 27.3 min and 262 min.
5. 2NBA. Isocratic elution: 70% A and 30% B. 2NBA: t_r = 5.4 min and λ_q = 230 nm.

2.2.6 UV-Vis absorption measurements

A Varian Cary 100 Scan UV-Vis spectrophotometer, equipped with Hellma quartz cuvettes with a path length of 1 cm, was used to measure the absorption spectra of the studied compounds. For the determination of molar absorption coefficients, each spectrum was corrected for the blank signals, and only the signals that were higher than the signal corresponding to the limit of

quantification (LoQ) were considered for calculations. The LoQ signals were estimated for each wavelength as $LoQ_\lambda = \mu_{b,\lambda} + 10\times\sigma_{b,\lambda}$, where $\mu_{b,\lambda}$ and $\sigma_{b,\lambda}$ are the wavelength-dependent mean signal and the associated standard deviation, respectively, of five replicates of the blank.

2.2.7 Laser flash photolysis (LFP) experiments

The LFP measurements and the associated data treatment to obtain the rate constants of ^{3}CBBP* quenching by the investigated water pollutants were carried out by Prof. Mohamed Sarakha (University of Auvergne, Blaise Pascal University, France) and Miss Silvia Comis (University of Torino, Italy) at the Institut de Chimie de Clermont-Ferrand (France). The time evolution of ^{3}CBBP* on a sub-μs scale was assessed using the third harmonic (355 nm) of a Quanta Ray GCR 130-01 Nd:YAG laser system instrument, used in a right-angle geometry with respect to the monitoring light beam. The single pulses energy was set to 35-40 mJ. A solution aliquot (3 mL) containing 0.1 mmol L^{-1} CBBP in water at pH ~7 was placed into a quartz cuvette (path length of 1 cm) and used for a maximum of four consecutive laser shots. Where applicable, the solution also contained variable concentrations of ^{3}CBBP* quenchers (i.e., ATZ, APAP, and IBP). The absorbance of ^{3}CBBP* at two alternative wavelengths (340 nm in the case of ATZ and IBP, 480 nm for APAP, to limit spectral interferences) was monitored over time by a detection system consisting of a pulsed xenon lamp (150 W), monochromator and photomultiplier (1P28). A spectrometer control unit was used for synchronizing the pulsed light source and programmable shutters with the laser output. The signal from the photomultiplier was digitized by a programmable digital oscilloscope (HP54522A). A 32 bits RISC-processor kinetic spectrometer workstation was used to analyze the digitized signal. A

Stern-Volmer approach was used to assess the quenching rate constant of the reaction ^{3}CBBP* + S, where S = IBP, APAP or ATZ. In particular, the decay of ^{3}CBBP* was monitored at different concentration values of S (i.e., the quencher), and the measured pseudo-first order quenching constant of ^{3}CBBP* (k_q) was reported as a function of the quencher concentration. The slopes of the linearly fitted data of k_q *vs.* [S] gave the second-order quenching rate constants of ^{3}CBBP* by IBP, APAP and ATZ ($k^q_{(^3CBBP^*+S)}$).

2.2.8 Photochemical modeling

The obtained values of $k_{(^3CBBP^*+S)}$ were used to model the photochemical fate of the investigated compounds in surface waters. The "*Aqueous Photochemistry of Environmentally occurring Xenobiotics"* (APEX) software (Bodrato and Vione, 2014; Vione, 2020) was used to this purpose. Overall, APEX is a suitable tool for modeling the photodegradation of pollutants in well-mixed surface waters, such as a lake epilimnion or a river. It has been previously used to assess the environmental fate of several photolabile xenobiotics, and the results have been validated for those compounds of which field data of photodegradation kinetics are known (Table 2.2.1). In particular, comparison between model results and data measured on the field have allowed for validation in the cases of carbamazepine (De Laurentiis et al., 2012a), ibuprofen (Vione et al., 2011), diclofenac and naproxen (Avetta et al., 2016), atrazine (Marchetti et al., 2013), 2-methyl-4-chlorophenoxyacetic acid (MCPA) (De Laurentiis et al., 2013b), and bentazon (Carena et al., 2020), as well as of pesticide phototransformation intermediates such as 2,4-dichloro-6-nitrophenol (Maddigapu et al., 2011), 2-nitro-4-chlorophenol (Sur et al., 2012), and 3,4-dichloroaniline (Carena et al., 2018).

Table 2.2.1 Comparison between the photochemical half-life time values modeled with APEX and those measured in the field, for some of the contaminants reported in the text.

Compound	Photochemical half-life time, days		Location	Ref.
	Model	Field		
Ibuprofen	60 ± 10	60 - 115	Lake Greifensee	(Vione et al., 2011)
Carbamazepine	110 ± 45	140 ± 50	Lake Greifensee	(De Laurentiis et al., 2012a)
Atrazine	17 ± 4	20 - 21	Chesapeake Bay (1 m depth)	(Marchetti et al., 2013)
	64 ± 18	67 - 100	Chesapeake Bay (10 m depth)	
Bentazon	6-20	5-15	Rhône delta	(Carena et al., 2020)

The complete set of kinetic equations used by APEX is described in detail in the user guide of the software, available for free as supporting electronic information to a recent paper by Vione (2020). Moreover, a similar mathematical approach is described in Chapter 4, where the photochemical modeling of surface waters is addressed in more detail. Very briefly, APEX requires as input data some photochemical parameters of the investigated compound (namely, direct photolysis apparent quantum yield, second-order rate constants of the reactions with the main PPRIs, and absorption spectrum), as well as environmental features of the water body (water depth and concentration of photosensitizers and scavengers, such as DOM, nitrate, nitrite, bicarbonate and carbonate). As far as sunlight is concerned, the model uses a *summer sunny day* (SSD) scenario that stems from an average solar spectrum reaching the ground on the 15th of July, with clear sky, at 45 °N latitude. From the model one gets both the half-life times and the pseudo-first

order rate constants of xenobiotic photodegradation, as well as the role of the different photochemical pathways in the process, as functions of the water chemical composition and depth (Bodrato and Vione, 2014; Vione, 2020).

2.3 Results and Discussion

2.3.1 Second-order rate constants of the reaction ^{3}CBBP* + S (S = IBP, APAP, CLO, ATZ)

Fig.2.3.1 shows the temporal profiles of the ^{3}CBBP*-induced degradation of IBP, APAP, CLO and ATZ, each of them used at different initial concentration values. No obvious direct photolysis of the studied compounds was observed at either their lowest or highest concentration values, mainly because of the poor overlap between absorption spectra and the lamp emission spectrum (see Fig.2.2.2). Indeed, direct photolysis of IBP, APAP and ATZ takes place under UVB radiation (λ < 320 nm), where both their molar absorption coefficients and, sometimes, also the apparent quantum yields are higher than under UVA (De Laurentiis et al., 2014b; Marchetti et al., 2013; Vione et al., 2011). CLO does not undergo significant direct photolysis, even in the UVB region of the spectrum (Avetta et al., 2016). Moreover, during the dark runs the studied compounds were stable towards hydrolysis. This likely happened beucase the solutions pH was ~7 and temperature ~30 °C, in which conditions the chemical hydrolysis of organic compounds is usually very slow (Clayden et al., 2012).

The degradation rate values were computed by fitting the data of Fig.2.3.1 with pseudo-first order kinetics, and were found to be linearly dependent on the initial concentration values of IBP, CLO and ATZ (Figs.2.3.2a;c;d). For these compounds linearity held well in the whole adopted concentration range, which means that the rate constants k' of S degradation did not change much with $[S]_0$, although they were not strictly constant (Fig.2.3.1). The issue is that the experimental variation of k' was lower than the variation of $[S]_0$, as k' varied by a factor of 1.7 (IBP) or 2 (CLO, ATZ), while at the same time the

$[S]_0$ variation factor was as large as 7.5 (ATZ), 25 (CLO), or 28 times (IBP). Therefore, the important $[S]_0$ variations overcame those of k' to produce the observed, practically linear trends.

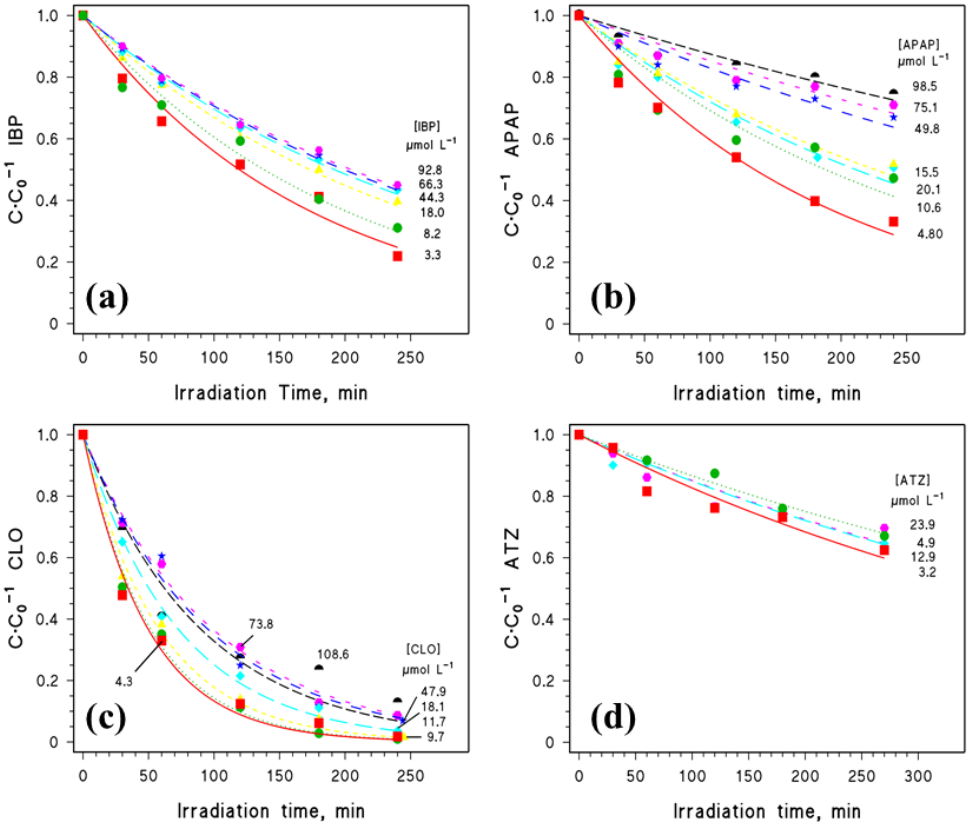

Fig.2.3.1 Temporal profiles of **(a)** IBP, **(b)** APAP, **(c)** CLO and **(d)** ATZ photodegradation due to reactions with ^{3}CBBP*. The initial concentration value of the organic substrate for each experiment is reported next to the relevant curve. The curves represent the pseudo-first order fit of the experimental data.

In the case of APAP, a good linearity was found only for [APAP] ≤ 20 µmol L^{-1} (Fig.2.3.2b), while at higher concentration values the curve R_{APAP} *vs.* [APAP] had a plateau trend. In the linear portion of the APAP curve k' varied by 1.6 times, while [APAP] varied by a factor of 4.2.

From the slope (m, s^{-1}) of the linear trends reported in Fig.2.3.2, the values of the second-order rate constants $k_{(^3CBBP^*+S)}$ were obtained for each compound through Eq. 2.2.6 (see Table 2.3.1 for the results). In particular, the photon absorption rate by CBBP ($P_{a,CBBP}$, E L^{-1} s^{-1}) was calculated as the integral $P_{a,CBBP} = \int_\lambda p°(\lambda) \times [1 - 10^{-b \times \varepsilon_{CBBP}(\lambda) \times [CBBP]}] d\lambda$.

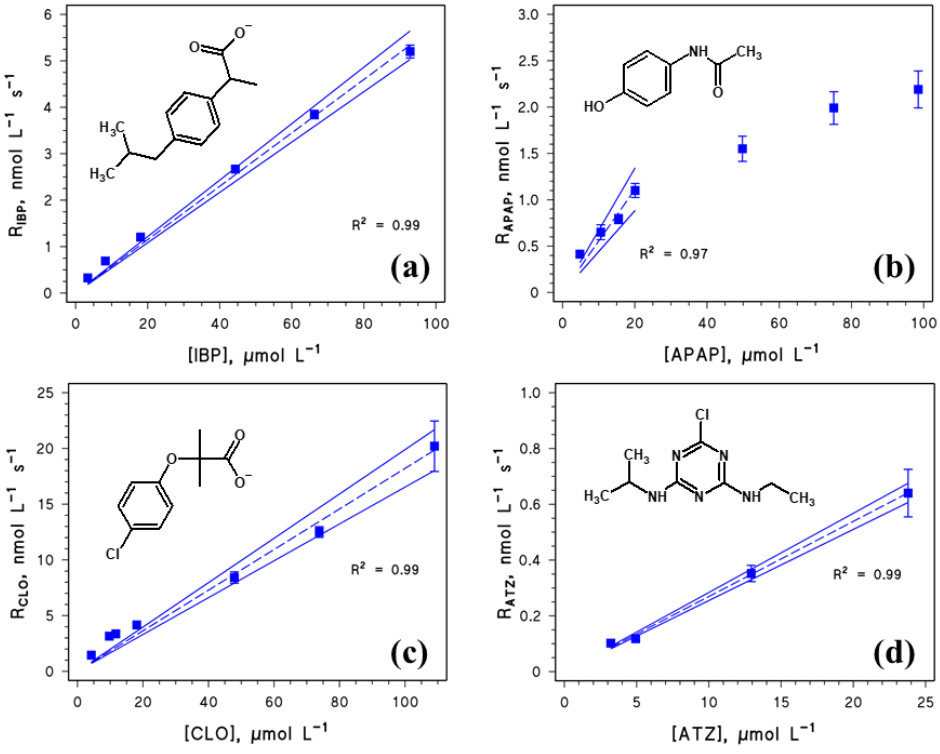

Fig.2.3.2 Dependence of the photodegradation rate R_S on the initial S concentration [S], for **(a)** IBP, **(b)** APAP, **(c)** CLO and **(d)** ATZ. The dotted lines represent the data-fit curves, while the solid lines are the 95% confidence bands of the fit. The R^2 parameter, which was close to unity in all the cases, shows the goodness of the fit.

All the values of the parameters used to calculate $P_{a,CBBP}$ were described in the previous sections. The inner-filter effect due to the presence of the organic

substrates (S) was neglected, because of poor light-absorption of S in the wavelength region where the UVA lamp emits radiation.

Interestingly, the values of $k_{(^3CBBP^*+S)}$ obtained with steady irradiation experiments were comparable with those measured by means of the LFP technique ($k^q_{(^3CBBP^*+S)}$, see Table 2.3.1). In the cases of APAP and ATZ, $k^q_{(^3CBBP^*+S)}$ was ~1.7× $k_{(^3CBBP^*+S)}$, which is reasonably accounted for by the fact that $k^q_{(^3CBBP^*+S)}$ takes into account both chemical and physical quenching. For IBP, instead, it was $k^q_{(^3CBBP^*+S)} \sim k_{(^3CBBP^*+S)}$. These findings show that the method applied here gives reasonable values of $k_{(^3CBBP^*+S)}$, and it has the considerable advantage of allowing for the determination of $k_{(^3CBBP^*+S)}$ with widely available instrumentation. Actually, time-resolved techniques such as LFP and pulse radiolysis require expensive instrumentation, and by measuring $k^q_{(^3CBBP^*+S)}$ they often overestimate $k_{(^3CBBP^*+S)}$ because of physical quenching.

Table 2.3.1 Kinetic parameters measured for IBP, APAP, CLO and ATZ, obtained by using Eq. 2.2.6 or representing the needed input data for the same equation. The second-order rate constants determined by means of steady irradiation experiments ($k_{(^3CBBP^*+S)}$) and those measured with LFP ($k^q_{(^3CBBP^*+S)}$) are reported for comparison, which is discussed in the text.

S	m, 10^{-5} s^{-1}	$P_{a,CBBP}$, 10^{-8} E L^{-1} s^{-1}	$k_{(^1O_2+S)}$, 10^5 L mol^{-1} s^{-1}	$k_{(^3CBBP^*+S)}$, 10^9 L mol^{-1} s^{-1}	$k^q_{(^3CBBP^*+S)}$, 10^9 L mol^{-1} s^{-1}
IBP	5.46 ± 0.06	2.18 ± 0.10	0.60 ± 0.06 [(a)]	1.53 ± 0.02	1.5
APAP	5.55 ± 0.36	2.13 ± 0.10	368 ± 73 [(b)]	1.56 ± 0.07	2.5
CLO	18.2 ± 0.7	2.12 ± 0.10	6.0 ± 1.9 [(c)]	5.23 ± 0.20	/
ATZ	2.49 ± 0.15	2.12 ± 0.10	< 0.4 [(d)]	0.72 ± 0.04	1.2

(a) Vione et al., 2011; (b) De Laurentiis et al., 2014; (c) Avetta et al., 2016; (d) Marchetti et al., 2013.

2.3.2 CBBP as model proxy-molecule for CDOM: comparison with anthraquinone-2-sulfonate (AQ2S)

The triplet state ^{3}AQ2S* has been used in several previous works as ^{3}CDOM* proxy, to assess the reactivity of water pollutants towards ^{3}CDOM* (Avetta et al., 2016; De Laurentiis et al., 2014b, 2012a; Gornik et al., 2020; Marchetti et al., 2013). However, there is evidence that ^{3}AQ2S* is more reactive than average ^{3}CDOM* (Avetta et al., 2016), causing an overestimation of the second-order reaction rate constants with ^{3}CDOM* themselves. This issue is likely due to the quite high one-electron reduction potential of ^{3}AQ2S* ($E^o_{^3AQ2S*/AQ2S^{\bullet-}}$ ~2.3 V vs. SHE; McNeill and Canonica, 2016) compared to

average ^{3}CDOM* ($E^o_{^3CDOM*/CDOM^{\bullet-}}$ ~1.4-1.9 V vs. SHE; Canonica et al., 2000). Indeed, because the reactions between ^{3}AQ2S*/^{3}CDOM* and organic substrates, such as phenols, anilines and sulfonamides usually occur through (proton-coupled) one-electron transfer (Canonica, 2007; Canonica et al., 2000; McNeill and Canonica, 2016; Wenk and Canonica, 2012), one has that by increasing the reduction potential difference between the redox couples involved in the reaction the electron transfer process gets faster (Eberson, 1982). For this reason, by using a strong oxidant such as ^{3}AQ2S* one can easily overestimate the ^{3}CDOM* rate constants. On the contrary, ^{3}CBBP* has a one-electron reduction potential $E^o_{^3CBBP*/CBBP^{\bullet-}}$= 1.84 V vs. SHE (McNeill and Canonica, 2016), which is lower than that of ^{3}AQ2S* and well within the reduction potential range of typical ^{3}CDOM*. Therefore, the rate constants of the reactions between ^{3}CBBP* and organic pollutants should be lower than those measured with ^{3}AQ2S*, and also more representative of the environmental scenarios.

Fig.2.3.3 compares the second-order rate constants of the reactions of IBP, APAP, CLO and ATZ with both ^{3}CBBP*, measured in this work, and ^{3}AQ2S* ($k_{(^3AQ2S^*+S)}$), reported in the literature. In all the cases, $k_{(^3CBBP^*+S)} < k_{(^3AQ2S^*+S)}$ as expected from the thermodynamic considerations reported above.

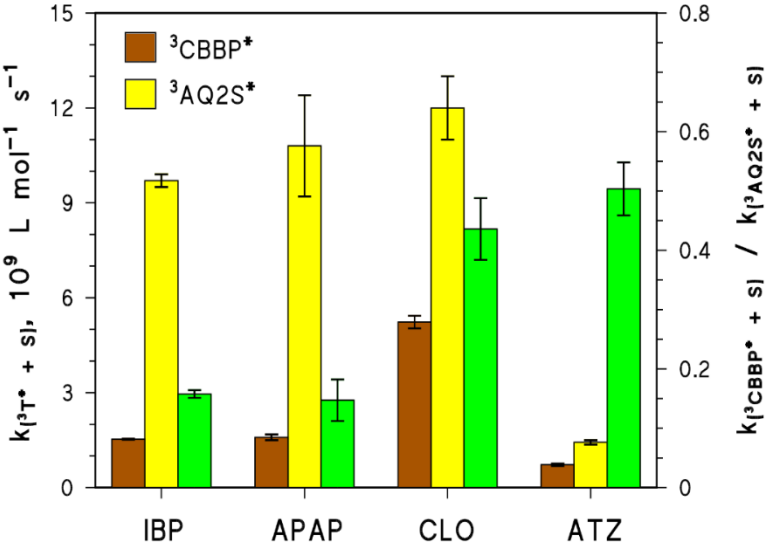

Fig.2.3.3 *Left Y-axis*: second-order rate constants of S = IBP, APAP, CLO or ATZ, for the reactions with ^{3}T* = ^{3}CBBP* (brown bars) or ^{3}AQ2S* (yellow bars). The values of $k_{(^3AQ2S^*+S)}$ were taken from the literature (Avetta et al., 2016; De Laurentiis et al., 2014b; Marchetti et al., 2013; Vione et al., 2011). *Right Y-axis*: ratio between $k_{(^3CBBP^*+S)}$ and $k_{(^3AQ2S^*+S)}$ (green bars).

In particular, $k_{(^3CBBP^*+S)}$ ~0.15× $k_{(^3AQ2S^*+S)}$ for IBP and APAP, while $k_{(^3CBBP^*+S)}$ ~0.45× $k_{(^3AQ2S^*+S)}$ for CLO and ATZ. Furthermore, note that the $k_{(^3AQ2S^*+S)}$ values for IBP, APAP and CLO are close to the diffusion-control limit of ~10^{10} L mol^{-1} s^{-1} for bimolecular reactions in aqueous solution (Buxton et al., 1988). Although such values respect the boundary conditions for reactions in water, they are probably poorly representative of quite big and complex structures as can be found in typical components of the natural CDOM, which act as ^{3}CDOM* precursors. In contrast, for all the investigated compounds one has $k_{(^3CBBP^*+S)} \leq 5\times10^9$ L mol^{-1} s^{-1}, which is a value that has been proposed as a possible upper limit for the reactions involving ^{3}CDOM* + S (Canonica et al., 2000).

Previous studies have shown that IBP is photodegraded by HO$^{\bullet}$ radicals, direct photolysis and irradiated fulvic acids (Jacobs et al., 2011; Packer et al., 2003), thereby suggesting that $k_{(^3CDOM^*+IBP)}$ should be at least 10^8 L mol^{-1} s^{-1} (and more likely quite higher than that; Vione et al., 2011). However, there is also evidence that the reactivity of IBP with ^{3}CDOM* is overestimated when AQ2S is used as CDOM-proxy molecule ($k_{(^3AQ2S^*+IBP)}$ ~9.7×10^9 L mol^{-1} s^{-1}; Vione et al., 2011). Therefore, the value obtained in this work ($k_{(^3CBBP^*+S)}$ ~1.5×10^9 L mol^{-1} s^{-1}) looks reasonable because it respects the boundary conditions that can be derived by the analysis of the existing literature.

The case of ATZ is very interesting, because the values $k_{(^3CBBP^*+ATZ)}$ and $k_{(^3AQ2S^*+ATZ)}$ can be compared with an independent estimate of $k_{(^3CDOM^*+ATZ)}$ reported in the literature. Zeng and Arnold (2013) have in fact determined $k_{(^3CDOM^*+ATZ)}$ ~1.2×10^9 L mol^{-1} s^{-1} as an average value of several CDOM samples, either collected in prairie potholes or purchased as standard materials from the International Humic Substances Society (IHSS). The available value of $k_{(^3CDOM^*+ATZ)}$ is quite closely bracketed by those of $k_{(^3AQ2S^*+ATZ)}$ ~1.4×10^9 L mol^{-1} s^{-1} (Marchetti et al., 2013) and $k_{(^3CBBP^*+ATZ)}$ ~0.7×10^9 L mol^{-1} s^{-1} (this work). It is thus suggested that, at least in the case of ATZ, both CBBP and AQ2S would be good CDOM proxy molecules to assess the reactivity of ^{3}CDOM*. However, in general one has that ^{3}CBBP* is more representative of average ^{3}CDOM* compared to ^{3}AQ2S*, as shown by the cases of IBP, APAP and CLO (this work), as well as naproxen (Avetta et al., 2016).

2.3.3 Re-examination of the importance of ^{3}CDOM* in the photochemical fate of water pollutants

The results of this work and the available data from the literature suggest that CBBP may be a viable proxy molecule to assess the reactivity of ^{3}CDOM* with organic pollutants. Unfortunately, up to now the photochemical fate of water pollutants has been often assessed on the basis of ^{3}AQ2S*-reactivity data (Avetta et al., 2016; De Laurentiis et al., 2014b; Marchetti et al., 2013; Vione et al., 2011). Because ^{3}AQ2S* is expected to overestimate the reactivity of actual ^{3}CDOM* (Avetta et al., 2016; McNeill and Canonica, 2016), it is very interesting to check the results of photochemical modeling when carried out with the ^{3}CBBP* reactivity data obtained in this work, comparing them with previous estimates based on ^{3}AQ2S*.

Table 2.3.2 Second-order reaction rate constants with $HO^\bullet$ and $CO_3^{\bullet-}$ ($k_{(HO^\bullet+S)}$ and $k_{(CO_3^{\bullet-}+S)}$, respectively) and apparent direct photolysis quantum yield (Φ_S) for S = IBP, APAP, CLO and ATZ used in the photochemical model. See previous sections for the photoreactivity parameters of S with T* and $^1O_2$.

S	$k_{(HO^\bullet+S)}$, 10^9 L mol^{-1} s^{-1}	$k_{(CO_3^{\bullet-}+S)}$, 10^7 L mol^{-1} s^{-1}	Φ_S, 10^{-2}
IBP (a)	10 ± 3.0	Negligible	3.3 ± 0.5
APAP (b)	1.87 ± 0.56	38 ± 11	4.57 ± 0.17
CLO (c)	7	Negligible	0.55
ATZ (d)	2.7 ± 0.3	0.4	1.58 ± 0.19

(a) Vione et al., 2011; (b) De Laurentiis et al., 2014; (c) Avetta et al., 2016; (d) Marchetti et al., 2013.

By using the APEX software (Bodrato and Vione, 2014; Vione, 2020), here we compare a scenario where $k_{(^3CDOM^*+S)} = k_{(^3AQ2S^*+S)}$ (AQ2S proxy), and a scenario where $k_{(^3CDOM^*+S)} = k_{(^3CBBP^*+S)}$ (CBBP proxy). The additional photochemical parameters used for the modeling of the investigated compounds are reported in Table 2.3.2. Computations were carried out for two aqueous systems, namely a shallow water body (water depth d = 0.5 m) and a deeper one (d = 5 m). The dissolved organic carbon (DOC), which quantifies the (C)DOM content within APEX (Vione, 2020), ranged between 1 and 10 $mg_C\ L^{-1}$. The latter is an interval that can be considered representative of the conditions found in lakes located in temperate areas, with a variety of trophic statuses (Wetzel, 2001).

Fig.2.3.4 shows the model results for APAP phototransformation in surface waters. The AQ2S- and CBBP-based scenarios are quite different overall, and significantly slower phototransformation is predicted in the case of CBBP. This is due to lower reactivity of ^{3}CBBP* compared to ^{3}AQ2S*, because in the case of APAP one has $k_{(^3CBBP^*+APAP)} \sim 0.15\times k_{(^3AQ2S^*+APAP)}$.

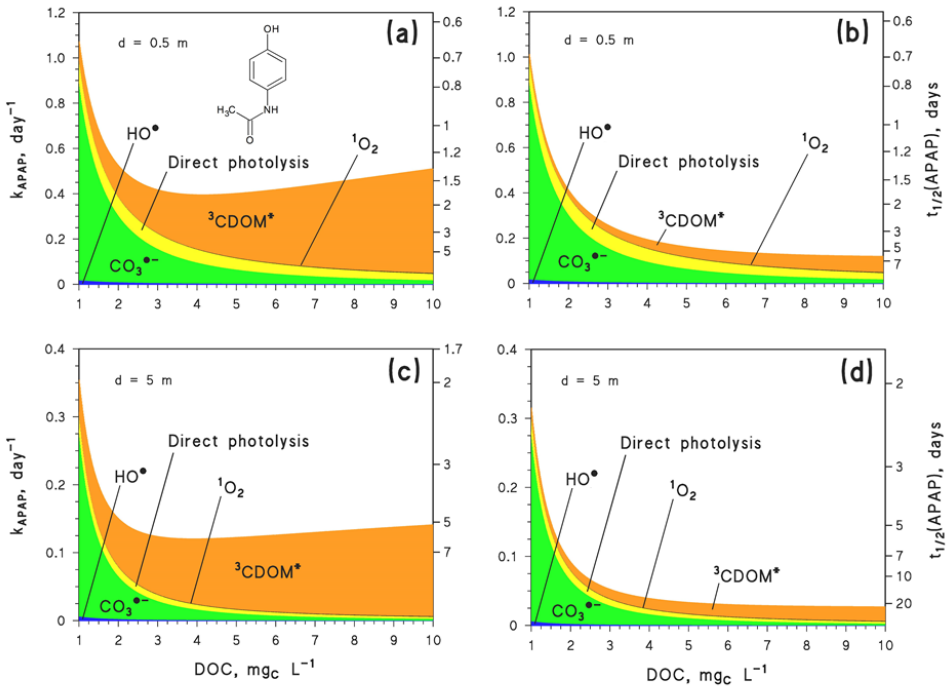

Fig.2.3.4 Modeled APAP photodegradation kinetics and pathways (*left Y-axis*: first-order rate constants; *right-Y axis*: lifetimes; color codes: pathways) for: **(a)** d = 0.5 m and $k_{(^3CDOM^*+APAP)} = k_{(^3AQ2S^*+APAP)}$; **(b)** d = 0.5 m and $k_{(^3CDOM^*+APAP)} = k_{(^3CBBP^*+APAP)}$; **(c)** d = 5 m and $k_{(^3CDOM^*+APAP)} = k_{(^3AQ2S^*+APAP)}$; **(d)** d = 5 m and $k_{(^3CDOM^*+APAP)} = k_{(^3CBBP^*+APAP)}$. Other water conditions: 10^{-4} mol L^{-1} NO_3^-, 10^{-6} mol L^{-1} NO_2^-, 10^{-3} mol L^{-1} HCO_3^-, 10^{-5} mol L^{-1} CO_3^{2-}. Adapted from Carena et al. (2019).

The fact that the predicted photodegradation kinetics of APAP is slower when using $k_{(^3CBBP^*+APAP)}$ instead of $k_{(^3AQ2S^*+S)}$ is particularly evident at medium-to-high values of the considered DOC range. In these conditions the modeled half-life times of APAP undergo a very significant increase when passing from ^{3}AQ2S to ^{3}CBBP* (the relevant increase is from ~1-1.5 days to ~1 week for d = 0.5 m, and from ~1 week to ~2-3 weeks for d = 5 m). This is the main difference between the AQ2S and CBBP scenarios.

Despite the mentioned (and important) quantitative changes, the situation looks quite different when seen from a merely qualitative point of view. Indeed, ^{3}CDOM* is predicted to be the main PPRI accounting for APAP phototransformation, irrespective of the use of either AQ2S or CBBP as CDOM proxies. The model results do in fact show that higher DOC values favor the formation of ^{3}CDOM*, and thus the reaction of APAP with these species. Singlet oxygen production is favored in these conditions as well (Vione et al., 2014), but APAP is poorly reactive towards $^1O_2$ (De Laurentiis et al., 2014b) and the relevant process is thus of scarce overall importance. Moreover, in both the CBBP and AQ2S scenarios, the degradation of APAP at low DOC by (mainly) $CO_3^{\bullet-}$ radicals and (to a lesser extent) direct photolysis prevails over reaction with ^{3}CDOM*.

The importance of the reaction between ^{3}CDOM* and APAP is predicted to increase with water depth, in particular at high DOC. Indeed, the photochemical processes triggered by $CO_3^{\bullet-}$ (which is produced indirectly upon light absorption by nitrate and nitrite; Vione et al., 2014; Wojnárovits et al., 2020) and the direct photolysis of APAP are peculiarly inhibited in a water column with depth d = 5 m, compared to d = 0.5 m. This happens because the relevant photoreactions are mainly triggered by UVB radiation (note that the absorption of UVA radiation by nitrite is not substantial; De Laurentiis et al., 2014; Mack and Bolton, 1999), which does not penetrate much into the water column (Häder et al., 2015; Sommaruga et al., 1999). In contrast, the transformation processes triggered by ^{3}CDOM* and $^1O_2$ involve the photosensitizing action of CDOM that also absorbs to a significant extent both UVA and visible light (Sharpless and Blough, 2014), which both show higher penetration in water compared to UVB. This issue explains why ^{3}CDOM* photochemistry becomes more important in the deep waters (Vione et al., 2014).

Similar results were obtained for IBP (Fig.2.3.5), in which case also one gets 3-4 times slower photodegradation kinetics at high DOC in the CBBP scenario, compared to AQ2S, at both water depths. However, the CBBP and AQ2S scenarios differ for shallow waters at high DOC, where ^{3}CDOM* is no longer the main PPRI involved in photodegradation when using the CBBP proxy data. The reason is a combination of significant IBP reactivity with HO$^\bullet$ and by direct photolysis, coupled with slower predicted ^{3}CDOM* reactions in the case of CBBP.

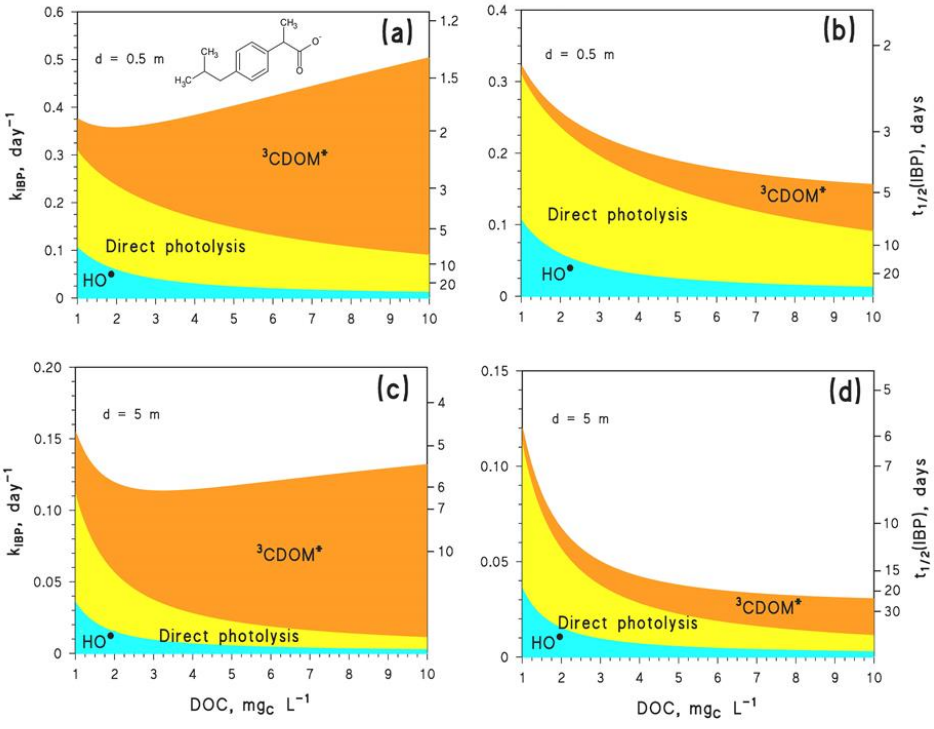

Fig.2.3.5 Modeled IBP photodegradation kinetics and pathways (*left Y-axis*: first-order rate constants; *right-Y axis*: lifetimes; color codes: pathways) for: **(a)** d = 0.5 m and $k_{(^3CDOM^*+IBP)} = k_{(^3AQ2S^*+IBP)}$; **(b)** d = 0.5 m and $k_{(^3CDOM^*+IBP)} = k_{(^3CBBP^*+IBP)}$; **(c)** d = 5 m and $k_{(^3CDOM^*+IBP)} = k_{(^3AQ2S^*+IBP)}$; **(d)** d = 5 m and $k_{(^3CDOM^*+IBP)} = k_{(^3CBBP^*+IBP)}$. Other water conditions: 10^{-4} mol L^{-1} NO_3^-, 10^{-6} mol L^{-1} NO_2^-, 10^{-3} mol L^{-1} HCO_3^-, 10^{-5} mol L^{-1} CO_3^{2-}. Adapted from Carena et al. (2019).

It is also noteworthy that, in both scenarios, ^{3}CDOM* would still dominate IBP phototransformation at high DOC in deep water (d = 5 m).

The previous findings hold quite well in the case of CLO, although in this case a further decrease of the photodegradation kinetics when passing from AQ2S to CBBP is due to inhibition processes induced by DOM antioxidants, such as (most notably) phenols (Canonica and Laubscher, 2008; Wenk and Canonica, 2012). The latter have not been considered in the AQ2S-based work reported in the literature (Avetta et al., 2016). The inhibition effect related to antioxidants will be addressed in more detail in the next chapter, for which reason the plots of CLO photochemistry are not reported here. The reader can find the relevant graphs in the published version of this work (Carena et al., 2019a). However, model results showed that CLO photodegradation would be dominated by ^{3}CDOM* reactions when using either AQ2S or CBBP as CDOM proxy. Although the photodegradation of CLO is slowed down by 2-3 times in the case of CBBP compared to AQ2S, this decrease is not completely accounted for by the fact that $k_{(^3CBBP^*+CLO)}$ ~0.45× $k_{(^3AQ2S^*+CLO)}$. Actually, one should also take the antioxidants-induced inhibition into account (Carena et al., 2019a).

Much lower differences between the AQ2S and CBBP scenarios were found for ATZ (Fig.2.3.6), mainly because $k_{(^3CBBP^*+ATZ)}$ ~0.45× $k_{(^3AQ2S^*+ATZ)}$. Actually, the obtained differences are practically well within the model uncertainty (Bodrato and Vione, 2014; Vione, 2020). Therefore, in this case the shift from the AQ2S to the CBBP scenario (which only involves the ^{3}CDOM* reaction kinetics) does not automatically translate into comparable changes in overall phototransformation.

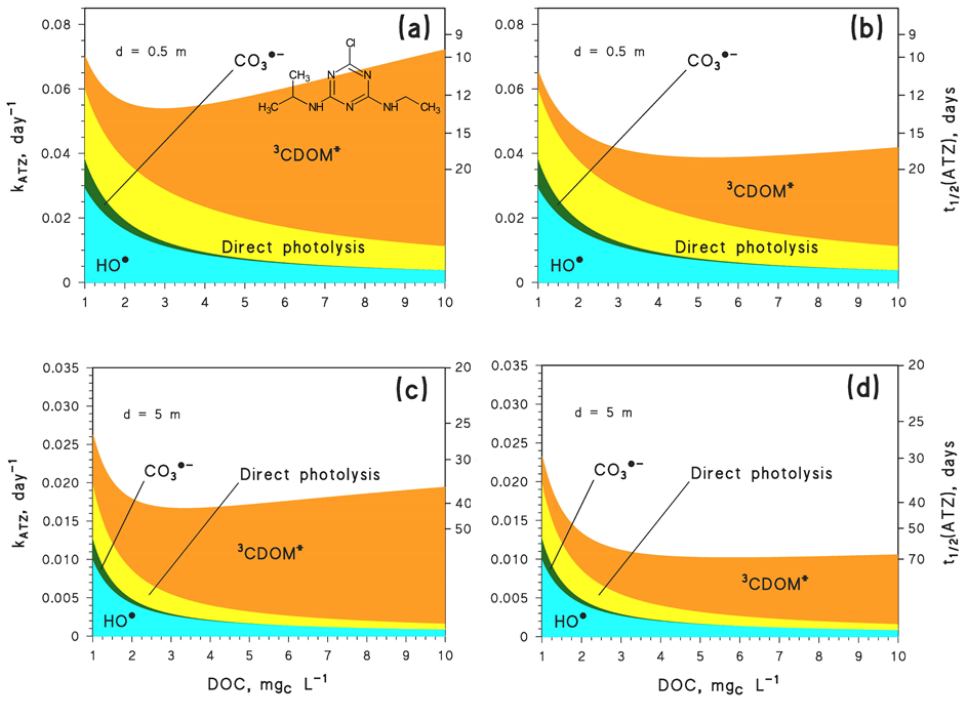

Fig.2.3.6 Modeled ATZ photodegradation kinetics and pathways (*left Y-axis*: first-order rate constants; *right-Y axis*: lifetimes; color codes: pathways) for: **(a)** d = 0.5 m and $k_{(^3CDOM^*+ATZ)} = k_{(^3AQ2S^*+ATZ)}$; **(b)** d = 0.5 m and $k_{(^3CDOM^*+ATZ)} = k_{(^3CBBP^*+ATZ)}$; **(c)** d = 5 m and $k_{(^3CDOM^*+ATZ)} = k_{(^3AQ2S^*+ATZ)}$; **(d)** d = 5 m and $k_{(^3CDOM^*+ATZ)} = k_{(^3CBBP^*+ATZ)}$. Other water conditions: 10^{-4} mol L^{-1} NO_3^-, 10^{-6} mol L^{-1} NO_2^-, 10^{-3} mol L^{-1} HCO_3^-, 10^{-5} mol L^{-1} CO_3^{2-}. Adapted from Carena et al. (2019).

The modeled photodegradation rate constants and lifetimes reported here allow for a comparison of the predicted AQ2S- and CBBP-based photodegradation kinetics with the available field or experimental data. In the case of IBP in lake Greifensee (Switzerland: 10^{-4} mol L^{-1} NO_3^-, 3.5 mg$_C$ L^{-1} DOC, 2 mmol L^{-1} HCO_3^-, 10^{-5} mol L^{-1} CO_3^{2-}, 5 m epilimnion depth), the photodegradation rate constant assessed in the field should be in the range of 0.006-0.012 day^{-1} during summer (Tixier et al., 2003; Vione et al., 2011). By

comparison, AQ2S-based photochemical modelling overestimates k at 0.049±0.017 day^{-1} (μ±σ), while in the CBBP scenario one gets k = 0.008±0.003 day^{-1}, well within the field-data range.

Laboratory irradiation of IBP in Mississippi river water (63 μmol L^{-1} NO_3^-, 8.9 mg_C L^{-1} DOC, 2.5 cm optical path length) yielded k_{exp} = 0.09 day^{-1} (Packer et al., 2003), to be compared with the model predictions: k_{APEX} = 0.31±0.11 day^{-1} (AQ2S) and k_{APEX} = 0.055±0.020 day^{-1} (CBBP). In the case of CLO, again in lake Greifensee, an upper limit for the photodegradation kinetics could be found ($k_{field} \leq 0.01$ day^{-1}; Tixier et al., 2003). By comparison, one has k_{APEX} = 0.06±0.02 day^{-1} (AQ2S) and k_{APEX} = 0.018±0.006 day^{-1} (CBBP). In all the cases, a better agreement with the field/experimental data could be obtained by using the CBBP compared to the AQ2S proxy.

2.4 Conclusions

The findings of this work strongly suggest that CBBP is more suitable as CDOM-proxy molecule compared to AQ2S. The ^{3}CDOM* reactivity towards the investigated compounds IBP, APAP, CLO and ATZ is in fact overestimated when AQ2S is used as proxy (Avetta et al., 2016; De Laurentiis et al., 2014b; Marchetti et al., 2013; Vione et al., 2011). The AQ2S scenario gives values of $k_{(^3AQ2S^*+S)}$ > 5×10^9 L mol^{-1} s^{-1}, which is the generally accepted upper limit for $k_{(^3CDOM+S)}$ (Canonica et al., 2000). In contrast, the values of $k_{(^3CBBP^*+S)}$ are coherent with the reported upper limit. Moreover, better agreement between the modeled and the available field or experimental data for the photodegradation of IBP and CLO could be obtained in the CBBP scenario, compared to the AQ2S one. AQ2S and CBBP both allowed for comparable estimates of $k_{(^3CDOM+S)}$ in the case of ATZ only.

The relationship $k_{(^3CBBP^*+S)}$ ~$0.15\times k_{(^3AQ2S^*+S)}$ for S = IBP or APAP resulted in the increase of the relevant lifetimes by 2-4 times in surface waters with medium-to-high DOC values (~5-10 mg$_C$ L^{-1}). In contrast, the AQ2S- and CBBP-based scenarios did not differ much for ATZ, partially because $k_{(^3CBBP^*+S)}$ ~$0.45\times k_{(^3AQ2S^*+S)}$, and partially due to the important role of other reaction pathways in ATZ photodegradation. In the case of CLO a similar relationship between $k_{(^3CBBP^*+S)}$ and $k_{(^3AQ2S^*+S)}$ was found as for ATZ, but the CLO half-life times are mainly affected by the occurrence of inhibition processes induced by antioxidant DOM moieties.

Despite significant changes in photochemical lifetimes, ^{3}CDOM* would still remain the PPRI that mostly accounts for the phototransformation of the studied compounds in deep and (C)DOM-rich water bodies. Therefore,

despite significant changes in the quantitative prediction of photodegradation kinetics, the qualitative conclusions that could be drawn by the use of the CBBP proxy do not differ much from those obtained previously within the AQ2S scenario. Despite this, our recommendation is that CBBP should be considered as a better CDOM proxy than AQ2S in the context of quantitative studies on the triplet-sensitized photodegradation of water pollutants, especially because now we have developed a protocol that allows for the measurement of ^{3}CBBP* reaction rate constants in steady-state irradiation experiments (Minella et al., 2018). It should be remarked that when the AQ2S-based studies were carried out, such a protocol was not yet available.

Chapter 3

Inhibition by dissolved organic matter (DOM) of the oxidation of aquatic contaminants carried out by carbonate radicals and the excited triplet states of DOM

Based on the results reported in the following papers in preparation and already published:

- **Carena, L.**, Canonica , S., Minella, M., Vione, D. Inhibition by dissolved organic matter of the oxidation of aquatic contaminants carried out by carbonate radicals. (*In preparation)*.
- **Carena, L.**, Vione, D. Phenol-induced back-reduction of anilines oxidized by carbonate radical and triplet aromatic ketones in aqueous solution: Application of the Marcus Theory. (*In preparation)*.
- Gornik, T., **Carena, L.**, Kosjek, T., Vione, D. Phototransformation study of the antidepressant paroxetine in surface waters. (*Submitted to Science of the Total Environment)*.
- **Carena, L.**, Puscasu, C.G., Comis, S., Sarakha, M., Vione, D., **2019**. Environmental photodegradation of emerging contaminants: A re-examination of the importance of triplet-sensitised processes, based on the use of 4-carboxybenzophenone as proxy for the chromophoric dissolved organic matter. *Chemosphere* 237, 124476. https://doi.org/10.1016/j.chemosphere.2019.124476

List of abbreviations:

2AN = 2-acetonaphthone

3CA = 3-chloroaniline

3,4DCA = 3,4-dichloroaniline

4CA = 4-chloroaniline

Ani = aniline

APAP = acetaminophen

ATZ = atrazine

CBBP = benzophenone-4-carboxylate

CLO = clofibric acid

DMA = N,N-dimethylaniline

ET = electron transfer

HSDZ = sulfadiazine (amphoteric form)

IBP = ibuprofen

LFER = Linear Free-Energy Relationship

MMA = N-methylaniline

PhOH = phenol

PXT = paroxetine

SDZ^- = sulfadiazine (anionic form)

PCET = proton-coupled electron transfer

PPRIs = Photochemically Produced Reactive Intermediates

3.1 Introduction

Dissolved organic matter (DOM) is the chemical species that usually plays the main role in the abiotic photochemical processes taking place in sunlit surface waters. Thanks to its chromophoric moieties, CDOM is able to photoproduce directly or indirectly all the reactive transient species (PPRIs, mostly $HO^{\bullet}$, $^{3}CDOM^{*}$, $CO_3^{\bullet-}$ and $^{1}O_2$) that are involved, for example, in the indirect photodegradation of water pollutants. However, at the same time, DOM can also inhibit the phototransformation of pollutants (Vione et al., 2014).

There are three main pathways by which DOM can inhibit photoreactions: *(i)* scavenging of $HO^{\bullet}$ and $CO_3^{\bullet-}$ radicals; *(ii)* competition with the xenobiotic/pollutant for sunlight absorption; *(iii)* back-reduction of the partially oxidized pollutant to the parent compound. A fourth pathway can be the sorption of hydrophobic contaminants and their sedimentation (Lee and Kuo, 1999; Maoz and Chefetz, 2010; Yu et al., 2019), although the hydrophobic core of DOM is also an environment where photodegradation processes triggered by $^{1}O_2$ can be enhanced (Appiani and McNeill, 2015).

DOM is the main scavenger of both $HO^{\bullet}$ and $CO_3^{\bullet-}$ radicals, often accounting for more than 90% of their scavenging (Page et al., 2014; Vione et al., 2014, 2006; Westerhoff et al., 2007; Yan et al., 2019). For this reason, photodegradation of xenobiotics by $HO^{\bullet}$ and $CO_3^{\bullet-}$ is favored in shallow water bodies with a low DOM content. By increasing the concentration of DOM, which is usually defined as the dissolved organic carbon (DOC), the steady-state concentrations of $HO^{\bullet}$ and $CO_3^{\bullet-}$ get decreased as DOC^{-1} and DOC^{-2}, respectively (Bodrato and Vione, 2014; Vione et al., 2014). Consequently, the photodegradation of pollutants that react fast with these PPRIs is slowed down when the DOC is high. This is the case of the UV absorber benzophenone-4

(2-hydroxy-4-methoxybenzophenone-5-sulphonic acid) (De Laurentiis et al., 2013c), the herbicide atrazine (Marchetti et al., 2013) or the pharmaceuticals acetaminophen (or, paracetamol) and sertraline (De Laurentiis et al., 2014b; Gornik et al., 2020). Because $HO^{\bullet}$ reacts with water pollutants with rates that are near the diffusion-control limit, the extent of the *scavenging effect* by DOM is approximately the same for several xenobiotics.

In surface waters, many pollutants undergo degradation by direct photolysis as well. Several studies have reported that increasing (C)DOM inhibits direct photolysis (Remucal, 2014), because of competition between CDOM and pollutants for sunlight absorption. Indeed, CDOM is the main sunlight-absorbing species occurring in inland surface waters (Clark et al., 2019; Nelson and Siegel, 2013), and radiation absorption by CDOM decreases the number of available photons for the direct photolysis process (C. Zhou et al., 2020; Zhou et al., 2013). This inhibition is called *light-screening effect* and depends on the ability of the xenobiotic to absorbs sunlight (i.e., its molar absorption coefficient ε_λ) and to convert the absorbed energy into new molecules (i.e., its direct photolysis quantum yield Φ_λ). The higher is the product $\varepsilon_\lambda \times \Phi_\lambda$, the lower is the light-screening effect by CDOM.

As shown in the previous Chapter 2, ^{3}CDOM* plays an important role in the photodegradation of several water pollutants, and its photochemistry is significant in deep water bodies with high DOC levels (see also Canonica, 2007; McNeill and Canonica, 2016). The first step of xenobiotic oxidation by ^{3}CDOM* often consists in charge transfer reactions (Canonica, 2007; McNeill and Canonica, 2016), which in the case of phenols oxidation have been found to follow the Marcus electron-transfer theory (Canonica et al., 2000). The produced radicals usually undergo subsequent reactions towards the final products. However, these partially oxidized radicals can also be reduced back to the parent compounds by reaction with the antioxidant moieties of DOM,

thereby inhibiting the net pollutant transformation. Experimental evidence of this *back-reduction effect* has been firstly reported by Canonica and Laubscher in 2008 for the photodegradation of anilines (aniline, 4-cyanoaniline and N,N-dimethylaniline), sulfadrugs (sulfamethoxazole and sulfadiazine) and trimethoprim by the excited triplet states of CDOM-proxy molecules (Canonica and Laubscher, 2008). However, back-reduction had been previously hypothesized by Canonica and co-workers in 2005 and 2007, by investigating the degradation of water pollutants by ^{3}CDOM* and $CO_3^{\bullet-}$ (Canonica, 2007; Canonica et al., 2005). Since 2008, some works have been published about the back-reduction effect, proving that this process is operational in the degradation of anilines and sulfonamides by ^{3}CDOM* and $SO_4^{\bullet-}$ (Canonica and Schönenberger, 2019; Leresche et al., 2016; Vione et al., 2018; Wenk et al., 2011; Wenk and Canonica, 2012), but not in the case of HO$^\bullet$-induced reactions (Wenk et al., 2011). Recently, the back-reduction effect has been observed during the degradation of the cyanotoxin cylindrospermopsin carried out by $CO_3^{\bullet-}$ radical (Hao et al., 2020).

The back-reduction has been quantified with the parameter $DOC_{1/2}$ or $[PhOH]_{1/2}$ (when DOM or phenol, respectively, are used as antioxidants), by which one measures the decrease of the rate constant of the reaction between ^{3}CDOM* and the xenobiotic using the factor $\psi = DOC_{1/2} \times \left(DOC + DOC_{1/2}\right)^{-1}$ or $\psi = [PhOH]_{1/2} \times \left([PhOH] + [PhOH]_{1/2}\right)^{-1}$ (Canonica and Laubscher, 2008; Wenk and Canonica, 2012). Phenol has been widely used as proxy-molecule for DOM antioxidant moieties (Leresche et al., 2016; Vione et al., 2018; Wenk and Canonica, 2012). Indeed, apart from some features that make phenol very suitable for lab experiments (e.g., good water solubility, right redox properties and low UVB-UVA absorption coefficients), it conveniently simulates the DOM phenolic fractions that are supposed to be

the main species responsible for back-reduction in the environment (Walpen et al., 2016; Wenk and Canonica, 2012).

The topic of this chapter is the back-reduction process. It was assessed first for the ^{3}CDOM*-induced degradation of N-containing compounds (3-chloroaniline, 3,4-dichloroaniline and the antidepressant paroxetine) and clofibric acid (Section 3.3.1), which are contaminants that are often detected in surface waters. Phenol was used as proxy-molecule for antioxidant DOM moieties. Secondly, the occurrence of phenol-induced back-reduction was investigated in the case of anilines degradation by $CO_3^{\bullet-}$. In all the cases, back reduction was quantified with the parameter $[PhOH]_{1/2}$ (Section 3.3.2). A first attempt to formulate a general statement about the (phenol-induced) back-reduction of anilines was carried out by applying the Marcus electron-transfer theory (Section 3.3.3 and Appendix I). Finally, the environmental importance of back-reduction was assessed by modeling the photodegradation of 3,4-dichloroaniline in a lake-water scenario (Section 3.3.4).

3.2 Materials and Methods

3.2.1 Reagents

All the compounds (analytical grade) were purchased from Sigma Aldrich and used as received, without any further purification step. Gradient-grade methanol and acetonitrile for HPLC analysis were from VWR Chemicals BDH®. Ultra-pure water was produced by a Milli-Q system (Millipore, 18.2 MΩ cm resistivity, 2 ppb TOC).

The acidic stock solution of 4-carboxybenzophenone (pKa ~4.5; NIST, 2004) was adjusted to pH 7.0 with NaOH 1 mol L^{-1}, to keep the compound in the deprotonated form and to operate at an environmentally significant pH value.

3.2.2 High-Pressure Liquid Chromatography / Diode Array Detection (HPLC-DAD) analysis

The compounds quantification after the irradiation experiments was performed by means of HPLC-DAD. The used instrument was a VWR-Hitachi LaChrom Elite chromatograph equipped with L-2200 autosampler (injection volume 60 µL), L-2130 quaternary pump for low-pressure gradients, Duratec vacuum degasser, L-2300 column oven (set at 40 °C), and L-2455 photodiode array detector. The column was a VWR LiChroCART 125-4 Cartridge, packed with LiChrospher 100 RP-18 (125mm×4mm×5µm), and the eluent flow rate was 1.0 mL min^{-1}. In the case of aniline, it was used a VWR Superspher® RP-18 HPLC Column (250mm×4mm×5µm) with a flow rate of 0.8 mL min^{-1}. All the analyses, with the exception of CLO (*vide infra*), were carried out in isocratic conditions. Methanol (A), 10 mmol L^{-1} phosphate

buffer at pH 7.0 (B), ultrapure water acidified at pH ~2.8 with phosphoric acid (C), phosphate buffer at pH = 3.7 (D) and acetonitrile (E) were used as eluents. In particular, the elution conditions, retention times (t_r) and quantification wavelengths (λ_q) were as follows: 35% A and 65% B for Ani (t_r = 9.9 min, λ_q = 230 nm); 45% A and 55% B for 3CA (t_r = 5.2 min, λ_q = 245 nm); 35% A and 65% B for 4CA (t_r = 7.3 min, λ_q = 243 nm); 45% A and 55% B for 3,4DCA (t_r = 8.7 min, λ_q = 249 nm); 12.5% A and 87.5% C for APAP (t_r = 3.9 min, λ_q = 245 nm); 25% D and 75% E for PXT (t_r = 5.0 min, λ_q = 293 nm); 40% A and 60% C for ATZ (t_r = 19.8 min, λ_q = 220 nm); 62.5% A and 37.5% C for IBP (t_r = 4.0 min, λ_q = 220 nm).

For CLO, the following gradient elution with eluents A and C was adopted: 30% A for 4 min, up to 55% A in 0.1 min, keep for 10.9 min, down to 30% A in 0.1 min, keep for 1.9 min (t_r = 12.8 min, λ_q = 227 nm).

3.2.3 Irradiation experiments

The details of the irradiation experiments are described case by case in the following sections. Overall, experimental runs consisted in the irradiation under a suitable lamp of aqueous solutions put in cylindrical Pyrex glass cells and continuously stirred. Solutions contained *(i)* a photosensitizer (CBBP or a mixture of $NaNO_3$ + $NaHCO_3$) able to photoproduce the desired PPRI, *(ii)* the organic substrate (i.e., water pollutant) to be degraded and *(iii)* phenol as antioxidant compound. The temperature of the solutions was ~30 °C during irradiation.

At scheduled times, solutions were withdrawn from the irradiation set-up and immediately analyzed by HPLC-DAD to quantify the above compounds, thereby monitoring their time trend. Dark experiments were carried out under the same irradiation device, by wrapping the glass cells with a double

aluminum foil. No dark degradation was observed for any of the studied compounds.

The emission spectra of the lamps were obtained with an Ocean Optics USB 2000 CCD spectrophotometer, and corrected for the transmittance of the Pyrex window of the irradiation cells. Irradiation of the cells was mainly from the top, and the lamp power per unit area (W m^{-2}) was measured with an irradiance meter by CO.FO.ME.GRA. (Milan, Italy).

3.3 Results and Discussion

3.3.1 Phenol-induced inhibition of the photodegradation of organic pollutants by ^{3}CBBP*

Experimental procedure

Aqueous solutions (5 mL, pH ~7) containing the organic substrate (S = 3CA, 3,4DCA, APAP, ATZ, CLO, IBP, or PXT, 5 μmol L^{-1}), benzophenone-4-carboxylate (CBBP, ~70 μmol L^{-1}) and phenol (PhOH, from 0 to 10 μmol L^{-1}) were put in Pyrex glass cells, magnetically stirred and irradiated under a UVA black lamp with emission maximum at 369 nm (Philips TL-D 18 W). The relevant photon flux density in the solutions ($p^0(\lambda)$, Fig.3.3.1) was determined by means of chemical actinometry (see Chapter 2, Section 2.2.4) (Galbavy et al., 2010; Willett and Hites, 2000).

The time trends of S concentration ($[S]$) showed pseudo-first order kinetic behavior, of the kind $[S] = [S]_0 \times e^{-k' \times t}$, where $[S]_0$ is the initial concentration of S (5 μmol L^{-1}, Vione et al., 2018; Wenk and Canonica, 2012), k' is the pseudo-first order rate constant of S photodegradation, and t is the irradiation time. After assessing k' upon data fit of $[S]$ vs. t, the initial S degradation rate was calculated as $R = k' \times [S]_0$.

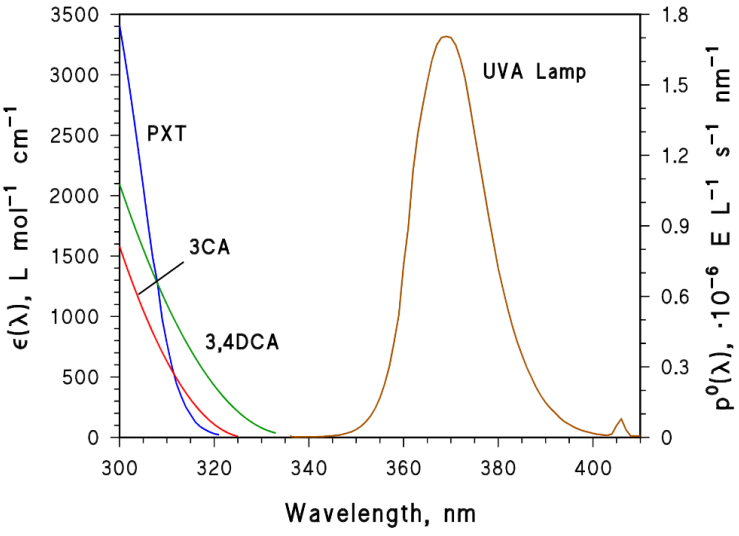

Fig.3.3.1 *Left axis*: molar absorption coefficient spectra of paroxetine (PXT), 3-chloroaniline (3CA) and 3,4-dichloroaniline (3,4DCA). *Right axis*: spectral photon flux density of the Philips TL-D 18 W UVA lamp used for the experiments of 3CA and 3,4DCA. In that case, the lamp irradiance on top of the irradiated glass cells was 42.6 ± 0.7 W m^{-2}. In the cases of ATZ, APAP, CLO and IBP it was 40.5 ± 2.5 W m^{-2}, and 32.2 ± 0.6 W m^{-2} for PXT. Despite these lamp-irradiance differences, comparison between the $[PhOH]_{1/2}$ values of different compounds (*vide infra*) is allowed.

Inhibition of the ^{3}CBBP-induced photodegradation of N-containing compounds and clofibric acid in the presence of phenol*

The degradation rates of 3-chloroaniline (3CA), 3,4-dichloroaniline (3,4DCA), paroxetine (PXT) and clofibric acid (CLO) decreased in the presence of phenol (PhOH). Inhibition became more pronounced when increasing the PhOH concentration (Fig.3.3.2). The direct photolysis of the organic substrates was negligible, because of the poor overlap between their absorption spectra and the photon flux density of the UVA lamp (Fig.3.3.1).

In contrast, no obvious effect of PhOH on the degradation rate of ATZ, APAP and IBP was observed (data not shown).

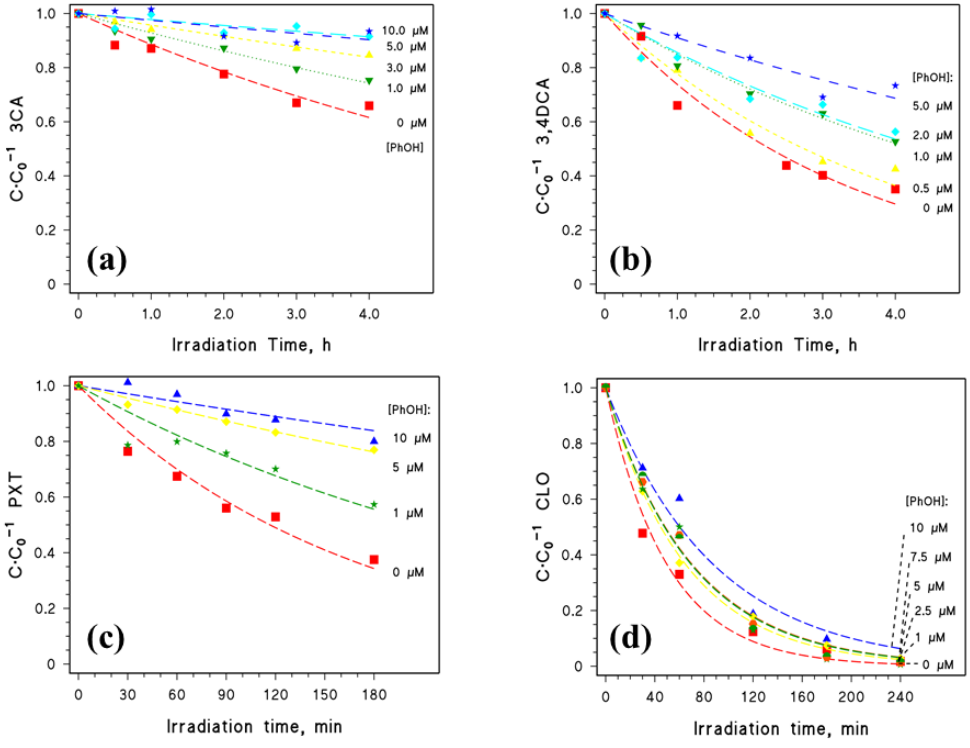

Fig.3.3.2 Temporal photodegradation profiles (experimental data and associated fit curves) of **(a)** 3CA, **(b)** 3,4DCA, **(c)** PXT, **(d)** CLO in the presence of CBBP + UVA light and different phenol (PhOH) concentrations. The values of phenol concentration are reported next to the fit curves. No significant direct photolysis of the compounds was observed under the adopted irradiation conditions.

The PhOH-induced inhibition of the degradation by ^{3}CDOM*-proxy molecules (CBBP and 2-acetonaphthone, hereinafter 2AN) has been previously observed for organic pollutants such as anilines, sulfonamides, and some phenols (Canonica and Laubscher, 2008; Leresche et al., 2016; Vione et al., 2018; Wenk et al., 2011; Wenk and Canonica, 2012). The proposed general mechanism which can account for this inhibition is a back-reduction

process, triggered by the ability of PhOH to react as an antioxidant (Canonica and Laubscher, 2008; Wenk et al., 2011; Wenk and Canonica, 2012).

The first step in the oxidation of an organic pollutant (S) by the excited triplet states of CDOM can occur through one-electron transfer (ET) or proton-coupled electron-transfer (PCET), producing a radical intermediate $S^{\bullet+}$ (Li et al., 2015; McNeill and Canonica, 2016; Tentscher et al., 2013; Wang et al., 2015; Wenk and Canonica, 2012). The $S^{\bullet+}$ intermediate can then react in several ways (e.g., bond cleavage, reaction with the solvent, dimerization; e.g., Houmam, 2008), forming the final oxidation products. However, in the presence of phenol, $S^{\bullet+}$ can be reduced back to the parent compound S by PhOH, which in turn gets oxidized to the phenoxy radical ($PhO^{\bullet}$), slowing down the net transformation of S itself. Furthermore, back-reduction would occur through ET/PCET (Davis et al., 2018), similarly to the oxidation step. Based on the experimental findings of this work and on literature results, we can reasonably infer that the back-reduction process is operational with 3CA, 3,4DCA, PXT and CLO.

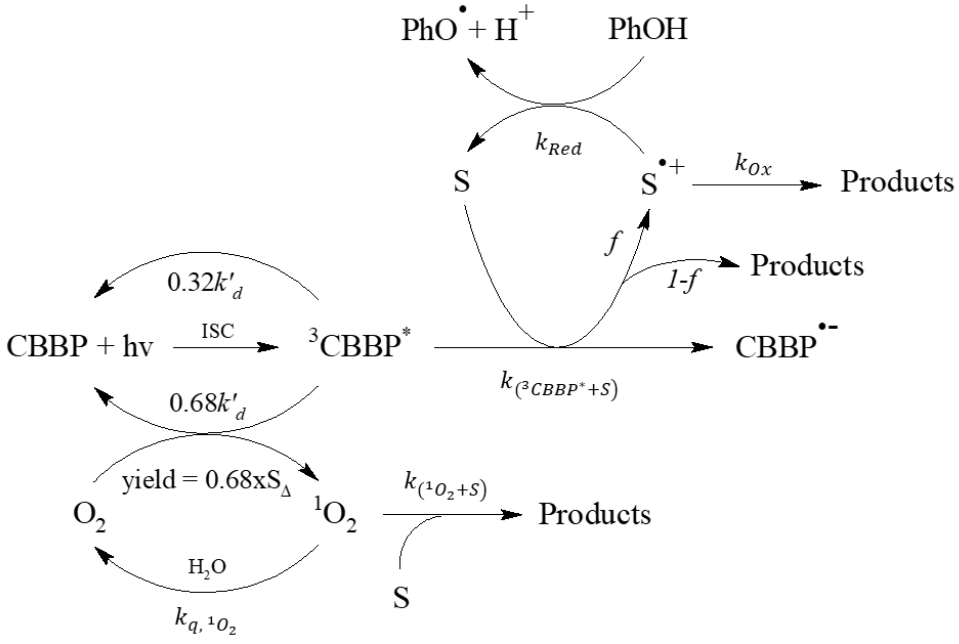

Scheme 3.3.1 Possible reactions taking place in the irradiated systems, used to assess phenol-induced back-reduction in the degradation of S by ^{3}CBBP*.

Scheme 3.3.1 shows the possible reactions taking place in the irradiated systems. The net degradation rate of S (S = 3CA, 3,4DCA, PXT or CLO) can be expressed as follows:

$$R_S = k_{(^3CBBP^*+S)} \times [^3CBBP^*] \times [S] - k_{Red} \times [S^{\bullet+}] \times [PhOH] \quad \text{(Eq. 3.3.1)}$$

where $k_{(^3CBBP^*+S)}$ and k_{Red} are the second-order rate constants of the reactions S + ^{3}CBBP* (the oxidation step) and $S^{\bullet+}$ + PhOH (the back-reduction step), respectively. Note that $k_{(^3CBBP^*+S)} \times [^3CBBP^*] \times [S] = R_S^0$, which is the degradation rate of S observed in the absence of PhOH. The concentration of $S^{\bullet+}$ can be considered in steady-state, thus $[S^{\bullet+}] = f \times k_{(^3CBBP^*+S)} \times [^3CBBP^*] \times [S] \times (k_{Red} \times [PhOH] + k_{Ox})^{-1}$, where f is the fraction of reacting S that produces intermediates (i.e., $S^{\bullet+}$), which undergo back-

reduction. For instance, it is known that chloroanilines can react with the excited triplet states of some CDOM proxy molecules undergoing transformation pathways that form hardly reducible by-products, such as dechlorinated compounds (Carena et al., 2018; Wenk and Canonica, 2012). Therefore, in that case $f < 1$.

Consequently, by introducing the expression for $[S^{\bullet+}]$ in Eq. 3.3.1 and by rearranging, one gets:

$$R_S = R_S^0 \times \left(\frac{f}{1+\frac{[PhOH]}{[PhOH]_{1/2}}} + 1 - f \right) \qquad \text{(Eq. 3.3.2)}$$

where $[PhOH]_{1/2} = k_{Ox} \times (k_{Red})^{-1}$ (see Scheme 3.3.1 for the relevant reactions) as defined by Wenk and Canonica (2012). In particular, $[PhOH]_{1/2}$ is the parameter that quantifies back-reduction and gives us information about how strong is the PhOH-induced inhibition. Indeed, $R_S = R_S^0 \times (1 - 0.5 \times f)$ when $[PhOH] = [PhOH]_{1/2}$, which means that $[PhOH]_{1/2}$ is the phenol concentration that halves the rate of the reaction S + ^{3}CBBP* → S$^{\bullet+}$ + CBBP$^{\bullet-}$. From a mechanistic point of view, $[PhOH]_{1/2}$ is the relative branching ratio (in molar units) between the final oxidation of S$^{\bullet+}$ (k_{Ox}) and its reduction (k_{Red}). As a consequence, the lower is $[PhOH]_{1/2}$, the stronger is inhibition of degradation by back-reduction.

Fig.3.3.3 shows the profiles of R_S *vs.* $[PhOH]$, obtained for 3CA, 3,4DCA, PXT and CLO. R_S^0 was measured as 0.17 ± 0.01 nmol L^{-1} s^{-1} for 3CA; 0.45 ± 0.03 nmol L^{-1} s^{-1} for 3,4DCA; 0.49 ± 0.02 nmol L^{-1} s^{-1} for PXT, and 1.45 ± 0.12 nmol L^{-1} s^{-1} for CLO. The fit of the experimental data with Eq. 3.3.2 allowed for calculating the value of $[PhOH]_{1/2}$ as a floating variable of the fit, together with f. In particular, for 3CA, $[PhOH]_{1/2}$ = 1.31 ± 0.17 µmol L^{-1}

and f = 0.93 ± 0.07; for 3,4DCA, $[PhOH]_{1/2}$ = 1.27 ± 0.32 µmol L^{-1} and f = 0.87 ± 0.17; for PXT, $[PhOH]_{1/2}$ = 1.46 ± 0.25 µmol L^{-1} and f = 1; for CLO, $[PhOH]_{1/2}$ = 0.26 ± 0.20 µmol L^{-1} and f = 0.33 ± 0.08.

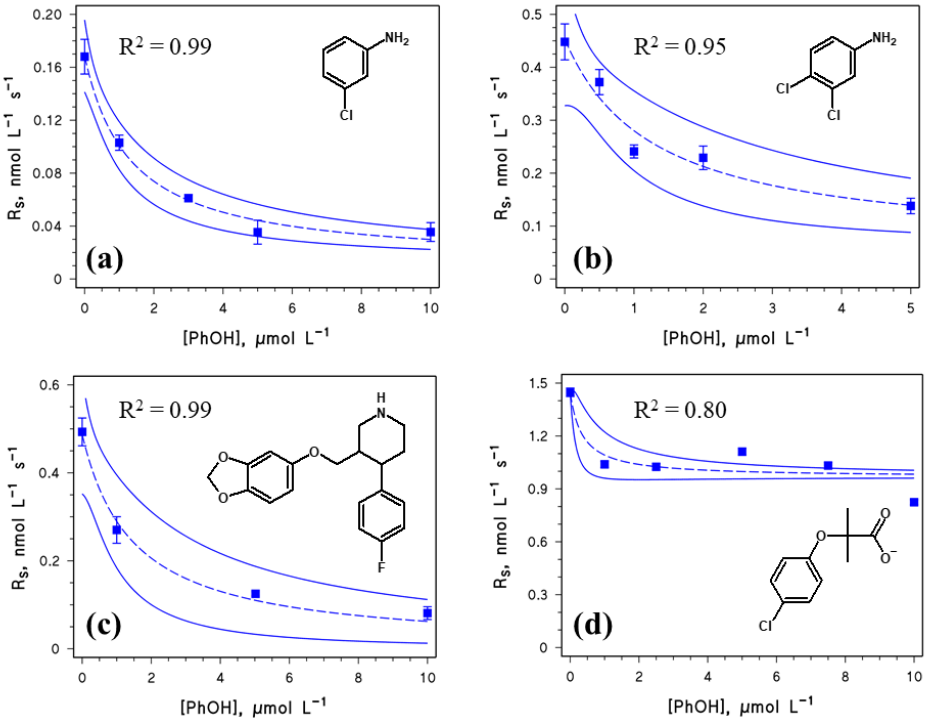

Fig.3.3.3 Observed degradation rates of **(a)** 3CA, **(b)** 3,4DCA, **(c)** PXT and **(d)** CLO, as a function of the concentration of added phenol, [PhOH]. The dotted lines represent the data-fit curves (Eq. 3.3.2), while the solid lines are the 95% confidence bands of the fit.

The obtained values of $[PhOH]_{1/2}$ for 3CA, 3,4DCA and PXT are pretty similar, suggesting that the intermediates (i.e., $S^{\bullet+}$) formed upon ET/PCET oxidation of these compounds by ^{3}CBBP* and undergoing back-reduction have some features in common. 3CA and 3,4DCA are likely to be mainly oxidized on the N atom (the fraction f), forming the corresponding anilino radical cations. The latter are weak acids and undergo deprotonation in

aqueous solution at pH ~7, forming the conjugated neutral anilino radicals (Jonsson et al., 1994). These species could be reduced back by phenol to the parent chloroanilines, in analogy with similar proposals made for aniline and 4-chloroaniline by Wenk and Canonica (2012). In the case of PXT, it can be inferred that ^{3}CBBP* oxidizes through ET/PCET the N atom of the piperidine ring, which should be the most easily oxidized group of the molecule. The piperidinyl radical cation thus formed should undergo deprotonation at pH ~7, producing the conjugated neutral radical (Jonsson et al., 1996; Vrček and Zipse, 2009). Therefore, 3CA, 3,4DCA and PXT could have in common the production of N-centered radicals upon oxidation by ^{3}CBBP*, and these radicals should be reduced by phenol. This issue will be addressed in more detail in the next sections. Finally, CLO showed a significantly lower value of $[PhOH]_{1/2}$ than the N-containing compounds. However, this is somehow offset by the quite low fraction of oxidized CLO undergoing back-reduction (i.e., f = 0.33 ± 0.08).

It should be pointed out that, in Eq. 3.3.1, the reaction S + $^1O_2$ was not considered (see Scheme 3.3.1), although a non-negligible fraction of ^{3}CBBP* produces singlet oxygen during its overall deactivation. It can be demonstrated that the fraction of S that is degraded by $^1O_2$ ($\chi_{(^1O_2+S)}$) is:

$$\chi_{(^1O_2+S)} = \frac{0.68\times S_\Delta \times k'_d \times k_{(^1O_2+S)}}{k_{q,^1O_2}\times k_{(^3CBBP^*+S)} + 0.68\times S_\Delta \times k'_d \times k_{(^1O_2+S)}} \qquad \text{(Eq. 3.3.3)}$$

where k'_d= 6×10^5 s^{-1} is the deactivation rate constant of ^{3}CBBP* in aerated solution, 0.68 is the fraction of ^{3}CBBP* that reacts with dissolved triplet O_2 (the remaining fraction of ^{3}CBBP* is likely deactivated by internal

conversion), S_Δ = 0.46 is the yield of $^1O_2$ upon reaction between ^{3}CBBP* and O_2 (Minella et al., 2018), and $k_{q,^1O_2}$ = 2.5×10^5 s^{-1} is the $^1O_2$ quenching rate constant by collision with water molecules (Wilkinson et al., 1995). $k_{(^1O_2+S)}$ is the second-order rate constant of the reaction S + $^1O_2$. Because $k_{(^1O_2+S)}$ ranges between 10^6 and 10^7 L mol^{-1} s^{-1} (Arnold et al., 2017; Wilkinson et al., 1995), one can expect that $\chi_{(^1O_2+S)}$ < 10^{-2} for $k_{(^3CBBP^*+S)}$ ~ 10^9 L mol^{-1} s^{-1}, which would result into a negligible role of $^1O_2$ in the overall S photodegradation. Concerning CLO, for example, it is $k_{(^1O_2+CLO)}$ = (6.0±1.9)×10^5 L mol^{-1} s^{-1} (Avetta et al., 2016) and, as a consequence, $\chi_{(^1O_2+CLO)}$ < 10^{-4}. There is no evidence of an important degradation of 3CA/3,4DCA by singlet oxygen, although aniline shows pretty high reactivity with $^1O_2$ ($k_{(^1O_2+aniline)}$ ~1.9×10^9 L mol^{-1} s^{-1}, Al-Nu'Airat et al., 2017). However, the reaction of aniline with $^1O_2$ occurs trough oxygen-addition rather than ET (Al-Nu'Airat et al., 2017), making back-reduction unlikely. For this reason, even if $\chi_{(^1O_2+3CA/3,4DCA)}$ were not negligible, the degradation of 3CA/3,4DCA by singlet oxygen would be included in the term (1 – f) of Eq. 3.3.2, preventing errors in the determination of $[PhOH]_{1/2}$.

3.3.2 Occurrence of the back-reduction process during the photodegradation of organic pollutants induced by the carbonate radicals ($CO_3^{\bullet-}$)

Experimental procedure

Synthetic aqueous solutions (5 mL) were magnetically stirred and irradiated in cylindrical Pyrex glass cells, under a Philips narrow band TL 20W/01 lamp.

This lamp mainly emits in the UVB wavelength range, with emission maximum at 313 nm, and the relevant spectral photon flux density ($p^0(\lambda)$, Fig.3.3.4) was assessed by means of chemical actinometry with 2-nitrobenzaldehyde (Galbavy et al., 2010; Willett and Hites, 2000).

The irradiated solutions contained a mixture of $NaNO_3$ + $NaHCO_3$ (pH 8.3), the organic substrate (S) to be degraded, as well as phenol (PhOH). The investigated organic substrates were aniline (Ani), 3-chloroaniline (3CA), 4-chloroaniline (4CA), 3,4-dichloroaniline (3,4DCA) and acetaminophen (paracetamol, APAP). Under UVB light, $NaNO_3$ + $NaHCO_3$ produce $CO_3^{\bullet-}$ radicals through the photolysis of nitrate, which forms $HO^{\bullet}$ (Mack and Bolton, 1999), and via the subsequent oxidation of HCO_3^-/CO_3^{2-} by $HO^{\bullet}$ to produce $CO_3^{\bullet-}$ and H_2O/HO^- (Buxton et al., 1988).

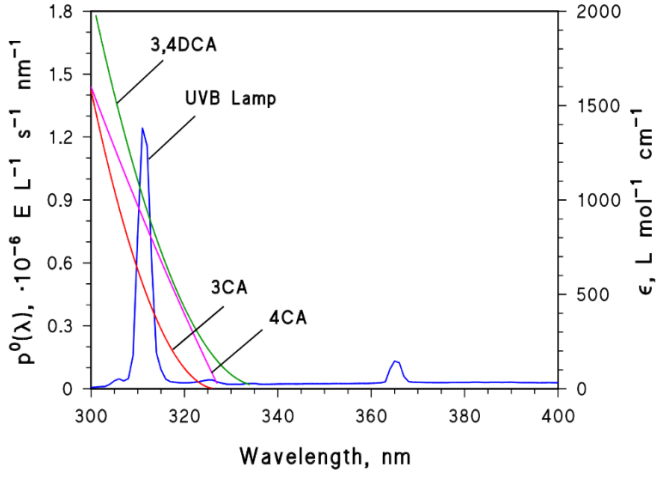

Fig.3.3.4 *Left Y axis*: spectral photon flux density of the Philips TL 20W/01 UVB lamp used for the irradiation experiments. *Right Y axis*: molar absorption coefficient spectra of 3-chloroaniline (3CA), 4-chloroaniline (4CA) and 3,4-dichloroaniline (3,4DCA), which underwent appreciable direct photolysis under UVB irradiation. The lamp irradiance on top of the irradiated glass cells was 2.9 ± 0.3 W m^{-2}, with the exception of aniline for which the lamp irradiance was 4.2 ± 0.2 W m^{-2}. In that case, the $p^0(\lambda)$ spectrum has to be multiplied by 1.45. Despite this lamp-irradiance difference, comparison between the $[PhOH]_{1/2}$ values of the different compounds (*vide infra*) is allowed.

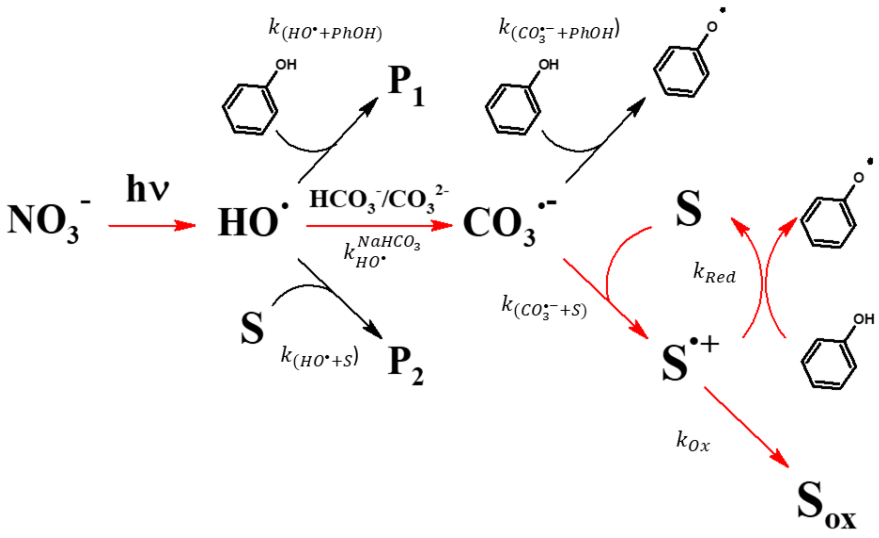

Scheme 3.3.2 Simplified scheme showing the possible reactions taking place in the irradiated solution, aimed at assessing the occurrence of the back-reduction during degradation of S by $CO_3^{\bullet-}$.

In such a system, S and PhOH could potentially be degraded by both $HO^{\bullet}$ and $CO_3^{\bullet-}$. With the aim in mind to investigate the occurrence of the back-reduction process during the degradation of S by $CO_3^{\bullet-}$ (i.e., $S + CO_3^{\bullet-} \rightarrow S^{\bullet+} + CO_3^{2-}$; $S^{\bullet+} + PhOH \rightarrow S + PhO^{\bullet} + H^+$), one should minimize the importance of the pathways that compete with the formation of $CO_3^{\bullet-}$ from $HO^{\bullet}$, and with the reaction of S with $CO_3^{\bullet-}$. Consequently, the reaction system should mainly proceed through the reaction pathway highlighted with red arrows in Scheme 3.3.2. This means that, first of all, the fractions of $HO^{\bullet}$ that react with S and PhOH ($\chi_{HO^{\bullet}}^{S}$ and $\chi_{HO^{\bullet}}^{PhOH}$, respectively) should be negligible compared to the fraction that oxidizes bicarbonate/carbonate to $CO_3^{\bullet-}$ ($\chi_{HO^{\bullet}}^{NaHCO_3}$, which takes into account the reaction of $HO^{\bullet}$ with both HCO_3^- and CO_3^{2-}). Note that

$\chi_{HO^\bullet}^{NaHCO_3}$ + $\chi_{HO^\bullet}^{S}$ + $\chi_{HO^\bullet}^{PhOH}$ = 1. Because a term in a sum can be neglected without significant errors if it is lower than 5% of the total sum (and 5% is also lower than the uncertainty observed in irradiation experiments), one can set $\chi_{HO^\bullet}^{S}$ + $\chi_{HO^\bullet}^{PhOH}$ < 0.05, which means $\chi_{HO^\bullet}^{NaHCO_3}$ > 0.95. By applying the same approach to the $CO_3^{\bullet-}$-scavenging pathways, one has that most of the produced $CO_3^{\bullet-}$ should react with the pollutant S rather than with PhOH ($\chi_{CO_3^{\bullet-}}^{S}$ > 0.95). The term $\chi_{HO^\bullet}^{NaHCO_3}$ can be expressed as the ratio between the sum of the rates of the reactions $HO^\bullet$ + HCO_3^- and $HO^\bullet$ + CO_3^{2-}, and the total scavenging rate of $HO^\bullet$. Note that $\chi_{HO^\bullet}^{NaHCO_3}$ considers the oxidation of both bicarbonate and carbonate by $HO^\bullet$. On the other hand, $\chi_{CO_3^{\bullet-}}^{S}$ can be expressed as the ratio between the rate of the reaction S + $CO_3^{\bullet-}$, and the total scavenging rate of $CO_3^{\bullet-}$. By so doing, one gets the following:

$$\chi_{HO^\bullet}^{NaHCO_3} = \frac{k_{HO^\bullet}^{NaHCO_3} \times C_{NaHCO_3}}{k_{(HO^\bullet+S)} \times [S] + k_{(HO^\bullet+PhOH)} \times [PhOH] + k_{HO^\bullet}^{NaHCO_3} \times C_{NaHCO_3}} > 0.95 \quad \text{(Eq. 3.3.4)}$$

$$\chi_{CO_3^{\bullet-}}^{S} = \frac{k_{(CO_3^{\bullet-}+S)} \times [S]}{k_{(CO_3^{\bullet-}+S)} \times [S] + k_{(CO_3^{\bullet-}+PhOH)} \times [PhOH]} > 0.95 \quad \text{(Eq. 3.3.5)}$$

Here, the $k_{(i+j)}$'s are the second-order rate constants of the reactions between the radical *i* ($HO^\bullet$ or $CO_3^{\bullet-}$) and the species *j* (HCO_3^-/CO_3^{2-}, S or PhOH), and the rate constant $k_{HO^\bullet}^{NaHCO_3} = \left(k_{(HO^\bullet+HCO_3^-)} \times \alpha_{HCO_3^-} + k_{(HO^\bullet+CO_3^{2-})} \times \alpha_{CO_3^{2-}}\right)$ accounts for the oxidation of HCO_3^-/CO_3^{2-}; finally, $C_{NaHCO_3} = [HCO_3^-] + [CO_3^{2-}] + [H_2CO_3^*]$. The parameters $\alpha_{HCO_3^-}$ and $\alpha_{CO_3^{2-}}$ are the molar fractions of bicarbonate and carbonate at pH 8.3, respectively,

computed taking into account the pK_a's of carbonic acid (Millero et al., 2002), while $k_{(HO^{\bullet}+HCO_3^-)}$ = 8.5×10^6 L mol^{-1} s^{-1}, and $k_{(HO^{\bullet}+CO_3^{2-})}$ = 3.9×10^8 L mol^{-1} s^{-1} (Buxton et al., 1988). Finally, [*S*] and [*PhOH*] are, respectively, the molar concentrations of S (fixed at 5 µmol L^{-1}; Vione et al., 2018; Wenk and Canonica, 2012) and of PhOH, and it is $C_{NaHCO_3} = [HCO_3^-] + [CO_3^{2-}] + [H_2CO_3^*]$ (it is also approximately equal to the initial concentration of $NaHCO_3$ added to the solution, *vide infra*).

If the values of $k_{(i+j)}$ are known (see Table 3.3.1), Eqs. 3.3.4 and 3.3.5 can be solved for the variables [*PhOH*] and C_{NaHCO_3} as follows:

$$C_{NaHCO_3} > \frac{[S]}{(1-0.95)\times k_{HO^{\bullet}}^{NaHCO_3}}\left[0.95k_{(S+HO^{\bullet})} + \frac{(1-0.95)\times k_{(S+CO_3^{\bullet-})}\times k_{(PhOH+HO^{\bullet})}}{k_{(PhOH+CO_3^{\bullet-})}}\right] \quad \text{(Eq. 3.3.6)}$$

$$[PhOH] < \frac{(1-0.95)\times[S]\times k_{(S+CO_3^{\bullet-})}}{0.95\times k_{(PhOH+CO_3^{\bullet-})}} \quad \text{(Eq. 3.3.7)}$$

The two equations indicate the minimum $NaHCO_3$ and the maximum phenol concentration that should be respectively added to the irradiated solutions in order to maximize the reactions $HO^{\bullet}$ + HCO_3^-/CO_3^{2-} and S + $CO_3^{\bullet-}$. By so doing, on could appreciate the back-reduction process with negligible interference from additional processes.

Table 3.3.1. **(a)** Second-order rate constants (L mol^{-1} s^{-1}) for the reactions between $HO^{\bullet}/CO_3^{\bullet-}$ and the organic substrates S (Buxton et al., 1988; Canonica et al., 2005; Carena et al., 2018; De Laurentiis et al., 2014b; Neta et al., 1988; Wojnárovits et al., 2020). $k_{(HO^{\bullet}+4CA)}$ was taken as the average of the $k_{(HO^{\bullet}+S)}$ values for Ani, 3CA and 3,4DCA. **(b)** The chosen bicarbonate, nitrate and maximum phenol concentrations (mol L^{-1}).

	Ani	3CA	4CA	3,4DCA	APAP	PhOH
			(a)			
$k_{(HO^{\bullet}+S)}$	1.5×10^{10}	1.4×10^{10}	1.4×10^{10}	1.3×10^{10}	9.0×10^{9}	1.4×10^{10}
$k_{(CO_3^{\bullet-}+S)}$	5.0×10^{8}	4.3×10^{8}	6.2×10^{8}	4.8×10^{8}	3.8×10^{8}	2.0×10^{7}
			(b)			
C_{NaHCO_3}	0.32	0.32	0.38	0.32	0.22	
$_{max}[PhOH]$	5.0×10^{-6}	5.0×10^{-6}	8.0×10^{-6}	5.0×10^{-6}	5.0×10^{-6}	
$[NaNO_3]$	1.0×10^{-2}	2.5×10^{-2}	2.5×10^{-2}	2.5×10^{-2}	2.5×10^{-2}	

The direct photolysis can be an additional degradation pathway for S. Indeed, direct photolysis has been observed in the case of chloro-substituted anilines (*vide infra*), which are known to be directly photodegraded under UVB irradiation (Carena et al., 2018; Guizzardi et al., 2001; Othmen et al., 2000). Although this process does not affect the branching ratios of the reactions involving $HO^{\bullet}$ and $CO_3^{\bullet-}$, it is nevertheless an experimental bias to be minimized. Therefore, the direct photolysis rate was made low by using both a relatively high $NaNO_3$ concentration (25 mmol L^{-1}), thus exploiting the inner-filter effect of $NaNO_3$ and increasing the formation rates of $HO^{\bullet}$ and, as a consequence $CO_3^{\bullet-}$ (which enhances the relevant processes at the expense of the direct photolysis), and a lower lamp irradiance (2.9 ± 0.3 W m^{-2}). In contrast, aniline did not show obvious direct photolysis, and lower nitrate (10 mmol L^{-1}) and slightly higher lamp irradiance (4.2 ± 0.2 W m^{-2}) were used in that case.

The quantification of S was carried out with the HPLC-DAD techniques that is described in section 3.2.2, together with the details of the chromatographic conditions for the analysis of each compound. Degradation of S followed pseudo-first order kinetics, and the relevant rate constants (k') were computed by fitting the S concentration profiles with the equation $[S] = [S]_0 \times exp(-k' \times t)$, where $[S]_0$ is the initial concentration (5 μmol L^{-1}) and t is the irradiation time. The initial degradation rate of S (R_S) was then calculated as $R_S = k' \times [S]_0$. Aniline was an exception, because its degradation by $CO_3^{\bullet-}$ showed zero-order kinetics ($[S] = [S]_0 - k^0 \times t$; $R_S = k^0$).

Inhibition by phenol of the degradation of anilines by $CO_3^{\bullet-}$

The addition of phenol (PhOH) to the irradiated solutions inhibited the degradation of the studied anilines by $CO_3^{\bullet-}$, and such an inhibition was more pronounced by increasing the PhOH concentration (Fig.3.3.5). A decrease of the anilines degradation rates because of a lower $HO^{\bullet}$ formation rate in the presence of PhOH can be ruled out, because PhOH is unable to absorb radiation efficiently around 313 nm and, therefore, it cannot inhibit nitrate photolysis. Furthermore, neither competition between anilines and PhOH for reaction with $CO_3^{\bullet-}$, nor a decrease of the $CO_3^{\bullet-}$ formation rate because of the reaction PhOH + $HO^{\bullet}$ can account for these findings, because the chemical composition of the irradiated solutions satisfied the conditions set by Eqs. 3.3.4 and 3.3.5. Consequently, by excluding these alternative explanations, we can arguably assume that the observed inhibition was caused by the reactions between phenol and the intermediates formed upon transformation of the anilines.

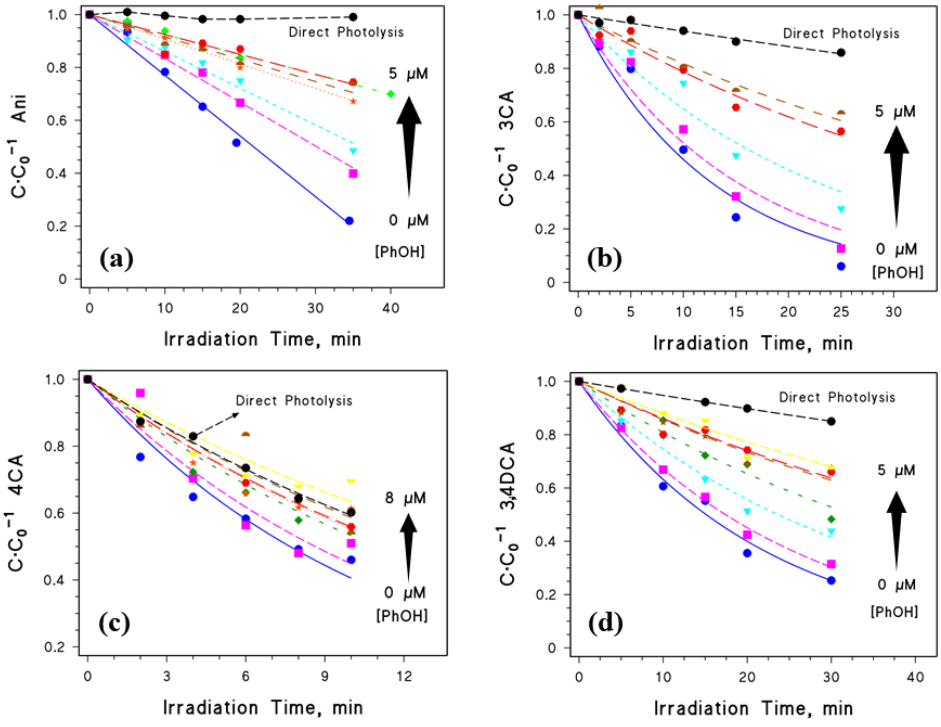

Fig.3.3.5. Temporal degradation profiles (experimental data and associated fit curves) of **(a)** Ani, **(b)** 3CA, **(c)** 4CA and **(d)** 3,4DCA, in the presence of $NaNO_3$ + $NaHCO_3$ + UVB light and different phenol (PhOH) concentrations. The direct photolysis curves were obtained by irradiating anilines in the presence of $NaHCO_3$ + UVB (pH 8.3).

The $CO_3^{\bullet-}$ radicals react with organic compounds mainly through electron transfer, while hydrogen abstraction is usually slower (Dell'Arciprete et al., 2012; Elango et al., 1985; Huang and Mabury, 2000; Neta et al., 1988). Anilines (Ar-NH_2) undergo mono-electronic oxidation by $CO_3^{\bullet-}$, forming radical cations (Ar-$NH_2^{\bullet+}$) that are weakly acidic compounds (Elango et al., 1984; Huang and Mabury, 2000; Jonsson et al., 1994; Liu et al., 2018; Wojnárovits et al., 2020). It has been reported previously that phenol can act as antioxidant during anilines photodegradation by the excited triplet states of CDOM-proxy molecules, such as CBBP and 2-acetonaphthone (2AN) (this

work, Canonica and Laubscher, 2008; Vione et al., 2018; Wenk and Canonica, 2012). In that case, the first step of aniline oxidation would occur *via* electron transfer (ET) and/or proton-coupled electron transfer (PCET) (Davis et al., 2018; Wang et al., 2015; Wenk and Canonica, 2012), followed by competition between further transformation and back-reduction by PhOH. We can infer that such a mechanism is operational in the present case as well.

$$Ar\text{-}NH_2 + CO_3^{\bullet -} \rightarrow Ar\text{-}NH_2^{\bullet +} + CO_3^{2-} \qquad k_{(CO_3^{\bullet -}+S)} \qquad \text{(Eq. 3.3.8)}$$

$$Ar\text{-}NH_2^{\bullet +} \leftrightarrows Ar\text{-}NH^{\bullet} + H^{+} \qquad \text{(Eq. 3.3.9)}$$

$$Ar\text{-}NH^{\bullet} \rightarrow \text{oxidized products} \qquad k_{Ox} \qquad \text{(Eq. 3.3.10)}$$

$$Ar\text{-}NH^{\bullet} + PhOH \rightarrow Ar\text{-}NH_2 + PhO^{\bullet} \qquad k_{Red} \qquad \text{(Eq. 3.3.11)}$$

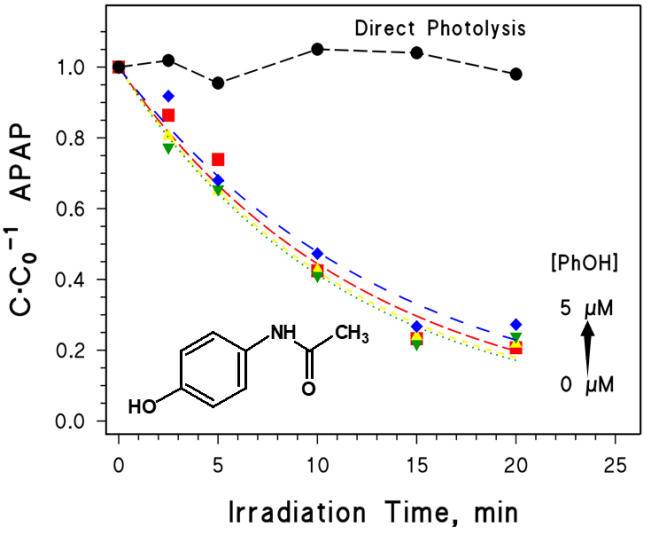

Fig.3.3.6. Temporal degradation profiles (experimental data and associated fit curves) of APAP in the presence of $NaNO_3$ + $NaHCO_3$ + UVB light and different phenol (PhOH) concentrations (1.0, 2.5 and 5.0 µmol L^{-1} PhOH). The direct photolysis data were obtained by irradiating APAP in the presence of $NaHCO_3$ + UVB (pH 8.3).

In contrast with the studied anilines, APAP did not show any significant inhibition in the presence of PhOH (Fig.3.3.6). Similar results were obtained for the ^{3}CBBP*-induced degradation of APAP (see the previous sections and Canonica and Laubscher, 2008). The triplet-sensitized oxidation of APAP should occur through ET/PCET on the OH-group and the amidic N atom of the molecule, forming both a phenoxy and a N-centered radical, respectively (Yanyun Li et al., 2017). The amidyl radical would be less stable than the phenoxy radical (Hioe et al., 2015), and thus less produced. The same electron-transfer reaction can be operational in the case of APAP + $CO_3^{\bullet-}$ as well. Concerning the OH-group oxidation, the resulting radical cation ($APAP^{\bullet+}$) would undergo deprotonation, because the radical cations of several para-substituted phenols are strong acids (with negative pK_a values). Deprotonation would stabilize the produced phenoxy radical ($APAP^{\bullet}$, conjugated base of the radical cation) towards reduction (Arnold et al., 2017; Li and Hoffman, 1999). Indeed, the standard reduction potential of the couple $APAP^{\bullet}$/APAP is ~0.12 V lower than that of the couple $PhO^{\bullet}$/PhOH at pH 8.3 (Arnold et al., 2017; Li and Hoffman, 1999). The N-centered radical could be stabilized as well through electron resonance on the adjacent aromatic ring and carbonyl group (Yanyun Li et al., 2017), preventing the reduction by PhOH. Therefore, $APAP^{\bullet}$ back-reduction should be very limited in our conditions where the maximum [*PhOH*] was 5 µmol L^{-1} for kinetic reasons. An increase of the PhOH concentration could trigger some back-reduction, but the present experimental approach (Eqs. 3.3.4 and 3.3.5) did not allow for a further increase in [*PhOH*]. Interestingly, the radicals produced by APAP oxidation through ET/PCET have been found to be reduced back to the parent compound by superoxide radical anion (Yanyun Li et al., 2017). Note that the

couple $O_2/O_2^{\bullet-}$ has a standard one-electron reduction potential ($E^o_{O_2/O_2^{\bullet-}}$ = -0.18 V vs NHE, Ma et al., 2020) that is much lower compared to PhO$^\bullet$/PhOH ($E^{o,\prime}_{PhO^\bullet/PhOH}$ = +0.96 V vs NHE at pH = 8.3, Li and Hoffman, 1999), which makes $O_2/O_2^{\bullet-}$ thermodynamically more prone than PhO$^\bullet$/PhOH to act as antioxidant.

Quantification of the phenol-induced back-reduction of anilines during their degradation carried out by $CO_3^{\bullet-}$

The back-reduction effect in the degradation of anilines by $CO_3^{\bullet-}$ was quantified in a similar way as done in the case of the ^{3}CBBP*-induced reactions (see the previous sections). The assessment of the degradation rate dependence on the added phenol concentration allowed for calculating the value of $[PhOH]_{1/2}$, which is the parameter that quantifies the back-reduction extent.

The overall degradation rate (R_S) of the organic substrate S (S = Ani, 3CA, 4CA or 3,4DCA) during UVB irradiation of a solution containing $NaNO_3$ + $NaHCO_3$ + S + phenol (PhOH) is $R_S = R_{(CO_3^{\bullet-}+S)} + R_{(HO^\bullet+S)} + R_{d.p.}$, where $R_{(CO_3^{\bullet-}+S)}$, $R_{(HO^\bullet+S)}$ and $R_{d.p.}$ are the rates of S degradation by $CO_3^{\bullet-}$, HO$^\bullet$ and the direct photolysis, respectively. $R_{(CO_3^{\bullet-}+S)}$ and $R_{(HO^\bullet+S)}$ can be expressed as follows:

$$R_{(CO_3^{\bullet-}+S)} = k_{(CO_3^{\bullet-}+S)} \times [CO_3^{\bullet-}] \times [S] - k_{Red} \times [S^{\bullet+}] \times [PhOH] \quad \text{(Eq. 3.3.12)}$$

$$R_{(HO^\bullet+S)} = k_{(HO^\bullet+S)} \times [HO^\bullet] \times [S] \quad \text{(Eq. 3.3.13)}$$

Under the irradiation conditions used in this work, the steady-state approximation can be applied to $HO^{\bullet}$, $CO_3^{\bullet-}$ and $S^{\bullet+}$, allowing their concentration values to be expressed as follows on the basis of the reaction system described in Scheme 3.3.2:

$$[HO^{\bullet}] = \frac{R_{f,HO^{\bullet}}}{k_{(HO^{\bullet}+S)}\times[S] + k_{(HO^{\bullet}+PhOH)}\times[PhOH] + k_{HO^{\bullet}}^{NaHCO_3}\times C_{NaHCO_3}} \quad \text{(Eq. 3.3.14)}$$

$$[CO_3^{\bullet-}] = \frac{k_{HO^{\bullet}}^{NaHCO_3}\times C_{NaHCO_3}\times[HO^{\bullet}]}{k_{(CO_3^{\bullet-}+S)}\times[S] + k_{(CO_3^{\bullet-}+PhOH)}\times[PhOH]} \quad \text{(Eq. 3.3.15)}$$

$$[S^{\bullet+}] = \frac{k_{(CO_3^{\bullet-}+S)}\times[CO_3^{\bullet-}]\times[S]}{k_{Red}\times[PhOH] + k_{Ox}} \quad \text{(Eq. 3.3.16)}$$

where $R_{f,HO^{\bullet}}$ is the photoproduction rate of $HO^{\bullet}$ upon nitrate photolysis, while all the other parameters were defined previously in the text.

By introducing these concentrations in Eqs. 3.3.12 and 3.3.13 and by taking into account the equations for $\chi_{HO^{\bullet}}^{NaHCO_3}$, $\chi_{CO_3^{\bullet-}}^{S}$ (Eqs. 3.3.4 and 3.3.5) and $\chi_{HO^{\bullet}}^{S}$ (see the 'Experimental procedure' section), one gets:

$$R_{(CO_3^{\bullet-}+S)} = R_{f,HO^{\bullet}} \times \chi_{HO^{\bullet}}^{NaHCO_3} \times \chi_{CO_3^{\bullet-}}^{S} \times \left(\frac{k_{Ox}}{k_{Red}\times[PhOH] + k_{Ox}}\right) \quad \text{(Eq. 3.3.17)}$$

$$R_{(HO^{\bullet}+S)} = R_{f,HO^{\bullet}} \times \chi_{HO^{\bullet}}^{S} \quad \text{(Eq. 3.3.18)}$$

Note that $R_{f,HO^{\bullet}} \times \chi_{HO^{\bullet}}^{NaHCO_3} \times \chi_{CO_3^{\bullet-}}^{S} = R_{(CO_3^{\bullet-}+S)}^{0}$, which is the value of $R_{(CO_3^{\bullet-}+S)}$ in the absence of phenol. $[PhOH]_{1/2}$ is operationally defined as the phenol concentration for which $R_{(CO_3^{\bullet-}+S)} = 0.5 \times R_{(CO_3^{\bullet-}+S)}^{0}$, or alternatively $k_{Ox} \times \left(k_{Red} \times [PhOH]_{1/2} + k_{Ox}\right)^{-1} = 0.5$. As a consequence, $[PhOH]_{1/2} = k_{Ox} \times (k_{Red})^{-1}$ and Eq. 3.3.17 can read as follows:

$$R_{(CO_3^{\bullet-}+S)} = R_{f,HO^\bullet} \times \chi_{HO^\bullet}^{NaHCO_3} \times \chi_{CO_3^{\bullet-}}^{S} \times \left(\frac{1}{1+\frac{[PhOH]}{[PhOH]_{1/2}}} \right) \qquad \text{(Eq. 3.3.19)}$$

Finally, by substituting Eqs. 3.3.18 and 3.3.19 in the expression for R_S, one gets:

$$R_S = R_{f,HO^\bullet} \times \left\{ \chi_{HO^\bullet}^{NaHCO_3} \times \chi_{CO_3^{\bullet-}}^{S} \times \frac{1}{1+\frac{[PhOH]}{[PhOH]_{1/2}}} + \chi_{HO^\bullet}^{S} \right\} + R_{d.p.}$$

(Eq. 3.3.20)

Equation 3.3.20 describes the dependence of R_S on phenol concentration, and it resembles Eq. 3.3.2 that was previously used to describe the back-reduction process during the phototransformation of organic compounds by ^{3}CDOM* (see also Vione et al., 2018; Wenk et al., 2011; Wenk and Canonica, 2012). However, contrary to Eq. 3.3.2, in this case the intermediates produced upon anilines oxidation by $CO_3^{\bullet-}$ are all considered to potentially undergo back-reduction, which means f = 1.

In the absence of phenol (*i.e.*, $[PhOH]$ = 0) one has $R_S^0 \cong R_{f,HO^\bullet} + R_{d.p.}$, because almost all the photochemically produced $HO^\bullet$ radicals react with HCO_3^-/CO_3^{2-} to give $CO_3^{\bullet-}$, and the carbonate radical reacts with S (*i.e.*, $\chi_{HO^\bullet}^{NaHCO_3} \sim 1$, $\chi_{CO_3^{\bullet-}}^{S} = 1$, and $\chi_{HO^\bullet}^{S}$ can be neglected). The addition of phenol decreases R_S and, when $[PhOH] = [PhOH]_{1/2}$, one has $R_S \cong 0.5 \times R_{f,HO^\bullet} + R_{d.p.}$. The extent of inhibition is more significant for higher values of the ratio $[PhOH] \times \left([PhOH]_{1/2}\right)^{-1} = k_{Red} \times [PhOH] \times (k_{Ox})^{-1}$, which represents the relative branching ratio of the Ar-$NH^\bullet$ reactions (back-reduction, Eq.

3.3.11, *vs.* further transformation, Eq. 3.3.10). If $[PhOH] \times \left([PhOH]_{1/2}\right)^{-1} >$ 1, then Ar-NH$^{\bullet}$ is mainly reduced back to Ar-NH$_2$. In contrast, transformation of Ar-NH$^{\bullet}$ into reaction products predominates if $[PhOH] \times \left([PhOH]_{1/2}\right)^{-1} <$ 1. Indeed, the lower is $[PhOH]_{1/2}$, the stronger is the inhibition of S degradation through the back-reduction effect.

The rate of S direct photolysis ($R_{d.p.}$) was assessed by correcting the direct photolysis rate measured in ultrapure water (pH 8.3) in the presence of $NaHCO_3$ ($R_{d.p.,exp}$; Fig.3.3.5) for the inner-filter effect of nitrate, because the direct photolysis of S is slower in the presence of nitrate.

$$R_{d.p.} = R_{d.p.,exp} \times \frac{\int_{\lambda} p^{\circ}(\lambda) \times \frac{\varepsilon_S(\lambda)[S]}{\varepsilon_{NO_3^-}(\lambda)[NO_3^-]+\varepsilon_S(\lambda)[S]} \times [1-10^{-b\times(\varepsilon_{NO_3^-}(\lambda)[NO_3^-]+\varepsilon_S(\lambda)[S])}] d\lambda}{\int_{\lambda} p^{\circ}(\lambda) \times [1-10^{-\varepsilon_S(\lambda)\times b\times[S]}] d\lambda}$$

(Eq. 3.3.21)

In Eq. 3.3.21, $p^{\circ}(\lambda)$ is the UVB lamp photon flux density incident on the solution (Fig.3.3.4), $\varepsilon(\lambda)$ is the molar absorption coefficient (of S, see Fig.3.3.4, or NO_3^-), and b is the solution optical path length (0.4 cm). The correction factor was ~0.94 (i.e., $R_{d.p.}$ ~0.94× $R_{d.p.,exp}$). Note that $R_{d.p.}$ was here considered not to vary with [*PhOH*], because the direct photolysis of chloroanilines should occur *via* loss of chlorine atoms rather than through photoionization of the amino group, producing hardly reducible intermediates (Carena et al., 2018; Guizzardi et al., 2001; Othmen et al., 2000). Therefore, the rate of a possible (but unlikely) back reduction might be negligible and, consequently, would not affect the direct photolysis process. In contrast, aniline undergoes photoionization of the N-atom forming the same anilino radical (Saito et al., 1996) that is expected to be produced upon reaction with

$CO_3^{\bullet-}$, and which can be reduced back to the starting compound by phenol. However, the direct photolysis of aniline was negligible, preventing the likely occurrence of an additional back-reduction process.

Fig.3.3.7 shows the experimental profiles of R_S vs. $[PhOH]$ for the studied anilines. A very good fit to the experimental data was obtained with Eq. 3.3.20, using $R_{f,HO^\bullet}$ and $[PhOH]_{1/2}$ as free-floating variables, which suggests that the kinetic model proposed for the back-reduction matches the experimental findings. When fitting the experimental data, the fractions of $HO^\bullet$ that react with bicarbonate/carbonate and S under our experimental conditions were set as, respectively, $\chi_{HO^\bullet}^{NaHCO_3}$ = 0.965-0.985 and $\chi_{HO^\bullet}^{S}$ = 0.016-0.018, while the fraction of $CO_3^{\bullet-}$ reacting with S was $\chi_{CO_3^{\bullet-}}^{S}$ = 0.97-0.99, depending on the compound. Finally, $[PhOH]_{1/2}$ (μmol L^{-1}) could be determined by data fit, which yielded $[PhOH]_{1/2}$ = 2.19 ± 0.23 μmol L^{-1} for aniline (Ani), 1.15 ± 0.25 μmol L^{-1} for 3-chloroaniline (3CA), 1.18 ± 0.26 μmol L^{-1} for 4-chloroaniline (4CA), and 1.18 ± 0.22 μmol L^{-1} for 3,4-dichloroaniline (3,4DCA).

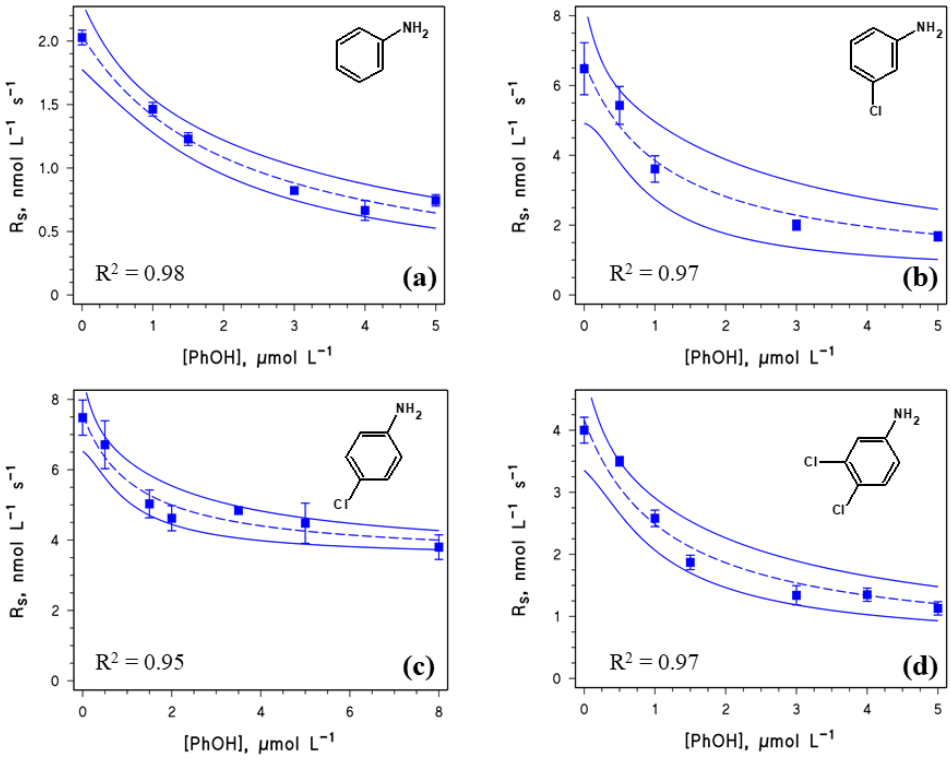

Fig.3.3.7. Experimental degradation rates of **(a)** Ani, **(b)** 3CA, **(c)** 4CA and **(d)** 3,4DCA, as a function of the concentration of added phenol. The dashed curves represent the fit results with (Eq. 3.3.20), while the solid curves are the 95% confidence bands of the fit. The R^2 parameter shows the goodness of the fit. The irradiated solutions (pH 8.3) contained $NaNO_3$ + $NaHCO_3$ and were exposed to UVB radiation.

Considerations about the experimental approach

Despite suitable for the present purposes, the described experimental approach can pose some limitations. Indeed, Eq. 3.3.7 sets the maximum phenol concentration to be used for preventing interference due to the reaction PhOH + $CO_3^{\bullet-}$ ($_{max}[PhOH]$). The result strongly depends on the value of $k_{(S+CO_3^{\bullet-})}$, and thus on the investigated organic pollutant S. In particular, $k_{(S+CO_3^{\bullet-})}$ (and, as a consequence, $[PhOH]_{1/2}$, see Eq. 3.3.7) should be high enough to ensure

that one can appreciably observe at least the halving of the rate R_S^0, which allows for calculating the value of $[PhOH]_{1/2}$ without data extrapolation. In other words, it should be $_{max}[PhOH] > [PhOH]_{1/2}$.

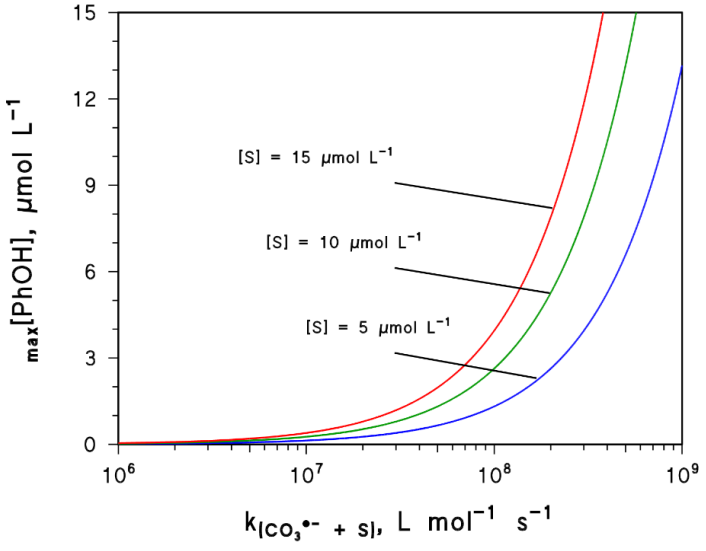

Fig.3.3.8 Plot showing the $_{max}$[PhOH] dependence on the second-order rate constant of the reaction between S and carbonate radical ($k_{(S+CO_3^{\bullet-})}$) at different initial concentrations of S. Note the logarithmic scale of $k_{(S+CO_3^{\bullet-})}$.

Fig.3.3.8 shows the dependence of $_{max}[PhOH]$ on the value of $k_{(S+CO_3^{\bullet-})}$. For most compounds that undergo significant back-reduction during ^{3}CDOM*-induced photodegradation, the reported values of $[PhOH]_{1/2}$ are in the range of few micromoles per liter (this work, Canonica and Laubscher, 2008; Leresche et al., 2016; Vione et al., 2018; Wenk et al., 2011; Wenk and Canonica, 2012). By analogy between oxidations by ^{3}CDOM* and $CO_3^{\bullet-}$, we can expect that a similar range is applicable to the $CO_3^{\bullet-}$–triggered reactions as well (more details about this assumption are described in the next sections). As a consequence, $_{max}[PhOH]$ should be > 1 µmol L^{-1} and, therefore,

$k_{(S+CO_3^{\bullet-})}$ > 1×10^8 L mol^{-1} s^{-1} for [S] = 5 μmol L^{-1}. The latter is the concentration of S that is commonly used in these kinds of studies (this work, Canonica and Laubscher, 2008; Leresche et al., 2016; Vione et al., 2018; Wenk et al., 2011; Wenk and Canonica, 2012). For those xenobiotics that do not satisfy this condition (namely, those having $k_{(S+CO_3^{\bullet-})}$ < 1×10^8 L mol^{-1} s^{-1}) such as, for instance, triazine and phenylurea herbicides (Wojnárovits et al., 2020), the experimental assessment of $[PhOH]_{1/2}$ could be quite tough. Fortunately, this would not be a huge problem in the framework of the assessment of the environmental fate of these compounds, because the $CO_3^{\bullet-}$ radicals play a negligible role in the overall photodegradation of triazines and phenylureas (Fabbri et al., 2015a; Marchetti et al., 2013). However, a doubling of [S] would allow for the critical value of $k_{(S+CO_3^{\bullet-})}$ to be halved to ~5×10^7 L mol^{-1} s^{-1}, while by triplicating [S] one would decrease it down to ~2.5×10^7 L mol^{-1} s^{-1}. Despite apparently convenient, the increase of [S] induces also the increase of C_{NaHCO_3} (Eq. 3.3.6) and thus of the ionic strength, which could affect the (photo)reactions (Zhang et al., 2019). Therefore, although an increase of [S] can be considered as feasible under particular circumstances, one should be mindful about the possible effects of the ionic strength on the photochemistry of S.

3.3.3 Thermodynamics and kinetics of the back-reduction of anilines induced by phenol

Linear free energy relationship for the phenol-induced back-reduction

It has been shown in previous sections that the photodegradation of 3-chloroaniline (3CA) and 3,4-dichloroaniline (3,4DCA) by both ^{3}CBBP* and

$CO_3^{\bullet-}$ is significantly inhibited in the presence of phenol, which acts as antioxidant. Furthermore, in the case of aniline (Ani) and 4-chloroaniline (4CA) it was possible to show the occurrence of the phenol-induced back-reduction upon reaction with $CO_3^{\bullet-}$ (the reaction with ^{3}CBBP* was not studied for these compounds). Wenk and Canonica (2012) reported that the photodegradation of Ani and 4CA by the excited triplet state of 2-acetonaphthone (^{3}2AN*) (an alternative to ^{3}CBBP* as ^{3}CDOM* proxy) is inhibited by phenol as well. Indeed, several if not all the (chloro)anilines undergo the back-reduction phenomenon after reaction with ^{3}CBBP* and/or $CO_3^{\bullet-}$ in the presence of phenol.

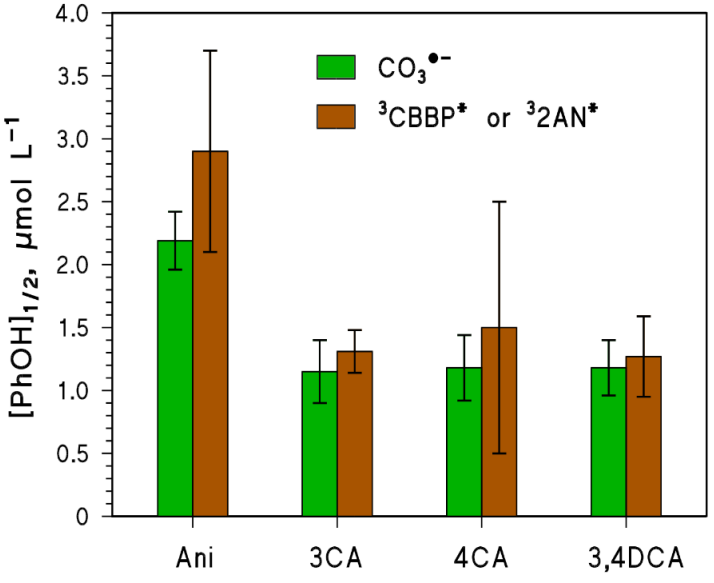

Fig.3.3.9 Comparison between the *[PhOH]$_{1/2}$* values measured for the degradation of anilines by $CO_3^{\bullet-}$, and those observed for ^{3}CBBP*- and ^{3}2AN*-induced oxidation. The data concerning the reactions Ani/4CA + ^{3}2AN* were taken from Wenk and Canonica (2012), those for 3CA/3,4DCA + ^{3}CBBP* as well as all the $CO_3^{\bullet-}$ reactions are from this work. Error bars represent standard errors (in the case of data from this work, they represent the goodness of the fit of the experimental data with Eq. 3.3.2 or Eq. 3.3.20).

Fig.3.3.9 compares the values of $[PhOH]_{1/2}$ obtained for the photodegradation of Ani, 3CA, 4CA and 3,4DCA in the presence of ^{3}CBBP*/^{3}2AN* and $CO_3^{\bullet-}$ (this work, as well as Wenk and Canonica, 2012). The $CO_3^{\bullet-}$-based dataset does not significantly differ from the ^{3}CBBP*/^{3}2AN*-based one. The $[PhOH]_{1/2}$ values in the former are slightly lower than those obtained with ^{3}CBBP*/^{3}2AN*, but differences are always within the experimental error. This finding suggests that the $[PhOH]_{1/2}$ value for the back-reduction of anilines does not depend on the photochemically produced transient species that is involved in the oxidation of the substrates.

The proposed mechanism for the oxidation of anilines (Ar-NH_2) by ^{3}CBBP*/^{3}2AN* or $CO_3^{\bullet-}$ takes place through one-electron abstraction at, most likely, the N-atom, forming the anilino radical cations (Ar-$NH_2^{\bullet+}$) (Elango et al., 1984; Heeb and Peters, 2006; Huang and Mabury, 2000; Wenk and Canonica, 2012; Wojnárovits et al., 2020). Ar-$NH_2^{\bullet+}$ usually occur as neutral radicals (Ar-$NH^{\bullet}$) at ~neutral and basic pH, because they are weakly acidic compounds (Jonsson et al., 1994). Therefore, when Ar-NH_2 is oxidized by ^{3}CBBP*/^{3}2AN* and/or $CO_3^{\bullet-}$, it is Ar-$NH^{\bullet}$ (and not Ar-$NH_2^{\bullet+}$) that should be involved in the back-reduction induced by phenol (Scheme 3.3.3). Note that the same conclusion is still valid if the mechanism of Ar-NH_2 oxidation occurs *via* PCET rather than ET, which directly yields Ar-$NH^{\bullet}$.

The production of similar reaction intermediates during anilines degradation by ^{3}CBBP*/^{3}2AN* or $CO_3^{\bullet-}$ should thus account for the results reported in Fig.3.3.9. Note that, although ^{3}CBBP* and ^{3}2AN* have different one-electron reduction potentials ($E^o_{^3CBBP*/CBBP^{\bullet-}}$ = 1.84 V and $E^o_{^3(2AN)*/2AN^{\bullet-}}$ = 1.34 V vs. NHE, respectively; McNeill and Canonica, 2016), they are not far from the one-electron reduction potential of $CO_3^{\bullet-}$, which is 1.6-1.8 V *vs.* NHE

(Arnold, 2014; Wojnárovits et al., 2020). Therefore, ^{3}CBBP*, ^{3}2AN* and $CO_3^{\bullet-}$ are all able to oxidize aniline and the chloroanilines to the corresponding Ar-$NH_2^{\bullet+}$ radicals, the reduction potentials of which ($E^o_{ArNH_2^{\bullet+}/ArNH_2}$) are lower: $E^o_{ArNH_2^{\bullet+}/ArNH_2}$ = 1.17 V *vs.* NHE for Ani, 1.24 V for 4CA, and 1.34 V for 3CA and 3,4DCA. These values are averages of computational data of $E^o_{ArNH_2^{\bullet+}/ArNH_2}$ reported in the literature (Arnold et al., 2017; Winget et al., 2000).

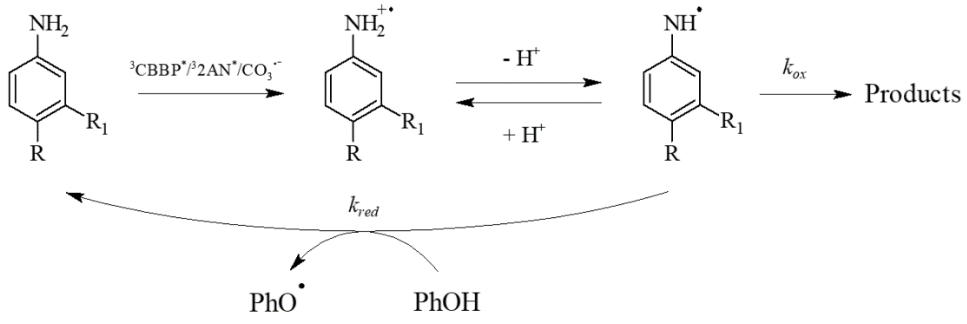

Scheme 3.3.3. Back-reduction process that follows the oxidation of (chloro)anilines by ^{3}CBBP*/^{3}2AN* or $CO_3^{\bullet-}$. R = R_1 = H for Ani; R = H and R_1 = Cl for 3CA; R = Cl and R_1 = H for 4CA; R = R_1 = Cl for 3,4DCA.

The difference in the standard reduction potential of the couples Ar-NH$^\bullet$/Ar-NH_2 ($E^o_{ArNH^\bullet/ArNH_2}$) and PhO$^\bullet$/PhOH ($E^o_{PhO^\bullet/PhOH}$) is an important driving force of the back-reduction process. On the basis of electrochemical rules, the higher is $E^o_{ArNH^\bullet/ArNH_2} - E^o_{PhO^\bullet/PhOH}$, the more favored is the back-reduction process. Unfortunately, the values of $E^o_{ArNH^\bullet/ArNH_2}$ are not available in the literature, because the anilines one-electron reduction potentials have been measured at pH values in between the pKa's of the anilinium cations (Ar-NH_3^+) and those of the conjugated anilino radicals (Ar-$NH_2^{\bullet+}$) (Jonsson et al., 1994; Pavitt et al., 2017). In such conditions, Ar-$NH_2^{\bullet+}$ and Ar-NH_2 are the

prevailing species. However, $E^o_{ArNH^\bullet/ArNH_2}$ can be assessed by considering the thermodynamics of both Ar-$NH_2^{\bullet+}$ deprotonation (Eq. 3.3.9) and reduction (Eq. 3.3.22), from which one gets the needed data for the reduction of Ar-$NH^\bullet$ to Ar-NH_2 (Eq. 3.3.23).

Ar-$NH_2^{\bullet+}$ + e^- ⇆ Ar-NH_2 (Eq. 3.3.22)

Ar-$NH^\bullet$ + H^+ + e^- ⇆ Ar-NH_2 (Eq. 3.3.23)

The standard Gibbs energy referred to Eq. 3.3.23 is $\Delta_rG_{23}^o = \Delta_rG_{22}^o - \Delta_rG_9^o$, where $\Delta_rG_{22}^o = -F\times E^o_{ArNH_2^{\bullet+}/ArNH_2}$ and $\Delta_rG_9^o = 2.303RT\times pK_a(Ar\text{-}NH_2^{\bullet+})$ are the standard Gibbs energies of Ar-$NH_2^{\bullet+}$ reduction (Eq. 3.3.22) and Ar-$NH_2^{\bullet+}$ deprotonation (Eq. 3.3.9), respectively, F is Faraday's constant (96,485 C mol^{-1}), R the gas constant (8.31 J mol^{-1} K^{-1}), and T the absolute temperature (K). Because $\Delta_rG_{23}^o = -F\times E^o_{ArNH^\bullet/ArNH_2}$, one gets $E^o_{ArNH^\bullet/ArNH_2}$(V) = $E^o_{ArNH_2^{\bullet+}/ArNH_2}$(V) + $0.06\times pK_a(Ar\text{-}NH_2^{\bullet+})$ at the temperature of our experiments (~303 K). The pK_a values of the para-substituted anilino radical cations (Ar-$NH_2^{\bullet+}$) have been assessed in previous work through the relationship $pK_a(Ar\text{-}NH_2^{\bullet+}) = 7.17 - 3.66\times\sigma_p^+$, where 7.17 is the pK_a of the anilino radical cation derived from Ani oxidation, and σ_p^+ is the Brown constant of the substituent in para position (Jonsson et al., 1994). For 4CA, $\sigma_p^+ = 0.11$ (Winget et al., 2000) and, therefore, $pK_a(4\text{-}ClPh\text{-}NH_2^{\bullet+}) = 6.77$. Because chlorine atoms in either para or meta positions have similar influence on the amino-group acidic properties, we can assume that the previous equation can be applied to 3CA as well ($\sigma_m^+ = 0.37$; Winget et al., 2000), obtaining $pK_a(3\text{-}ClPh\text{-}NH_2^{\bullet+}) = 5.82$. Finally, the sum of the contributions of the chlorine atoms in para and meta position ($\sigma_p^+ + \sigma_m^+$; Li and Hoffman, 1999) allows for the determination of $pK_a(3,4\text{-}diClPh\text{-}NH_2^{\bullet+}) = 5.41$. Therefore, the

resulting values of $E^{o}_{ArNH^{\bullet}/ArNH_2}$ (*vs.* NHE) are 1.60 V for Ani, 1.65 V for 4CA, 1.69 for 3CA, and 1.66 V for 3,4DCA. The sequence of the $E^{o}_{ArNH^{\bullet}/ArNH_2}$ values thus obtained is in good agreement with the Hammet plot for the substituted phenylaminyl radicals *vs.* the Brown constant σ_p^+, which shows an increasing trend of Ar-NH$^{\bullet}$ destabilization with σ_p^+ (Hioe et al., 2015). Furthermore, note that $E^{o}_{ArNH^{\bullet}/ArNH_2} > E^{o}_{ArNH_2^{\bullet+}/ArNH_2}$, supporting the fact that Ar-NH$^{\bullet}$ may be more prone than Ar-NH$_2^{\bullet+}$ to be involved in back-reduction. These values are decreased by ~0.5 V at pH 8.3, but they are still higher than the formal redox potential of the couple PhO$^{\bullet}$/PhOH, which is 0.96 V *vs.* NHE at the same pH value according to Li and Hoffman (1999). This issue makes the back-reduction of Ar-NH$^{\bullet}$ by PhOH thermodynamically favorable.

As previously described, the phenol-induced back-reduction process is quantified by means of the parameter $[PhOH]_{1/2} = k_{Ox} \times (k_{Red})^{-1}$. In the case of anilines, k_{Ox} refers to the oxidation of the intermediate Ar-NH$^{\bullet}$ and k_{Red} to the reduction of Ar-NH$^{\bullet}$ by phenol. The latter reaction should occur through ET/PCET between the two species involved (Davis et al., 2018). Indeed, a recent work has shown that the radical intermediate formed from the ^{3}CDOM*-induced one-electron oxidation of mefenamic acid (a substituted diarylamine) undergoes back-reduction in the presence of sesamol (a substituted phenol). The reduction process is slightly affected by the kinetic solvent isotope effect (KSIE) (Davis et al., 2018). This finding supports the PCET mechanism of the back-reduction (Davis et al., 2018).

Because the Marcus theory relates the thermodynamics of (PC)ET reactions to their kinetics (Marcus, 1956; R. A. Marcus, 1957; R.A. Marcus, 1957; Mayer, 2004; Savéant, 2014), it should also be valid for the present back-

reduction process. Although a rigorous application of the Marcus theory to back reduction is beyond the scope of this work, it is shown here a first attempt to relate the kinetic parameter $[PhOH]_{1/2}$ to the one-electron reduction potential $E^o_{ArNH^\bullet/ArNH_2}$. The latter is representative of the back-reduction thermodynamics, because $\Delta_r G_{red}^o = -F\times(E^o_{ArNH^\bullet/ArNH_2} - E^o_{PhO^\bullet/PhOH})$ (note that $E^o_{PhO^\bullet/PhOH}$ is here considered as a constant, if phenol is used as antioxidant).

The semi-log plot of Fig.3.3.10 shows that $\ln[PhOH]_{1/2} = -\ln k_{red} + \ln k_{ox}$ is linearly dependent on $E^o_{ArNH^\bullet/ArNH_2}$. This finding suggests a linear free-energy relationship (LFER) of the type $\ln k_{red} = \beta \times \Delta_r G_{11}^\circ + \gamma = \beta' \times E^o_{ArNH^\bullet/ArNH_2} + \gamma$ (Mayer, 2004), where $\Delta_r G_{11}^\circ$ is the standard Gibbs energy of Eq. 3.3.11. In particular, $\ln[PhOH]_{1/2}$ = (–2.98±0.27 V^{-1}) $\times E^o_{ArNH^\bullet/ArNH_2}$ + (5.32±0.42). It should be pointed out that such an approach assumes a similar reorganization energy (λ) among the anilines (see Appendix I for further details), which is reasonably accounted for by similar molecular structures of the investigated anilines, as well as similar reactivity with ^{3}CBBP*/^{3}2AN* and $CO_3^{\bullet-}$ (Heeb and Peters, 2006; Mayer, 2004; Nad and Pal, 2000). Therefore, we can infer that by increasing $E^o_{ArNH^\bullet/ArNH_2}$, k_{red} gets enhanced and the back-reduction effect becomes stronger (*i.e.*, $[PhOH]_{1/2}$ becomes lower, and so does $\ln[PhOH]_{1/2}$). This is reasonable, because the stronger is Ar-NH$^\bullet$ as an oxidant, the easier is its reduction by PhOH.

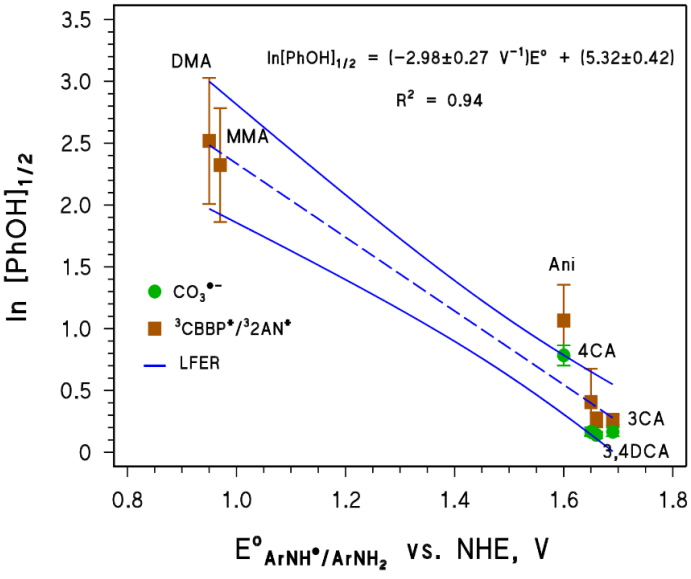

Fig.3.3.10 Semi-log plot showing the dependence of $[PhOH]_{1/2}$ (µmol L^{-1}), measured for the reaction Ar-NH_2 + ^{3}CBBP*/^{3}2AN*/$CO_3^{\bullet-}$, on the reduction potential of the anilino radicals. Note that in the case of N,N-dimethylaniline (DMA) and N-methylaniline (MMA), the redox couple is Ar-$NR_2^{\bullet+}$/Ar-NR_2 (the $[PhOH]_{1/2}$ values for these compounds were obtained from the work of Wenk and Canonica, (2012). The plot shows the linear fit function (linear free-energy relationship, LFER) with the associated 95% confidence band (solid blue lines) and R^2 value (0.94), which are indicators of the goodness of the fit.

Application of the LFER

We tested the obtained LFER of Fig.3.3.10 in the cases of two anilines (N,N-dimethyl-4-cyanoaniline and sulfadiazine), a phenylpiperidine (paroxetine, PXT) and clofibric acid (CLO).

N,N-dimethyl-4-cyanoaniline (or 4-(dimethylamino)benzonitrile, DMABN) has been found to be oxidized by triplet states of aromatic ketones through electron transfer, forming the radical cation DMABN$^{\bullet+}$ (Leresche et al., 2019). This radical cation can be reduced back to DMABN by reaction with phenol, showing $[PhOH]_{1/2}$ = 3.7 ± 1.2 µmol L^{-1} (Leresche et al., 2016). By

introducing in the LFER the value of the one-electron reduction potential of DMABN$^{\bullet+}$, $E^{o}_{DMABN^{\bullet+}/DMABN}$ ~1.30 V vs. SHE (Leresche et al., 2019), one gets $[PhOH]_{1/2}$ = 4.4 ± 0.6 µmol L^{-1}, in good agreement with the experimental result.

Previous works have shown that both the amphoteric (HSDZ) and basic (SDZ^{-}) forms of sulfadiazine (pK_{a2}(HSDZ/SDZ^{-}) ~6.5) undergo oxidation by ^{3}CDOM* through ET/PCET (Tentscher et al., 2013; Wang et al., 2015), and back-reduction in the presence of phenol (Vione et al., 2018; Wenk and Canonica, 2012). In particular, HSDZ undergoes a very weak back-reduction by phenol with $[PhOH]_{1/2}$ = 19.5 ± 2.5 µmol L^{-1} at pH 5.5 (Vione et al., 2018), while the back-reduction of SDZ^{-} at pH 8.0 is stronger, with $[PhOH]_{1/2}$ = 3.2 ± 0.8 µmol L^{-1} (Wenk and Canonica, 2012). The oxidation of HSDZ and SDZ^{-} produces HSDZ$^{\bullet+}$ and SDZ$_1^{\bullet}$, respectively, which are linked together and with two additional species (SDZ$_2^{\bullet}$ and SDZ$^{\bullet-}$) through acid-base chemical equilibria (Fig.3.3.11a) (Tentscher et al., 2013). The one-electron reduction potentials of HSDZ$^{\bullet+}$ and SDZ$_1^{\bullet}$ have been computationally assessed as $E^{o}_{HSDZ^{\bullet+}/HSDZ}$ = 1.3 V and $E^{o}_{SDZ_1^{\bullet}/SDZ^{-}}$ = 1.1 V vs. SHE (Tentscher et al., 2013). However, these reduction potentials do not match the experimental conditions used for the measurement of $[PhOH]_{1/2}$ (Vione et al., 2018; Wenk and Canonica, 2012), because at pH 5.5 and 8 the prevailing redox couples involved in the reduction process should be SDZ$_2^{\bullet}$/HSDZ + SDZ$^{\bullet-}$/HSDZ and SDZ$^{\bullet-}$/ SDZ^{-}, respectively, as the pH-dependent distribution functions suggest (Fig.3.3.11b).

The reduction potentials of the redox couples mentioned before can be calculated by considering the redox and acid-base equilibria shown in Fig.3.3.11a. Indeed, it is possible to demonstrate that $E^{o}_{SDZ^{\bullet-}/SDZ^{-}}$ =

$E^o_{SDZ_1^{\bullet}/SDZ^-} + 2.303RT(F)^{-1}pKa_6$, which is 1.48 V *vs.* SHE at 303 K. Similarly, $E^o_{SDZ_2^{\bullet}/HSDZ} = E^o_{HSDZ^{\bullet+}/HSDZ} + 2.303RT(F)^{-1}pKa_4$ (1.53 V *vs.* SHE at 303 K) and $E^o_{SDZ^{\bullet-}/HSDZ} = E^o_{SDZ^{\bullet-}/SDZ^-} + 2.303RT(F)^{-1}pKa_2$ (1.87 V *vs.* SHE at 303 K).

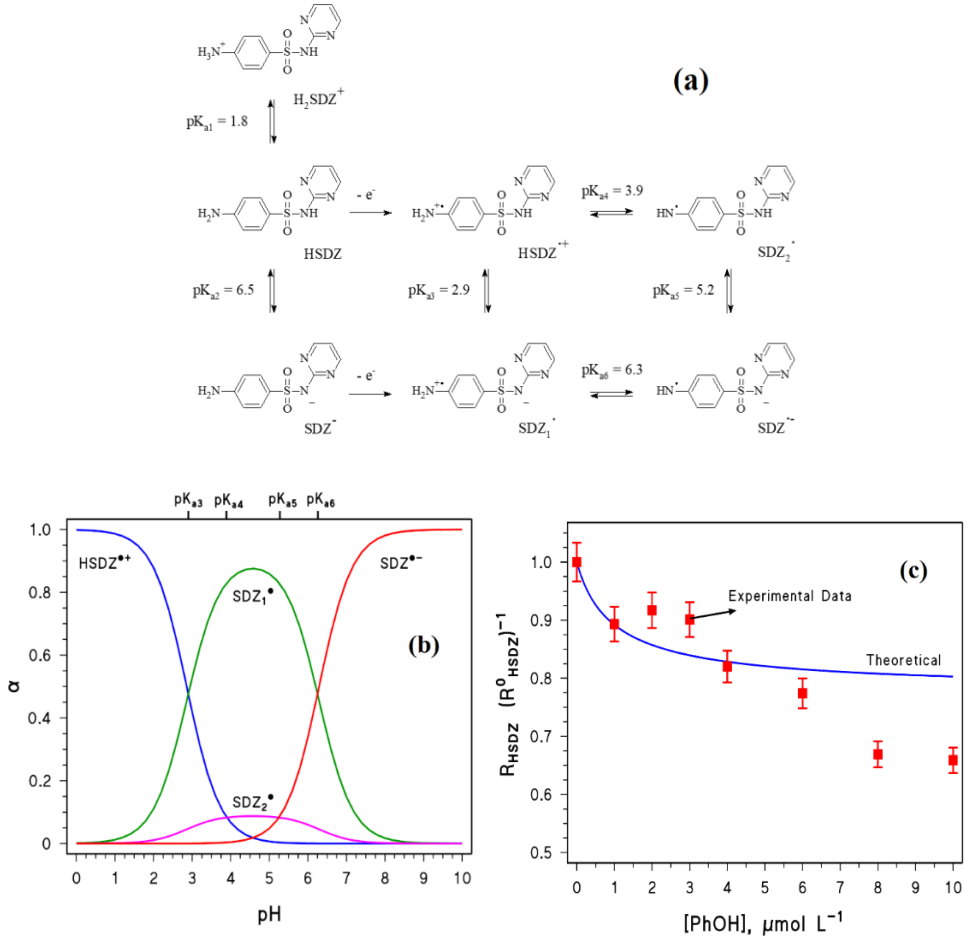

Fig.3.3.11 (a) One-electron oxidation of sulfadiazine and acid-base equilibria taking place among the oxidized products. Modified from Tentscher et al. (2013). **(b)** Related distribution functions of the radical species. **(c)** Inhibition of HSDZ photodegradation by ^{3}CBBP* at pH 5.5 due to theoretical (blue line) and experimental (red points) back-reduction. The experimental data were taken from Vione et al. (2018).

By substituting the calculated $E^{o}_{SDZ^{\bullet-}/SDZ^{-}}$ value in the LFER, one gets $[PhOH]_{1/2}$ = 2.5 ± 0.5 µmol L^{-1}. This value is in good agreement with the experimental finding that $[PhOH]_{1/2}$ = 3.2 ± 0.8 µmol L^{-1} at pH = 8 (Wenk and Canonica, 2012).

The case of HSDZ is more complicated. The oxidation of HSDZ at pH 5.5 forms, in order of importance, $SDZ_1^{\bullet}$, $SDZ^{\bullet-}$ and $SDZ_2^{\bullet}$ (see Fig.3.3.11b), which could undergo back-reduction. However, $SDZ_1^{\bullet}$ undergoes fast further transformation through a uni-molecular reaction, with k_{ox} ~10^7 s^{-1} (Tentscher et al., 2013). Even if the k_{red} of $SDZ_1^{\bullet}$ were diffusion-limited (around 10^{10} L mol^{-1} s^{-1}), the product $k_{red} \times [PhOH]$ would be two orders of magnitude lower than k_{ox} in the presence of 10 µmol L^{-1} PhOH, as used by Vione and co-workers (2018). Therefore, back-reduction is a negligible reaction pathway for $SDZ_1^{\bullet}$.

The radicals $SDZ^{\bullet-}$ and $SDZ_2^{\bullet}$ undergo uni-molecular transformation reactions as well, but the respective k_{ox} values are ~10^{-6} s^{-1} and ~10^{-14} s^{-1} (Tentscher et al., 2013). Therefore, there is room for the back-reduction of $SDZ^{\bullet-}$ and $SDZ_2^{\bullet}$ to HSDZ. These findings suggest that a high reduction potential of Ar-$NH^{\bullet}$ is a necessary but not sufficient condition for the occurrence of back-reduction by phenol. As a consequence, the present LFER can only be applied to anilines that are oxidized to Ar-$NH^{\bullet}$ species that have low and similar values of k_{ox}.

The degradation kinetics of HSDZ takes into account the back-reduction contributions of both $SDZ_2^{\bullet}$ and $SDZ^{\bullet-}$ (Scheme 3.3.4), as per Eq. 3.3.24.

$$R_{HSDZ} = R^{0}_{HSDZ} - [PhOH] \times \left(k_{Red,SDZ_2^{\bullet}} [SDZ_2^{\bullet}] + k_{Red,SDZ^{\bullet-}} [SDZ^{\bullet-}]\right) \quad \text{(Eq. 3.3.24)}$$

R^0_{HSDZ} is the transformation rate of HSDZ in the absence of phenol. The steady-state concentrations of $SDZ_2^{\bullet}$ and $SDZ^{\bullet-}$ are, respectively, $[SDZ_2^{\bullet}] = \alpha_{SDZ_2^{\bullet}} \times R^0_{HSDZ} \times \left(k_{(Ox,SDZ_2^{\bullet})} + k_{(Red,SDZ_2^{\bullet})} \times [PhOH]\right)^{-1}$ and $[SDZ^{\bullet-}] = \alpha_{SDZ^{\bullet-}} \times R^0_{HSDZ} \times \left(k_{(Ox,SDZ^{\bullet-})} + k_{(Red,SDZ^{\bullet-})} \times [PhOH]\right)^{-1}$, where $\alpha_{SDZ_2^{\bullet}}$ (Eq. 3.3.25) and $\alpha_{SDZ^{\bullet-}}$ (Eq. 3.3.26) are, respectively, the pH-dependent distribution functions of $SDZ_2^{\bullet}$ and $SDZ^{\bullet-}$ (Fig.3.3.11b).

$$\alpha_{SDZ_2^{\bullet}} = \frac{[H^+]\times K_{a4}}{[H^+]^2 + [H^+]\times(K_{a3} + K_{a4}) + (K_{a3}\times K_{a4}\times K_{a5}\times K_{a6})^{1/2}} \qquad \text{(Eq. 3.3.25)}$$

$$\alpha_{SDZ^{\bullet-}} = \frac{(K_{a3}\times K_{a4}\times K_{a5}\times K_{a6})^{1/2}}{[H^+]^2 + [H^+]\times(K_{a3} + K_{a4}) + (K_{a3}\times K_{a4}\times K_{a5}\times K_{a6})^{1/2}} \qquad \text{(Eq. 3.3.26)}$$

Because $[PhOH]_{1/2} = k_{Ox} \times (k_{Red})^{-1}$ is compound-specific, by rearranging Eq. 3.3.24 one gets:

$$R_{HSDZ} = R^0_{HSDZ} \times \left(1 - \frac{\alpha_{SDZ_2^{\bullet}} \times \frac{[PhOH]}{[PhOH]_{1/2,\,SDZ_2^{\bullet}}}}{1 + \frac{[PhOH]}{[PhOH]_{1/2,\,SDZ_2^{\bullet}}}} - \frac{\alpha_{SDZ^{\bullet-}} \times \frac{[PhOH]}{[PhOH]_{1/2,SDZ^{\bullet-}}}}{1 + \frac{[PhOH]}{[PhOH]_{1/2,SDZ^{\bullet-}}}}\right) \qquad \text{(Eq. 3.3.27)}$$

where $[PhOH]_{\frac{1}{2},\,SDZ_2^{\bullet}}$ = 2.1 ± 0.5 µmol L^{-1} and $[PhOH]_{\frac{1}{2},SDZ^{\bullet-}}$ = 0.7 ± 0.4 µmol L^{-1}, as derived by substituting the values of $E^o_{SDZ_2^{\bullet}/HSDZ}$ and $E^o_{SDZ^{\bullet-}/HSDZ}$ in the observed LFER (Fig.3.3.10). Fig.3.3.11c shows the theoretical (Eq. 3.3.27) and experimental (Vione et al., 2018) dependence of the ratio $R_{HSDZ} \times (R^0_{HSDZ})^{-1}$ on phenol concentration, at pH 5.5. The model described by Eq. 3.3.27 is in reasonable agreement with the experimental data only at low PhOH concentrations. At higher $[PhOH]$ (8-10 µmol L^{-1}) the system

likely becomes more complex and can no longer be described by the mere combination of the back reduction of just $SDZ^{\bullet-}$ and $SDZ_2^{\bullet}$.

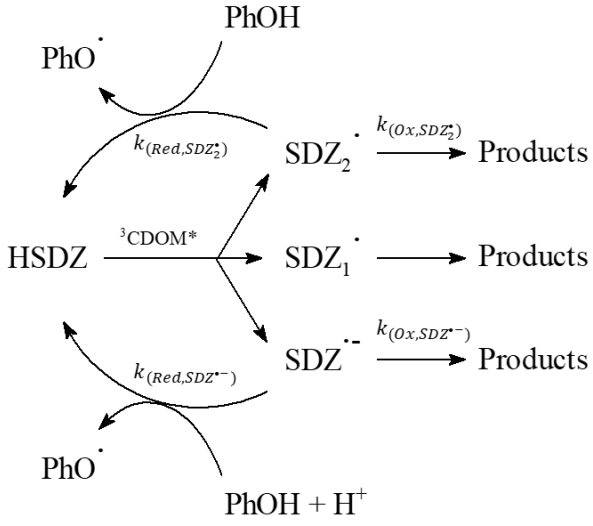

Scheme 3.3.4. Simplified scheme showing the proposed back-reduction process of sulfadiazine at pH 5.5.

In previous sections, it was reported the occurrence of back-reduction in the case of paroxetine degradation by ^{3}CBBP*. Differently from sulfadiazine, which has an aniline moiety, PXT is a phenylpiperidine (i.e., a dialkylamine). Unfortunately, there is no experimental evidence of the PXT functional group that participates to the (PC)ET reaction with ^{3}CBBP*. However, the piperidine N-atom could be a good candidate for the first step of PXT oxidation. This is partially supported by the fact that *(i)* the main environmental metabolite of PXT ((3S,4R)-4-(4-fluorophenyl)-3-(hydroxymethyl)piperidine) undergoes photolysis of the N-H atom forming a N-centered phenylpiperidine radical, which is thought to be responsible of the PXT photochemical fate (Šakić et al., 2013), and *(ii)* the other functional groups of PXT should be less easily oxidized than the N atom (Hioe et al., 2015). Therefore, a N-centered

phenylpiperidine radical cation (R_2-$NH^{\bullet+}$) is potentially produced upon reaction of PXT with ^{3}CBBP*. By assuming piperidine as a proxy-molecule that is representative of PXT during oxidation by ^{3}CBBP*, R_2-$NH^{\bullet+}$ should be in equilibrium with its conjugated neutral form (R_2-$N^{\bullet}$), with pK_a(R_2-$NH^{\bullet+}$) ~5.8 (Jonsson et al., 1996; Šakić et al., 2013; Vrček and Zipse, 2009). Because in this work the PXT experiments were carried out at pH 7, the prevailing form of oxidized PXT should be R_2-$N^{\bullet}$, which is more likely than R_2-$NH^{\bullet+}$ to be the species that is involved in the back-reduction. However, as additional transformation pathways, R_2-$N^{\bullet}$ can also undergo 1-2 and 1-4 H-atom shifts assisted by water as solvent (where '1' is the position of the N atom, while '2' or '4' are the relative positions of the C atoms of the piperidine ring that participate in the rearrangement) (Šakić et al., 2013; Vrček and Zipse, 2009). Under the adopted assumptions, the reduction potential of R_2-$N^{\bullet}$ can be calculated as $E^o_{R_2N^{\bullet}/R_2NH}$(V) = $E^o_{R_2NH^{\bullet+}/R_2NH}$(V) + 0.06×$pK_a$($R_2$-$NH^{\bullet+}$), where $E^o_{R_2NH^{\bullet+}/R_2NH}$ ~1.28 V vs. NHE is the one-electron reduction potential of piperidine (Arnold, 2014; Jonsson et al., 1996). Note that for dialkylamines such as PXT, the one-electron reduction potentials of the relevant radical cations have been previously set at 1.30 ± 0.05 V vs. NHE, as a general approximation for aqueous solutions (Jonsson et al., 1996). Consequently, $E^o_{R_2N^{\bullet}/R_2NH}$ would be ~1.6 V vs. NHE in the case of PXT. By introducing this value in the observed LFER (Fig.3.3.10), one gets $[PhOH]_{1/2}$ = 1.55 ± 0.69 μmol L^{-1} that is in good agreement with the experimental value $[PhOH]_{1/2}$ = 1.46 ± 0.25 μmol L^{-1}.

Finally, the LFER was applied to the case of CLO, that undergoes back-reduction upon oxidation by ^{3}CBBP*. Unfortunately, to the best of our knowledge, the one-electron reduction potential of CLO ($E^o_{CLO^{\bullet}/CLO}$) has not been assessed in previous works. However, the thermodynamics of CLO

transformation by sulfate radical ($SO_4^{\bullet-}$) has been recently investigated, showing that $SO_4^{\bullet-}$ oxidizes one of the methyl groups of CLO through single electron transfer with $\Delta_r G° = -3.90$ kcal mol^{-1} (i.e., -16.32 kJ mol^{-1}; Qin et al., 2020). Because in that case $\Delta_r G° = -F \times \left(E^o_{SO_4^{\bullet-}/SO_4^{2-}} - E^o_{CLO^{\bullet}/CLO}\right)$, where $E^o_{SO_4^{\bullet-}/SO_4^{2-}}$ ~2.44 V vs. SHE (Canonica and Schönenberger, 2019), one has $E^o_{CLO^{\bullet}/CLO}$ ~2.27 V. By assuming that the same electron transfer mechanism occurs also in the case of CLO oxidation by ^{3}CBBP*, and by introducing the obtained value of $E^o_{CLO^{\bullet}/CLO}$ in the LFER of Fig.3.3.10, one gets $[PhOH]_{1/2}$ = 0.20 ± 0.03 µmol L^{-1}, which is in good agreement with the experimental result $[PhOH]_{1/2}$ = 0.26 ± 0.20 µmol L^{-1}. However, in this case the LFER does not allow for the assessment of the low fraction of CLO$^{\bullet}$ that undergoes back-reduction (f = 0.33 ± 0.08).

3.3.4 Environmental significance of the back-reduction process

The back-reduction process has the potential to affect the indirect photodegradation of several water pollutants (this work; Canonica and Laubscher, 2008; Leresche et al., 2016; Vione et al., 2018; Wenk et al., 2011; Wenk and Canonica, 2012). Vione et al. (2018) have assessed the photochemical fate of sulfadiazine in surface waters by including the back-reduction kinetics in the APEX model and, in particular, in the part of the model that describes the ^{3}CDOM*-induced degradation of the contaminant. Here, the same model was modified to include the back-reduction in the ^{3}CDOM*- and $CO_3^{\bullet-}$-induced phototransformation of 3,4DCA. 3,4DCA is a secondary pollutant that derives from biological transformation of the herbicide propanil (Kanawi et al., 2016; Milan et al., 2006). It mainly

undergoes photodegradation in environmental waters by direct photolysis and reaction with $CO_3^{\bullet-}$, ^{3}CDOM* and $HO^{\bullet}$ (Carena et al., 2018).

In the environment, DOM would be the main antioxidant species thanks to its abundant phenolic moieties (Walpen et al., 2016; Wenk and Canonica, 2012). However, irradiation of CDOM can produce further potential reducing species such as excited phenolic moieties, reduced quinone-like species and superoxide radicals (Ma et al., 2020; Zhang et al., 2012; Zhang and Blough, 2016). All these species could participate as well to the back-reduction of the partially oxidized water pollutants (Davis et al., 2018; Yanyun Li et al., 2017). Despite the complexity of the species presumably involved in the environmental back-reduction processes, it is fortunately possible to convert the values of $[PhOH]_{1/2}$ obtained, in the case of this work, for 3,4DCA (1.18 ± 0.22 μmol L^{-1} for $CO_3^{\bullet-}$, 1.27 ± 0.32 μmol L^{-1} for ^{3}CBBP*), into the equivalent values of $DOM_{1/2}$ for irradiated Suwannee River fulvic acids (SRFA). Conversion was possible using the equation $DOM_{1/2}$ (mg_C L^{-1}) = $0.4\times[PhOH]_{1/2}$ (μmol L^{-1}), where $DOM_{1/2}$ refers to SRFA, which has been found to hold well in the cases of N,N-dimethyl-4-cyanoaniline and sulfadiazine (Leresche et al., 2016; Vione et al., 2018). Here, the rationale is the similarity in behavior between the phenolic moieties of SRFA and phenol itself, although irradiated SRFA may produce other potential reducing species, as described above. In the photochemical model, the apparent second-order rate constants (k*) for the reactions of 3,4DCA with $CO_3^{\bullet-}$ and ^{3}CDOM* were computed, respectively, as $k^*_{(3,4DCA+CO_3^{\bullet-})} = \psi \times k_{(3,4DCA+CO_3^{\bullet-})}$ and $k^*_{(3,4DCA+{}^3CDOM^*)} = \psi \times k_{(3,4DCA+{}^3CDOM^*)}$, where $\psi = DOM_{1/2} \times \left(DOC + DOM_{1/2}\right)^{-1}$. Finally, $k_{(3,4DCA+CO_3^{\bullet-})}$ = 4.8×10^8 L mol^{-1} s^{-1} and $k_{(3,4DCA+{}^3CDOM^*)}$ = 1.1×10^9 L mol^{-1} s^{-1} (Carena et al., 2018).

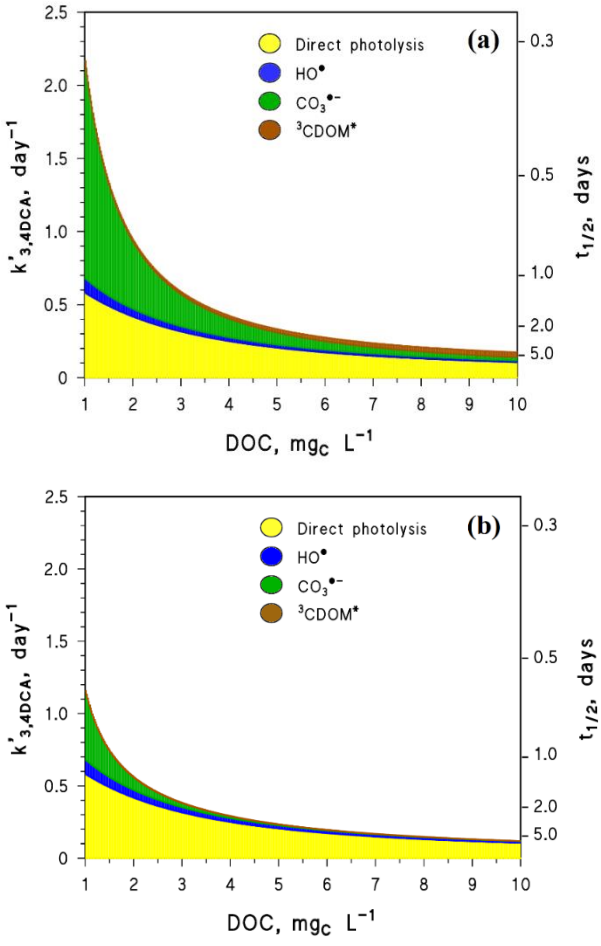

Fig.3.3.12. Modeled pseudo-first order photodegradation rate constants (left Y-axis) and photochemical half-life times (right Y-axis) of 3,4DCA in lake water as a function of the DOM content, quantified as DOC (dissolved organic carbon). In **(a)** the back-reduction processes were not considered, while in **(b)** the APEX model took into account the back-reduction during 3,4DCA photodegradation by both $CO_3^{\bullet-}$ and ^{3}CDOM*. The lake water chemical composition was set as 100 μmol L^{-1} NO_3^-, 1 μmol L^{-1} NO_2^-, 2 mmol L^{-1} alkalinity and pH 8.0, whereas the water-column optical depth was 1 m.

The model calculations, performed for a lake-water scenario (Fig.3.3.12), suggest that the transformation reactions of 3,4DCA with ^{3}CDOM* and $CO_3^{\bullet-}$

would be highly inhibited by the DOM-induced back-reduction process. The comparison of 3,4DCA photodegradation kinetics by neglecting (Fig.3.3.12a) and by considering the back reduction (Fig.3.3.12b) suggests the following: *(i)* back reduction would approximately double the photochemical lifetime of 3,4DCA at low DOC, compared to the case of no back-reduction, mostly because of the inhibition of the $CO_3^{\bullet-}$ process (overall, the ^{3}CDOM* reaction would be less important than $CO_3^{\bullet-}$ in the photodegradation of 3,4DCA, especially at low DOC), while lower differences are expected at high DOC; *(ii)* because of the important inhibition of the $CO_3^{\bullet-}$ reaction, direct photolysis would be the main pathway for the phototransformation of 3,4DCA in practically all surface-water conditions.

These findings show that the environmental fate of photolabile water pollutants can be highly affected by the back-reduction process, which can significantly increase the lifetime of some compounds and, therefore, their environmental impact. For this reason, the assessment of the occurrence of back-reduction is extremely important when investigating the environmental photochemistry (and, more in general, the environmental fate) of a xenobiotic. Particular attention should be paid to the photochemistry of N-containing compounds that are highly reactive with $CO_3^{\bullet-}$ and/or ^{3}CDOM* through (proton-coupled) electron transfer. In this case, the one-electron reduction potentials (Arnold, 2014) can be used as an explorative parameter to get information about the extent of back-reduction. Interestingly, the back-reduction process can be particularly important for anilines, which are usually degraded significantly by both ^{3}CDOM* and $CO_3^{\bullet-}$.

3.4 Conclusions

The results of this work suggest that:

1- Photodegradation of 3CA, 3,4DCA, PXT and CLO by ^{3}CBBP* undergoes inhibition in the presence of phenol, which reduces the partially oxidized pollutants back to the parent compounds.

2- Back-reduction by phenol is also operational in the case of the degradation of anilines carried out by $CO_3^{\bullet-}$ radicals.

3- The Marcus theory (and the related Rehm-Weller extension) fit well the data ($\ln[PhOH]_{1/2}$ vs. $E^o_{ArNH^\bullet/ArNH_2}$) of the phenol-induced back-reduction of anilines oxidized by ^{3}CBBP* and $CO_3^{\bullet-}$, suggesting that the process occurs through a (proton-coupled) electron transfer.

4- $[PhOH]_{1/2}$ does not depend on the specific PPRI (^{3}CBBP* or $CO_3^{\bullet-}$) that oxidizes the aniline (Ar-NH_2) through electron transfer, as the process would in any case form the same radical Ar-$NH^\bullet$. In contrast, $[PhOH]_{1/2}$ is a function of the standard one-electron reduction potential of the couple Ar-$NH^\bullet$/Ar-NH_2 ($E^o_{ArNH^\bullet/ArNH_2}$).

5- $E^o_{ArNH^\bullet/ArNH_2}$ can be a good predictor for $[PhOH]_{1/2}$ in the case of anilines and, probably, alkylamines.

6- Back-reduction significantly affects the photochemical fate of xenobiotics in surface waters.

Appendix I

The following section describes a first attempt to apply the Marcus theory to the back-reduction process induced by phenol during the photodegradation of anilines by ^{3}CDOM*/$CO_3^{\bullet-}$. The mathematical treatment allowed for calculating the rate constants that define $[PhOH]_{1/2}$ (i.e., k_{Red} and k_{Ox}), as well as the reorganization energy of the reaction. It will be shown that k_{Red} approaches the diffusion-control limit for chloroanilines, while it is lower for N-substituted anilines. In contrast, k_{Ox} can be considered as a constant among the investigated compound, and an approximate average value could be ~7.5×10^3 s^{-1}.

The (proton-coupled) electron transfer of the back-reduction reaction can occur after diffusion of Ar-NH$^\bullet$ and PhOH from the solution bulk to a closer distance, forming an encounter complex [Ar-NH$^\bullet$···PhOH] (Eq. 3.A1). Then, [Ar-NH$^\bullet$···PhOH] undergoes molecular reorganization reaching a transition state, from which the (PC)ET can take place producing the complex [Ar-NH$_2$···PhO$^\bullet$] (Eq. 3.A2). Finally, the dissociation of the complex gives the products Ar-NH$_2$ and PhO$^\bullet$ in the bulk (Eq. 3.A3). The general conceptual model of this mechanism has been at the basis of the development of the Marcus theory (Marcus, 1956).

Ar-NH$^\bullet$ + PhOH ⇆ [Ar-NH$^\bullet$···PhOH] $\quad K_1 = k_d \times (k_{-d})^{-1}$ (Eq. 3.A1)

[Ar-NH$^\bullet$···PhOH] → [Ar-NH$_2$···PhO$^\bullet$] $\quad k_{ET}$ (Eq. 3.A2)

[Ar-NH$_2$···PhO$^\bullet$] ⇆ Ar-NH$_2$ + PhO$^\bullet$ $\quad K_2$ (Eq. 3.A3)

Note that Eq. 3.A2 takes into account only the forward reaction, because the reverse electron transfer is usually unlikely for energetic considerations (Nad and Pal, 2000). Additionally, Eq. 3.A3 is commonly written just with the forward reaction (Marcus, 1956; Nad and Pal, 2000; Premsingh et al., 2004). However, here an equilibrium is considered because one of the reaction products (Ar-NH_2) is in relatively high concentration, as it is the studied organic substrate, which makes the reverse reaction more likely.

The net reaction resulting from Eqs. 3.A1, 3.A2, and 3.A3 is the back-reduction process:

$$\text{Ar-NH}^{\bullet} + \text{PhOH} \rightarrow \text{Ar-NH}_2 + \text{PhO}^{\bullet} \qquad k_{Red} \qquad \text{(Eq. 3.A4)}$$

The standard Gibbs energy of Eq. 3.A4 is $\Delta_r G_{Red}^{\circ} = \Delta G_{ET}^{\circ} + W_R - W_P$, where ΔG_{ET}° is the standard Gibbs energy of the (PC)ET (Eq. 3.A2), while W_R and W_P are the coulomb energies needed to bring, respectively, the reactants (Eq. 3.A1) and the products (Eq. 3.A3) from the solution bulk (considered as an infinite distance between the species) to the distance of the encounter complexes. Because the species involved in the present mechanism are uncharged (the van der Waals forces are here neglected; Eberson, 1982), one has that $W_R = W_P = 0$. Therefore, $\Delta_r G_{Red}^{\circ} = \Delta G_{ET}^{\circ}$.

The net transformation rate of Ar-$NH^{\bullet}$ is $R_{ArNH^{\bullet}} = k_{Red}[ArNH^{\bullet}][PhOH] = k_d[ArNH^{\bullet}][PhOH] - k_{-d}[ArNH^{\bullet} \cdots PhOH]$. By applying the steady-state approximation to the concentration of the encounter complex ($[ArNH^{\bullet} \cdots PhOH]$), one gets a relationship between k_{Red} and k_{ET} (Eberson, 1982; Nad and Pal, 2000; Sandrini et al., 1985):

$$k_{Red} = \frac{k_d \times K_1 \times k_{ET}}{k_d + K_1 \times k_{ET}} \qquad \text{(Eq. 3.A5)}$$

The diffusion rate constant k_d can be calculated with some approximations from the Debye theory as $k_d = 8RT \times (3\eta)^{-1}$, where η is the solvent viscosity. For water, k_d = 7.4×10^9 L mol^{-1} s^{-1} at 298.15 K (Mortimer, 2000). Moreover, the equilibrium constant K_1 depends on the cube of the sum of the radii of Ar-NH$^{\bullet}$ and PhOH, which can be considered similar and ~3.5 Å (Nad and Pal, 2000; Sandrini et al., 1985), and on W_R. Because W_R = 0, K_1 ~0.86 L mol^{-1} (Eberson, 1982).

The (PC)ET rate constant of Eq. 3.A2 can be expressed as follows:

$$k_{ET} = \kappa Z \times e^{-\frac{\Delta^{\ddagger}G}{RT}} \qquad \text{(Eq. 3.A6)}$$

where κZ is a pre-exponential factor derived from the molecular collision theory and $\Delta^{\ddagger}G$ is the free activation energy of Eq. 3.A2. The Marcus theory relates $\Delta^{\ddagger}G$ with $\Delta G_{ET}°$ through Eq. 3.A7, where λ is the reorganization energy of the reaction (Marcus, 1956; R. A. Marcus, 1957; R.A. Marcus, 1957).

$$\Delta^{\ddagger}G = \frac{(\Delta G_{ET}° + \lambda)^2}{4\lambda} \qquad \text{(Eq. 3.A7)}$$

After its minimum, this parabolic function of $\Delta G_{ET}°$ predicts an increase of the free activation energy when the reaction becomes more and more exothermic: this behavior is part of the so-called ‘inverted region’. However, another relationship between the kinetics and thermodynamics of the electron transfer is represented by the Rehm-Weller equation (Eq. 3.A8), which considers a plateau of $\Delta^{\ddagger}G$, rather than an inverted region, for highly exothermic reactions (Eberson, 1982; Piechota and Meyer, 2019; Silverstein,

2012). Eq. 3.A8 resembles the Scandola-Balzani equation for the electron transfer processes (Eberson, 1982; Sandrini et al., 1985), which is sometimes preferred over the Rehm-Weller one.

$$\Delta^{\ddagger}G = \frac{\Delta G_{ET}^{\circ}}{2} + \left[\left(\frac{\Delta G_{ET}^{\circ}}{2}\right)^2 + \left(\frac{\lambda}{4}\right)^2\right]^{1/2} \quad \text{(Eq. 3.A8)}$$

By substituting Eq. 3.A7 in Eq. 3.A6, one gets:

$$ln\, k_{ET} = ln\, \kappa Z - \frac{(\Delta G_{ET}^{\circ} + \lambda)^2}{4RT\lambda} \quad \text{(Eq. 3.A9)}$$

Eq. 3.A5 and Eq. 3.A9 allow for a relationship to be obtained between the thermodynamics of the phenol-induced back-reduction of anilines and its kinetics. Indeed, by considering that $k_{Red} = k_{Ox} \times \left([PhOH]_{1/2}\right)^{-1}$ in Eq. 3.A5, and that $\Delta_r G_{Red}^{\circ} = \Delta G_{ET}^{\circ}$ in Eq. 3.A9, one gets the following Eq. 3.A10:

$$-\log_{10}\left(k_d[PhOH]_{1/2} - k_{Ox}\right) = -\frac{(\Delta_r G_{Red}^{\circ})^2}{9.212RT\lambda} - \frac{\Delta_r G_{Red}^{\circ}}{4.606RT} + C \quad \text{(Eq. 3.A10)}$$

where $C = -\frac{\lambda}{9.212RT} + \log_{10}\frac{\kappa Z K_1}{k_d k_{Ox}}$.

Fig.3.A1a shows the fit of experimental data with Eq. 3.A10 for different values of k_{Ox}. Indeed, the actual values of k_{Ox} are unfortunately unknown, but an approximate upper limit can be set at ~7×10^3 s^{-1}, if k_{Red} is considered to be diffusion controlled and $[PhOH]_{1/2}$ ~1×10^{-6} mol L^{-1} (as in the case of chloro-substituted anilines). Note that this proposed value satisfies the

existence conditions for the argument of the log as well. Furthermore, k_{Ox} was considered to be constant among the different anilines under examination.
Data fit was also carried out by considering the Rehm-Weller equation, as follows:

$$-\log_{10}\left(k_d[PhOH]_{1/2} - k_{Ox}\right) = -\frac{\Delta_r G_{Red}^{\circ}}{4.606RT} - \frac{\sqrt{\lambda^2 + 4(\Delta_r G_{Red}^{\circ})^2}}{9.212RT} + C' \quad \text{(Eq. 3.A11)}$$

where $C' = \log_{10}\frac{\kappa Z K_1}{k_d k_{Ox}}$.

Few words have to be spent for the calculation of $\Delta_r G_{Red}^{\circ}$. The standard Gibbs energy of back-reduction was calculated from the standard potential difference $E^o_{ArNH^{\bullet}/ArNH_2} - E^o_{PhO^{\bullet}/PhOH}$, as $\Delta_r G_{Red}^{\circ} = -F \times \left(E^o_{ArNH^{\bullet}/ArNH_2} - E^o_{PhO^{\bullet}/PhOH}\right)$. No dependence of $\Delta_r G_{Red}^{\circ}$ on the concentrations of the chemical species involved in the reaction was considered, as for example [H^+], although the pH varied among the experimental runs (~7 for ^{3}CBBP* and 8.3 for the $CO_3^{\bullet-}$ experiments). Indeed, in this kind of analysis the standard (conformational) redox potentials have to be used (Krishtalik, 2003). However, because the redox semi-reactions of the couples Ar-NH$^{\bullet}$/Ar-NH$_2$ and PhO$^{\bullet}$/PhOH have the same pH-dependence, one obtains that the apparent potential difference $E^{o\,\prime}_{ArNH^{\bullet}/ArNH_2} - E^{o\,\prime}_{PhO^{\bullet}/PhOH} = E^o_{ArNH^{\bullet}/ArNH_2} - E^o_{PhO^{\bullet}/PhOH}$ at any pH value. Particular attention was paid to the cases of N,N-dimethylaniline (DMA) and N-methylaniline (MMA). Their back-reduction reactions would be PCETs, where the proton is accepted by a base that is different from the radicals of oxidized DMA/MMA. The latter should be present as radical cations (Heeb and Peters, 2006; Jonsson et al., 1996), in contrast with the other anilines investigated in this work (Jonsson et

al., 1994). Usually, the needed base is the solvent (e.g., water) or a buffer (e.g., phosphate ions) (Savéant, 2014). Data for DMA and MMA were taken from the work of Wenk and Canonica (2012), who measured the relevant values of $[PhOH]_{1/2}$ in a phosphate buffered aqueous solution at pH 8. Consequently, the expected base involved in the PCET process should be the hydrogenphosphate anion, while PhOH is the species that releases the proton. For this reason, $E^{o}_{PhO^{\bullet}/PhOH}$ had to be calculated at pH = pK_a of the buffer couple $H_2PO_4^-/HPO_4^{2-}$ (Bonin et al., 2013; Costentin et al., 2010; Savéant, 2014).

As shown in Fig.3.A1a, Eqs. 3.A10 and 3.A11 give the same fit for k_{Ox} = 7×10^3 s^{-1}, while they differ for lower values of k_{Ox}. However, in the latter case the fit becomes non-dependent on the used $k_{Ox} \leq 1\times10^3$ s^{-1}.

The first derivative of Eq. 3.A10 (Fig.3.A1b and Eq. 3.A12), computed geometrically as the slope of the tangent line to the curves shown in Fig.3.A1a and obtained from the Marcus model, allowed for the assessment of the reorganization energy of the reaction (λ).

$$-\frac{\partial \log_{10}\left(k_d[PhOH]_{1/2}-k_{Ox}\right)}{\partial \Delta_r G_{Red}^{\circ}} = -\frac{\Delta_r G_{Red}^{\circ}}{4.606RT\lambda} - \frac{1}{4.606RT} \qquad \text{(Eq. 3.A12)}$$

$$-\frac{\partial \log_{10}\left(k_d[PhOH]_{1/2}-k_{Ox}\right)}{\partial \Delta_r G_{Red}^{\circ}} = -\frac{\Delta_r G_{Red}^{\circ}}{2.303RT\sqrt{4(\Delta_r G_{Red}^{\circ})^2+\lambda^2}} - \frac{1}{4.606RT} \qquad \text{(Eq. 3.A13)}$$

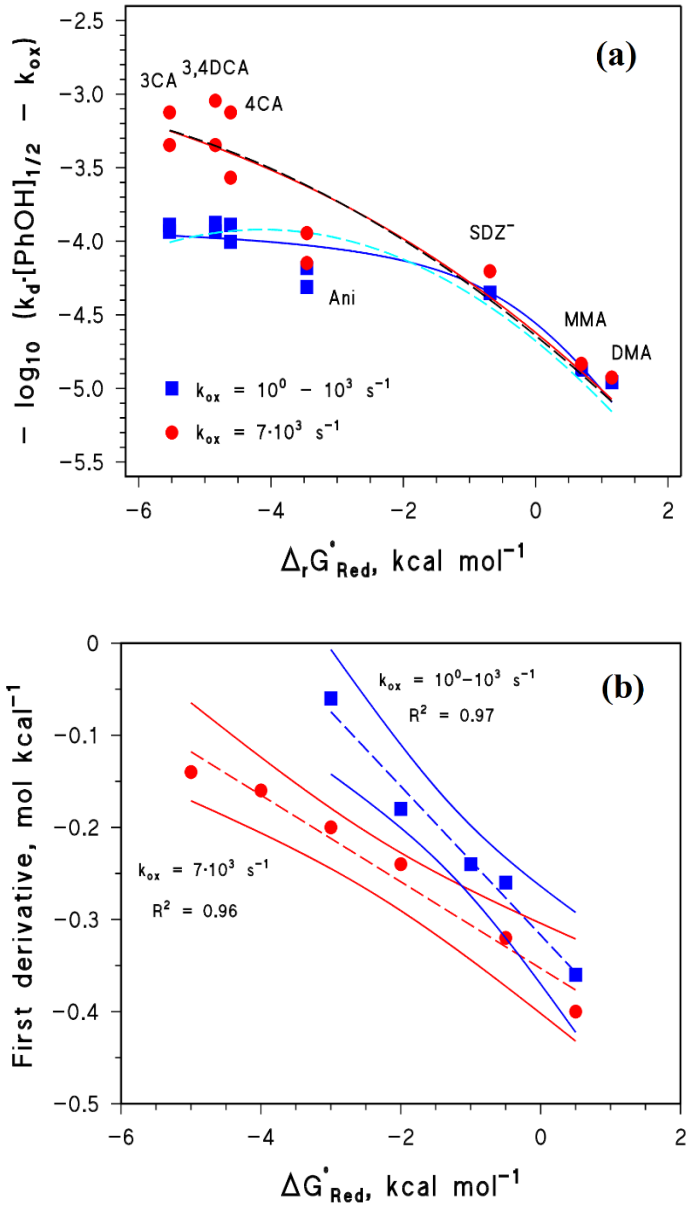

Fig.3.A1. **(a)** Experimental data fit with Eq. 3.A10 (dashed lines) and Eq. 3.A11 (solid lines) for different values of k_{Ox}. **(b)** Data (■, ●) and linear fit (dashed lines) of the first derivative of the curves shown in (a), derived from Eq. 3.A10 for different values of k_{Ox}. The fit confidence bands (solid blue lines) and the R^2 parameters, which represent the goodness of the fit, are also reported.

Table 3.A1. Kinetic parameters of the phenol-induced back-reduction obtained for the investigated anilines. Data of the back-reduction of Ani, 4CA, DMA, MMA and SDZ^- for the photodegradation by ^{3}CDOM* were from Canonica and Laubscher (2008) and Wenk and Canonica (2012).

Compound	PPRI	$[PhOH]_{1/2}$, µmol L^{-1}	k_{Red}, 10^9 L mol^{-1} s^{-1}	
			λ = 10 kcal mol^{-1}	λ = 4 kcal mol^{-1}
			k_{ox} = 1.0×10^4 s^{-1}	k_{ox} = 5.9×10^3 s^{-1}
Ani	^{3}CDOM*	2.9 ± 0.8	3.5	2.0
	$CO_3^{\bullet-}$	2.19 ± 0.23	4.7	2.7
3CA	^{3}CDOM*	1.31 ± 0.17	7.9	4.5
	$CO_3^{\bullet-}$	1.15 ± 0.25	8.9	5.1
4CA	^{3}CDOM*	1.5 ± 1.0	6.8	3.9
	$CO_3^{\bullet-}$	1.18 ± 0.26	8.7	5.0
3,4DCA	^{3}CDOM*	1.27 ± 0.32	7.9	4.5
	$CO_3^{\bullet-}$	1.18 ± 0.22	8.7	5.0
DMA	^{3}CDOM*	12.4 ± 2.5	0.8	0.5
MMA	^{3}CDOM*	10.2 ± 2.0	1.0	0.6
SDZ^-	^{3}CDOM*	3.2 ± 0.8	3.2	1.8

In particular, the slope of the linear plot shown in Fig.3.A1b gave λ = 8 ± 1 kcal mol^{-1} for $k_{Ox} = 7\times10^3$ s^{-1}, while the intercept was –0.35 ± 0.01 mol $kcal^{-1}$ that is in very good agreement with the theoretical value of –0.37 mol $kcal^{-1}$. In a similar way, the first derivative of Eq. 3.A11 (Eq. 3.A13, fit-R^2 = 0.99), based on the Rehm-Weller model, gave λ = 12.2 ± 1.5 kcal mol^{-1} and an intercept of –0.36 ± 0.01 mol $kcal^{-1}$, which is still in agreement with the theoretical value. The obtained average value of λ ~10 kcal mol^{-1} is in agreement with the results reported in the literature for ET reactions in polar solvents involving aromatic amines and substituted phenoxy radicals (λ ~16

kcal mol^{-1}), triplet dyes (λ ~15-20 kcal mol^{-1}), heteroaromatics (λ ~18 kcal mol^{-1}), excited aromatic molecules (λ ~11 kcal mol^{-1}), excited benzophenone (λ ~10 kcal mol^{-1}) (Eberson, 1982; Heeb and Peters, 2006; Nad and Pal, 2000) or substituted phenols and excited triplet states of aromatic ketones (λ ~16 kcal mol^{-1}) (Canonica et al., 2000). For k_{Ox} = 10^0-10^3 s^{-1}, λ was 4.0 ± 0.5 kcal mol^{-1} for both models, whereas the intercept of Eq. 3.A12 was = –0.32 ± 0.01 mol kcal^{-1}, a bit different from the theoretical value.

Finally, by knowing the value of λ, one can work backwards to assess the actual value of k_{Ox} by means of Eq. 3.A14, which is a combination of Eqs. 3.A5, 3.A6 and 3.A7.

$$[PhOH]_{1/2} = \frac{k_{Ox}}{K_1 \kappa Z} \times e^{\frac{(\Delta_r G_{Red}^{\circ} + \lambda)^2}{4RT\lambda}} + \frac{k_{Ox}}{k_d} \qquad \text{(Eq. 3.A14)}$$

Indeed, from the intercept and the slope of the linear trend $[PhOH]_{1/2}$ *vs.* exp $[\frac{(\Delta_r G_{Red}^{\circ} + \lambda)^2}{4RT\lambda}]$ (R^2 ~0.97), the values k_{Ox} ~1×10^4 s^{-1} and κZ ~2×10^{11} s^{-1} were respectively obtained for λ ~10 kcal mol^{-1}, while it was k_{Ox} ~5.9×10^3 s^{-1} and κZ ~9×10^9 s^{-1} for λ = 4 kcal mol^{-1}. Table 3.A1 reports the values of k_{Red} calculated through the relationship $k_{Red} = k_{Ox} \times \left([PhOH]_{1/2}\right)^{-1}$.

Note that the average value of k_{Ox} approaches the value ~7.5×10^3 s^{-1} obtained when k_{Red} is considered to be diffusion controlled (i.e., $k_{Red} \approx k_d$). Furthermore, the obtained k_{Ox} would represent an average value of the whole anilines set considered in this work and it closely approaches the experimental average of k_{Ox} measured to be ~6.8×10^3 s^{-1} for the radical cation of N,N-dimethyl-4-cyanoaniline (Leresche et al., 2019). Moreover, very recently, the value of k_{Red} for the same radical cation has been measured to be ~1.3×10^9 L

mol^{-1} s^{-1} by means of laser flash photolysis and steady-state irradiation experiments (Leresche et al., 2020). By considering *(i)* Eq. 3.A14, *(ii)* k_{Ox} ~7.5×10^{3} s^{-1} and *(iii)* that this radical has $[PhOH]_{1/2}$ = 3.7 ± 1.2 µmol L^{-1} (Leresche et al., 2016), one gets k_{Red} ~2×10^{9} L mol^{-1} s^{-1} in good agreement with the experimental value.

Chapter 4

Climate change and photochemistry of surface waters: possible effects of hydrological drought on the decontamination potential of water bodies from pollutants

Based on the results reported in the following published papers:

- **Carena, L**., Comis, S., Vione, D., **2021**. Geographical and temporal assessment of the photochemical decontamination potential of river waters from agrochemicals: A first application to the Piedmont region (NW Italy). *Chemosphere* 263, 127921. https://doi.org/https://doi.org/10.1016/j.chemosphere.2020.127921
- **Carena, L**., Terrenzio, D., Mosley, L.M., Toldo, M., Minella, M., Vione, D., **2019**. Photochemical consequences of prolonged hydrological drought: A model assessment of the Lower Lakes of the Murray-Darling Basin (Southern Australia). *Chemosphere* 236, 124356. https://doi.org/10.1016/j.chemosphere.2019.124356
- **Carena, L**., Vione, D., **2020**. Mapping the photochemistry of European mid-Latitudes rivers: An assessment of their ability to photodegrade contaminants. *Molecules* 25. https://doi.org/10.3390/molecules25020424
- Vione, D., **Carena, L**., **2020**. The Possible Production of Harmful Intermediates Is the "Dark Side" Of the Environmental Photochemistry of Contaminants (Potentially Adverse Effects, And Many Knowledge Gaps).

Environ. Sci. Technol. 54, 5328–5330. https://doi.org/10.1021/acs.est.0c01049

- **Carena, L.*,** Fabbri, D., Passananti, M., Minella, M., Pazzi, M., Vione, D., **2020**. The role of direct photolysis in the photodegradation of the herbicide bentazone in natural surface waters. *Chemosphere* 246, 125705. https://doi.org/https://doi.org/10.1016/j.chemosphere.2019.125705

List of abbreviations:

AOPs = Advanced Oxidation Processes

ENSO = El-Niño Southern-Oscillation

IOD = Indian Ocean Dipole

ITCZ = Inter-Tropical Convection Zone

NAO = North Atlantic Oscillation

PDO = Pacific Decadal Oscillation

PPRIs = Photochemically Produced Reactive Intermediates

SST = Sea Surface Temperature

WWTPs = Wastewater Treatment Plants

4.1 Introduction

Contamination of surface waters by xenobiotic compounds, such as pesticides and pharmaceuticals is a worldwide problem (Ebele et al., 2017; Schwarzenbach et al., 2006). Because of the increase of world population, urbanization, water use, loss of soil fertility, and climate change, we will likely face scarcity of water in the future, which in turn will also be largely contaminated (Schwarzenbach et al., 2010). Before reaching water bodies, part of the water used by human activities can be treated to decrease the pollutants content, as done in the *Wastewater Treatment Plants* (WWTPs). However, the non-point sources of water contamination (e.g., soil runoff) are actual problems to be solved (Petrie et al., 2015). Additionally, it must be said that WWTPs are often not able to efficiently remove all contaminants from water (including the emerging contaminants), unless the advanced oxidation processes (AOPs) are used (Okaikue-Woodi et al., 2020; Tran et al., 2018; Wang and Wang, 2016).

Fortunately, although they are slower than the AOPs used in WWTPs, abiotic photochemical reactions taking place naturally in surface waters can act as self-depollution processes that decontaminate the aquatic environments (Fenner et al., 2013). This means that when a biorecalcitrant pollutant reaches the sunlit surface of a water body, it can be degraded by direct and indirect photolysis (Vione et al., 2014) and its concentration (which is directly proportional to the degree of water pollution by that compound) gets lowered as a consequence. Being biorecalcitrant, the same compound will not be degraded by microbial processes.

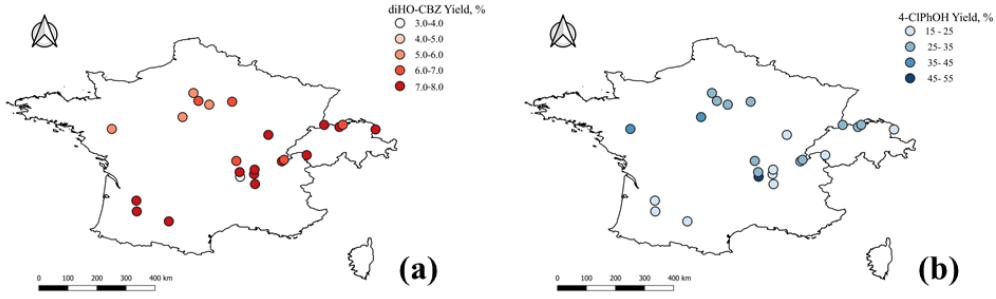

Fig.4.1.1 Maps showing the formation yields in sunlit river water of **(a)** 10,11-dihydro-10,11-trans-dihydroxycarbamazepine from carbamazepine, and **(b)** 4-chlorophenol from clofibric acid in France and Switzerland. The values are averages over the years 1990-1996. The detailed calculation procedure is described in Carena and Vione (2020). Many sites of central-southern France have the highest potential to produce the former intermediate, and the lowest potential to produce the latter. Adapted from Vione and Carena (2020).

Unfortunately, the phototransformation of pollutants can sometimes yield environmentally harmful intermediates or products, the toxicity (or mutagenicity, or endocrine-disrupting potential) of which can be comparable to, or even higher than that of the parent compounds (Buth et al., 2010; Erickson et al., 2012; Halladja et al., 2007; Vogna et al., 2004). The possible formation of harmful intermediates is actually the "dark side" of the environmental photochemistry of contaminants. Although several previous studies have investigated the formation of harmful intermediates upon photodegradation of xenobiotics, efforts have still to be made in order to increase knowledge about, e.g., photoproduction pathways and yields of harmful molecules (Vione and Carena, 2020). For instance carbamazepine and clofibric acid, which are widely detected in surface waters, produce upon photodegradation the toxic compounds 10,11-dihydro-10,11-trans-dihydroxycarbamazepine and 4-chlorophenol, respectively (Avetta et al., 2016; De Laurentiis et al., 2012a). Because photochemical processes and pathways strongly depend on the chemistry of the water body where they take

place (De Laurentiis et al., 2012b; McCabe and Arnold, 2016; Vione et al., 2014; Xu et al., 2020), the photodegradation of the parent contaminants and the formation of the toxic intermediates vary both spatially (Fig.4.1.1) and temporally.

Recently, we have developed a photochemical model that is able to compute the steady-state concentrations of the main PPRIs ($HO^{\bullet}$, $CO_3^{\bullet-}$, ^{3}CDOM* and $^1O_2$) as well as the direct and indirect photolysis of water pollutants, on the basis of data about the chemical composition of water bodies (Carena and Vione, 2020). To date, modeling is the only suitable way to assess the photochemistry of surface waters in both the space and time dimensions, because of the very low PPRIs concentration values occurring in the environment (10^{-18}-10^{-13} mol L^{-1}) that make the detection of these species very hard (McCabe and Arnold, 2016; Vione et al., 2014; Xu et al., 2020; Zeng and Arnold, 2013). Large datasets about the water chemical composition of lakes and rivers (i.e., the concentration values of DOC, nitrate and inorganic carbon species; *vide infra*), over a time range and in a spatial region, are highly needed for photochemical modeling. Some datasets are fortunately freely available, thanks to the efforts of both scientific groups and global/regional water-monitoring programs (ARPA, 2020; EEA, 2020; Filazzola et al., 2020; United Nations Environment Programme, 2019). Moreover, very recently the photodegradation of pollutants in surface waters has been assessed from satellite imagery of CDOM absorbance rather than from water chemistry data, which makes satellite remote sensing another potential tool in the framework of photochemistry modelling (Chen et al., 2020).

It is well known that the chemistry and hydrology of water bodies is and will be affected by anthropogenic climate change, and the relevant effects depend (and will do so in the future) on the considered region of the world (Couture et al., 2015; Garmo et al., 2014; Solomon et al., 2015; Ukkola et al., 2020;

Zhang et al., 2015). For instance, several areas around the world will face (and are facing nowadays) drought events (Miao et al., 2020; Van Loon et al., 2016), which will likely be longer, more frequent and possibly more intense than in the past (Ukkola et al., 2020). Globally, extended drought events have been shown to be the consequence of anthropogenic climate change (Marvel et al., 2019; Williams et al., 2020), but the regional effects on water bodies can highly depend on the natural climatic variability (Fatichi et al., 2014). In the context of climate change and environmental photochemistry, few theoretical studies have been published (Calderaro and Vione, 2020; De Laurentiis et al., 2014a; Minella et al., 2013; Vione and Scozzaro, 2019), while there is a clear lack of actual case studies showing the effects of climate phenomena on surface-water photoreactions.

In this work, modeling was carried out to assess *(i)* the photochemical consequences of hydrological drought in lakes located in Southern Australia, and *(ii)* the decontamination potential from agrochemicals of rivers located in the Piedmont region (NW Italy). The choice of these water bodies relies in the fact that lakes in Southern Australia have experienced a marked and prolonged drought event in the first decade of the 21st century, while Piedmontese rivers have been affected by both anthropogenic pollution and water scarcity in the same years. Therefore, these scenarios were suitable to investigate how the photochemistry of surface waters responds to (anthropogenic) climatic and pollution pressures.

4.2 Methods

4.2.1 Photochemical modeling

The photochemical model used in this work derives from the APEX code (*Aqueous Photochemistry of Environmentally occurring Xenobiotics*), which is described in detail in two papers by Vione (Bodrato and Vione, 2014; Vione, 2020). Here, a brief explanation is given of the set of kinetic equations used in the model. As already described in Chapter 2, the model has been validated by comparing field data of photoreactivity parameters with the computation results from the model for several water contaminants (Avetta et al., 2016; Carena et al., 2020, 2018; De Laurentiis et al., 2013b, 2012a; Maddigapu et al., 2011; Marchetti et al., 2013). Although APEX is available for free as electronic supplementary material of Bodrato and Vione (2014) and Vione (2020) the slightly different software used here is not yet available for public use. However, the relevant results derived from it have been recently published in peer-review scientific journals (Carena et al., 2021, 2019b; Carena and Vione, 2020).

Kinetic equations set

The model is able to compute the steady-state concentrations of the main PPRIs occurring in inland surface waters, namely $HO^{\bullet}$ and $CO_3^{\bullet-}$ radicals, $^1O_2$ and ^{3}CDOM*. The concentrations are calculated as average values for a water column with area of 12.5 cm^2 and depth *d*. Eqs. 4.2.1-4.2.10 are the (simplified) reactions considered by the model to carry out the calculations, where ISC means inter-system crossing (Buxton et al., 1988; Canonica et al., 2005; Mack and Bolton, 1999; McNeill and Canonica, 2016; Vione, 2020;

Vione et al., 2014; Westerhoff et al., 2007; Wilkinson et al., 1995; Wojnárovits et al., 2020).

$NO_3^- + h\nu + H^+ \rightarrow {}^{\bullet}NO_2 + HO^{\bullet}$ (Eq. 4.2.1)

$NO_2^- + h\nu + H^+ \rightarrow {}^{\bullet}NO + HO^{\bullet}$ (Eq. 4.2.2)

$CDOM + h\nu \rightarrow\rightarrow\rightarrow HO^{\bullet}$ (Eq. 4.2.3)

$CDOM + h\nu \rightarrow {}^1CDOM^* \xrightarrow{ISC} {}^3CDOM^* \xrightarrow{O_2} CDOM + {}^1O_2$ (Eq. 4.2.4)

$HO^{\bullet} + HCO_3^- \rightarrow H_2O + CO_3^{\bullet-}$ (Eq. 4.2.5)

$HO^{\bullet} + CO_3^{2-} \rightarrow HO^- + CO_3^{\bullet-}$ (Eq. 4.2.6)

${}^3CDOM^* + CO_3^{2-} \rightarrow CDOM^{\bullet-} + CO_3^{\bullet-}$ (Eq. 4.2.7)

$HO^{\bullet} + DOM \rightarrow Products$ (Eq. 4.2.8)

$CO_3^{\bullet-} + DOM \rightarrow Products$ (Eq. 4.2.9)

${}^1O_2 \xrightarrow{H_2O} O_2$ (Eq. 4.2.10)

The assumption of steady-state conditions is supported by considering continuous sunlight irradiation and complete water mixing. In particular, the solar spectrum reaching the surface at noon ± 3 h during a clear-sky day ($i^0(\lambda)$, units of E $(12.5\ cm^2)^{-1}\ s^{-1}\ nm^{-1}$, where 1 E = 1 mol of photons), which is a reasonable approximation of the daily-averaged solar spectrum under fair-weather conditions, was used to model the daily-averaged photochemistry (Bodrato and Vione, 2014). Consequently, one can reasonably assume that the

formation rate of a PPRI equals its scavenging rate and derive the relevant kinetic equations.

In the case of HO• radicals, one gets:

$$R_{f,HO^\bullet} = [HO^\bullet] \times (k_{(HO^\bullet + DOM)} \times DOC + k_{(HO^\bullet + HCO_3^-)} \times [HCO_3^-] + + k_{(HO^\bullet + CO_3^{2-})} \times [CO_3^{2-}]) \quad \text{(Eq. 4.2.11)}$$

where $R_{f,HO^\bullet}$ is the total formation rate of HO• upon sunlight absorption by CDOM, nitrate and nitrite (Eqs. 4.2.1-4.2.3), while the right part of the equation represents the total scavenging rate of hydroxyl radicals accounted for by reactions with DOM, bicarbonate and carbonate (Eqs. 4.2.5,4.2.6,4.2.8). The values of $k_{(HO^\bullet + DOM)}$ = 5×10^4 L mg_C^{-1} s^{-1}, $k_{(HO^\bullet + HCO_3^-)}$ = 8.5×10^6 L mol^{-1} s^{-1} and $k_{(HO^\bullet + CO_3^{2-})}$ = 3.9×10^8 L mol^{-1} s^{-1} were taken from the literature (Buxton et al., 1988; Vione et al., 2014; Westerhoff et al., 2007). DOC is the dissolved organic carbon (mg_C L^{-1}), while $[HCO_3^-]$ and $[CO_3^{2-}]$ are the molar concentrations of bicarbonate and carbonate, respectively (*vide infra* for their values).

Therefore, the steady-state concentration of HO• radicals can be expressed as follows:

$$[HO^\bullet] = \frac{R_{f,HO^\bullet}}{k_{(HO^\bullet + DOM)} \times DOC + k_{(HO^\bullet + HCO_3^-)} \times [HCO_3^-] + k_{(HO^\bullet + CO_3^{2-})} \times [CO_3^{2-}]} \quad \text{(Eq. 4.2.12)}$$

The total formation rate of HO• is computed as the sum of the rates of Eqs. 4.2.1-4.2.3, namely $R_{f,HO^\bullet} = R_{f,HO^\bullet}(NO_3^-) + R_{f,HO^\bullet}(NO_2^-) + R_{f,HO^\bullet}(CDOM)$. To compute each term of the sum, one has to know the

photon flux (P_a) absorbed by each photosensitizer i (where i = NO_3^-, NO_2^- and CDOM). One has $R_{f,HO^\bullet}(NO_3^-) = \Phi_{HO^\bullet,NO_3^-} \times P_{a,NO_3^-}$, $R_{f,HO^\bullet}(NO_2^-) = \Phi_{HO^\bullet,NO_2^-} \times P_{a,NO_2^-}$, and $R_{f,HO^\bullet}(CDOM) = \Phi_{HO^\bullet,CDOM} \times P_{a,CDOM}$, where $\Phi_{HO^\bullet,i}$ is the apparent quantum yield of $HO^\bullet$ formation by the irradiated photosensitiser i. Although the photolysis of nitrate and nitrite is well known (e.g. Mack and Bolton, 1999), the mechanistic details that control $\Phi_{HO^\bullet,CDOM}$ are still rather obscure (Eq. 4.2.3, see also Chapter 1). Fortunately the value of $\Phi_{HO^\bullet,CDOM}$ is known experimentally, but it may vary among different aquatic environments (Carena et al., 2017; McCabe and Arnold, 2016; Niu and Croué, 2019; Vione et al., 2014, 2006; Xu et al., 2020). Interestingly, such variations are more limited than the environmental variability might suggest (Marchisio et al., 2015; McCabe and Arnold, 2016; Xu et al., 2020). Therefore, average values from available literature sources were used as the relevant quantum yield, which is $\Phi_{HO^\bullet,CDOM}$ = (3.0±0.4)×10^{-5} (Vione, 2020; Vione et al., 2014). CDOM is the main sunlight absorber in surface waters below 500 nm, thus its absorption can be easily assimilated to the total absorption of water (Nelson and Siegel, 2013). The total photon flux absorbed by CDOM ($P_{a,CDOM}$, E L^{-1} s^{-1}; Eq. 4.2.13) can be calculated as the integral over wavelengths λ of the spectral light-absorption rate by CDOM itself, $p_{a,CDOM}(\lambda)$ (E L^{-1} s^{-1} nm^{-1}, Eq. 4.2.14) The numerical integration was carried out with the trapezoidal rule (Bodrato and Vione, 2014; Braslavsky, 2007).

$$P_{a,CDOM} = \sum_i (\lambda_i - \lambda_{i-1}) \times \frac{p_{a,CDOM}(\lambda_i) + p_{a,CDOM}(\lambda_{i-1})}{2} \qquad \text{(Eq. 4.2.13)}$$

$$p_{a,CDOM}(\lambda_i) = p^0(\lambda_i) \times \left[1 - 10^{-d \times DOC \times A_1(\lambda_i)}\right] \qquad \text{(Eq. 4.2.14)}$$

$p^0(\lambda)$ is the spectral photon flux density of sunlight (E L^{-1} s^{-1} nm^{-1}), computed as $p^0(\lambda) = i^0(\lambda) \times d^{-1}$, where d is the water column depth. $A_1(\lambda_i)$ (L mg_C^{-1} cm^{-1}) is the specific CDOM absorbance at the wavelength λ_i, over an optical path length of 1 cm ($A_1(\lambda, nm) = 0.45 \times \exp(-0.015 \times \lambda)$) (Vione, 2020; Vione et al., 2010).

Differently from CDOM, which is assumed to be the main light-absorbing species, the photon flux absorbed by nitrate has to take into account the fact that nitrate absorbs radiation in a mixture with CDOM.

$$P_{a,NO_3^-} = \sum_i (\lambda_i - \lambda_{i-1}) \times \frac{p_{a,NO_3^-}(\lambda_i) + p_{a,NO_3^-}(\lambda_{i-1})}{2} \quad \text{(Eq. 4.2.15)}$$

$$p_{a,NO_3^-}(\lambda_i) = p^0(\lambda_i) \times \frac{\varepsilon_{NO_3^-}(\lambda_i) \times [NO_3^-]}{A_1(\lambda_i) \times DOC} \times \left[1 - 10^{-d \times DOC \times A_1(\lambda_i)}\right] \quad \text{(Eq. 4.2.16)}$$

In Eq. 4.2.16, $\varepsilon_{NO_3^-}(\lambda_i)$ (L mol^{-1} cm^{-1}) is the molar absorption coefficient of nitrate, and $[NO_3^-]$ its molar concentration (*vide infra* for its value). The photon flux absorbed by nitrite is computed in a similar way.

By summarizing, the photon absorption rates by CDOM, nitrate and nitrite (Eqs. 4.2.13 and 4.2.15) were used to compute $R_{f,HO^\bullet}$, from which the steady-state $[HO^\bullet]$ was obtained (Eq. 4.2.12). A similar approach was used to compute the steady-state concentration of the other PPRIs.

The carbonate radical is formed upon oxidation of inorganic carbon species by $HO^\bullet$ (Eqs. 4.2.5, 4.2.6; Buxton et al., 1988) and by the one-electron oxidation of the carbonate anion by ^{3}CDOM* (Eq. 4.2.7), while the oxidation of bicarbonate by ^{3}CDOM* is less likely (Canonica et al., 2005; Wojnárovits et al., 2020). The two $CO_3^{\bullet-}$ formation processes have respective rates $R_{f,CO_3^{\bullet-}}(HO^\bullet)$ (Eq. 4.2.17) and $R_{f,CO_3^{\bullet-}}(^3CDOM^*)$ (Eq. 4.2.18), and in most

cases one has $R_{f,CO_3^{\bullet-}}(HO^{\bullet}) > R_{f,CO_3^{\bullet-}}(^3CDOM^*)$ (Canonica et al., 2005; Carena and Vione, 2016; Vione et al., 2014; Wojnárovits et al., 2020). In Eq. 4.2.18, $\eta_{CO_3^{\bullet-}}^{CDOM}$ = 6.5×10^{-3} is the yield of $CO_3^{\bullet-}$ upon light absorption by CDOM. At the same time, $CO_3^{\bullet-}$ is mostly scavenged by DOM (Eq. 4.2.9; Wojnárovits et al., 2020; Yan et al., 2019), with a rate constant $k_{(CO_3^{\bullet-}+DOM)}$ = 100 L mg$_C^{-1}$ s^{-1} (Bodrato and Vione, 2014; Canonica et al., 2005). By combining the formation and scavenging reaction kinetics, one gets the steady-state $[CO_3^{\bullet-}]$ (Eq. 4.2.19).

$$R_{f,CO_3^{\bullet-}}(HO^{\bullet}) = [HO^{\bullet}]\left(k_{(HO^{\bullet}+HCO_3^-)} \times [HCO_3^-] + k_{(HO^{\bullet}+CO_3^{2-})} \times [CO_3^{2-}]\right) \quad \text{(Eq. 4.2.17)}$$

$$R_{f,CO_3^{\bullet-}}(^3CDOM^*) = P_{a,CDOM} \times [CO_3^{2-}] \times \eta_{CO_3^{\bullet-}}^{CDOM} \quad \text{(Eq. 4.2.18)}$$

$$[CO_3^{\bullet-}] = \frac{R_{f,CO_3^{\bullet-}}(HO^{\bullet}) + R_{f,CO_3^{\bullet-}}(^3CDOM^*)}{k_{(CO_3^{\bullet-}+DOM)} \times DOC} \quad \text{(Eq. 4.2.19)}$$

Finally, the excited triplet states of CDOM are produced upon sunlight absorption by CDOM itself, with an apparent quantum yield $\Phi_{CDOM,^3CDOM^*}$ = 1.28×10^{-3} (Bodrato and Vione, 2014; Vione et al., 2014), and deactivated mainly through triplet-to-triplet energy transfer with dissolved O_2 and internal conversion (McNeill and Canonica, 2016). Usually, the former process prevails over the latter one. Indeed, the overall deactivation rate constant $k'_{d,CDOM}$ = 5×10^5 s^{-1} is very close to the pseudo-first order rate constant of the reaction with dioxygen in air-saturated water (McNeill and Canonica, 2016).

$$[^3CDOM^*] = \frac{\Phi_{CDOM,^3CDOM^*} \times P_{a,CDOM}}{k'_{d,CDOM}} \quad \text{(Eq. 4.2.20)}$$

The deactivation of ^{3}CDOM* through energy transfer with dioxygen yields $^1O_2$, with a rate $R_{f,^1O_2}$ ~0.5× $\Phi_{CDOM,^3CDOM^*} \times P_{a,CDOM}$. At the same time, $^1O_2$ is quenched by water with a rate constant $k_{q,^1O_2}$ = 2.5×10^5 s^{-1} (Wilkinson et al., 1995), thus $k_{q,^1O_2}$ = 0.5× $k'_{d,CDOM}$. Because $[^1O_2] = R_{f,^1O_2} \times \left(k_{q,^1O_2}\right)^{-1}$, one gets $[^1O_2] \sim [^3CDOM^*]$ (McNeill and Canonica, 2016).

Input Data

Our model requires as input data the solar spectra (one for each month, where the 15th day of the month of the sampling is used as reference; solar spectra have units of E (12.5cm^2)$^{-1}$ s^{-1} nm^{-1}), the water depth (m), and the concentration values of DOM, nitrate, nitrite, bicarbonate and carbonate. In particular, DOM is quantified as the DOC (mg$_C$ L^{-1}) and the other concentrations are expressed in molar units (i.e., mol L^{-1}).

The data sources about water chemical composition will be reported later, and the details of the input data will be described in the relevant sub-sections of 'Results and Discussion' for better readability. However, the concentrations data were generally provided in the appropriate units and, in some cases, simple conversions were used. Still, the concentrations of bicarbonate and carbonate are rarely reported in datasets of chemical composition of surface waters, and their values have to be derived from other available parameters. In this work, bicarbonate and carbonate concentrations were computed starting from water alkalinity and pH.

Water alkalinity (or total alkalinity, Alk) and pH are frequently measured parameters in the analysis of surface-water samples, thus they are often available. Indeed, Alk and pH are among the main indicators of the chemical

status of surface waters and are important to assess ecosystems health (Mattson, 2014). Alk is operationally defined as the number of equivalents per liter of strong acid needed to titrate the water sample to a pH of 4.5, and is mathematically expressed as in Eq. 4.2.21, where $[H^+] = 10^{-pH}$ and $[HO^-] = 10^{pH-14}$ (Lower, 1999).

$$Alk = [HCO_3^-] + 2 \times [CO_3^{2-}] + [HO^-] - [H^+] \quad \text{(Eq. 4.2.21)}$$

$[HCO_3^-]$ and $[CO_3^{2-}]$ are the molar concentrations of bicarbonate and carbonate, respectively, and are related by the stoichiometric equilibrium constant ($K_{a,s}$) of bicarbonate acidic dissociation ($HCO_3^- \leftrightarrows CO_3^{2-} + H^+$):

$$K_{a,s} = \frac{[CO_3^{2-}] \times [H^+]}{[HCO_3^-]} \quad \text{(Eq. 4.2.22)}$$

By combining Eq. 4.2.22 with Eq. 4.2.21, $[HCO_3^-]$ and $[CO_3^{2-}]$ can be expressed as follows:

$$[HCO_3^-] = \frac{[H^+]}{[H^+] + 2 \times K_{a,s}} \times (Alk + [H^+] - [HO^-]) \quad \text{(Eq. 4.2.23)}$$

$$[CO_3^{2-}] = \frac{K_{a,s}}{[H^+] + 2 \times K_{a,s}} \times (Alk + [H^+] - [HO^-]) \quad \text{(Eq. 4.2.24)}$$

Note that $(Alk + [H^+] - [HO^-])$ is the total ionic charge concentration (mol L^{-1}) accounted for by HCO_3^- and CO_3^{2-}, while $[H^+] \times \left([H^+] + 2 \times K_{a,s}\right)^{-1}$ and $K_{a,s} \times \left([H^+] + 2 \times K_{a,s}\right)^{-1}$ are, respectively, their charge fractions normalized for the ion charge.

The constant $K_{a,s}$ depends on both water temperature and ionic strength and it is related to the thermodynamic equilibrium constant $\boldsymbol{K}_a = a_{CO_3^{2-}} \times a_{H^+} \times \left(a_{HCO_3^-}\right)^{-1}$, where a_i is the activity of the species *i*, by the relationship $K_{a,s} = \boldsymbol{K}_a \times \gamma_{HCO_3^-} \times \left(\gamma_{CO_3^{2-}} \times \gamma_{H^+}\right)^{-1}$. $\gamma_{HCO_3^-}$, $\gamma_{CO_3^{2-}}$ and γ_{H^+} are the activity coefficients of bicarbonate, carbonate and H^+, respectively.

$\boldsymbol{K}_a$ depends on water temperature (T), and a useful expression of this dependence in the interval $0 < T < 50$°C is the following (Harned and Scholes, 1941; Millero et al., 2002; Millero and Pierrot, 1998):

$$ln\boldsymbol{K}_a = 207.6548 - (33.6485) \times lnT - \frac{11843.79}{T} \qquad \text{(Eq. 4.2.25)}$$

Concerning the calculation of the activity coefficients, the Davies model was here adopted (Eq. 4.2.26; Millero and Pierrot, 1998), where $I = 0.5 \times \sum_i^t (z_i^2 \times [i])$ is the water ionic strength, z_i is the charge of the ion *i* with concentration $[i]$, while it is A~0.5 between 0 and 50°C (Manov et al., 1943).

$$log_{10}\gamma_i = 0.24 \times I - \frac{A \times z_i^2 \times \sqrt{I}}{1+\sqrt{I}} \qquad \text{(Eq. 4.2.26)}$$

Finally, by considering the relationships reported above, one gets the expression for the calculation of $K_{a,s}$ at a given temperature and ionic strength (*pX* means -*log*$_{10}$*X*):

$$pK_{a,s} = p\boldsymbol{K}_a + 0.24 \times I - \frac{2 \times \sqrt{I}}{1+\sqrt{I}} \qquad \text{(Eq. 4.2.27)}$$

For the calculation of I, based on the fact that Ca^{2+}, Mg^{2+} and HCO_3^- are the most concentrated ions in most surface waters (Mattson, 2014), we considered a solution of $Ca(HCO_3)_2$ and $Mg(HCO_3)_2$, where $[HCO_3^-]$ » $[CO_3^{2-}]$. Consequently, $I = 0.5 \times \{4 \times [Ca^{2+}] + 4 \times [Mg^{2+}] + [HCO_3^-]\}$ and $2 \times [Ca^{2+}] + 2 \times [Mg^{2+}] = [HCO_3^-]$, from which Eq. 4.2.28 is obtained.

$$I = \frac{3}{2} \times [HCO_3^-] \qquad \text{(Eq. 4.2.28)}$$

The use of Eq. 4.2.28 can seem paradoxical, because $[HCO_3^-]$ is the parameter which has to be determined, while I is a needed variable to estimate $[HCO_3^-]$. However, in the first step of the computation $[HCO_3^-]$ and $[CO_3^{2-}]$ were calculated at ionic strength I = 0 mol L^{-1}, which means $K_{a,s} = \boldsymbol{K}_a$. A first assessment of I was then obtained, and the calculation of the new values of $[HCO_3^-]$ and $[CO_3^{2-}]$ was thus allowed. On this basis, the values of $[HCO_3^-]$ and $[CO_3^{2-}]$ were computed with an iterative approach, until convergence of method results was reached (Scheme 4.2.1). The iterative method was written and run with Microsoft Excel®.

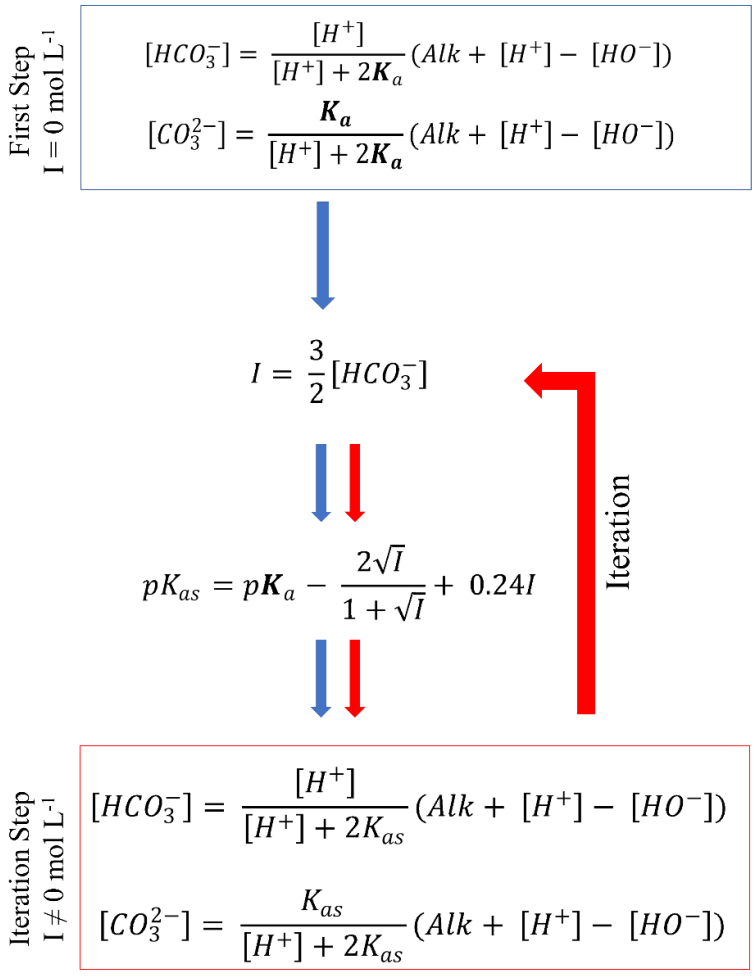

Scheme 4.2.1 Iterative method used for the calculation of bicarbonate and carbonate concentrations.

Output Data

The steady-state concentrations of $HO^{\bullet}$, $CO_3^{\bullet-}$, $^1O_2$ and $^3CDOM^*$ are computed as the main output data of the model. The results are values averaged over the entire water column, with depth d and area = 12.5 cm^2. The calculated steady-state concentrations allow for the calculation of the (first

order) degradation rate constant of a xenobiotic S, accounted for by indirect photochemical processes ($k'_{i.p.}$, s^{-1}). Indeed, $k'_{i.p.}$ equals the sum of the products between the second-order reaction rate constant with the PPRI *i* ($k_{(i+S)}$, L mol^{-1} s^{-1}) and the steady-state concentration of the PPRI $[i]$ (mol L^{-1}) (Eq. 4.2.29).

$$k'_{i.p.} = \sum_i k_{(i+S)} \times [i] \qquad \text{(Eq. 4.2.29)}$$

The first-order rate constant for the direct photolysis of S ($k'_{d.p.}$, s^{-1}) can be calculated by multiplying the polychromatic apparent quantum yield of the contaminant direct photolysis (Φ_S, unitless) for the photon-absorption rate constant of S ($P'_{a,S}$, s^{-1}): $k'_{d.p.} = \Phi_S \times P'_{a,S}$. $P'_{a,S}$ was calculated as the numerical integral of the spectral photon-absorption rate constants of the compound S ($p'_{a,S}(\lambda)$, s^{-1} nm^{-1}), by using the trapezoidal rule for integration over the wavelength spectrum ranging from 292.5 to 450 nm (Eq. 4.2.30).

$$P'_{a,S} = \sum_i (\lambda_i - \lambda_{i-1}) \times \frac{p'_{a,S}(\lambda_i) + p'_{a,S}(\lambda_{i-1})}{2} \qquad \text{(Eq. 4.2.30)}$$

In Eq. 4.2.30, $(\lambda_i - \lambda_{i-1})$ was 2.5 nm from 292.5 to 330 nm and 10 nm from 330 to 450 nm. The spectral photon-absorption rate constant of S at the wavelength λ was calculated as follows:

$$p'_{a,S}(\lambda_i) = p^0(\lambda_i) \times \frac{\varepsilon_S(\lambda_i)}{DOC \times A_1(\lambda_i)} \times \left[1 - 10^{-d \times DOC \times A_1(\lambda_i)}\right] \qquad \text{(Eq. 4.2.31)}$$

where $p^0(\lambda_i)$, $A_1(\lambda_i)$ and d have the same meaning as in Eq. 4.2.14. $\varepsilon_S(\lambda)$ is the (wavelength-dependent) molar absorption coefficient of S (L mol^{-1} cm^{-1}).

Finally, the total (direct + indirect) photodegradation rate constant of S (k'_{tot}, s^{-1}) can be expressed as the sum of the rate constants of both direct and indirect photoreactions (Eq. 4.2.32).

$$k'_{tot} = k'_{d.p.} + k'_{i.p.} \qquad \text{(Eq. 4.2.32)}$$

The values of k'_{tot} can then be converted into the relevant photochemical half-life times ($t_{1/2}$, units of s) through the relationship $t_{1/2} = ln2 \times (k'_{tot})^{-1}$. Scheme 4.2.2 shows a simplified diagram of the entire photochemical model described above.

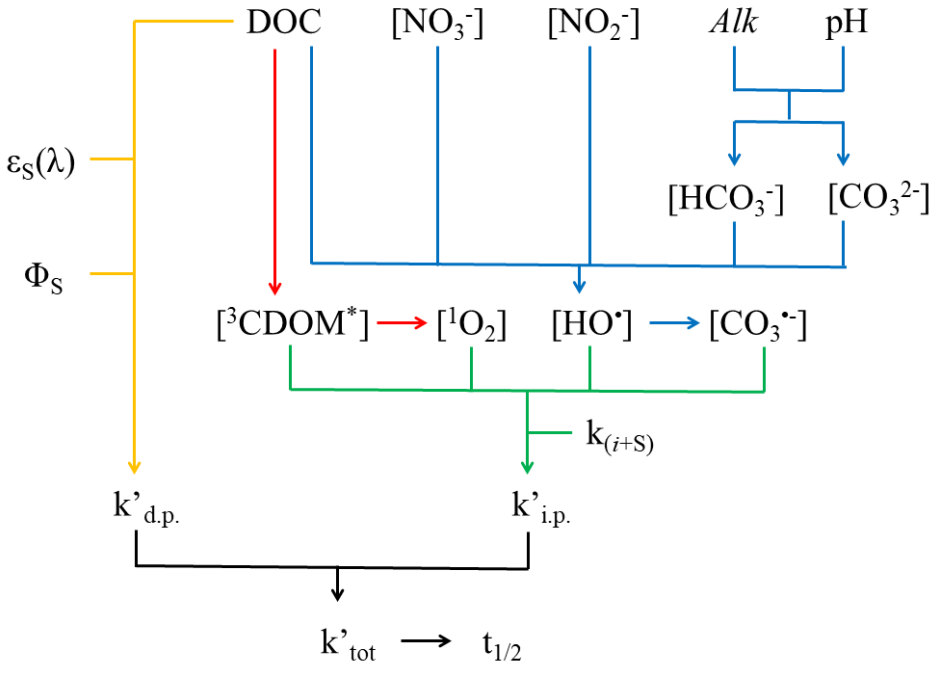

Scheme 4.2.2 Schematic of the photochemical model used in this work for a given solar spectrum and water depth. The meaning of each parameter is explained in the text.

4.2.2 Study areas and data sources

Lower Lakes (Southern Australia)

Lakes Alexandrina and Albert have surfaces of 650 and 170 km^2, respectively, and are collectively known as the Lower Lakes (Fig.4.2.1). These lakes belong to the Lower Murray region in South Australia, which is part of the bigger Murray-Darling Basin (total catchment area = 1,061,469 km^2, corresponding to ~14 % of Australia's total area). They are connected with a narrow channel ("the Narrung Narrows"), with Lake Albert being a terminal lake. The Lower Lakes are quite shallow, with mean depths of ~2.4 m (Lake Alexandrina) and ~1.5 m (Lake Albert). The water level is regulated by the inflow of the Murray Lower River (821.7 km^2 total surface area), which enters Lake Alexandrina in the northern side, and by a series of barrages separating the lakes from the nearby coastal lagoon (Coorong), out the river mouth and into the ocean (Mosley et al., 2012). Under normal hydrological conditions water flows from the lakes to the coastal ocean, because the barrages (built in 1940s) prevent seawater intrusion into the lakes and help keep the freshwater status of the lakes themselves (Department for Environment and Water-Government of South Australia, 2020). The system of these gated structures allows the two lakes to be maintained at near full capacity. The Lower Lakes are freshwater bodies, eutrophic and highly turbid, because of the high nutrient content and turbidity of the Murray Lower River. Together with Coorong, Lakes Alexandrina and Albert have been recognized as areas of both national and international importance, as one of the most significant resources in Australia. Indeed, the Lower Lakes region supplies drinking water for the nearby city of Adelaide (population ~1.3 million) and water for irrigation of the surrounding

agricultural areas. Furthermore, the region is an important touristic destination (Mosley et al., 2012).

The water quality parameters have been measured from 2003 to 2010 in five sites: two in the Lower Murray River (Tailem Bend and Murray Bridge), two in Lake Alexandrina (Milang and Goolwa), and one in Lake Albert (Meningie). In this work, the photochemistry was modeled in the stations of Milang, Goolwa and Meningie (Fig.4.2.1). In particular, the analyzed parameters included salinity/total dissolved solids (TDS), temperature, pH, turbidity, nutrients (total nitrogen, TN; oxidised nitrogen, NO_x; total phosphorus, TP; filterable reactive phosphorus, FRP) and chlorophyll a.

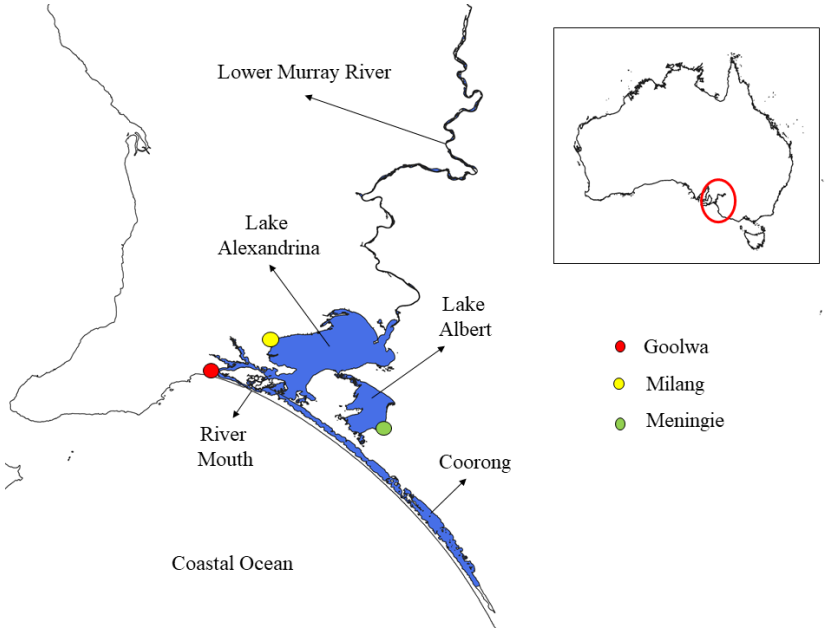

Fig.4.2.1 Map showing the Lower Lakes region with the main watercourse (Lower Murray River) and lakes. The inset shows the position of the region in Australia. The map was made with QGIS (QGIS, 2020), and the needed shapefiles were taken from WaterConnect (Department for Environment and Water-Government of South Australia, 2020).

Samples have been collected with polyethylene plastic bottles (APHA, 2005), approximately monthly by grab sampling at the lake sites and weekly at the river sites, located at the drinking water treatment stations. Immediately after collection, sample have been filtered through 0.45 µm membrane filters and stored in the dark at 4ºC for determination of dissolved nutrients (NO_x, FRP). All analyses were undertaken at the Australian Water Quality Centre, a National Association of Testing Authorities (NATA) accredited laboratory, using standard methods (APHA, 2005). For further details see Mosley et al. (2012).

Data of water chemistry for the photochemical modeling of the Lower Lakes (DOC, nitrate, alkalinity and pH) were kindly provided by Prof. Luke M. Mosley at the University of Adelaide (School of Biological Sciences, Adelaide, Australia). As sunlight irradiance we used the solar spectrum relevant to the month of the sampling, which is representative of a day-averaged spectrum (local time 09:00 a.m.) at 35.63° S, 138.28° E (coordinates of Adelaide, Australia). To do this, we used the *TUV Quick Calculator* software for clear-sky conditions (absence of clouds, 300 Dobson units for the total ozone layer, with aerosols optical depth = 0.235; NCAR, 2015). The water depth values were obtained from the Department for Environment and Water (South Australia) and corrected to the Australian Height Datum (AHD) of the water surface, i.e., the water height relative to the standard seawater level.

Rivers of Piedmont (North-Western Italy)

Piedmont is a region in NW Italy that extends for ~25,400 km^2, of which ~43% is constituted by mountains and 30% by hills, whereas the plain covers ~27% of its territory (Debernardi et al., 2008). Fig.4.2.2a shows an elevation map of

the territory with a chromatic scale. Although the plain covers a minor part of the region, it is under an important anthropogenic pressure because of the presence of several large cities (the main of which is Turin, with population of ~880,000) and of industrial and agricultural activities (Bassanino et al., 2011). A multitude of watercourses flow in Piedmont (Fig.4.2.2b) and supplies anthropogenic activities. All the hydrological basins of the region eventually flow into the Po river, which is the main river in Piedmont as well as the longest in Italy.

The chemical composition data of Piedmontese river waters were provided by the regional environmental protection agency (ARPA Piemonte; ARPA, 2020) on request, and Dr. Elio Sesia (ARPA Piemonte) is thankfully acknowledged for this. They include the time series of the main water parameters, measured monthly, such as those relevant for our photochemical model (DOC, nitrate, nitrite, and inorganic carbon species). The concentration values of a wide range of pollutants were available as well, for several sampling stations.

The period between 2000 and 2008 showed the most complete dataset, because it complied with EU legislation requirements to assess the chemical and ecological status of rivers (Achleitner et al., 2005).

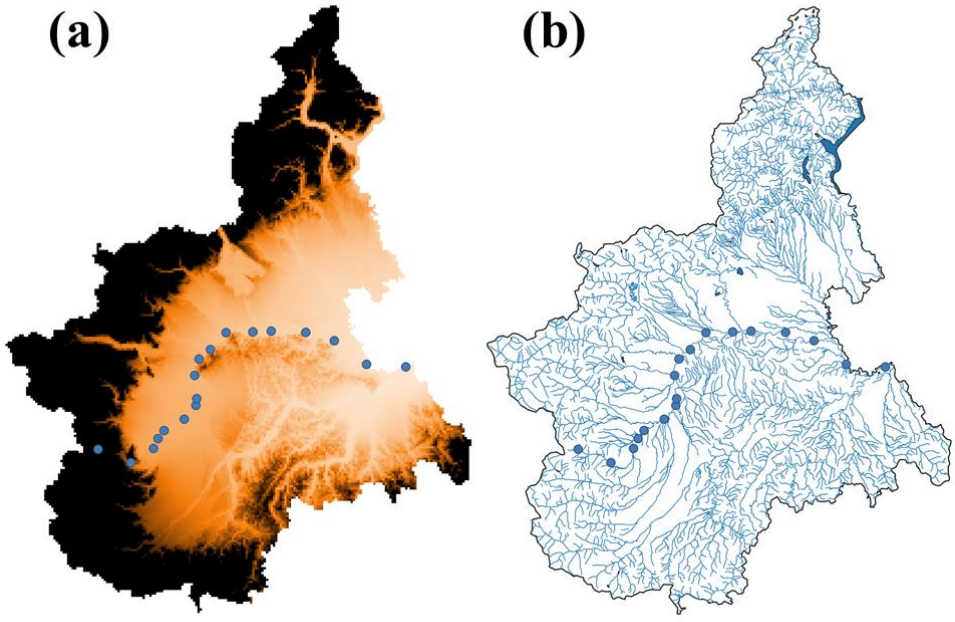

Fig.4.2.2 (a) Elevation map of Piedmont, from light brown (plain, < 300 m a.s.l.) to black (mountain, > 800 m a.s.l., reaching over 4,000 m a.s.l.). **(b)** Map of Piedmontese watercourses. The blue points in both (a) and (b) represents the sampling stations along the Po river. The maps were made with QGIS (QGIS, 2020).

After 2008, rivers with a good status could be sampled less frequently than monthly, and more recent data were thus less suitable to derive year-round averages of photochemical reactivity. Therefore, river-water photochemistry was modelled for 2000-2008. In this time period, the environmental status of watercourses (which is a combination of both their ecological and chemical status) was at least "good" for ~35% of Piedmontese rivers in 2000 and for ~50% in 2008 (increasing trend from 2000 to 2008), while ~40-50% of them showed a "sufficient" status, which means that anthropogenic pollution was not able to induce significant alterations of the aquatic ecosystem. For the remaining ≤ 15%, which mostly represented minor watercourses under significant anthropogenic pressure, the environmental status was classified as

"poor" or "bad" (ARPA, 2020). The Po river shows a decreasing trend of the environmental status when passing from uplands to the plain, where urban areas and anthropogenic activities are more intense (ARPA, 2020). In 2009-2011, 87% of rivers in Piedmont had a "good" chemical status. For the others, pesticides were the main cause of pollution and prevailed over toxic metals and industrial chemicals (ARPA, 2020).

The photochemistry of the pesticides atrazine (ATZ), bentazon (BTZ), chlortoluron (CTL), dimethomorph (DMM), and isoproturon (IPT) was modeled in the Piedmontese rivers. The choice of these pesticides was based on two parameters: *(i)* actual occurrence in Piedmontese surface waters in the period 2000-2008, and *(ii)* availability of photoreactivity data (absorption spectrum, direct photolysis quantum yield, second-order reaction rate constants with the PPRIs). The occurrence of ATZ, BTZ, CTL, DMM, and IPT in Piedmont (ARPA, 2020) is reported in Fig.4.2.3. Each symbol means that the given pesticide was detected at least once in the relevant site. In the vast majority of cases, in particular for IPT, CTL and DMM in Fig.4.2.3a, the pesticides concentrations were below the quantification limit (<20 to 50 ng L^{-1}). Pesticide concentrations seldom approached 100 ng L^{-1}, and only sporadically reached hundreds ng L^{-1} or µg L^{-1} (ARPA, 2020).

ATZ was widespread in Piedmont's surface waters in 2000-2008 (Fig.4.2.3a), although this compound has been banned in the EU in 2003 (Bethsass and Colangelo, 2006). The presence of ATZ after its ban can be accounted for by its persistence in groundwaters (ARPA, 2020; Silva et al., 2012), from which it can reach surface waters, and by the relatively few years that had passed since the ban. Indeed, a decrease in the geographical distribution of ATZ was observed in 2009-2014 (Fig.4.2.3b) compared to the period 2000-2008 (ARPA, 2020). In contrast, an increase of the detection of the other pesticides

occurred in 2009-2014 (ARPA, 2020), which might suggest a gradual replacement in the used agrochemicals.

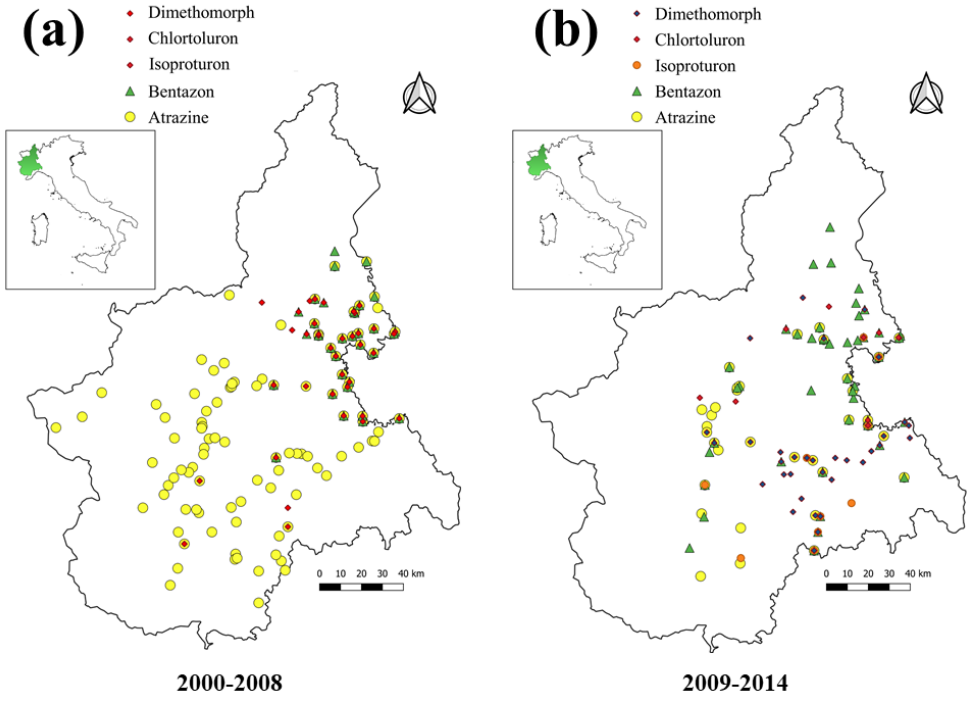

Fig.4.2.3 Geographical distribution of the five studied pesticides in the Piedmont region, in the years **(a)** 2000-2008 and **(b)** 2009-2014. The pesticides dimethomorph (DMM), chlortoluron (CTL) and isoproturon (IPT) were looked for in the same sampling sites in 2000-2008, but they were always below the quantification limit. For this reason, they are identified with the same symbols and colors in 2000-2008. The situation was different in 2009-2014. The maps were made with QGIS (QGIS, 2020), while the data where from ARPA (ARPA, 2020).

The photochemistry of the investigated pesticides was assessed in a model water column with depth d = 50 cm, considering that water in many rivers is quite shallow, and under solar spectra relevant for northern mid-latitudes (Bodrato and Vione, 2014; NCAR, 2015). The obtained monthly values of k'_{tot} (s^{-1}) were converted into day^{-1} units by considering the number of hours

of solar irradiation for each month at 45°N – 7°E (9 hours for December and January, 10.5 for February, 12 for March, 13.5 for April, 15 for May, 16 for June, 15.5 for July, 14.3 for August, 12.5 for September, 11 for October, and 9.5 for November; NCAR, 2015). Finally, the photochemical half-life time (days) for each month was calculated, and lifetime mapping is here reported as year averages.

Table 4.2.1 reports the photoreactivity parameters of the studied pesticides, which were used in the model. The table also describes pesticides use and their main phototransformation pathways. Pesticides absorption spectra are shown in Fig.4.2.4.

Note that BTZ has a strong absorption band in the UVB-UVA region (Carena et al., 2020); therefore, it is the studied pesticide that undergoes direct photolysis to the highest extent, despite the fact that it has the second-lowest quantum yield of direct photolysis.

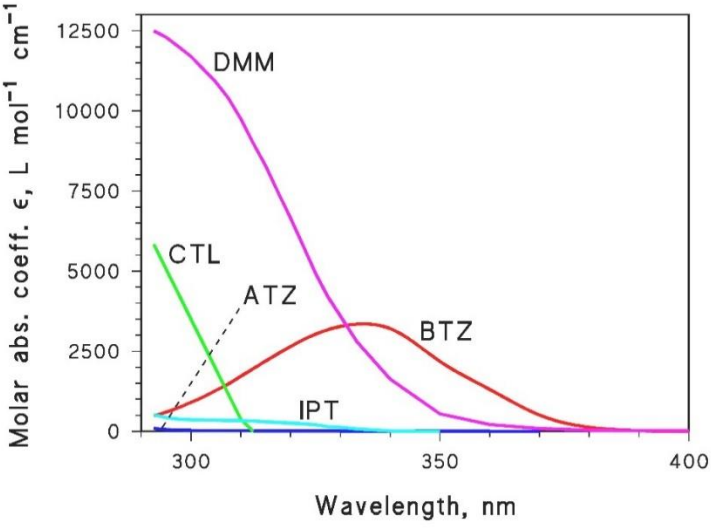

Fig.4.2.4 Molar absorption coefficients (ε, L mol^{-1} cm^{-1}) of the five studied pesticides in the wavelength range relevant to the photochemical model.

Table 4.2.1 *Upper part*: photoreactivity parameters of ATZ, BTZ, CTL, DMM, and IPT used in the model. *Lower part*: pesticides use and their main photodegradation pathways.

Pesticide	Φ_S, unitless	L mol^{-1} s^{-1}			
		$k_{(HO^{\bullet}+S)}$	$k_{(CO_3^{\bullet-}+S)}$	$k_{(^1O_2+S)}$	$k_{(^3CDOM^*+S)}$
ATZ[(a)]	1.6×10^{-2}	2.7×10^{9}	4×10^{6}	Negligible	7.2×10^{8}
BTZ[(b)]	4.4×10^{-4}	5.7×10^{9}	2.5×10^{7}	3.1×10^{7}	9.7×10^{8}
CTL[(c)]	3×10^{-2}	6.9×10^{9}	1.7×10^{7}	Negligible	2.7×10^{9}
DMM[(d)]	2.6×10^{-5}	2.6×10^{10}	Negligible	8.5×10^{5}	1.6×10^{9}
IPT[(e)]	2×10^{-3}	7.9×10^{9}	3×10^{7}	Negligible	3.2×10^{9}

	Pesticide use	Main photodegradation pathway(s)
ATZ	Herbicide (maize, banned)	$HO^{\bullet}$, $CO_3^{\bullet-}$, ^{3}CDOM*, d.p.
BTZ	Herbicide	d.p.
CTL	Herbicide (cereals)	$HO^{\bullet}$, $CO_3^{\bullet-}$, ^{3}CDOM*, d.p.
DMM	Fungicide	$HO^{\bullet}$, ^{3}CDOM*
IPT	Herbicide (cereals)	$HO^{\bullet}$, $CO_3^{\bullet-}$, ^{3}CDOM*

(a) (Marchetti et al., 2013); (b) (Carena et al., 2020); (c) and (e) (Fabbri et al., 2015a); (d) (Avetta et al., 2014)

4.2.3 Photochemical mapping

The mapping of the photochemical parameters (steady-state concentrations of PPRIs, half-life times of water pollutants) was carried out with the free and open source geographic information system QGIS (QGIS, 2020). The software allows for the mapping of georeferenced points, to which different features/parameters are related. In this case, each georeferenced point represents a sampling station of a water body where photochemistry was modeled. Furthermore, QGIS allowed for carrying out statistical analysis to compare the variables between different single points/geographical areas. Moreover, Microsoft Excel® was used for statistical analysis as well.

4.3 Results and Discussion

4.3.1 Photochemical consequences of prolonged hydrological drought in the Lower Lakes (Southern Australia)

The 'Millennium Drought' (also called 'the Big Dry') affected Southern Australia in the first decade of the 21st century (Heberger, 2012; van Dijk et al., 2013). This drought had profound effects on the water quality of Lakes Alexandrina and Albert, with a significant decrease of water depth and volume during the extreme drought period (2007-2010; Fig.4.3.1) that combined with a marked increase in turbidity and concentrations of nutrients (total nitrogen, nitrate, total phosphorus) relative to the previous period (Mosley et al., 2012). The flooding observed in the post-drought phase resulted in input of water rich in dissolved organic carbon, because of rewetting of floodplains and microbial breakdown of organic material (Biswas and Mosley, 2019). Also the concentrations of metal cations were higher in the post-drought phase (Mosley et al., 2014).

The climatic causes of the Big Dry could have been the concomitance of recurrent positive phases of the Indian Ocean Dipole (IOD) due to warming of the Western Indian Ocean, frequent El-Niño Southern-Oscillation (ENSO) phenomena, strengthening of the subtropical ridge, and frequent positive phases of the Pacific Decal Oscillation (PDO), which produced a long-lasting high-pressure zone over Southern and Eastern Australia, resulting in weak rainfalls and warm air (Heberger, 2012; Timbal and Drosdowsky, 2013; Timbal and Hendon, 2011; Ummenhofer et al., 2009; van Dijk et al., 2013). Additionally, drought events in Southern Australia are expected to be more frequent in the future, because of anthropogenic climate change (Marvel et al., 2019; Ukkola et al., 2020).

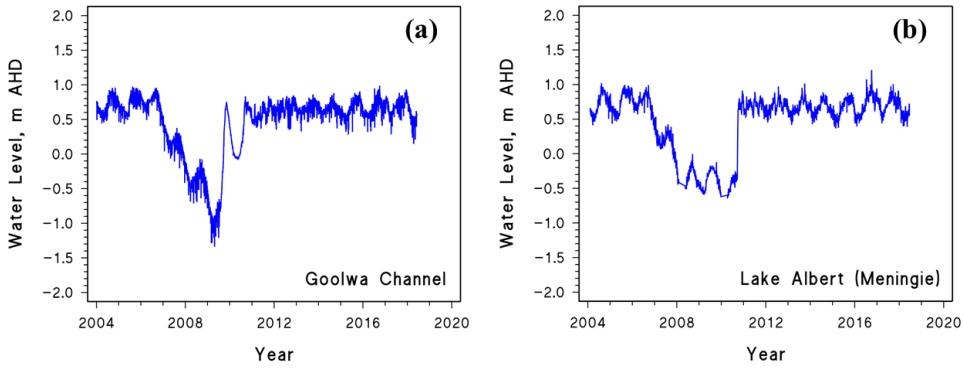

Fig.4.3.1 Evolution of water depth of **(a)** Lake Alexandrina (at Goolwa channel station) and **(b)** Lake Albert (at Meningie) during and after the Millennium Drought. The water depth values are expressed as Australian Height Datum (AHD) of the water surface, namely the water height relative to the standard seawater level. Data were obtained from WaterConnect (Department for Environment and Water-Government of South Australia, 2020).

Evolution of lakes-water chemistry relevant to photochemistry, in the drought and post-drought periods

Overall, the concentrations of the chemical species that affect abiotic photochemical processes (DOC, nitrate and inorganic carbon species) increased during the drought. This behavior was partially due to the decrease in water depth, which occurred also through evaporation (Mosley et al., 2012) and caused lesser dilution of solutes (evapoconcentration). In the case of the Goolwa channel, the maximum concentrations of DOC, bicarbonate and nitrate during the drought were ~2 times higher than the corresponding values in the post-drought phase (Figs.4.3.2 and 4.3.3c,e). Water depth followed an opposite trend, with post-drought values about twice higher than during the drought (Fig.4.3.3f). Therefore, evapoconcentration can account for the increase in DOC, HCO_3^- and NO_3^- between 2007 and 2010. However, water

evaporation was not the only cause of the higher solutes concentrations. For instance, the Milang station of Lake Alexandrina experienced the same drought-related water-depth halving, but HCO_3^- and NO_3^- were actually ~3 times more concentrated during drought (Figs.4.3.4c,e). Sediment resuspension could have caused more mobilization of dissolved nutrients (Mosley et al., 2012), and the resuspension of sediments is actually higher in shallower water bodies (as under drought) than in deeper ones (as during post-drought conditions) (Yiping Li et al., 2017). Nitrate was generally more concentrated during drought, although its levels were always $< 3\times10^{-4}$ mol L^{-1} as often found in water bodies (Chen et al., 2014; Hemond and Lin, 2010). Increasing nitrate might lower total alkalinity (Schlesinger and Bernhardt, 2013), but in Lake Alexandrina bicarbonate was more concentrated during drought because of higher alkalinity values (Figs.4.3.4b,c). Indeed, water pH did not undergo significant variations when passing from drought to post-drought conditions (Fig.4.3.4a), although hotspots of pH decrease were observed in particular areas (one is located near Goolwa) due to pyrite oxidation after air exposure of sediments (Mosley et al., 2014). Probably, increasing alkalinity was due to the release of cations such as calcium and magnesium, after sediment resuspension or because of higher inputs from groundwater (Mosley, 2015).

In contrast, HCO_3^- did not show significant changes between drought and post-drought in Lake Albert (at Meningie station), as observed also in other environments (Caruso, 2002, 2001). This finding is likely accounted for by the terminal Lake Albert system, which reaches and maintains saturation with calcium carbonate that could offset the lower degree of dilution. Differently from bicarbonate, in Lake Albert the DOC was ~4-5 times higher during drought, while nitrate was ~3 times higher. This is likely accounted for by

evapoconcentration (the water depth was ~3 times lower during drought than under post-drought conditions), higher productivity (chlorophyll a actually increased during drought; Mosley et al., 2012), and the related release of water-soluble compounds upon algae cell lysis (Wetzel, 2001).

As described above, DOC was higher during drought and underwent a decline when the lakes were flooded after 2010. The main causes for flooding were heavy rainfalls in the region, because of strong La Niña events (van Dijk et al., 2013). Although heavy precipitations often induce the increase of water DOC because of the export of DOM from soils to the water body (Fasching et al., 2016; Li et al., 2016), as slightly observed in Goolwa (Fig.4.3.2), in some cases the dilution due to huge water inputs prevails over DOM exports from the surroundings soils (Y. Zhou et al., 2020), in particular if the rainfalls last for a while (Clark et al., 2007).

Finally, some words have to be spent for salinity. In Goolwa channel, the backflow of seawater into lake water has been sometimes observed during drought because of an inverse hydraulic gradient, coupled to a higher input of groundwater that caused an increase of salinity (Mosley et al., 2012). Seawater contains bromide and chloride that act as scavengers of, respectively, $HO^{\bullet}$ (Vione et al., 2014) and $^{3}CDOM^{*}$ (Brigante et al., 2014), producing reactive species that are able to transform both natural and xenobiotic compounds (Parker and Mitch, 2016; Vione, 2018). However, no suitable data about concentrations of Cl^{-} and Br^{-} were available to include the effects of seawater intrusion into the photochemical model. Therefore, one can only speculate about this and possibly expect that only bromide affected lake-water photochemistry by lowering the steady-state concentration of $HO^{\bullet}$ (Vione et al., 2014), while chloride is usually a minor scavenger of $^{3}CDOM^{*}$ compared to dissolved oxygen (Brigante et al., 2014). However, dissolved oxygen could have been lowered during drought as well, because of the increase of salinity

that induces a salting-out effect on dissolved gases. Therefore, although these effects cannot be considered without real data, a drastic change in the results of the model (at least those for ^{3}CDOM* and $^{1}O_2$) can be excluded.

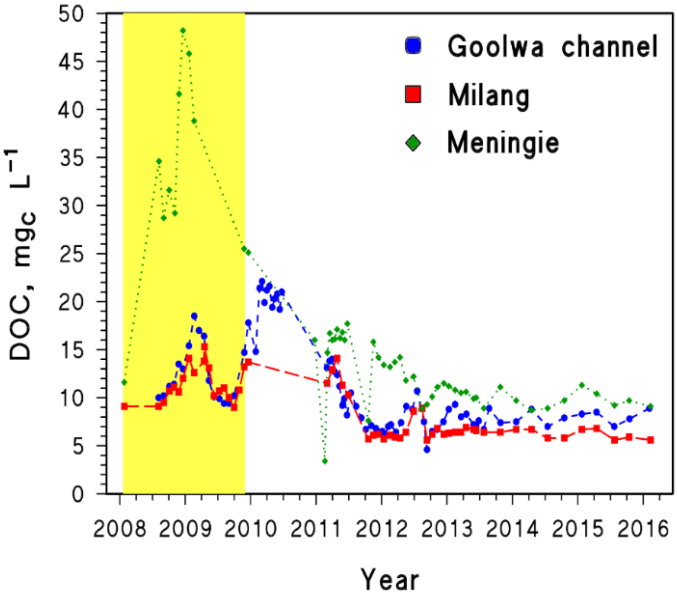

Fig.4.3.2 Time trends of the DOC in the three sampling stations under study (Goolwa channel, Milang, Meningie). The yellow band refers to the extreme drought period (from March 2007 to November 2009) as reported in Mosley et al. (2012). Adapted from Carena et al. (2019b).

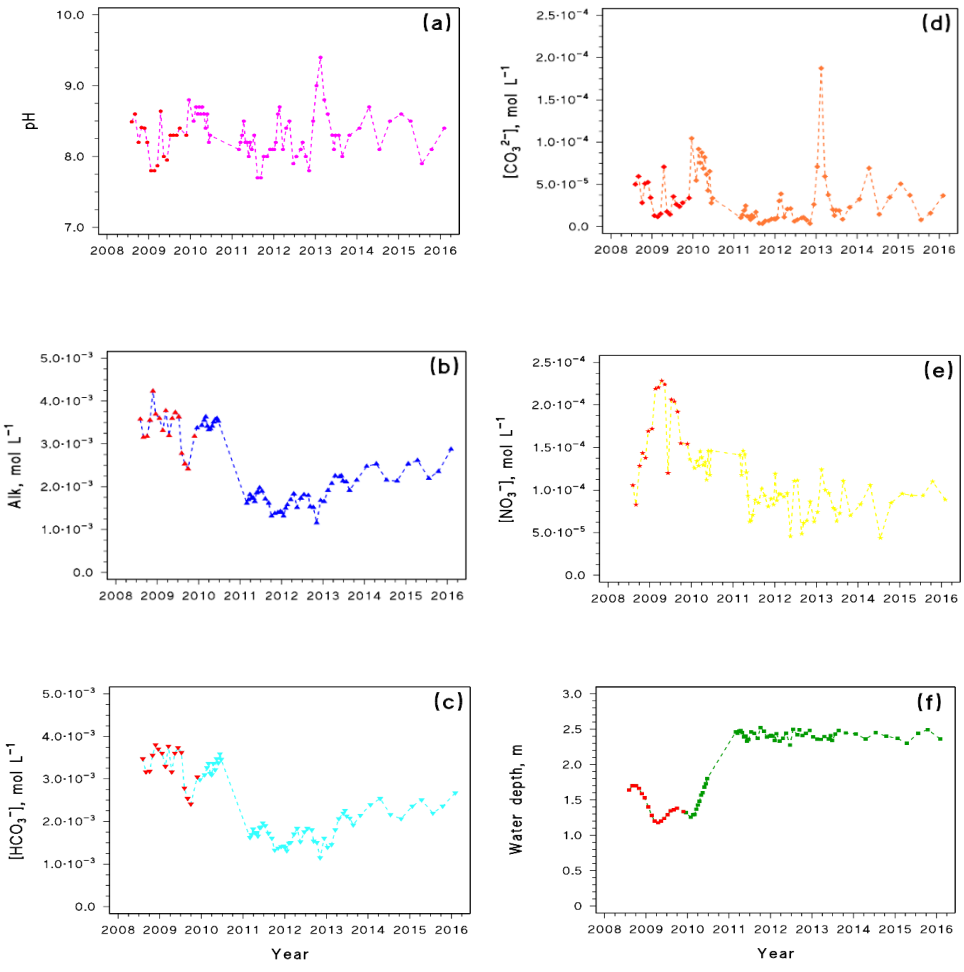

Fig.4.3.3 Time trends of chemical and physical parameters of photochemical significance in the Goolwa channel station. **(a)** pH; **(b)** Alkalinity; **(c)** Bicarbonate; **(d)** Carbonate; **(e)** Nitrate, and **(f)** water depth. Note that the concentration values of bicarbonate and carbonate were derived from alkalinity and pH. The red-labelled data refer to the extreme drought period (March 2007 – November 2009) as reported in Mosley et al. (2012). Adapted from Carena et al. (2019b).

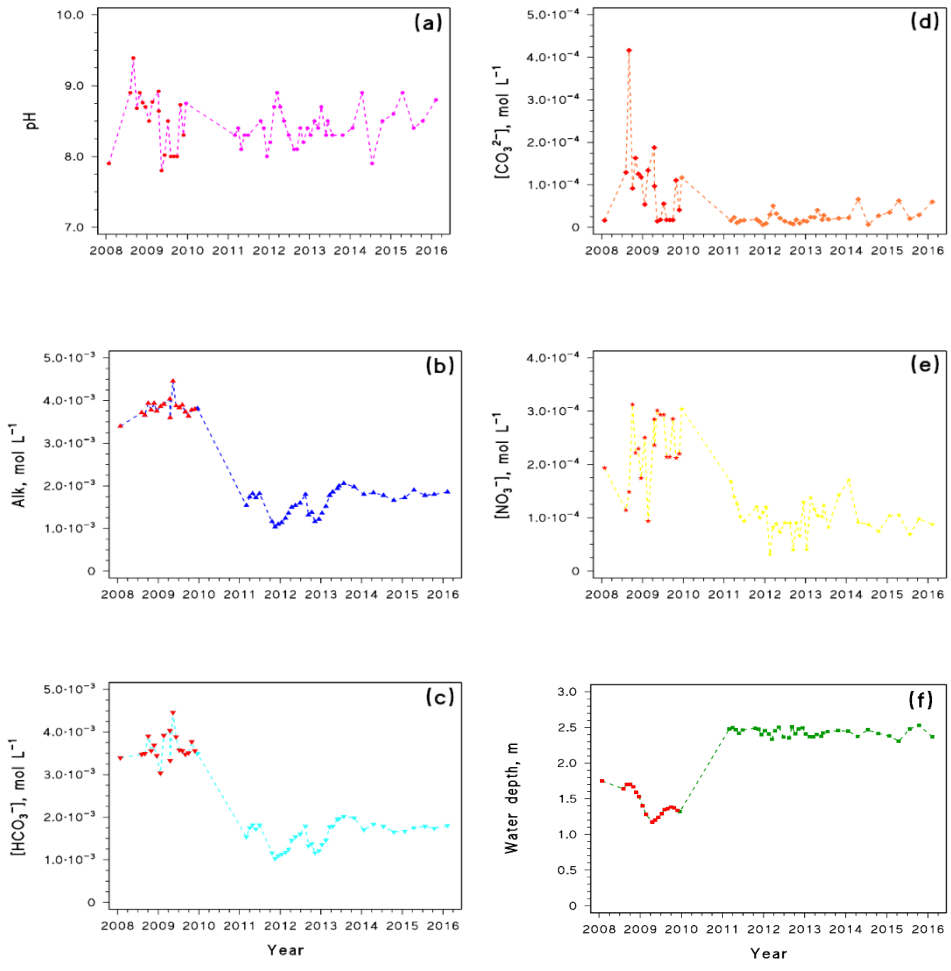

Fig.4.3.4 Time trends of chemical and physical parameters of photochemical significance in Lake Alexandrina (Milang station). **(a)** pH; **(b)** Alkalinity; **(c)** Bicarbonate; **(d)** Carbonate; **(e)** Nitrate, and **(f)** water depth. Note that the concentration values of bicarbonate and carbonate were derived from alkalinity and pH. The red-labelled data refer to the extreme drought period (March 2007 – November 2009) as reported in Mosley et al. (2012). Adapted from Carena et al. (2019b).

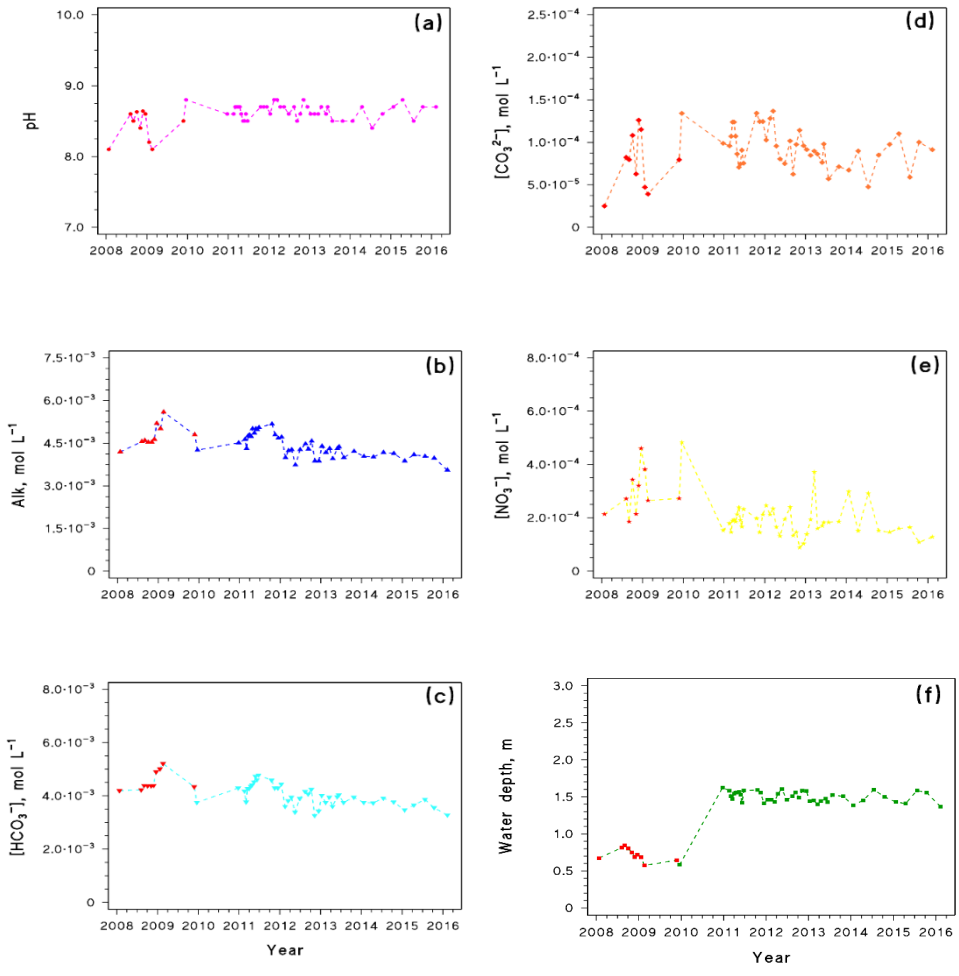

Fig.4.3.5 Time trends of chemical and physical parameters of photochemical significance in Lake Albert (Meningie station). **(a)** pH; **(b)** Alkalinity; **(c)** Bicarbonate; **(d)** Carbonate; **(e)** Nitrate, and **(f)** water depth. Note that the concentration values of bicarbonate and carbonate were derived from alkalinity and pH. The red-labelled data refer to the extreme drought period (March 2007 – November 2009) as reported in Mosley et al. (2012). Adapted from Carena et al. (2019b).

Hydrological-drought effects on PPRIs photochemistry

Variations of both water depth and chemistry can affect the photochemistry of a water body, but the direction of photochemistry changes is difficult to predict in advance (Minella et al., 2016). Fig.4.3.6 shows the time trends of the steady-state concentrations of $HO^{\bullet}$, $CO_3^{\bullet-}$ and ^{3}CDOM* (the evolution of $[^1O_2]$ was not reported here because it is very close to that of ^{3}CDOM*), computed with the data reported in Figs.4.3.3-4.3.5. In general, the concentrations of the PPRIs followed the seasonal variations of solar irradiation (which were considered as well in the photochemical model, see the previous sections), with peaks during austral summers and minima during winters. However, separate discussions can be made for $HO^{\bullet}$/$CO_3^{\bullet-}$ and ^{3}CDOM*.

$HO^{\bullet}$ radicals did not show any significant variation between drought and post-drought periods in the three sites under study. This is likely accounted for by the time trends of nitrate (a source of $HO^{\bullet}$) and DOC (note that DOM is the main $HO^{\bullet}$ scavenger; Vione et al., 2014; Westerhoff et al., 2007). The water-chemistry time evolution showed that both nitrate and DOC were higher during drought and underwent similar dilution after drought. Consequently, both the sources and scavengers of $HO^{\bullet}$ varied in the same way, making $[HO^{\bullet}]$ basically unchanged (see Eq. 4.2.12). A similar issue applies to $[CO_3^{\bullet-}]$, which is produced upon oxidation of bicarbonate and carbonate by $HO^{\bullet}$. However, an appreciable variation of $[CO_3^{\bullet-}]$ was found in Milang (Lake Alexandrina; Fig.4.3.6b), because of a higher gradient of bicarbonate concentration between drought and post-drought compared to what happened in the other sampling sites (Fig.4.3.4c). Finally, it should be pointed out that in Lake Albert (at Meningie station), both $[HO^{\bullet}]$ and $[CO_3^{\bullet-}]$ peaked just after the post-drought lake-flooding in the 2011 summer. That event could have likely been due to

the minimum reached by the DOC, which reached the lowest value reported in the whole available dataset (Fig.4.3.3).

Differently from $HO^{\bullet}$ and $CO_3^{\bullet-}$, ^{3}CDOM* photochemistry was more affected by drought. Indeed, higher [^{3}CDOM*] values were found in the years 2008-2010 than during the post-drought period (Fig.4.3.6). The rationale of this consistent finding in the model results is linked to the fact that the content of (C)DOM (quantified as the DOC) was very high in all the stations during drought (Fig.4.3.3). [^{3}CDOM*] could have been even higher if the dissolved oxygen content, the main ^{3}CDOM* scavenger (McNeill and Canonica, 2016) were lower because of the salinity increase (salting-out effect). Finally, increases in organic carbon concentrations in lakes and rivers have been observed globally during droughts (Mosley, 2015), thus the related [^{3}CDOM*] increase might be a key photochemical change that occurs across different systems.

The drought-induced photochemical scenario found here (unchanged $HO^{\bullet}/CO_3^{\bullet-}$ and increased ^{3}CDOM* concentrations during drought) agrees with what has been found in a previous modeling work that investigated the effects of water-depth fluctuations on photochemistry (Minella et al., 2013). The scenario found here has been predicted for water loss by evaporation rather than outflow (Minella et al., 2013). Of course, the photochemical scenario of the Lower Lakes cannot be ascribed to water evaporation alone, because groundwater inputs to the lakes were observed as well (Mosley et al., 2012), but the contribution of evaporation was almost certainly very significant.

The data of PPRIs steady-state concentrations allow for an assessment of the photochemistry of natural-occurring compounds or xenobiotics. However, data about pollution of Lower Lakes by xenobiotics (for instance, pesticides and pharmaceuticals) are very scarce in the literature, and the majority of

which concerns sediments rather than the surface water (Jenkins, 2013). Indeed, although the presence of water contaminants can be reasonably expected because of anthropogenic activities, the lack of data does not allow for choosing a pollutant that is representative for these water bodies. Therefore, the naturally occurring tripeptide glutathione (hereafter, GSH) was chosen instead for photochemical modeling purposes.

GSH is produced by microorganisms for its antioxidant and detoxicant actions, being a compound with high redox reactivity that occurs in the photic zone of natural waters upon extracellular release. In the aquatic environment GSH is consumed by microbiota and is also degraded by photochemical processes (Chu et al., 2017).

A previous work has shown that the present photochemical model is able to predict the GSH photochemical fate in good agreement with experimental results, highlighting that ^{3}CDOM* plays a potential role in the overall GSH phototransformation while direct photolysis is almost negligible (Vione, 2018).

The photochemistry of GSH during drought was modeled by taking into account the PPRIs steady-state concentrations obtained for January 2009 (austral summer), in order to describe the worst drought phase for the Lower Lakes. For the post-drought period, average values of summertime concentrations of PPRIs were assessed from 2010 onwards (Table 4.3.1). In general, the kinetics of GSH photodegradation was higher during drought than in the post-drought phase (Fig.4.3.7). This is mainly accounted for by the important role of ^{3}CDOM* in GSH phototransformation. Indeed, higher [^{3}CDOM*] values were observed during drought because of the elevated DOC and low water depth, while [^{3}CDOM*] decreased in post-drought conditions due to DOM dilution. These variations cause a decrease in the pseudo-first

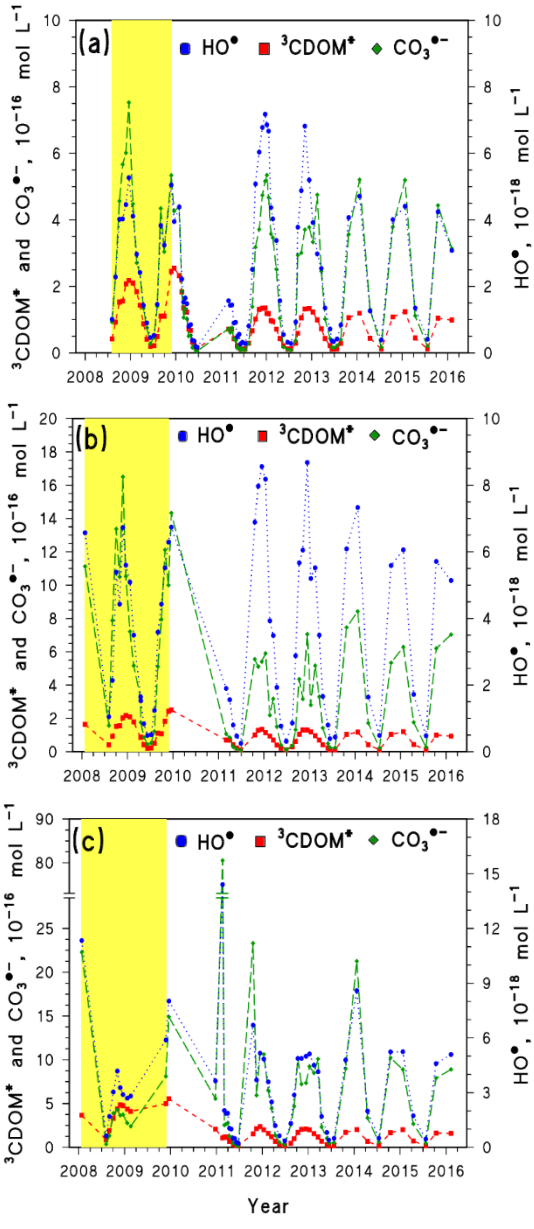

Fig.4.3.6 Model-predicted steady-state concentrations of $HO^{\bullet}$, $CO_3^{\bullet-}$ and $^3CDOM^*$ in **(a)** Goolwa channel; **(b)** Milang sampling station (Lake Alexandrina), and **(c)** Meningie sampling station (Lake Albert). Water chemistry and depth data refer to the sampling time, and so does the fair-weather sunlight irradiance and spectrum (35.63° S; 138.28° E, 9.00 a.m., month of the sampling) used in model calculations. The yellow band refers to the extreme drought period (up to November 2009) as reported in Mosley et al. (2012). Adapted from Carena et al. (2019b).

order rate constant of the reaction GSH + ^{3}CDOM*, and in the overall photodegradation rate constant of GSH as a consequence. This finding thus shows how important the ^{3}CDOM*-induced photochemistry could be under drought conditions.

Differently from ^{3}CDOM*, GSH photodegradation by $HO^\bullet$ was less affected by drought in Lake Alexandrina (at Goolwa and Milang sites), because [$HO^\bullet$] did not change much over time. Similar results were found for the $CO_3^{\bullet-}$-induced photodegradation, although a slight decrease in GSH photodegradation by $CO_3^{\bullet-}$ was observed for Milang, because of the [HCO_3^-] trend described previously. In the site of Meningie (Lake Albert), despite the higher decrease of the ^{3}CDOM* contribution, GSH degradation by both $HO^\bullet$ and $CO_3^{\bullet-}$ increased when passing from drought to post-drought conditions. This result can be accounted for by the very high DOC levels in Lake Albert compared to Lake Alexandrina, especially during drought (DOC ~40-50 mg_C L^{-1}), combined with a considerable decrease in the post-drought period (down to DOC ~10-15 mg_C L^{-1}; see Fig.4.3.2). In these conditions (DOC > 10 mg_C L^{-1}), the steady-state [$HO^\bullet$] and [$CO_3^{\bullet-}$] are dominated by DOM scavenging and are thus inversely proportional to the DOC (Vione et al., 2014). In contrast, in Lake Alexandrina the DOC levels were generally lower and did not undergo a comparably important decrease between the drought and post-drought periods.

Table 4.3.1 *Upper part*: PPRIs steady-state concentrations used to assess GSH photochemistry. *Lower part*: PPRIs second-order reaction rate constants with GSH, taken from the literature (Buxton et al., 1988; Chu et al., 2017; Neta et al., 1988). Adapted from Carena et al. (2019b).

	$HO^{\bullet}$	**$CO_3^{\bullet-}$**	**^{3}CDOM***
	Concentration, mol L^{-1}		
Goolwa channel (drought)	4.1×10^{-18}	4.5×10^{-16}	2.1×10^{-16}
Goolwa channel (post-drought)	3.7×10^{-18}	3.3×10^{-16}	1.2×10^{-16}
Milang (drought)	5.1×10^{-18}	7.2×10^{-16}	2.1×10^{-16}
Milang (post-drought)	5.0×10^{-18}	4.3×10^{-16}	9.7×10^{-17}
Meningie (drought)	2.7×10^{-18}	2.8×10^{-16}	4.4×10^{-16}
Meningie (post-drought)	4.7×10^{-18}	4.3×10^{-15}	1.6×10^{-16}
	Reaction rate constant with GSH, L mol^{-1} s^{-1}		
$k_{(i+GSH)}$	3.5×10^{9}	5.3×10^{6}	8×10^{7}

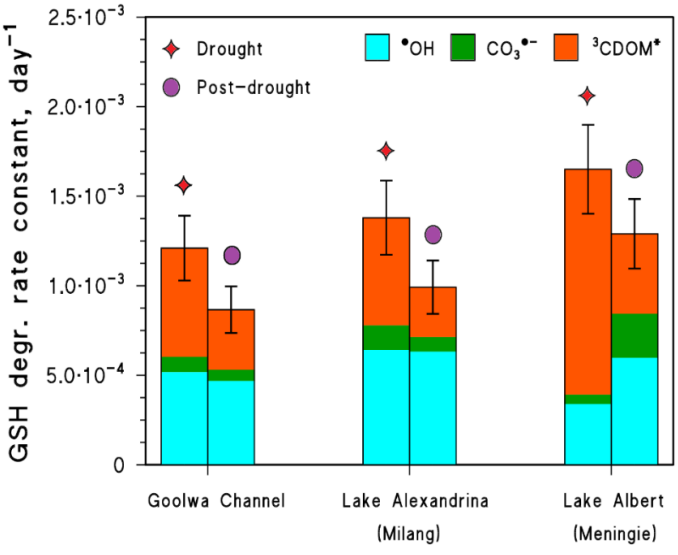

Fig.4.3.7 Model-predicted photodegradation kinetics of GSH by reactions with $HO^{\bullet}$, $CO_3^{\bullet-}$ and ^{3}CDOM* in Goolwa channel, Milang sampling station (Lake Alexandrina), and Meningie sampling station (Lake Albert). The error bars represent the uncertainties of model predictions. Adapted from Carena et al. (2019b).

4.3.2 Geographical and temporal assessment of the photochemical decontamination potential of Piedmontese rivers from agrochemicals

Although extreme drought events comparable to the Millennium Drought in Southern Australia have not been observed in Piedmont (NW Italy), this region has been affected by drought periods and could face them again in the future. The Po river, which is the main watercourse of the region as well as of Italy, experienced alternation of high (1914-1941, average flow = 1593 m^3 s^{-1}), low (1942-1974, 1390 m^3 s^{-1}), and again high (1975-2002, 1626 m^3 s^{-1}) flow, followed by the strongest drought event between 2003 and 2008 (1058 m^3 s^{-1}) (Cozzi et al., 2019). A runoff increase then reoccurred from 2009 to 2012 (1551 m^3 s^{-1}) (Cozzi et al., 2019). Values above the mean flow observed in the last decades could have been consequences of intense levee works and extreme rainfall events (Zanchettin et al., 2008). However, a significant temporal decrease of the Po runoff has been observed between 1975 and 2008 (Cozzi and Giani, 2011), possibly because of the decrease of precipitations and the increase of evapotranspiration on the Po basin (Zanchettin et al., 2008). The water discharge of the Po river can be a good proxy for the monitoring of the hydrologic conditions of both Piedmont and other regions in Northern Italy where the river flows through (Cozzi and Giani, 2011).

The drought intensities experienced by the Po were higher during summers and may have been caused by the weakening of precipitations in autumn, the backward shift of the spring floods from June to May because of anticipated snowmelt, and the water-use increase by agricultural activities because of higher evapotranspiration in spring/summer (Zampieri et al., 2015; Zanchettin et al., 2008). Note that the annual flow maxima of the Po usually occur in

autumn and spring (Cozzi et al., 2019), and a discharge reduction in these periods could highly affect the hydrology of the basin.

Finally, drought events in the Po (as well as in other European watersheds) could be linked to global climatic events (Pociask-Karteczka, 2006). For instance, positive phases of the North Atlantic Oscillation (NAO) index, which leads to increased air temperatures and weakens precipitations over Southern Europe (especially during winter) (Bader et al., 2011), as well as warming of the Indian and Extra-Tropical Pacific Oceans (Bader and Latif, 2005; Jiang and Li, 2019; Stenseth et al., 2003) have been correlated with drought periods in the Po basin, suggesting that they could have a global origin (Zanchettin et al., 2008). NAO positive phases have also been correlated with meteorological and hydrological droughts in several regions of the Mediterranean basin (Brandimarte et al., 2011; Corona et al., 2018; Luppichini et al., 2021). Positive NAO index and positive anomalies of sea surface temperature (SST) in the Indian and Extra-Tropical Pacific Oceans are projected to become more frequent with anthropogenic climate change under different RCPs scenarios (i.e., *Representative Concentration Profiles* of greenhouse gases causing a given radiative forcing) (Ault, 2020; Bader et al., 2011; Bader and Latif, 2005; IPCC, 2014). Moreover, the duration, frequency (and possibly intensity) of droughts are expected to be higher over several land areas of the world (~50%), including the Mediterranean region (IPCC, 2014; Ukkola et al., 2020). For these reasons, drought events in the Southern European watersheds are likely to occur more frequently in the future but, at the same time, future projections of drought effects on the Po river discharge can be affected by significant uncertainty because of internal climate variability (Fatichi et al., 2014).

Taking the previous considerations into account, the photochemistry of Piedmontese rivers was modeled and their decontamination potential from

pesticides assessed. The relevant results allowed for the assessment of how watercourses in Piedmont behave in terms of xenobiotics photodegradation under climatic and pollution pressures.

PPRIs-induced photochemistry in Piedmontese rivers

Figs.4.3.8-4.3.10 show the maps of the steady-state concentrations of $HO^{\bullet}$, $CO_3^{\bullet-}$ and ^{3}CDOM* in 2000-2008 (the singlet oxygen map largely resembles that of ^{3}CDOM* and is not shown here). The reported values were used to compute the indirect photodegradation rate constants of the investigated pesticides, as per Eq. 4.2.29.

The steady-state concentration of $HO^{\bullet}$ radicals was found to be higher in the northern and north-western parts of the region, relatively to the southern and eastern sides (see Fig.4.A1a in Appendix II). In contrast, in the latter area the photoproduction of ^{3}CDOM* would be more favored (Fig.4.A1b), probably because of higher DOC values over the years 2000-2008 (Fig.4.A3). Indeed, DOC values were generally lower and nitrate sometimes higher in the northern and north-western parts of Piedmont, which would favor the photoproduction of $HO^{\bullet}$ rather than its scavenging by DOM.

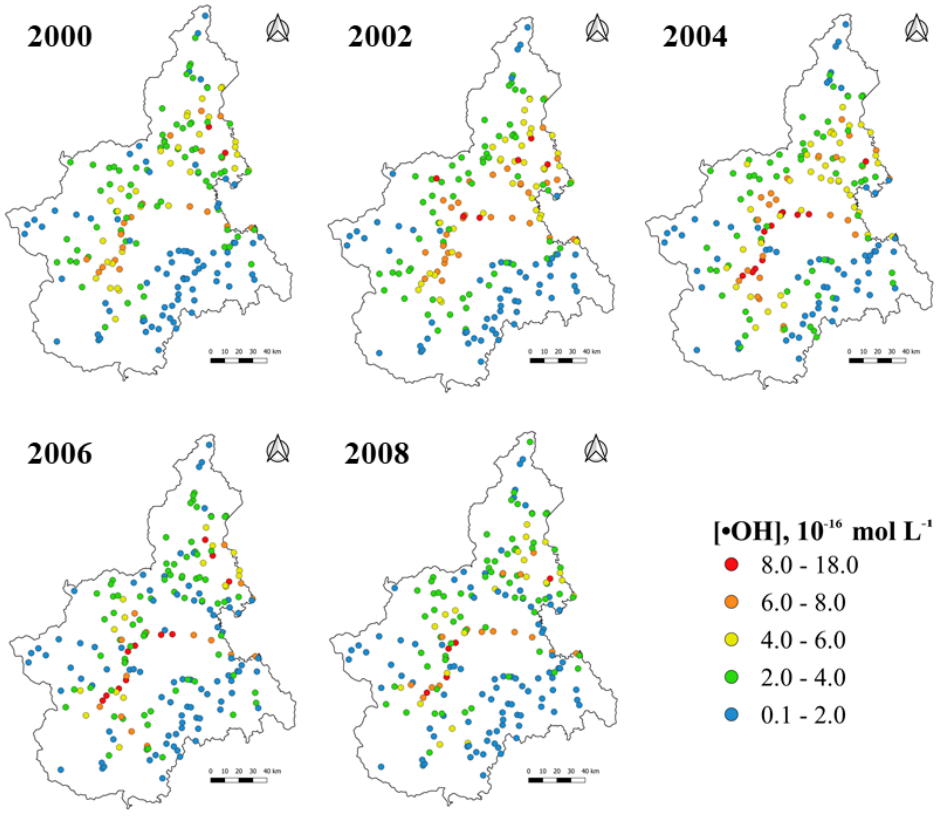

Fig.4.3.8. Photochemical maps of Piedmont over the years 2000-2008, showing the annual mean values of the steady-state concentrations of HO• in the different sampling points. Adapted from Carena et al. (2021).

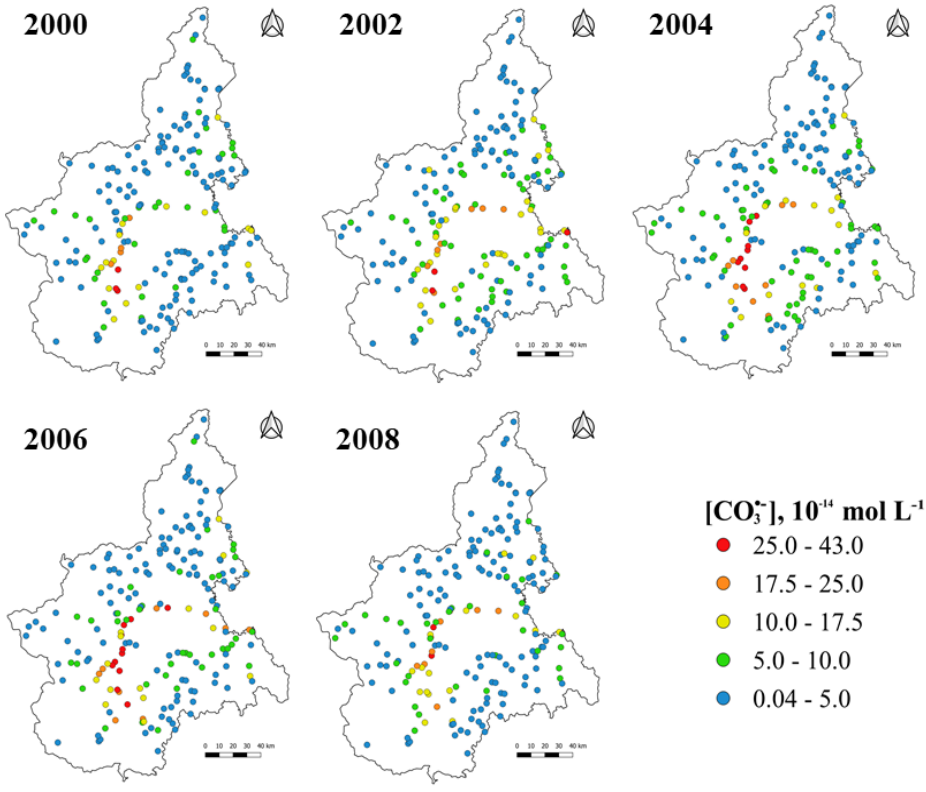

Fig.4.3.9. Photochemical maps of Piedmont over the years 2000-2008, showing the annual mean values of the steady-state concentrations of $CO_3^{\bullet-}$ in the different sampling points. Adapted from Carena et al. (2021).

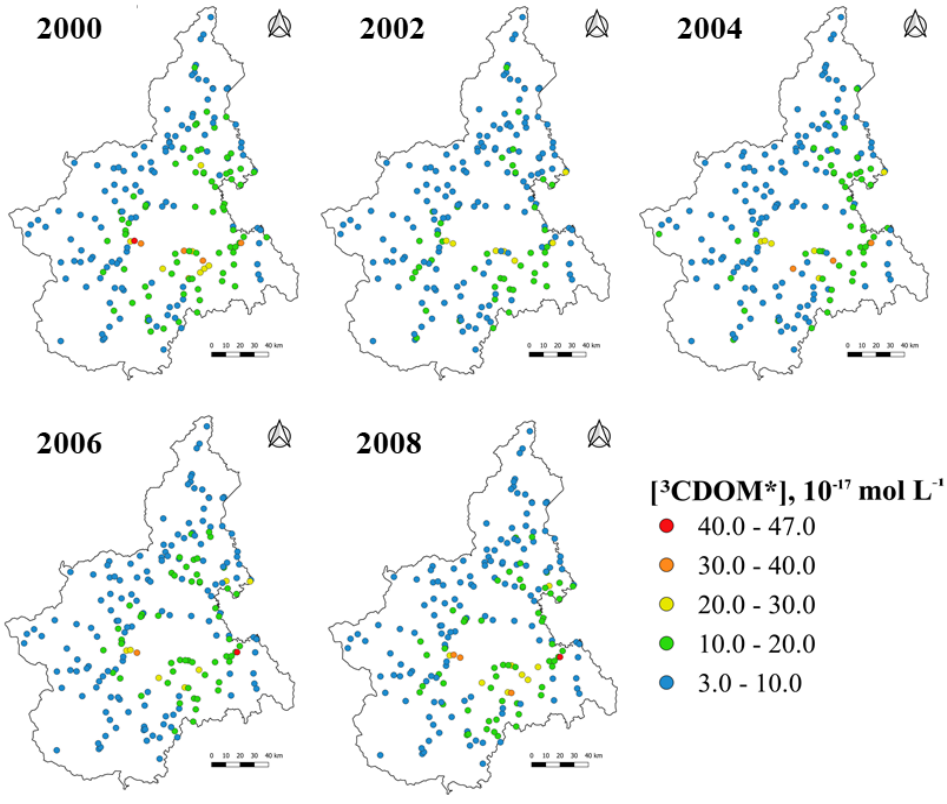

Fig.4.3.10. Photochemical maps of Piedmont over the years 2000-2008, showing the annual mean values of the steady-state concentrations of ^{3}CDOM* in the different sampling points. Adapted from Carena et al. (2021).

Interestingly, a statistically significant difference in $HO^{\bullet}$ and $CO_3^{\bullet-}$ concentrations (t-test for paired data with $\alpha = 0.05$) was observed between the Po river and the other watercourses of the region (Figs.4.3.11a,b). Indeed, the Po river showed higher values of both [$HO^{\bullet}$] and [$CO_3^{\bullet-}$], while a significant difference was not found for the steady-state concentrations of ^{3}CDOM* (Fig.4.3.11c).

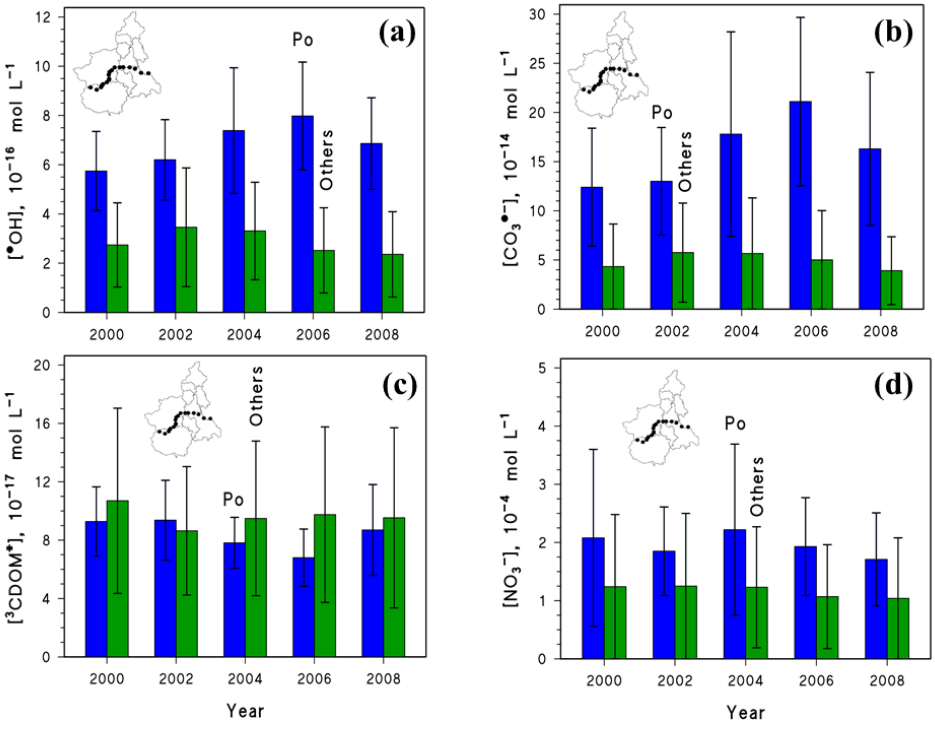

Fig.4.3.11. Annual averages of **(a)** $HO^{\bullet}$, **(b)** $CO_3^{\bullet-}$, **(c)** $^3CDOM^*$ and **(d)** nitrate concentration in the Po river (blue bars) and all the other rivers of Piedmont (average values, green bars). The associated variability is the spatial standard deviation. The insets show the Piedmont map with the relevant administrative (provinces) boundaries, and the data points along the Po river. The dataset of nitrate concentration was provided by the regional environmental protection agency (ARPA Piemonte), while the statistical analysis was carried out with Microsoft Excel®. Adapted from Carena et al. (2021).

The peculiarly high values of $[HO^{\bullet}]$ and $[CO_3^{\bullet-}]$ in the Po compared to the other rivers and streams of the region are at least partly caused by high nitrate levels (Fig.4.3.11d). Indeed, the DOC that is the additional main parameter that affects both $HO^{\bullet}$ and $CO_3^{\bullet-}$ photochemistry (McCabe and Arnold, 2016; Xu et al., 2020) did not show statistically significant differences.

The high nitrate concentration in the Po river can be accounted for by interaction of its surface waters with the groundwater of the surrounding plain.

Previous studies have shown that the river Po, after it leaves the uplands and enters the plain behaves as a 'gaining stream' by receiving water supply from surrounding groundwater (Lasagna et al., 2016a). The hydraulic gradient is higher near the Alps and decreases in the lower plain towards the Po, thus shallow aquifers can flow from the Alps to the river by passing through the plain. The latter is mainly characterized by soils with high permeability (Lasagna et al., 2016a, 2016b; Martinelli et al., 2018). One of the important anthropogenic impacts in this area is the contamination of shallow aquifers by nitrate, due to the high use of N-based fertilisers and zootechnical effluents in agricultural activities (Franchino et al., 2014; Lasagna and De Luca, 2019). The concentration values of nitrate in aquifers in the investigated period usually ranged from some tens to ~100 mg L^{-1}, with locally high contamination of up to ~300 mg L^{-1} (Bassanino et al., 2011; Debernardi et al., 2008; Lasagna et al., 2016a; Martinelli et al., 2018). Furthermore, nitrogen inputs to aquifers from agricultural activities are higher in the lower plain than near the Alps (Bassanino et al., 2011). As a consequence, one observes a gradual increase of nitrate concentration values in both ground- and surface waters when going from the Alps to the lower plain, and shallow aquifers in the plain can discharge nitrate into the Po river (Lasagna et al., 2016a). Although nitrate concentrations are generally lower in rivers than in groundwater because of denitrification and dilution processes taking place in the riparian and hyporheic areas (Lasagna et al., 2016b), watercourses affected by nitrate-contaminated groundwater are understandably more nitrate-rich than non-affected ones (Balestrini et al., 2021).

There was a noteworthy increase of both $HO^{\bullet}$ and $CO_3^{\bullet-}$ concentrations in the Po river during the years 2004-2006, as well as an important difference between the Po and the other watercourses of the region (Figs.4.3.11a,b). This period coincides with the strongest drought event that the Po ever experienced

during the last century (Cozzi et al., 2019). In 2008, [$HO^{\bullet}$] and [$CO_3^{\bullet-}$] decreased but their values were still above the annual averages observed in the pre-drought period (i.e., before 2003). Note that nitrate concentrations in the Po river did not undergo high variations over the years 2000-2008 (Fig.4.3.11d), while the DOC slightly decreased and the same did the observed steady-state concentrations of ^{3}CDOM* (Fig.4.3.11c). The DOC trend can explain the increase in both $HO^{\bullet}$ and $CO_3^{\bullet-}$ concentrations. However, a discussion can be made also by considering the drought event and the consequential water depth fluctuations.

Although a constant water depth = 0.5 m was used in the photochemical model, so that water depth fluctuations cannot here account directly for PPRI-concentration variations, this value is generally lower that the actual depth of the Po river, even during drought conditions (AIPo, 2020). Drought causes water loss from the river, which can occur through evaporation, outflow or a combination of both (Minella et al., 2013). As outflow one usually means water loss by drainage and seepage (Minella et al., 2013), although here the decrease in water inputs to the river from alpine-glacier melting would be important as well. In general, the reduction of the water volume by outflow does not change drastically the solutes concentrations, while it can account for an increase in both $HO^{\bullet}$ and $CO_3^{\bullet-}$ concentrations in a water body because of depth reduction. In contrast, the same phenomenon would leave [^{3}CDOM*] basically unchanged (Minella et al., 2013). In contrast, water evaporation enhances the solutes concentrations (DOM, nitrate) as well as [^{3}CDOM*], while it keeps almost constant the concentrations of $HO^{\bullet}$ and $CO_3^{\bullet-}$ (Minella et al., 2013). A similar scenario was found in this work for the case of the Australian Lower Lakes.

Although strong evapotranspiration and weak rainfalls occurred on the Po basin in the years under consideration (Zanchettin et al., 2008), no significant

increases in nitrate concentration, DOC (and [^{3}CDOM*]) were observed during the drought of the Po (Figs.4.3.11c,d). It is thus suggested that evaporation did not play an important contribution to either water loss or photochemistry changes, which is reasonable when taking into account a flowing system such as a river that is very different from a stationary water body such as a lake.

In contrast, water outflow from the Po to the surrounding plain could have partly affected the river drought because of *(i)* reduction in the groundwater table and/or *(ii)* increase in water use by agricultural activities, aimed at offsetting the decreasing rainfalls. Actually, a significant decrease in the groundwater level of the Po-surrounding plains was observed between 2003 and 2009 because of the drought, possibly causing a reversal of the hydraulic gradient between surface and groundwater. The groundwater level rose up again after 2009, due to increased rainfalls (Lasagna et al., 2020). Therefore, besides the DOC decrease during drought, water outflow could have partially affected the observed trends of PPRIs concentrations in the Po river (Fig.4.3.11).

This is in contrast with the Australian scenario of the Lower Lakes, where water evaporation caused by drought induced an increase in [^{3}CDOM*] and no significant variations of [$HO^{\bullet}$] and [$CO_3^{\bullet-}$].

A similar issue may hold for the Rhône river, which is one of the largest watersheds in Southern Europe together with the Po, Ebro and Danube. The water flow trend shown by the Rhône river over the last decades was similar to that of the Po. Alternation of high (1920-1941, average flow = 1772 $m^3 s^{-1}$), low (1942-1976, 1614 $m^3 s^{-1}$), high (1977-2002, 1797 $m^3 s^{-1}$) and low flow conditions (2003-2012, 1478 $m^3 s^{-1}$) occurred in the last century (Cozzi et al., 2019). Of particular relevance was the flow regime observed between 2002-2012, which was the lowest in a century. No significant variations of the

annual mean values of both nitrate concentration and DOC were observed in the Rhône between 1978 and 2012 (Figs.4.3.12a,b), although an important increase of nitrate content was observed in the period 2013-2015. The latter made statistically significant the nitrate increase from 1978 to 2015. However, a slight increase of nitrate concentration and a weak DOC decrease occurred passing form the 1977-2002 flow regime to that of 2003-2012. These trends can account for the significant positive trend found for the annual mean values of $HO^{\bullet}$ concentration in the Rhône over the years 1978-2015 (Fig.4.3.12c). Additionally, a slightly decreasing HCO_3^- profile might have partially contributed to this finding (data not shown). In contrast, [^{3}CDOM*] did not undergo significant variations during the last 38 years (Fig.4.3.12d), mainly because of unchanged DOC content. This scenario is similar to that found for the Po river as well as for other rivers in Southern Europe (Fig.4.A2). Because no significant increase in solutes concentrations was observed, water loss by evapotranspiration from the Rhône basin may have been low (Ruiz-Villanueva et al., 2015).

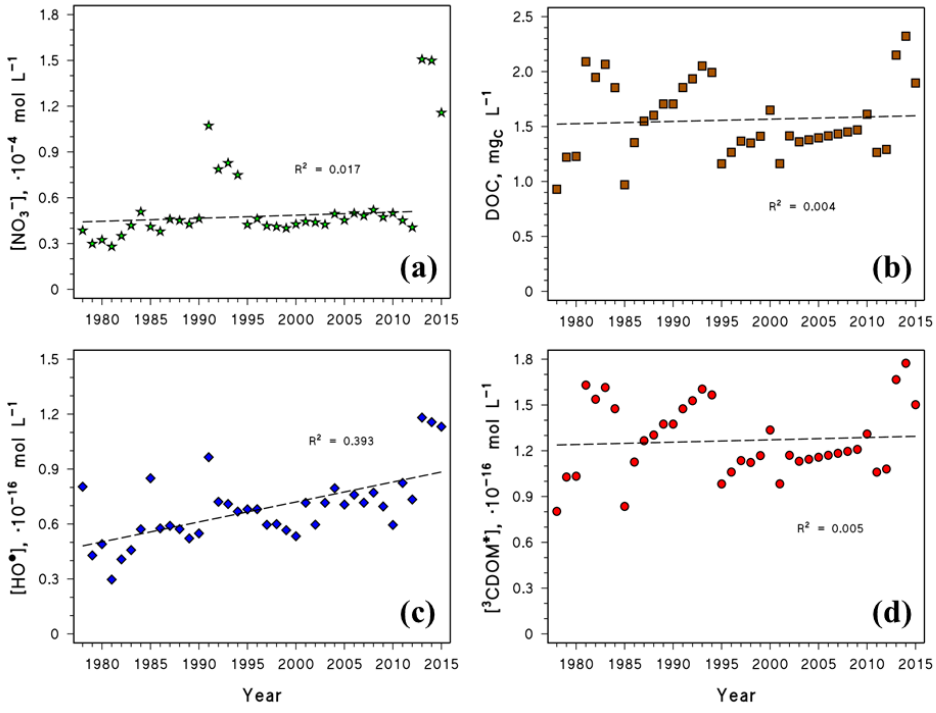

Fig.4.3.12. Temporal trends of the annual averages of **(a)** NO_3^-, **(b)** DOC, **(c)** $HO^{\bullet}$, and **(d)** ^{3}CDOM* concentrations in the Rhône river. The PPRIs concentrations were computed for a water depth d = 0.5 m. The data about annual mean values of the Rhône-water chemical composition, used as input for the photochemical model, were taken from the statistic reports of the GEMStat database (United Nations Environment Programme, 2019), while the statistical analysis was carried out with Microsoft Excel®.

In contrast, water outflow could have played a more important role, which would corroborate the results for the PPRIs temporal profiles.

Finally, note that the Australian Big Dry and the strongest drought event in the Po basin occurred in the same years (i.e., 2003-2009; Cozzi et al., 2019; Mosley et al., 2012). Several previous works have described the possible climatic factors that triggered these droughts, such as the warming of the Western Indian Ocean and the consequential strong, positive phases of IOD (Ummenhofer et al., 2009), intensification of the Inter-Tropical Convection

Zone (ITCZ) (Timbal and Drosdowsky, 2013; Timbal and Hendon, 2011), and strong ENSO events (van Dijk et al., 2013) for the Australian Big Dry. These took place at the same time as the increase of strong, positive phases of the NAO index for the Po-basin drought (Zanchettin et al., 2008). All these climatic phenomena could be linked with one another by circumglobal patterns (Bader and Latif, 2005), showing that drought events in different, remote areas of the world can be connected by the same climatic origin (Ault, 2020). Despite this, consequences on surface-waters photochemistry can be different and highly dependent on how water is lost from the water body.

Decontamination potential of Piedmontese rivers from pesticides

Lifetime maps of DMM, IPT, ATZ, BTZ and CTL are reported in Figs.4.3.13-4.3.17. The photodegradation of DMM and IPT was generally faster in the central part of the region in 2002 and 2004 (see the parts highlighted with the bigger circles in Figs.4.3.13;4.3.14). A similar issue, but to a lesser extent was observed as well for ATZ and CTL, but not for BTZ. This observation can be explained by the fact that BTZ is mainly photodegraded by direct photolysis (Carena et al., 2020), while indirect photolysis is quite important for the other pesticides (Avetta et al., 2014; Fabbri et al., 2015b; Marchetti et al., 2013). Indeed, in the highlighted area one has higher steady-state [$HO^{\bullet}$] and [$CO_3^{\bullet-}$] in 2002 and 2004 compared to the other years (Fig.s4.3.8;4.3.9), which could account for faster photodegradation in 2002 and 2004. More concentrated sources of these radicals, such as nitrate, and less concentrated sinks (mostly DOM, quantified as the DOC, Fig.4.A3) likely favored their occurrence. Faster photodegradation kinetics in 2002 and 2004 in the central-eastern part of the region would be particularly significant, because this is the zone where

the concentration of pesticides is the highest due to intense agricultural activities (see Fig.4.2.3; Bassanino et al., 2011).

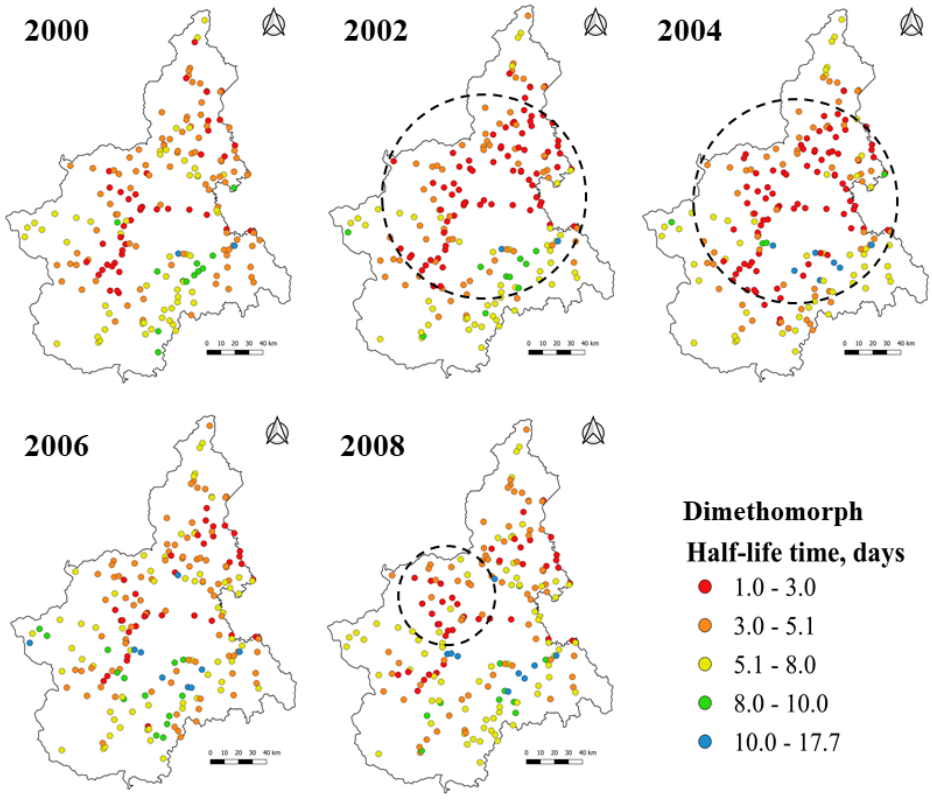

Fig.4.3.13. Photochemical maps of Piedmont over the years 2000-2008, showing the half-life times of DMM (annual mean values) in the different sampling points. The circles in the 2002 and 2004 maps show the zones where photodegradation was peculiarly fast in 2002 and 2004 (for DMM, as well as for the other pesticides except BTZ). Similar issue holds for the circle in the map for 2008, but in that case photodegradation was fast for BTZ as well. Adapted from Carena et al. (2021).

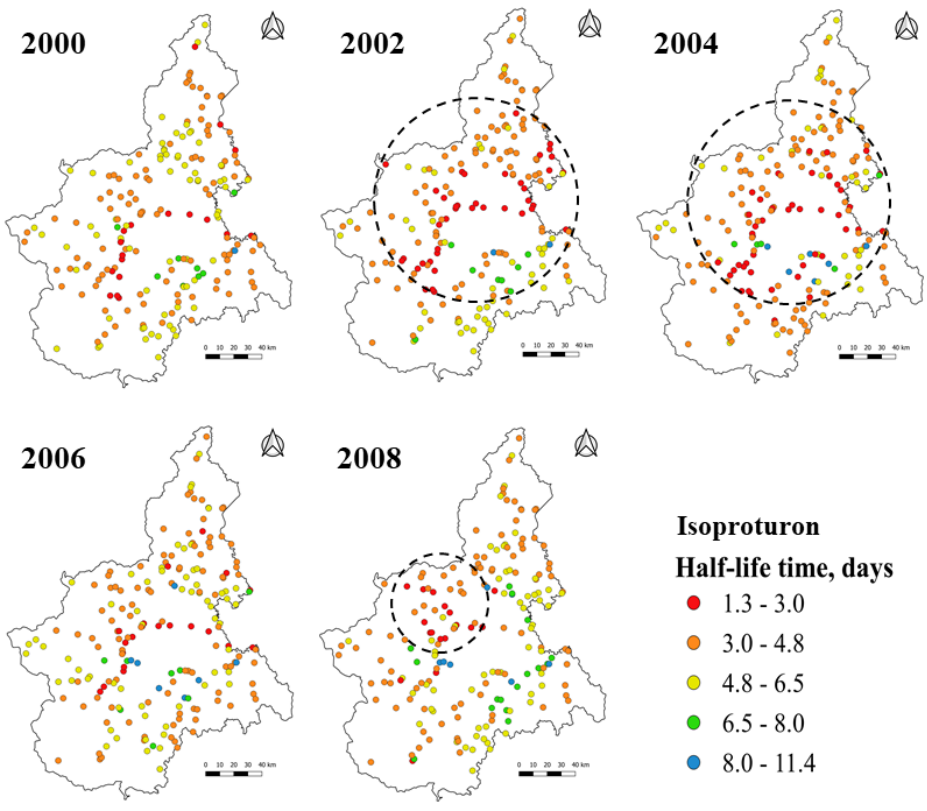

Fig.4.3.14. Photochemical maps of Piedmont over the years 2000-2008, showing the half-life times of IPT (annual mean values) in the different sampling points. The circles in the 2002 and 2004 maps show the zones where photodegradation was peculiarly fast in 2002 and 2004 (for IPT, as well as for the other pesticides except BTZ). Similar issue holds for the circle in the map for 2008, but in that case photodegradation was fast for BTZ as well. Adapted from Carena et al. (2021).

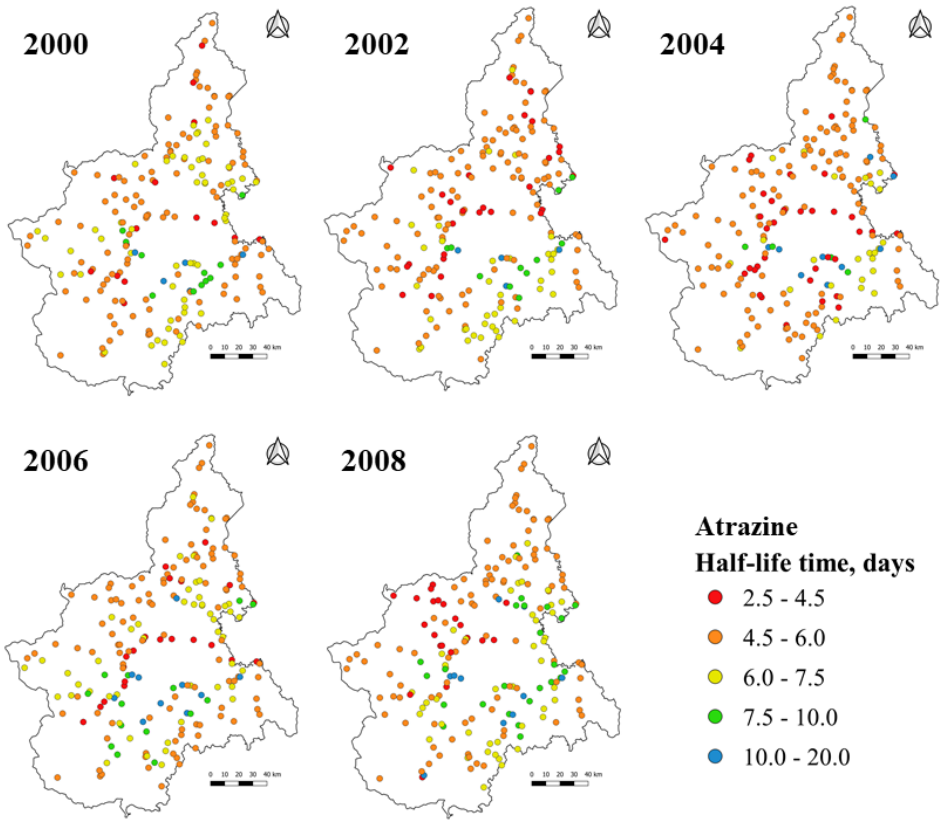

Fig.4.3.15. Photochemical maps of Piedmont over the years 2000-2008, showing the half-life times of ATZ (annual mean values) in the different sampling points. Adapted from Carena et al. (2021).

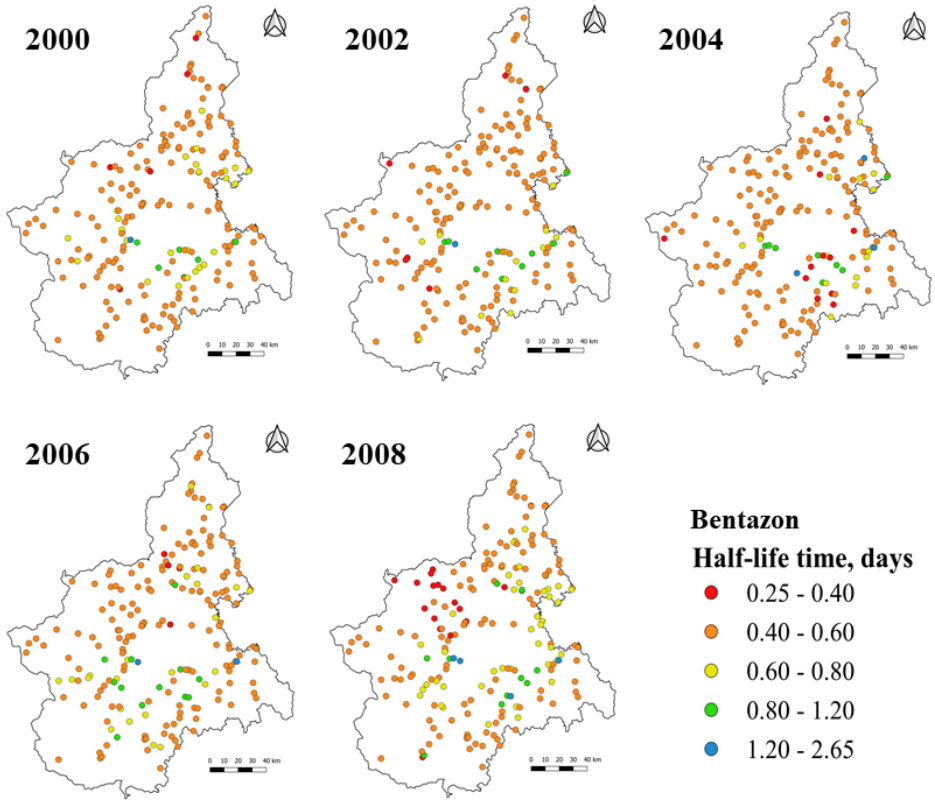

Fig.4.3.16. Photochemical maps of Piedmont over the years 2000-2008, showing the half-life times of BTZ (annual mean values) in the different sampling points. Adapted from Carena et al. (2021).

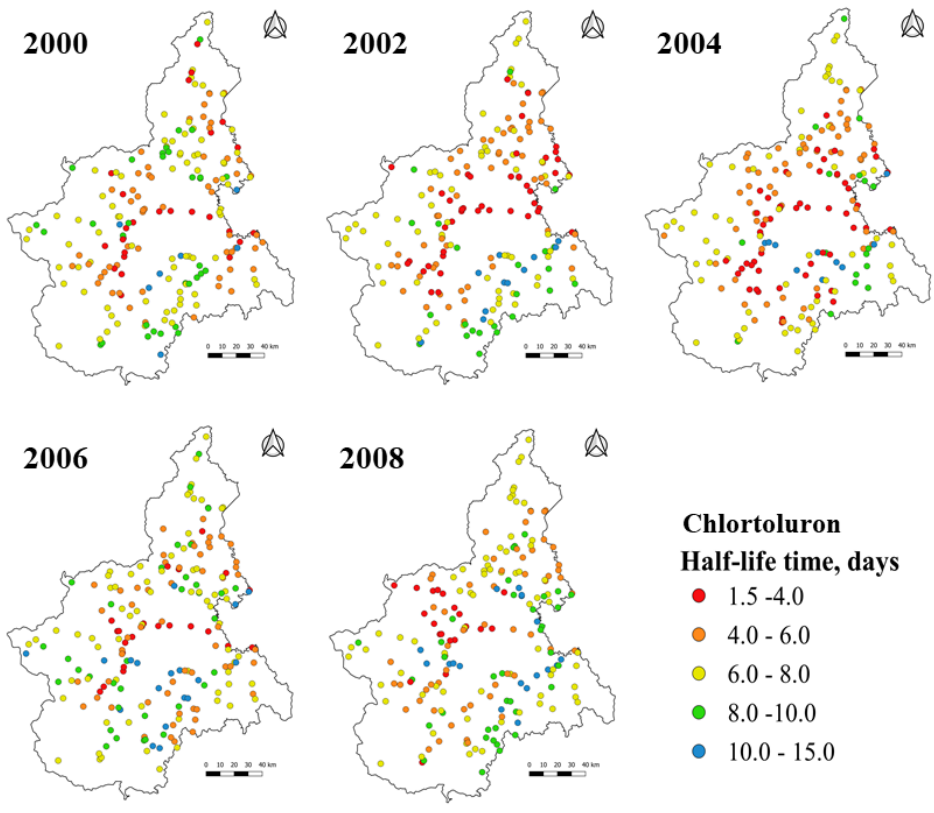

Fig.4.3.17. Photochemical maps of Piedmont over the years 2000-2008, showing the half-life times of CTL (annual mean values) in the different sampling points. Adapted from Carena et al. (2021).

Another interesting issue is that the photodegradation of all the pesticides, including BTZ, was peculiarly fast in a limited part of the region during the year 2008 (area highlighted with the smaller circle in Figs.4.3.13 and 4.3.14). The phenomenon is particularly evident for IPT, ATZ, BTZ and CTL, but a bit less for DMM. The relevant area is characterized by quite low DOC values (around 0.5-1.0 $mg_C\ L^{-1}$, see Fig.4.A4), which allows for excluding significant contributions by ^{3}CDOM* or $^1O_2$ in the enhanced phototransformation of the pesticides. In contrast, photoreactions triggered by $HO^\bullet$ and $CO_3^{\bullet-}$ as well as

the direct photolysis are favored in DOM-poor waters (Vione et al., 2014). Although [HO•] was slightly higher in that area compared to the regional average, fast BTZ photodegradation suggests that water conditions were mostly favorable to the direct photolysis process. Moreover, photolysis is a secondary pathway for DMM, which could explain why the trend was less marked for this compound. A likely explanation for these findings is connected to the peculiarly low values of the DOC (and of CDOM as a consequence, see Fig.4.A4) in the area of interest in 2008, which would enhance the direct photolysis processes.

Because the investigated water bodies are rivers, the pesticides lifetimes have to be put in the context of flowing water. This means that the half-life time ($t_{1/2}$) represents also a sunlit stretch of the river course where the concentration of the pollutant is halved. The length of this stretch is defined as the half-life length ($l_{1/2}$), and the relevant relationship with $t_{1/2}$ takes into account the average water flow velocity, $\bar{v}$, as $l_{1/2} = \bar{v} \times t_{1/2}$. Fig.4.3.18 shows the dependence of the half-life length on $t_{1/2}$, for different values of $\bar{v}$. $\bar{v}$ = 1 m s^{-1} is often found under normal hydrological conditions (Schulze et al., 2005), while it can increase or decrease during floods or droughts, respectively. In the case of the Po river, $\bar{v}$ ~2 m s^{-1} during floods, while $\bar{v}$ ~0.4-0.6 m s^{-1} under drought conditions (AIPo, 2020).

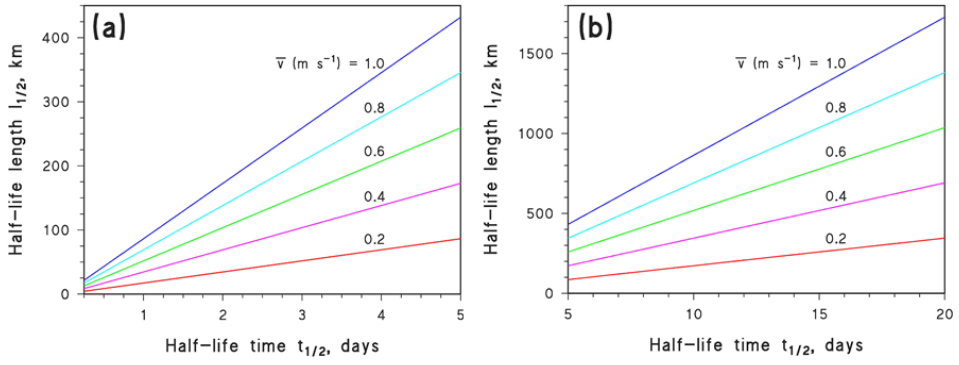

Fig.4.3.18. Trends of the half-life lengths $l_{1/2}$ of a generic pollutant in a river course, as a function of the (average) half-life time $t_{1/2}$, for different values of the mean water flow velocity $\bar{v}$. The $t_{1/2}$ range found for the different pesticides (0.5-20 days) is here split into two parts for ease of readability, namely 0.25-5 days (**a**) and 5-20 days (**b**). Adapted from Carena et al. (2021).

Given the $l_{1/2}$ values and the typical lengths of rivers and streams within the regional borders of Piedmont, effective pesticide photodegradation is highly likely if $t_{1/2}$ < 2 days, almost irrespective of the flow conditions if $\bar{v}$ < 1 m s^{-1} (floods could be an exception, because $\bar{v}$ > 1 m s^{-1}; AIPo, 2020). Under drought conditions, photodegradation is significant if $t_{1/2}$ < 5 days, while it would be minor to negligible if $t_{1/2}$ > 5 days unless strong water scarcity is operational. However, it must be pointed out that all watercourses in Piedmont end up in the Po river, where photoactivity is higher than average. Therefore, in several cases photodegradation could be slow in the initial tract but would then accelerate once the main river is reached. Therefore, the nitrate-rich Po waters would play a key role in collecting water-carried pesticides and in ensuring their effective photoinduced degradation, in particular during droughts. Fig.4.3.19 shows the decontamination potential of the Piedmontese rivers over the years 2000-2008: the higher is the red bar height, the greater is the decontamination potential of the Piedmont watershed.

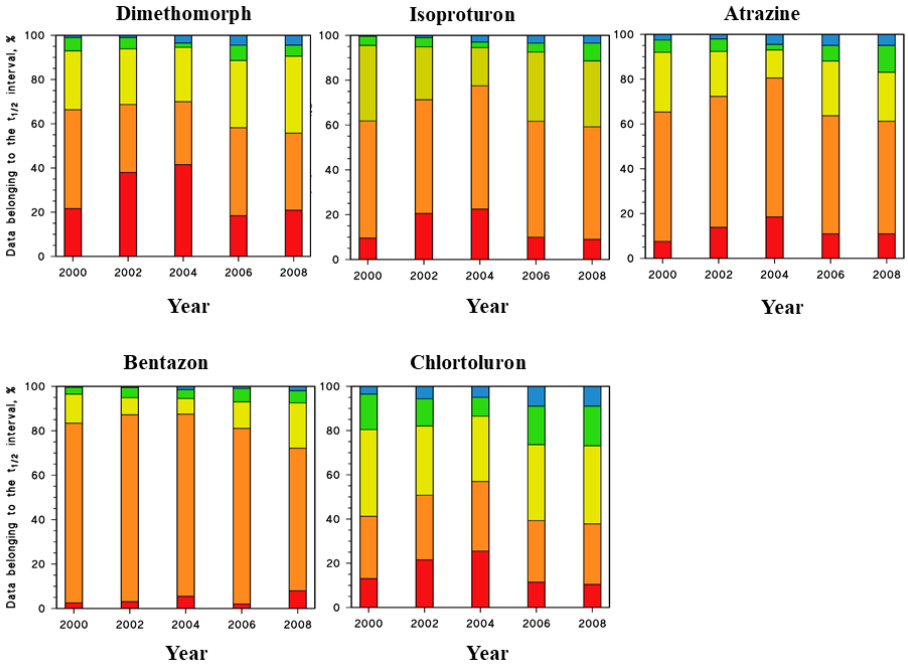

Fig.4.3.19. Trends of the photochemical decontamination potential of Piedmontese rivers from the investigated pesticides. The colors refer to the legends of the maps showed in the above figures above. Adapted from Carena et al. (2021).

However, photochemical degradation processes of water pollutants may produce harmful intermediates. Given the features of the regional waters and of the studied pesticides, the $HO^{\bullet}$ reactions are particularly relevant with the single exception of BTZ. Although fast BTZ photodegradation by direct photolysis would produce effective decontamination (Carena et al., 2020), phenylurea herbicides such as IPT and CTL are known to produce toxic N-formyl compounds upon reaction with $HO^{\bullet}$ (Galichet et al., 2002; Halladja et al., 2007; Poulain et al., 2003; Shankar et al., 2008). Moreover, the reaction of ATZ + $HO^{\bullet}$ produces desethyl atrazine with high yield, and the two compounds have comparable environmental effects (Marchetti et al., 2013). Therefore, in several cases a complete decontamination by photochemical processes would require longer time than the mere disappearance of the parent

compound. From this point of view, BTZ appears to be the safest pesticide among those under study.

4.4 Conclusions

The main findings of this work show that:

- Hydrological drought favors the photochemistry of ^{3}CDOM* when evaporation plays an important role in water loss from a shallow lake, such as the Lower Lakes in Southern Australia.
- Water pollutants that are highly reactive with ^{3}CDOM* are thus more photodegraded in this scenario. In contrast, pollutants that are reactive towards $HO^{\bullet}$ and/or $CO_3^{\bullet-}$ radicals would not be much affected by drought, because evaporation keeps both [$HO^{\bullet}$] and [$CO_3^{\bullet-}$] about constant.
- Nitrate contamination of groundwaters by human activities can highly affect the photochemistry of rivers, triggering photoreactions by $HO^{\bullet}$ as well as $CO_3^{\bullet-}$ radicals in alkaline waters.
- Additionally, under nitrate-pollution pressure, the production of $HO^{\bullet}$ is even more favored during drought if the river loses water by reduced outflow.
- The decontamination potential of watercourses from contaminants highly depends on water chemistry. However, drought conditions increase the decontamination potential of rivers, because pollutants photodegradation can occur in a shorter river stretch than during floods.

- Drought events are projected to become more frequent, longer, and possibly more intense in the future because of anthropogenic climate change in several regions of the world, such as the Mediterranean and Southern Australia (Ault, 2020; Marvel et al., 2019; Ukkola et al., 2020). The consequences on photochemistry of surface waters in Southern Europe and Southern Australia will likely depend on two main parameters, namely how water is lost and how anthropogenic activities affect the chemistry of water bodies.

Appendix II

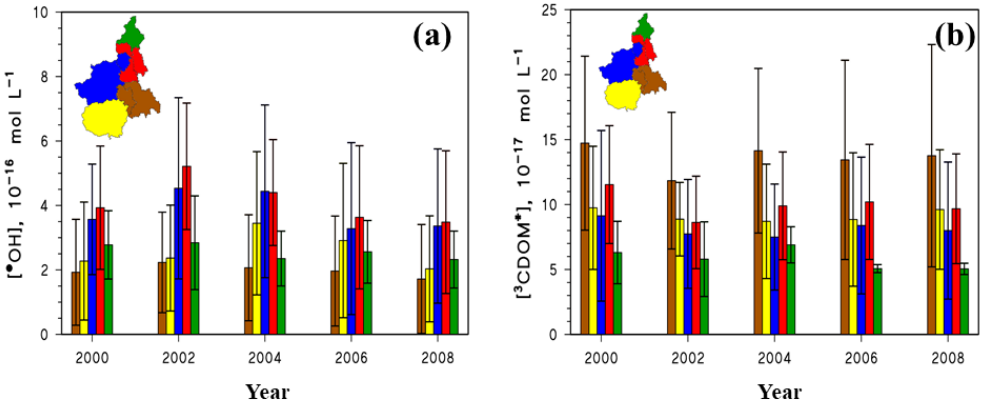

Fig.4.A1. Steady-state concentration values of (a) HO• radicals and (b) ^{3}CDOM* in different areas of Piedmont. The region subdivision reflects the administrative borders of the regional provinces. Bar color refers to the area color.

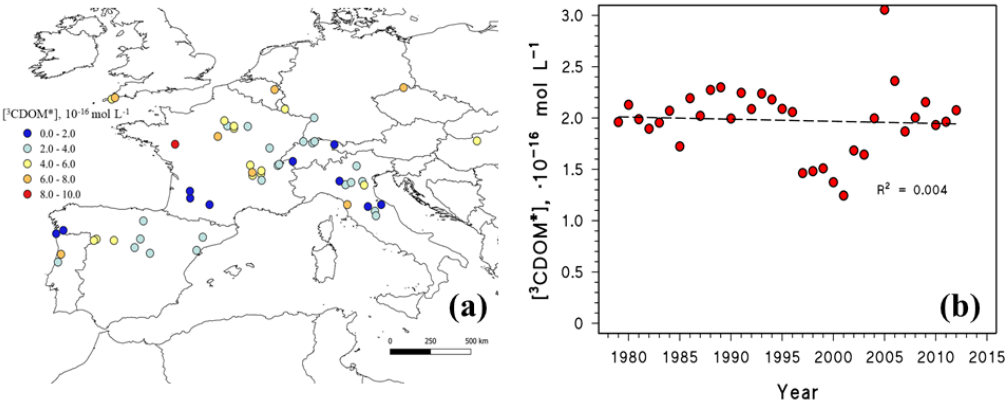

Fig.4.A2. (a) Map showing the steady-state concentration values of ^{3}CDOM* in Southern Europe over the years 1990-1995. In this case the water optical path was 0.1 m. Adapted from Carena and Vione (2020). **(b)** Temporal profile of [^{3}CDOM*] in Southern Europe over the years 1978-2012, for a water optical path = 0.5 m. The values are reported as annual averages. Water chemical composition data for the photochemical model were taken from the GEMStat database (United Nations Environment Programme, 2019).

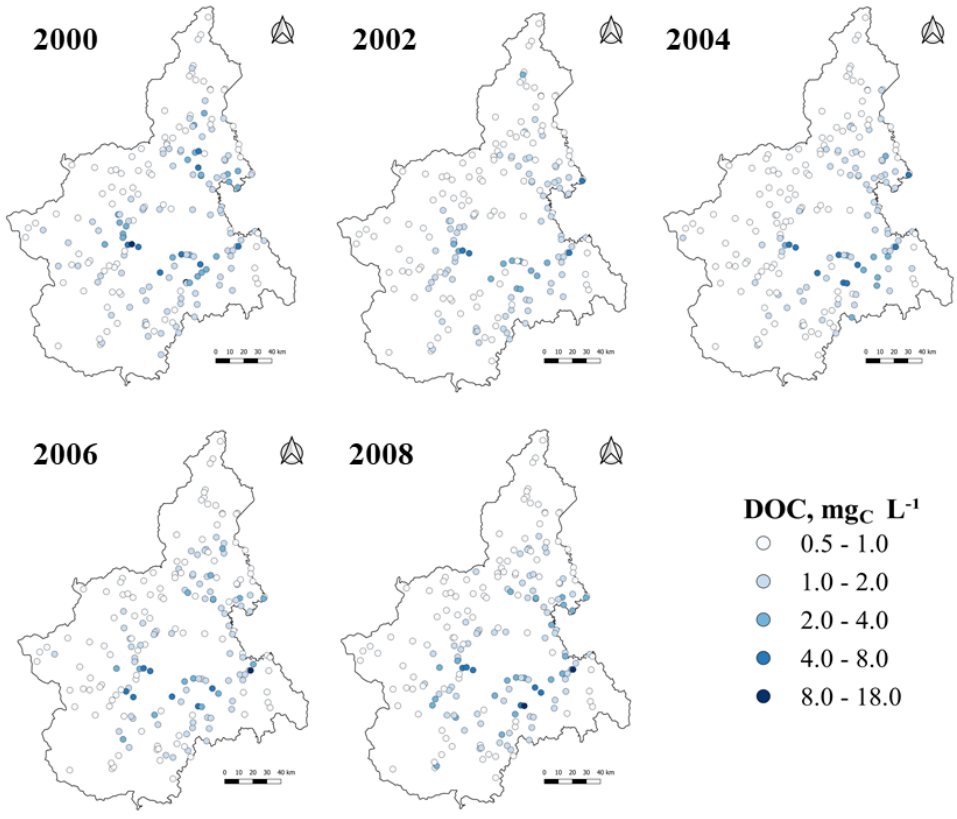

Fig.4.A3 DOC maps of Piedmont over the years 2000-2008. Adapted from Carena et al. (2021).

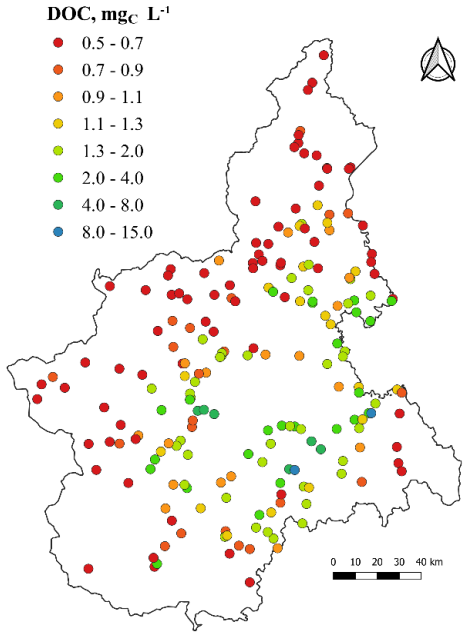

Fig.4.A4 DOC map of Piedmont for the year 2008. Adapted from Carena et al. (2021).

Chapter 5

Conclusions

In this work, the photoreactivity of ^{3}CDOM* with water pollutants was (re)determined by using the triplet state of benzophenone-4-carboxylate (^{3}CBBP*) as proxy for ^{3}CDOM*. The choice for this aromatic ketone molecule was made on the basis of the observed spectral and energetic properties of CDOM/^{3}CDOM* (McNeill and Canonica, 2016; Sharpless and Blough, 2014).

The application of a new protocol based on steady-state irradiation experiments allowed us to determine representative values for the second-order rate constants of the reactions of ^{3}CDOM* with ibuprofen, acetaminophen, clofibric acid and atrazine ($k_{(^3CDOM+S)}$, with S = contaminant). The results were in good agreement with the values of the same constants as measured by means of time-resolved techniques (i.e., the laser flash photolysis), showing that the protocol is suitable for the quantitative assessment of ^{3}CDOM* reactivity with water pollutants. Furthermore, our findings strongly suggest that ^{3}CBBP* is a more suitable surrogate of ^{3}CDOM* than the triplet state of anthraquinone-2-sulfonate (^{3}AQ2S*), which has been adopted in previous works as ^{3}CDOM* proxy (e.g., Avetta et al., 2016; De Laurentiis et al., 2014; Marchetti et al., 2013; Vione et al., 2011). Indeed, ^{3}AQ2S often overestimates the photoreactivity of ^{3}CDOM* with water pollutants, as significantly shown in the case of naproxen (Avetta et al., 2016), ibuprofen and acetaminophen (this work). It is also interesting to observe that, differently from ^{3}AQ2S*, the ^{3}CBBP*-based second-order rate

constants measured here were < 5×10^9 L mol^{-1} s^{-1}, which is the generally accepted upper limit for $k_{(^3CDOM+S)}$ (Canonica et al., 2000).

By means of photochemical modeling, the half-life times of the investigated contaminants were computed for surface waters, by comparing the ^{3}CBBP* photoreactivity with that of ^{3}AQ2S*. Overall, even with the ^{3}CBBP*-based data, ^{3}CDOM* would still play an important role in the photodegradation of pollutants in both scenarios, in particular in CDOM-rich, deep waters. However, ^{3}CBBP*-based lifetimes were higher than those predicted by considering the ^{3}AQ2S* rate constants, with the partial exceptions of atrazine and clofibric acid.

The photoreactions of (chloro)anilines and clofibric acid with ^{3}CBBP* were inhibited in the presence of phenol, here used as proxy for antioxidant DOM. The inhibition effect was most likely to operate through back-reduction of the partially oxidized pollutants to the parent compounds (Canonica and Laubscher, 2008; Wenk and Canonica, 2012). This process was also found in this work to be operational in the case of the $CO_3^{\bullet-}$-induced photodegradation of (chloro)anilines. The quantification of the back-reduction extent by means of the $[PhOH]_{1/2}$ parameter (Wenk and Canonica, 2012) allowed us to conclude that the inhibition process does not depend much on the PPRI that oxidizes the contaminant (^{3}CDOM* or $CO_3^{\bullet-}$), but rather on the one-electron reduction potential of the partially oxidized compound (in this case, $E^o_{ArNH^\bullet/ArNH_2}$). The ^{3}CDOM*- and $CO_3^{\bullet-}$-based results are well described by the Marcus' electron-transfer theory (and the related Rehm-Weller extension), suggesting that in both cases the back-reduction should take place through (proton-coupled) electron transfer from phenol to the partially oxidized pollutant.

Therefore, as a general statement, it can be said that when a compound produces a radical intermediate via one-electron oxidation by ^{3}CDOM* or $CO_3^{\bullet-}$, the radical intermediate can be back-reduced to the parent molecule in the presence of phenols or their equivalents contained in antioxidant DOM moieties. In such a case, the higher is the one-electron reduction potential difference between the radical intermediate and the antioxidant DOM, the stronger is the inhibition of photodegradation. To the best of our knowledge, this is the first general statement of the phenol-induced back-reduction effect, based on both experiments and Marcus electron-transfer Theory.

Finally, as far as the possible effects of climate change and anthropogenic activities on surface-water photochemistry are concerned, the case studies of the Australian Lower Lakes and NW-Italian rivers showed that, respectively, *(i)* ^{3}CDOM* production would be favored by drought events if water is lost from the lake catchment by evaporation, while *(ii)* enhanced photoproduction of $HO^\bullet$ and $CO_3^{\bullet-}$ radicals in rivers can occur under nitrate contamination of groundwaters. Furthermore, in the latter scenario, the production of $HO^\bullet$ is even more favored during drought if the river loses water by outflow. These results are in agreement with modeling predictions reported in previous work (Minella et al., 2013).

Because drought events are projected to become more frequent, longer, and possibly more intense in the future in both the Mediterranean region and Southern Australia (Ault, 2020; Marvel et al., 2019; Ukkola et al., 2020), the climatic consequences on the photochemistry of surface waters will likely depend on two main parameters: *(i)* how water is lost and *(ii)* how anthropogenic activities affect the chemistry of the water bodies. During drought conditions, the decontamination potential of rivers can increase because water flows more slowly. Therefore, at equal photoreaction time scales, the photodegradation of pollutants will occur in a much shorter river

stretch during droughts than during floods. However, the formation of harmful transformation products can be enhanced as well during drought events and, depending on the pollutant(s) and on the environmental conditions, it can pose environmental concerns.

References

Achleitner, S., DE Toffol, S., Engelhard, C., Rauch, W., 2005. The European Water Framework Directive: Water Quality Classification and Implications to Engineering Planning. Environ. Manage. 35, 517–525. https://doi.org/10.1007/s00267-004-0066-1

AIPo, 2020. Agenzia Interregionale per il fiume Po [WWW Document].

Al-Nu'Airat, J., Altarawneh, M., Gao, X., Westmoreland, P.R., Dlugogorski, B.Z., 2017. Reaction of Aniline with Singlet Oxygen (O21Δg). J. Phys. Chem. A 121, 3199–3206. https://doi.org/10.1021/acs.jpca.7b00765

Allen, J.M., Allen, S.K., Baertschi, S.W., 2000. 2-Nitrobenzaldehyde: a convenient UV-A and UV-B chemical actinometer for drug photostability testing. J. Pharm. Biomed. Anal. 24, 167–178. https://doi.org/https://doi.org/10.1016/S0731-7085(00)00423-4

APHA, 2005. Standard Methods for the Examination ofWater andWastewater, 21st ed. American Public Health Association, American Water Works Association and Water Environment Federation, Washington, DC.

Appiani, E., McNeill, K., 2015. Photochemical Production of Singlet Oxygen from Particulate Organic Matter. Environ. Sci. Technol. 49, 3514–3522. https://doi.org/10.1021/es505712e

Arnold, W.A., 2014. One electron oxidation potential as a predictor of rate constants of N-containing compounds with carbonate radical and triplet excited state organic matter. Environ. Sci. Process. Impacts 16, 832–838. https://doi.org/10.1039/c3em00479a

Arnold, W.A., Oueis, Y., O'Connor, M., Rinaman, J.E., Taggart, M.G., McCarthy, R.E., Foster, K.A., Latch, D.E., 2017. QSARs for phenols and phenolates: oxidation potential as a predictor of reaction rate constants with photochemically produced oxidants. Environ. Sci. Process. Impacts 19, 324–338. https://doi.org/10.1039/c6em00580b

ARPA, 2020. ARPA (Agenzia Regionale per la Protezione Ambientale del

Piemonte) [WWW Document]. URL http://www.arpa.piemonte.it/approfondimenti/temi-ambientali/acqua/acque-superficiali-corsi-dacqua/documentazione-e-dati

Ault, T.R., 2020. On the essentials of drought in a changing climate. Science (80-.). 368, 256 LP – 260. https://doi.org/10.1126/science.aaz5492

Avetta, P., Fabbri, D., Minella, M., Brigante, M., Maurino, V., Minero, C., Pazzi, M., Vione, D., 2016. Assessing the phototransformation of diclofenac , clofibric acid and naproxen in surface waters: Model predictions and comparison with fi eld data. Water Res. 105, 383–394. https://doi.org/10.1016/j.watres.2016.08.058

Avetta, P., Marchetti, G., Minella, M., Pazzi, M., De Laurentiis, E., Maurino, V., Minero, C., Vione, D., 2014. Phototransformation pathways of the fungicide dimethomorph ((E,Z) 4-[3-(4-chlorophenyl)-3-(3,4-dimethoxyphenyl)-1-oxo-2-propenyl]morpholine), relevant to sunlit surface waters. Sci. Total Environ. 500–501, 351–360. https://doi.org/https://doi.org/10.1016/j.scitotenv.2014.08.067

Bader, J., Latif, M., 2005. North Atlantic Oscillation Response to Anomalous Indian Ocean SST in a Coupled GCM. J. Clim. 18, 5382–5389. https://doi.org/10.1175/JCLI3577.1

Bader, J., Mesquita, M.D.S., Hodges, K.I., Keenlyside, N., Østerhus, S., Miles, M., 2011. A review on Northern Hemisphere sea-ice, storminess and the North Atlantic Oscillation: Observations and projected changes. Atmos. Res. 101, 809–834. https://doi.org/https://doi.org/10.1016/j.atmosres.2011.04.007

Baena-Nogueras, R.M., González-Mazo, E., Lara-Martín, P.A., 2017. Degradation kinetics of pharmaceuticals and personal care products in surface waters: photolysis vs biodegradation. Sci. Total Environ. 590–591, 643–654. https://doi.org/https://doi.org/10.1016/j.scitotenv.2017.03.015

Balestrini, R., Delconte, C.A., Sacchi, E., Buffagni, A., 2021. Groundwater-dependent ecosystems as transfer vectors of nitrogen from the aquifer to surface waters in agricultural basins: The fontanili of the Po Plain (Italy). Sci.

Total Environ. 753, 141995. https://doi.org/https://doi.org/10.1016/j.scitotenv.2020.141995

Bassanino, M., Sacco, D., Zavattaro, L., Grignani, C., 2011. Nutrient balance as a sustainability indicator of different agro-environments in Italy. Ecol. Indic. 11, 715–723. https://doi.org/10.1016/j.ecolind.2010.05.005

Bedini, A., De Laurentiis, E., Sur, B., Maurino, V., Minero, C., Brigante, M., Mailhot, G., Vione, D., 2012. Phototransformation of anthraquinone-2-sulphonate in aqueous solution. Photochem. Photobiol. Sci. 11, 1445–1453. https://doi.org/10.1039/C2PP25111F

Berg, S.M., Whiting, Q.T., Herrli, J.A., Winkels, R., Wammer, K.H., Remucal, C.K., 2019. The Role of Dissolved Organic Matter Composition in Determining Photochemical Reactivity at the Molecular Level. Environ. Sci. Technol. 53, 11725–11734. https://doi.org/10.1021/acs.est.9b03007

Berto, S., De Laurentiis, E., Scapuzzi, C., Chiavazza, E., Corazzari, I., Turci, F., Minella, M., Buscaino, R., Daniele, P.G., Vione, D., 2018. Phototransformation of l-tryptophan and formation of humic substances in water. Environ. Chem. Lett. 16, 1035–1041. https://doi.org/10.1007/s10311-018-0714-y

Berto, S., De Laurentiis, E., Tota, T., Chiavazza, E., Daniele, P.G., Minella, M., Isaia, M., Brigante, M., Vione, D., 2016. Properties of the humic-like material arising from the photo-transformation of l-tyrosine. Sci. Total Environ. 545–546, 434–444. https://doi.org/https://doi.org/10.1016/j.scitotenv.2015.12.047

Bethsass, J., Colangelo, A., 2006. European Union Bans Atrazine, While the United States Negotiates Continued Use. Int. J. Occup. Environ. Health 12, 260–267. https://doi.org/10.1179/oeh.2006.12.3.260

Bianca, M.R., Baluha, D.R., Gonsior, M., Schmitt-Kopplin, P., Del Vecchio, R., Blough, N. V, 2020. Contribution of ketone/aldehyde-containing compounds to the composition and optical properties of Suwannee River fulvic acid revealed by ultrahigh resolution mass spectrometry and deuterium labeling. Anal. Bioanal. Chem. 412, 1441–1451. https://doi.org/10.1007/s00216-019-

02377-x

Bianco, A., Minella, M., De Laurentiis, E., Maurino, V., Minero, C., Vione, D., 2014. Photochemical generation of photoactive compounds with fulvic-like and humic-like fluorescence in aqueous solution. Chemosphere 111, 529–536. https://doi.org/https://doi.org/10.1016/j.chemosphere.2014.04.035

Biswas, T.K., Mosley, L.M., 2019. From Mountain Ranges to Sweeping Plains, in Droughts and Flooding Rains; River Murray Water Quality over the Last Four Decades. Water Resour. Manag. 33, 1087–1101. https://doi.org/10.1007/s11269-018-2168-1

Bodrato, M., Vione, D., 2014. APEX (Aqueous Photochemistry of Environmentally occurring Xenobiotics): a free software tool to predict the kinetics of photochemical processes. Environ. Sci. Process. Impacts 16, 732–740. https://doi.org/10.1039/c3em00541k

Bonin, J., Costentin, C., Robert, M., Routier, M., Savéant, J.-M., 2013. Proton-Coupled Electron Transfers: pH-Dependent Driving Forces? Fundamentals and Artifacts. J. Am. Chem. Soc. 135, 14359–14366. https://doi.org/10.1021/ja406712c

Bonvin, F., Omlin, J., Rutler, R., Schweizer, W.B., Alaimo, P.J., Strathmann, T.J., McNeill, K., Kohn, T., 2013. Direct Photolysis of Human Metabolites of the Antibiotic Sulfamethoxazole: Evidence for Abiotic Back-Transformation. Environ. Sci. Technol. 47, 6746–6755. https://doi.org/10.1021/es303777k

Brandimarte, L., Di Baldassarre, G., Bruni, G., D'Odorico, P., Montanari, A., 2011. Relation Between the North-Atlantic Oscillation and Hydroclimatic Conditions in Mediterranean Areas. Water Resour. Manag. 25, 1269–1279. https://doi.org/10.1007/s11269-010-9742-5

Braslavsky, S.E., 2007. Glossary of terms used in photochemistry 3rd edition. Pure Appl. Chem. 79, 293–465. https://doi.org/10.1351/pac200779030293

Brezonik, P.L., Fulkerson-Brekken, J., 1998. Nitrate-Induced Photolysis in Natural Waters: Controls on Concentrations of Hydroxyl Radical Photo-Intermediates by Natural Scavenging Agents. Environ. Sci. Technol. 32, 3004–3010.

https://doi.org/10.1021/es9802908

Brigante, M., Minella, M., Mailhot, G., Maurino, V., Minero, C., Vione, D., 2014. Formation and reactivity of the dichloride radical (Cl2-) in surface waters: A modelling approach. Chemosphere 95, 464–469. https://doi.org/https://doi.org/10.1016/j.chemosphere.2013.09.098

Buth, J.M., Steen, P.O., Sueper, C., Blumentritt, D., Vikesland, P.J., Arnold, W.A., McNeill, K., 2010. Dioxin Photoproducts of Triclosan and Its Chlorinated Derivatives in Sediment Cores. Environ. Sci. Technol. 44, 4545–4551. https://doi.org/10.1021/es1001105

Buxton, G. V, Greenstock, C.L., Helman, P.W., Ross, A.B., 1988. Critical Review of rate constants for reactions of hydrated electrons, hydrogen atoms and hydroxyl radicals (·OH/·O−) in Aqueous Solution. J. Phys. Chem. Ref. Data 17, 513–886. https://doi.org/https://doi.org/10.1063/1.555805

Calderaro, F., Vione, D., 2020. Possible Effect of Climate Change on Surface-Water Photochemistry: A Model Assessment of the Impact of Browning on the Photodegradation of Pollutants in Lakes during Summer Stratification. Epilimnion vs. Whole-Lake Phototransformation. Molecules 25, 2795. https://doi.org/https://doi.org/10.3390/molecules25122795

Canonica, S., 2007. Oxidation of Aquatic Organic Contaminants Induced by Excited Triplet States. Chimia (Aarau). 61, 641–644. https://doi.org/10.2533/chimia.2007.641 Chimia

Canonica, S., Hellrung, B., Wirz, J., 2000. Oxidation of Phenols by Triplet Aromatic Ketones in Aqueous Solution. J. Phys. Chem. A 104, 1226–1232. https://doi.org/10.1021/jp9930550

Canonica, S., Kohn, T., Mac, M., Real, F.J., Wirz, J., Von Gunten, U., 2005. Photosensitizer method to determine rate constants for the reaction of carbonate radical with organic compounds. Environ. Sci. Technol. 39, 9182–9188. https://doi.org/10.1021/es051236b

Canonica, S., Laubscher, H.U., 2008. Inhibitory effect of dissolved organic matter on triplet-induced oxidation of aquatic contaminants. Photochem. Photobiol.

Sci. 7, 547–551. https://doi.org/10.1039/b719982a

Canonica, S., Schönenberger, U., 2019. Inhibitory Effect of Dissolved Organic Matter on the Transformation of Selected Anilines and Sulfonamide Antibiotics Induced by the Sulfate Radical. Environ. Sci. Technol. 53, 11783–11791. https://doi.org/10.1021/acs.est.9b04105

Carena, L., Comis, S., Vione, D., 2021. Geographical and temporal assessment of the photochemical decontamination potential of river waters from agrochemicals: A first application to the Piedmont region (NW Italy). Chemosphere 263, 127921. https://doi.org/https://doi.org/10.1016/j.chemosphere.2020.127921

Carena, L., Fabbri, D., Passananti, M., Minella, M., Pazzi, M., Vione, D., 2020. The role of direct photolysis in the photodegradation of the herbicide bentazone in natural surface waters. Chemosphere 246, 125705. https://doi.org/https://doi.org/10.1016/j.chemosphere.2019.125705

Carena, L., Minella, M., Barsotti, F., Brigante, M., Milan, M., Ferrero, A., Berto, S., Minero, C., Vione, D., 2017. Phototransformation of the Herbicide Propanil in Paddy Field Water. Environ. Sci. Technol. 51, 2695 – 2704. https://doi.org/10.1021/acs.est.6b05053

Carena, L., Proto, M., Minella, M., Ghigo, G., Giovannoli, C., Brigante, M., Mailhot, G., Maurino, V., Minero, C., Vione, D., 2018. Evidence of an Important Role of Photochemistry in the Attenuation of the Secondary Contaminant 3,4-Dichloroaniline in Paddy Water. Environ. Sci. Technol. 52, 6334–6342. https://doi.org/10.1021/acs.est.8b00710

Carena, L., Puscasu, C.G., Comis, S., Sarakha, M., Vione, D., 2019a. Environmental photodegradation of emerging contaminants: A re-examination of the importance of triplet-sensitised processes, based on the use of 4-carboxybenzophenone as proxy for the chromophoric dissolved organic matter. Chemosphere 237, 124476. https://doi.org/10.1016/j.chemosphere.2019.124476

Carena, L., Terrenzio, D., Mosley, L.M., Toldo, M., Minella, M., Vione, D., 2019b.

Photochemical consequences of prolonged hydrological drought: A model assessment of the Lower Lakes of the Murray-Darling Basin (Southern Australia). Chemosphere 236, 124356. https://doi.org/10.1016/j.chemosphere.2019.124356

Carena, L., Vione, D., 2020. Mapping the Photochemistry of European Mid-Latitudes Rivers: An Assessment of Their Ability to Photodegrade Contaminants. Molecules 25, 424. https://doi.org/10.3390/molecules25020424

Carena, L., Vione, D., 2016. Photochemical reaction of peroxynitrite and carbon dioxide could account for up to 15 % of carbonate radicals generation in surface waters. Environ. Chem. Lett. 14. https://doi.org/10.1007/s10311-016-0549-3

Caruso, B.S., 2002. Temporal and spatial patterns of extreme low flows and effects on stream ecosystems in Otago, New Zealand. J. Hydrol. 257, 115–133. https://doi.org/https://doi.org/10.1016/S0022-1694(01)00546-7

Caruso, B.S., 2001. Regional river flow, water quality, aquatic ecological impacts and recovery from drought. Hydrol. Sci. J. 46, 677–699. https://doi.org/10.1080/02626660109492864

Cawley, K.M., Korak, J.A., Rosario-Ortiz, F.L., 2014. Quantum Yields for the Formation of Reactive Intermediates from Dissolved Organic Matter Samples from the Suwannee River. Environ. Eng. Sci. 32, 31–37. https://doi.org/10.1089/ees.2014.0280

Chen, Y., Hozalski, R.M., Olmanson, L.G., Page, B.P., Finlay, J.C., Brezonik, P.L., Arnold, W.A., 2020. Prediction of Photochemically Produced Reactive Intermediates in Surface Waters via Satellite Remote Sensing. Environ. Sci. Technol. 54, 6671–6681. https://doi.org/10.1021/acs.est.0c00344

Chen, Z.-X., Yu, L., Liu, W.-G., Lam, M.H.W., Liu, G.-J., Yin, X.-B., 2014. Nitrogen and oxygen isotopic compositions of water-soluble nitrate in Taihu Lake water system, China: implication for nitrate sources and biogeochemical process. Environ. Earth Sci. 71, 217–223. https://doi.org/10.1007/s12665-013-2425-9

Chu, C., Stamatelatos, D., McNeill, K., 2017. Aquatic indirect photochemical transformations of natural peptidic thiols: impact of thiol properties, solution pH, solution salinity and metal ions. Environ. Sci. Process. Impacts 19, 1518–1527. https://doi.org/10.1039/C7EM00324B

Clark, J.B., Neale, P., Tzortziou, M., Cao, F., Hood, R.R., 2019. A mechanistic model of photochemical transformation and degradation of colored dissolved organic matter. Mar. Chem. 214, 103666. https://doi.org/https://doi.org/10.1016/j.marchem.2019.103666

Clark, J.M., Lane, S.N., Chapman, P.J., Adamson, J.K., 2007. Export of dissolved organic carbon from an upland peatland during storm events: Implications for flux estimates. J. Hydrol. 347, 438–447. https://doi.org/https://doi.org/10.1016/j.jhydrol.2007.09.030

Clayden, J., Greeves, N., Warren, S., 2012. Organic Chemistry, Second. ed. Oxford University Press.

Corona, R., Montaldo, N., Albertson, J.D., 2018. On the Role of NAO-Driven Interannual Variability in Rainfall Seasonality on Water Resources and Hydrologic Design in a Typical Mediterranean Basin. J. Hydrometeorol. 19, 485–498. https://doi.org/10.1175/JHM-D-17-0078.1

Costentin, C., Robert, M., Savéant, J.M., 2010. Concerted proton-electron transfers in the oxidation of phenols. Phys. Chem. Chem. Phys. 12, 11179–11190. https://doi.org/10.1039/c0cp00063a

Couture, R.-M., de Wit, H.A., Tominaga, K., Kiuru, P., Markelov, I., 2015. Oxygen dynamics in a boreal lake responds to long-term changes in climate, ice phenology, and DOC inputs. J. Geophys. Res. Biogeosciences 120, 2441–2456. https://doi.org/10.1002/2015JG003065

Cozzi, S., Giani, M., 2011. River water and nutrient discharges in the Northern Adriatic Sea: Current importance and long term changes. Cont. Shelf Res. 31, 1881–1893. https://doi.org/https://doi.org/10.1016/j.csr.2011.08.010

Cozzi, S., Ibáñez, C., Lazar, L., Raimbault, P., Giani, M., 2019. Flow regime and nutrient-loading trends from the largest South European watersheds:

Implications for the productivity of mediterranean and Black Sea's Coastal Areas. Water 11. https://doi.org/10.3390/w11010001

Davis, C.A., McNeill, K., Janssen, E.M.L., 2018. Non-Singlet Oxygen Kinetic Solvent Isotope Effects in Aquatic Photochemistry. Environ. Sci. Technol. 52, 9908–9916. https://doi.org/10.1021/acs.est.8b01512

De Laurentiis, E., Buoso, S., Maurino, V., Minero, C., Vione, D., 2013a. Optical and Photochemical Characterization of Chromophoric Dissolved Organic Matter from Lakes in Terra Nova Bay, Antarctica. Evidence of Considerable Photoreactivity in an Extreme Environment. Environ. Sci. Technol. 47, 14089–14098. https://doi.org/10.1021/es403364z

De Laurentiis, E., Chiron, S., Kouras-Hadef, S., Richard, C., Minella, M., Maurino, V., Minero, C., Vione, D., 2012a. Photochemical Fate of Carbamazepine in Surface Freshwaters: Laboratory Measures and Modeling. Environ. Sci. Technol. 46, 8164−8173. https://doi.org/10.1021/es3015887

De Laurentiis, E., Minella, M., Bodrato, M., Maurino, V., Minero, C., Vione, D., 2013b. Modelling the photochemical generation kinetics of 2-methyl-4-chlorophenol, an intermediate of the herbicide MCPA (2-methyl-4-chlorophenoxyacetic acid) in surface waters. Aquat. Ecosyst. Health Manag. 16, 216–221. https://doi.org/10.1080/14634988.2013.788433

De Laurentiis, E., Minella, M., Maurino, V., Minero, C., Brigante, M., Mailhot, G., Vione, D., 2012b. Photochemical production of organic matter triplet states in water samples from mountain lakes, located below or above the tree line. Chemosphere 88, 1208–1213. https://doi.org/https://doi.org/10.1016/j.chemosphere.2012.03.071

De Laurentiis, E., Minella, M., Maurino, V., Minero, C., Vione, D., 2014a. Effects of climate change on surface-water photochemistry: a review. Environ. Sci. Pollut. Res. 21, 11770–11780. https://doi.org/10.1007/s11356-013-2343-0

De Laurentiis, E., Minella, M., Sarakha, M., Marrese, A., Minero, C., Mailhot, G., Brigante, M., Vione, D., 2013c. Photochemical processes involving the UV methoxybenzophenone-5-sulphonic acid) in aqueous solution: Reaction

pathways and implications for surface waters. Water Res. 47, 5943–5953. https://doi.org/10.1016/j.watres.2013.07.017

De Laurentiis, E., Prasse, C., Ternes, T.A., Minella, M., Maurino, V., Minero, C., Sarakha, M., Brigante, M., Vione, D., 2014b. Assessing the photochemical transformation pathways of acetaminophen relevant to surface waters: Transformation kinetics, intermediates, and modelling. Water Res. 53, 235–248. https://doi.org/10.1016/j.watres.2014.01.016

Debernardi, L., De Luca, D.A., Lasagna, M., 2008. Correlation between nitrate concentration in groundwater and parameters affecting aquifer intrinsic vulnerability. Enviornmental Geol. 55, 539–558. https://doi.org/10.1007/s00254-007-1006-1

Del Vecchio, R., Schendorf, T.M., Blough, N. V, 2017. Contribution of Quinones and Ketones/Aldehydes to the Optical Properties of Humic Substances (HS) and Chromophoric Dissolved Organic Matter (CDOM). Environ. Sci. Technol. 51, 13624–13632. https://doi.org/10.1021/acs.est.7b04172

Dell'Arciprete, M.L., Soler, J.M., Santos-Juanes, L., Arques, A., Mártire, D.O., Furlong, J.P., Gonzalez, M.C., 2012. Reactivity of neonicotinoid insecticides with carbonate radicals. Water Res. 46, 3479–3489. https://doi.org/https://doi.org/10.1016/j.watres.2012.03.051

Department for Environment and Water-Government of South Australia, 2020. WaterConnect [WWW Document]. URL https://www.waterconnect.sa.gov.au/Pages/Home.aspx

Ebele, A.J., Abou-Elwafa Abdallah, M., Harrad, S., 2017. Pharmaceuticals and personal care products (PPCPs) in the freshwater aquatic environment. Emerg. Contam. 3, 1–16. https://doi.org/https://doi.org/10.1016/j.emcon.2016.12.004

Eberson, L., 1982. Electron-Transfer Reactions in Organic Chemistry, in: Gold, V., Bethell, D.B.T.-A. in P.O.C. (Eds.), Advances in Physical Organic Chemistry. Academic Press, pp. 79–185. https://doi.org/https://doi.org/10.1016/S0065-3160(08)60139-2

EEA, 2020. European Environment Agency [WWW Document]. URL

https://www.eea.europa.eu/

Elango, T.P., Ramakrishnan, V., Vancheesan, S., Kuriacose, J.C., 1985. Reactions of the carbonate radical with aliphatic amines. Tetrahedron 41, 3837–3843. https://doi.org/https://doi.org/10.1016/S0040-4020(01)91404-8

Elango, T.P., Ramakrishnan, V., Vancheesan, S., Kuriacose, J.C., 1984. Reaction of the carbonate radical with substituted anilines. Proc. Indian Acad. Sci. - Chem. Sci. 93, 47–52. https://doi.org/10.1007/BF02841982

Erickson, P.R., Grandbois, M., Arnold, W.A., McNeill, K., 2012. Photochemical Formation of Brominated Dioxins and Other Products of Concern from Hydroxylated Polybrominated Diphenyl Ethers (OH-PBDEs). Environ. Sci. Technol. 46, 8174–8180. https://doi.org/10.1021/es3016183

Erickson, P.R., Moor, K.J., Werner, J.J., Latch, D.E., Arnold, W.A., McNeill, K., 2018. Singlet Oxygen Phosphorescence as a Probe for Triplet-State Dissolved Organic Matter Reactivity. Environ. Sci. Technol. 52, 9170–9178. https://doi.org/10.1021/acs.est.8b02379

Fabbri, D., Minella, M., Maurino, V., Minero, C., Vione, D., 2015a. Photochemical transformation of phenylurea herbicides in surface waters: A model assessment of persistence , and implications for the possible generation of hazardous intermediates. Chemosphere 119, 601–607. https://doi.org/10.1016/j.chemosphere.2014.07.034

Fabbri, D., Minella, M., Maurino, V., Minero, C., Vione, D., 2015b. Photochemical transformation of phenylurea herbicides in surface waters: A model assessment of persistence, and implications for the possible generation of hazardous intermediates. Chemosphere 119, 601–607. https://doi.org/https://doi.org/10.1016/j.chemosphere.2014.07.034

Fasching, C., Ulseth, A.J., Schelker, J., Steniczka, G., Battin, T.J., 2016. Hydrology controls dissolved organic matter export and composition in an Alpine stream and its hyporheic zone. Limnol. Oceanogr. 61, 558–571. https://doi.org/10.1002/lno.10232

Fatichi, S., Rimkus, S., Burlando, P., Bordoy, R., 2014. Does internal climate

variability overwhelm climate change signals in streamflow? The upper Po and Rhone basin case studies. Sci. Total Environ. 493, 1171–1182. https://doi.org/https://doi.org/10.1016/j.scitotenv.2013.12.014

Fenner, K., Canonica, S., Wackett, L.P., Elsner, M., 2013. Evaluating Pesticide Degradation in the Environment: Blind Spots and Emerging Opportunities. Science (80-.). 341, 752 LP – 758. https://doi.org/10.1126/science.1236281

Filazzola, A., Mahdiyan, O., Shuvo, A., Ewins, C., Moslenko, L., Sadid, T., Blagrave, K., Imrit, M.A., Gray, D.K., Quinlan, R., O'Reilly, C.M., Sharma, S., 2020. A database of chlorophyll and water chemistry in freshwater lakes. Sci. Data 7, 310. https://doi.org/10.1038/s41597-020-00648-2

Fujii, M., Otani, E., 2017. Photochemical generation and decay kinetics of superoxide and hydrogen peroxide in the presence of standard humic and fulvic acids. Water Res. 123, 642–654. https://doi.org/https://doi.org/10.1016/j.watres.2017.07.015

Galbavy, E.S., Ram, K., Anastasio, C., 2010. Chemistry 2-Nitrobenzaldehyde as a chemical actinometer for solution and ice photochemistry. J. Photochem. Photobiol. A Chem. 209, 186–192. https://doi.org/10.1016/j.jphotochem.2009.11.013

Galichet, F., Mailhot, G., Bonnemoy, F., Bohatier, J., Bolte, M., 2002. Iron(III) photo-induced degradation of isoproturon: correlation between degradation and toxicity. Pest Manag. Sci. 58, 707–712. https://doi.org/doi:10.1002/ps.505

Garg, S., Jiang, C., Waite, T.D., 2018. Impact of pH on Iron Redox Transformations in Simulated Freshwaters Containing Natural Organic Matter. Environ. Sci. Technol. 52, 13184–13194. https://doi.org/10.1021/acs.est.8b03855

Garg, S., Rose, A.L., Waite, T.D., 2011. Photochemical production of superoxide and hydrogen peroxide from natural organic matter. Geochim. Cosmochim. Acta 75, 4310–4320. https://doi.org/https://doi.org/10.1016/j.gca.2011.05.014

Garg, S., Rose, A.L., Waite, T.D., 2007. Superoxide Mediated Reduction of Organically Complexed Iron(III): Comparison of Non-Dissociative and

Dissociative Reduction Pathways. Environ. Sci. Technol. 41, 3205–3212. https://doi.org/10.1021/es0617892

Garg, S., Xing, G., Waite, T.D., 2020. Influence of pH on the Kinetics and Mechanism of Photoreductive Dissolution of Amorphous Iron Oxyhydroxide in the Presence of Natural Organic Matter: Implications to Iron Bioavailability in Surface Waters. Environ. Sci. Technol. 54, 6771–6780. https://doi.org/10.1021/acs.est.0c01257

Garmo, Ø.A., Skjelkvåle, B.L., de Wit, H.A., Colombo, L., Curtis, C., Fölster, J., Hoffmann, A., Hruška, J., Høgåsen, T., Jeffries, D.S., Keller, W.B., Krám, P., Majer, V., Monteith, D.T., Paterson, A.M., Rogora, M., Rzychon, D., Steingruber, S., Stoddard, J.L., Vuorenmaa, J., Worsztynowicz, A., 2014. Trends in Surface Water Chemistry in Acidified Areas in Europe and North America from 1990 to 2008. Water, Air, Soil Pollut. 225, 1880. https://doi.org/10.1007/s11270-014-1880-6

Ge, L., Zhang, P., Halsall, C., Li, Y., Chen, C.-E., Li, J., Sun, H., Yao, Z., 2019. The importance of reactive oxygen species on the aqueous phototransformation of sulfonamide antibiotics: kinetics, pathways, and comparisons with direct photolysis. Water Res. 149, 243–250. https://doi.org/https://doi.org/10.1016/j.watres.2018.11.009

Goldstone, J. V, Voelker, B.M., 2000. Chemistry of Superoxide Radical in Seawater: CDOM Associated Sink of Superoxide in Coastal Waters. Environ. Sci. Technol. 34, 1043–1048. https://doi.org/10.1021/es9905445

Gonsior, M., Hertkorn, N., Conte, M.H., Cooper, W.J., Bastviken, D., Druffel, E., Schmitt-Kopplin, P., 2014. Photochemical production of polyols arising from significant photo-transformation of dissolved organic matter in the oligotrophic surface ocean. Mar. Chem. 163, 10–18. https://doi.org/https://doi.org/10.1016/j.marchem.2014.04.002

Gornik, T., Vozic, A., Heath, E., Trontelj, J., Roskar, R., Zigon, D., Vione, D., Kosjek, T., 2020. Determination and photodegradation of sertraline residues in aqueous environment. Environ. Pollut. 256, 113431.

https://doi.org/https://doi.org/10.1016/j.envpol.2019.113431

Guizzardi, B., Mella, M., Fagnoni, M., Freccero, M., Albini, A., 2001. Generation and reactivity of the 4-aminophenyl cation by photolysis of 4-chloroaniline. J. Org. Chem. 66, 6353–6363. https://doi.org/10.1021/jo0104680

Häder, D.-P., Williamson, C.E., Wängberg, S.-Å., Rautio, M., Rose, K.C., Gao, K., Helbling, E.W., Sinha, R.P., Worrest, R., 2015. Effects of UV radiation on aquatic ecosystems and interactions with other environmental factors. Photochem. Photobiol. Sci. 14, 108–126. https://doi.org/10.1039/C4PP90035A

Halladja, S., Amine-Khodja, A., ter Halle, A., Boulkamh, A., Richard, C., 2007. Photolysis of fluometuron in the presence of natural water constituents. Chemosphere 69, 1647–1654. https://doi.org/https://doi.org/10.1016/j.chemosphere.2007.05.035

Hao, Z., Ma, J., Miao, C., Song, Y., Lian, L., Yan, S., Song, W., 2020. Carbonate Radical Oxidation of Cylindrospermopsin (Cyanotoxin): Kinetic Studies and Mechanistic Consideration. Environ. Sci. Technol. 54, 10118–10127. https://doi.org/10.1021/acs.est.0c03404

Harned, H.S., Scholes, S.R., 1941. The Ionization Constant of HCO3- from 0 to 50°. J. Am. Chem. Soc. 63, 1706–1709. https://doi.org/10.1021/ja01851a058

Heberger, M., 2012. Australia's Millennium Drought: Impacts and Responses. https://doi.org/10.5822/978-1-59726-228-6_5

Heeb, L.R., Peters, K.S., 2006. Further Evidence of an Inverted Region in Proton Transfer within the Benzophenone/Substituted Aniline Contact Radical Ion Pairs; Importance of Vibrational Reorganization Energy. J. Phys. Chem. A 110, 6408–6414. https://doi.org/10.1021/jp056188w

Heller, M.I., Croot, P.L., 2010. Kinetics of superoxide reactions with dissolved organic matter in tropical Atlantic surface waters near Cape Verde (TENATSO). J. Geophys. Res. Ocean. 115. https://doi.org/10.1029/2009JC006021

Hemond, H.F., Lin, K., 2010. Nitrate suppresses internal phosphorus loading in an

eutrophic lake. Water Res. 44, 3645–3650. https://doi.org/https://doi.org/10.1016/j.watres.2010.04.018

Hioe, J., Šakić, D., Vrček, V., Zipse, H., 2015. The stability of nitrogen-centered radicals. Org. Biomol. Chem. 13, 157–169. https://doi.org/10.1039/c4ob01656d

Houmam, A., 2008. Electron transfer initiated reactions: Bond formation and bond dissociation. Chem. Rev. 108, 2180–2237. https://doi.org/10.1021/cr068070x

Huang, J., Mabury, S.A., 2000. A New Method for Measuring Carbonate Radical Reactivity toward Pesticides. Environ. Toxicol. Chem. 19, 1501–1507. https://doi.org/https://doi.org/10.1002/etc.5620190605

Huang, Y., Kong, M., Westerman, D., Xu, E.G., Coffin, S., Cochran, K.H., Liu, Y., Richardson, S.D., Schlenk, D., Dionysiou, D.D., 2018. Effects of HCO3– on Degradation of Toxic Contaminants of Emerging Concern by UV/NO3–. Environ. Sci. Technol. 52, 12697–12707. https://doi.org/10.1021/acs.est.8b04383

IPCC, 2014. Climate Change 2014: Synthesis Report. Contribution of Working Groups I, II and III to the Fifth Assessment Report of the Intergovernmental Panel on Climate Change [Core Writing Team, R.K. Pachauri and L.A. Meyer (eds.)]. Geneva, Switzerland.

Jacobs, L.E., Fimmen, R.L., Chin, Y.-P., Mash, H.E., Weavers, L.K., 2011. Fulvic acid mediated photolysis of ibuprofen in water. Water Res. 45, 4449–4458. https://doi.org/https://doi.org/10.1016/j.watres.2011.05.041

Jenkins, C., 2013. A snapshot of pesticides in South Australian aquatic sediments.

Jiang, L., Li, T., 2019. Relative roles of El Niño-induced extratropical and tropical forcing in generating Tropical North Atlantic (TNA) SST anomaly. Clim. Dyn. 53, 3791–3804. https://doi.org/10.1007/s00382-019-04748-7

Jin, X., Xu, H., Qiu, S., Jia, M., Wang, F., Zhang, A., Jiang, X., 2017. Direct photolysis of oxytetracycline: Influence of initial concentration, pH and temperature. J. Photochem. Photobiol. A Chem. 332, 224–231. https://doi.org/https://doi.org/10.1016/j.jphotochem.2016.08.032

Jones, O.A.H., Voulvoulis, N., Lester, J.N., 2002. Aquatic environmental assessment of the top 25 English prescription pharmaceuticals. Water Res. 36, 5013–5022. https://doi.org/https://doi.org/10.1016/S0043-1354(02)00227-0

Jonsson, M., Lind, J., Eriksen, T.E., Merényi, G., 1994. Redox and Acidity Properties of 4-Substituted Aniline Radical Cations in Water. J. Am. Chem. Soc. 116, 1423–1427. https://doi.org/10.1021/ja00083a030

Jonsson, M., Wayner, D.D.M., Lusztyk, J., 1996. Redox and Acidity Properties of Alkyl- and Arylamine Radical Cations and the Corresponding Aminyl Radicals 1. J. Phys. Chem. 100, 17539–17543. https://doi.org/10.1021/jp961286q

Kanawi, E., Scoy, A.R. Van, Budd, R., Tjeerdema, R.S., 2016. Environmental fate and ecotoxicology of propanil : a review. Toxicol. Environ. Chem. 98, 689–704. https://doi.org/10.1080/02772248.2015.1133816

Katagi, T., 2018. Direct photolysis mechanism of pesticides in water. J. Pestic. Sci. 43, 57–72. https://doi.org/10.1584/jpestics.D17-081

Koehler, B., Landelius, T., Weyhenmeyer, G.A., Machida, N., Tranvik, L.J., 2014. Sunlight-induced carbon dioxide emissions from inland waters. Global Biogeochem. Cycles 28, 696–711. https://doi.org/doi:10.1002/2014GB004850

Krishtalik, L.I., 2003. pH-dependent redox potential: How to use it correctly in the activation energy analysis. Biochim. Biophys. Acta - Bioenerg. 1604, 13–21. https://doi.org/10.1016/S0005-2728(03)00020-3

Kuhn, H.J., Braslavsky, S.E., Schmidt, R., 2004. Chemical actinometry (IUPAC Technical Report). Pure Appl. Chem. 76, 2105–2146.

Lasagna, M., De Luca, D.A., 2019. Evaluation of sources and fate of nitrates in the western Po plain groundwater (Italy) using nitrogen and boron isotopes. Environ. Sci. Pollut. Res. 26, 2089–2104. https://doi.org/https://doi.org/10.1007/s11356-017-0792-6 GROUNDWATER

Lasagna, M., De Luca, D.A., Franchino, E., 2016a. Nitrate contamination of groundwater in the western Po Plain (Italy): the effects of groundwater and surface water interactions. Environ. Earth Sci. 75, 240.

https://doi.org/10.1007/s12665-015-5039-6

Lasagna, M., De Luca, D.A., Franchino, E., 2016b. The role of physical and biological processes in aquifers and their importance on groundwater vulnerability to nitrate pollution. Environ. Earth Sci. 75. https://doi.org/10.1007/s12665-016-5768-1

Lasagna, M., Mancini, S., De Luca, D.A., 2020. Groundwater hydrodynamic behaviours based on water table levels to identify natural and anthropic controlling factors in the Piedmont Plain (Italy). Sci. Total Environ. 716, 137051. https://doi.org/https://doi.org/10.1016/j.scitotenv.2020.137051

Lee, C.-L., Kuo, L.-J., 1999. Quantification of the dissolved organic matter effect on the sorption of hydrophobic organic pollutant: Application of an overall mechanistic sorption model. Chemosphere 38, 807–821. https://doi.org/https://doi.org/10.1016/S0045-6535(98)00228-8

Leresche, F., Ludvíková, L., Heger, D., Klán, P., von Gunten, U., Canonica, S., 2019. Laser flash photolysis study of the photoinduced oxidation of 4-(dimethylamino)benzonitrile (DMABN). Photochem. Photobiol. Sci. 18, 534–545. https://doi.org/10.1039/C8PP00519B

Leresche, F., Ludvíková, L., Heger, D., von Gunten, U., Canonica, S., 2020. Quenching of an Aniline Radical Cation by Dissolved Organic Matter and Phenols: A Laser Flash Photolysis Study. Environ. Sci. Technol. https://doi.org/10.1021/acs.est.0c05230

Leresche, F., Von Gunten, U., Canonica, S., 2016. Probing the Photosensitizing and Inhibitory Effects of Dissolved Organic Matter by Using N,N-dimethyl-4-cyanoaniline (DMABN). Environ. Sci. Technol. 50, 10997–11007. https://doi.org/10.1021/acs.est.6b02868

Lewis, K.A., Tzilivakis, J., Warner, D., Green, A., 2016. An international database for pesticide risk assessments and management. Hum. Ecol. Risk Assess. An Int. J. 22, 1050–1064. https://doi.org/10.1080/10807039.2015.1133242

Li, C., Hoffman, M.Z., 1999. One-Electron Redox Potentials of Phenols in Aqueous Solution. J. Phys. Chem. B 103, 6653–6656.

https://doi.org/10.1021/jp983819w

Li, P., Lee, Sang Hee, Lee, Soo Hyung, Lee, J.-B., Lee, Y.K., Shin, H.-S., Hur, J., 2016. Seasonal and storm-driven changes in chemical composition of dissolved organic matter: a case study of a reservoir and its forested tributaries. Environ. Sci. Pollut. Res. 23, 24834–24845. https://doi.org/10.1007/s11356-016-7720-z

Li, Yanyun, Pan, Y., Lian, L., Yan, S., Song, W., Yang, X., 2017. Photosensitized degradation of acetaminophen in natural organic matter solutions: The role of triplet states and oxygen. Water Res. 109, 266–273. https://doi.org/10.1016/j.watres.2016.11.049

Li, Yiping, Tang, C., Wang, J., Acharya, K., Du, W., Gao, X., Luo, L., Li, H., Dai, S., Mercy, J., Yu, Z., Pan, B., 2017. Effect of wave-current interactions on sediment resuspension in large shallow Lake Taihu, China. Environ. Sci. Pollut. Res. 24, 4029–4039. https://doi.org/10.1007/s11356-016-8165-0

Li, Y., Wei, X., Chen, J., Xie, H., Zhang, Y., 2015. Photodegradation mechanism of sulfonamides with excited triplet state dissolved organic matter: A case of sulfadiazine with 4-carboxybenzophenone as a proxy. J. Hazard. Mater. 290, 9–15. https://doi.org/10.1016/j.jhazmat.2015.02.040

Lipczynska-Kochany, E., 2018. Effect of climate change on humic substances and associated impacts on the quality of surface water and groundwater: A review. Sci. Total Environ. 640–641, 1548–1565. https://doi.org/https://doi.org/10.1016/j.scitotenv.2018.05.376

Liu, T., Yin, K., Liu, C., Luo, J., Crittenden, J., Zhang, W., Luo, S., He, Q., Deng, Y., Liu, H., Zhang, D., 2018. The role of reactive oxygen species and carbonate radical in oxcarbazepine degradation via UV , UV/H2O2 : Kinetics , mechanisms and toxicity evaluation. Water Res. 147, 204–213. https://doi.org/10.1016/j.watres.2018.10.007

Loiselle, S., Vione, D., Minero, C., Maurino, V., Tognazzi, A., Dattilo, A.M., Rossi, C., Bracchini, L., 2012. Chemical and optical phototransformation of dissolved organic matter. Water Res. 46, 3197–3207.

https://doi.org/https://doi.org/10.1016/j.watres.2012.02.047

Lower, S.K., 1999. Carbonate equilibria in natural waters.

Luo, S., Wei, Z., Spinney, R., Zhang, Z., Dionysiou, D.D., Gao, L., Chai, L., Wang, D., Xiao, R., 2018. UV direct photolysis of sulfamethoxazole and ibuprofen: An experimental and modelling study. J. Hazard. Mater. 343, 132–139. https://doi.org/https://doi.org/10.1016/j.jhazmat.2017.09.019

Luppichini, M., Barsanti, M., Giannecchini, R., Bini, M., 2021. Statistical relationships between large-scale circulation patterns and local-scale effects: NAO and rainfall regime in a key area of the Mediterranean basin. Atmos. Res. 248, 105270. https://doi.org/https://doi.org/10.1016/j.atmosres.2020.105270

Ma, J., Nie, J., Zhou, H., Wang, H., Lian, L., Yan, S., Song, W., 2020. Kinetic Consideration of Photochemical Formation and Decay of Superoxide Radical in Dissolved Organic Matter Solutions. Environ. Sci. Technol. https://doi.org/10.1021/acs.est.9b06018

Ma, J., Zhou, H., Yan, S., Song, W., 2019. Kinetics studies and mechanistic considerations on the reactions of superoxide radical ions with dissolved organic matter. Water Res. 149, 56–64. https://doi.org/https://doi.org/10.1016/j.watres.2018.10.081

Mack, J., Bolton, J.R., 1999. Photochemistry of nitrite and nitrate in aqueous solution: a review. J. Photochem. Photobiol. A Chem. 128, 1–13. https://doi.org/https://doi.org/10.1016/S1010-6030(99)00155-0

Maddigapu, P.R., Bedini, A., Minero, C., Maurino, V., Vione, D., Brigante, M., Mailhot, G., Sarakha, M., 2010. The pH-dependent photochemistry of anthraquinone-2-sulfonate. Photochem. Photobiol. Sci. 9, 323–330. https://doi.org/10.1039/B9PP00103D

Maddigapu, P.R., Minella, M., Vione, D., Maurino, V., Minero, C., 2011. Modeling Phototransformation Reactions in Surface Water Bodies: 2,4-Dichloro-6-Nitrophenol As a Case Study. Environ. Sci. Technol. 45, 209–214. https://doi.org/10.1021/es102458n

Manov, G.G., Bates, R.G., Hamer, W.J., Acree, S.F., 1943. Values of the Constants in the Debye—Hückel Equation for Activity Coefficients1. J. Am. Chem. Soc. 65, 1765–1767. https://doi.org/10.1021/ja01249a028

Maoz, A., Chefetz, B., 2010. Sorption of the pharmaceuticals carbamazepine and naproxen to dissolved organic matter: Role of structural fractions. Water Res. 44, 981–989. https://doi.org/https://doi.org/10.1016/j.watres.2009.10.019

Marchetti, G., Minella, M., Maurino, V., Minero, C., Vione, D., 2013. Photochemical transformation of atrazine and formation of photointermediates under conditions relevant to sunlit surface waters: Laboratory measures and modelling. Water Res. 47, 6211–6222. https://doi.org/10.1016/j.watres.2013.07.038

Marchisio, A., Minella, M., Maurino, V., Minero, C., Vione, D., 2015. Photogeneration of reactive transient species upon irradiation of natural water samples: Formation quantum yields in different spectral intervals , and implications for the photochemistry of surface waters. Water Res. 73, 145–156. https://doi.org/10.1016/j.watres.2015.01.016

Marciniak, B., Bobrowski, K., Hug, G.L., Rozwadowski, J., 1994. Photoinduced Electron Transfer between Sulfur-Containing Carboxylic Acids and the 4-Carboxybenzophenone Triplet State in Aqueous Solution. J. Phys. Chem. 98, 4854–4860. https://doi.org/10.1021/j100069a014

Marcus, R. A., 1957. On the theory of oxidation-reduction reactions involving electron transfer. II. Applications to data on the rates of isotopic exchange reactions. J. Chem. Phys. 26, 867–871. https://doi.org/10.1063/1.1743423

Marcus, R.A., 1957. On the theory of oxidation-reduction reactions involving electron transfer. III. applications to data on the rates of organic redox reactions. J. Chem. Phys. 26, 872–877. https://doi.org/10.1063/1.1743424

Marcus, R.A., 1956. On the Theory of Oxidation-Reduction Reactions Involving Electron Transfer. I*. J. Chem. Phys. 24, 966–978. https://doi.org/10.1063/1.1742723

Martinelli, G., Dadomo, A., De Luca, D.A., Mazzola, M., Lasagna, M., Pennisi, M.,

Pilla, G., Sacchi, E., Saccon, P., 2018. Nitrate sources, accumulation and reduction in groundwater from Northern Italy: Insights provided by a nitrate and boron isotopic database. Appl. Geochemistry 91, 23–35. https://doi.org/10.1016/j.apgeochem.2018.01.011

Marvel, K., Cook, B.I., Bonfils, C.J.W., Durack, P.J., Smerdon, J.E., Williams, A.P., 2019. Twentieth-century hydroclimate changes consistent with human influence. Nature 569, 59–65. https://doi.org/10.1038/s41586-019-1149-8

Mattson, M.D.B.T.-R.M. in E.S. and E.S., 2014. Alkalinity of Freshwater. Elsevier. https://doi.org/https://doi.org/10.1016/B978-0-12-409548-9.09397-0

Maurino, V., Borghesi, D., Vione, D., Minero, C., 2008. Transformation of phenolic compounds upon UVA irradiation of anthraquinone-2-sulfonate. Photochem. Photobiol. Sci. 7, 321–327. https://doi.org/10.1039/B709331D

Mayer, J.M., 2004. Proton-Coupled Electron Transfer: A Reaction Chemist's View. Annu. Rev. Phys. Chem. 55, 363–390. https://doi.org/10.1146/annurev.physchem.55.091602.094446

McCabe, A.J., Arnold, W.A., 2018. Multiple linear regression models to predict the formation efficiency of triplet excited states of dissolved organic matter in temperate wetlands. Limnol. Oceanogr. 63, 1992–2014. https://doi.org/10.1002/lno.10820

McCabe, A.J., Arnold, W.A., 2016. Seasonal and spatial variabilities in the water chemistry of prairie pothole wetlands influence the photoproduction of reactive intermediates. Chemosphere 155, 640–647. https://doi.org/10.1016/j.chemosphere.2016.04.078

Mckay, G., Huang, W., Romera-Castillo, C., Crouch, J.E., Rosario-Ortiz, F.L., Jaffé, R., 2017. Predicting Reactive Intermediate Quantum Yields from Dissolved Organic Matter Photolysis Using Optical Properties and Antioxidant Capacity. Environ. Sci. Technol. 51, 5404–5413. https://doi.org/10.1021/acs.est.6b06372

McKay, G., Korak, J.A., Erickson, P.R., Latch, D.E., McNeill, K., Rosario-Ortiz, F.L., 2018. The Case Against Charge Transfer Interactions in Dissolved

Organic Matter Photophysics. Environ. Sci. Technol. 52, 406–414. https://doi.org/10.1021/acs.est.7b03589

McNeill, K., Canonica, S., 2016. Triplet state dissolved organic matter in aquatic photochemistry: reaction mechanisms, substrate scope, and photophysical properties. Environ. Sci. Process. Impacts 18, 1381–1399. https://doi.org/10.1039/C6EM00408C

Miao, L., Li, S., Zhang, F., Chen, T., Shan, Y., Zhang, Y., 2020. Future Drought in the Dry Lands of Asia Under the 1.5 and 2.0 °C Warming Scenarios. Earth's Futur. 8, e2019EF001337. https://doi.org/10.1029/2019EF001337

Milan, M., Vidotto, F., Piano, S., Ferrero, A., 2006. Dissipation of Propanil and 3,4 Dichloroaniline in Three Diff erent Rice Management Systems. J. Environ. Qual. 41, 1487–1496. https://doi.org/10.2134/jeq2012.0175

Millero, F.J., Pierrot, D., 1998. A Chemical Equilibrium Model for Natural Waters. Aquat. Geochemistry 4, 153–199. https://doi.org/10.1023/A:1009656023546

Millero, F.J., Pierrot, D., Lee, K., Wanninkhof, R., Feely, R., Sabine, C.L., Key, R.M., Takahashi, T., 2002. Dissociation constants for carbonic acid determined from field measurements. Deep. Res. Part I Oceanogr. Res. Pap. 49, 1705–1723. https://doi.org/https://doi.org/10.1016/S0967-0637(02)00093-6

Minella, M., De Laurentiis, E., Maurino, V., Minero, C., Vione, D., 2015. Dark production of hydroxyl radicals by aeration of anoxic lake water. Sci. Total Environ. 527–528, 322–327. https://doi.org/https://doi.org/10.1016/j.scitotenv.2015.04.123

Minella, M., Leoni, B., Salmaso, N., Savoye, L., Sommaruga, R., Vione, D., 2016. Long-term trends of chemical and modelled photochemical parameters in four Alpine lakes. Sci. Total Environ. 541, 247–256. https://doi.org/https://doi.org/10.1016/j.scitotenv.2015.08.149

Minella, M., Maurino, V., Minero, C., Vione, D., 2013. Modelling photochemical transformation of emerging organic pollutants in surface waters: effect of water level fluctuations following outflow or evaporation, relevant to arid and

semi-arid environments. Int. J. Environ. Anal. Chem. 93, 1698–1717. https://doi.org/10.1080/03067319.2013.803284

Minella, M., Rapa, L., Carena, L., Pazzi, M., Maurino, V., Minero, C., Brigante, M., Vione, D., 2018. An experimental methodology to measure the reaction rate constants of processes sensitised by the triplet state of 4-carboxybenzophenone as a proxy of the triplet states of chromophoric dissolved organic matter, under steady-state irradiation conditions. Environ. Sci. Process. Impacts 20, 1007–1019. https://doi.org/10.1039/c8em00155c

Mortimer, R.G., 2000. Chemical Reaction Mechanisms, in: Mortimer, R.G.B.T.-P.C. (Second E. (Ed.), Physical Chemistry. Academic Press, Burlington, pp. 435–492. https://doi.org/https://doi.org/10.1016/B978-012508345-4/50016-2

Mosley, L.M., 2015. Drought impacts on the water quality of freshwater systems; review and integration. Earth-Science Rev. 140, 203–214. https://doi.org/https://doi.org/10.1016/j.earscirev.2014.11.010

Mosley, L.M., Zammit, B., Jolley, A.M., Barnett, L., 2014. Acidification of lake water due to drought. J. Hydrol. 511, 484–493. https://doi.org/https://doi.org/10.1016/j.jhydrol.2014.02.001

Mosley, L.M., Zammit, B., Leyden, E., Heneker, T.M., Hipsey, M.R., Skinner, D., Aldridge, K.T., 2012. The Impact of Extreme Low Flows on the Water Quality of the Lower Murray River and Lakes (South Australia). Water Resour. Manag. 26, 3923–3946. https://doi.org/10.1007/s11269-012-0113-2

Mostafa, S., Rosario-Ortiz, F.L., 2013. Singlet Oxygen Formation from Wastewater Organic Matter. Environ. Sci. Technol. 47, 8179–8186. https://doi.org/10.1021/es401814s

Nad, S., Pal, H., 2000. Electron Transfer from Aromatic Amines to Excited Coumarin Dyes: Fluorescence Quenching and Picosecond Transient Absorption Studies. J. Phys. Chem. A 104, 673–680. https://doi.org/10.1021/jp993206z

NCAR, 2015. Quick TUV calculator [WWW Document]. URL http://cprm.acom.ucar.edu/Models/TUV/Interactive_TUV/

Nebbioso, A., Piccolo, A., 2013. Molecular characterization of dissolved organic matter (DOM): a critical review. Anal. Bioanal. Chem. 405, 109–124. https://doi.org/10.1007/s00216-012-6363-2

Nelson, N.B., Siegel, D.A., 2013. The Global Distribution and Dynamics of Chromophoric Dissolved Organic Matter. Ann. Rev. Mar. Sci. 5, 447–476. https://doi.org/10.1146/annurev-marine-120710-100751

Neta, P., Huie, R.E., Ross, A.B., 1988. Rate Constants for Reactions of Inorganic Radicals in Aqueous Solution. J. Phys. Chem. Ref. Data 17, 1027. https://doi.org/https://doi.org/10.1063/1.555808

NIST, 2004. Critically Selected Stability Constants of Metal Complexes Database. Stand. Ref. Data Program, Vol.46. Natl. Inst. Stand. Technol. U.S. Dep. Commer.

Niu, X.-Z., Harir, M., Schmitt-Kopplin, P., Croué, J.-P., 2018. Characterisation of dissolved organic matter using Fourier-transform ion cyclotron resonance mass spectrometry: Type-specific unique signatures and implications for reactivity. Sci. Total Environ. 644, 68–76. https://doi.org/https://doi.org/10.1016/j.scitotenv.2018.06.351

Niu, X.-Z., Liu, C., Gutierrez, L., Croué, J.-P., 2014. Photobleaching-induced changes in photosensitizing properties of dissolved organic matter. Water Res. 66, 140–148. https://doi.org/https://doi.org/10.1016/j.watres.2014.08.017

Niu, X.Z., Croué, J.P., 2019. Photochemical production of hydroxyl radical from algal organic matter. Water Res. 161, 11–16. https://doi.org/10.1016/j.watres.2019.05.089

O'Sullivan, D.W., Neale, P.J., Coffin, R.B., Boyd, T.J., Osburn, C.L., 2005. Photochemical production of hydrogen peroxide and methylhydroperoxide in coastal waters. Mar. Chem. 97, 14–33. https://doi.org/https://doi.org/10.1016/j.marchem.2005.04.003

Okaikue-Woodi, F.E.K., Cherukumilli, K., Ray, J.R., 2020. A critical review of contaminant removal by conventional and emerging media for urban stormwater treatment in the United States. Water Res. 187, 116434.

https://doi.org/https://doi.org/10.1016/j.watres.2020.116434

Osburn, C.L., Kinsey, J.D., Bianchi, T.S., Shields, M.R., 2019. Formation of planktonic chromophoric dissolved organic matter in the ocean. Mar. Chem. 209, 1–13. https://doi.org/https://doi.org/10.1016/j.marchem.2018.11.010

Othmen, K., Boule, P., Szczepanik, B., Rotkiewicz, K., Grabner, G., 2000. Photochemistry of 4-chloroaniline in solution. formation and kinetic properties of a new carbene, 4-iminocyclohexa-2,5-dienylidene. J. Phys. Chem. A 104, 9525–9534. https://doi.org/10.1021/jp0010381

Packer, J.L., Werner, J.J., Latch, D.E., McNeill, K., Arnold, W.A., 2003. Photochemical fate of pharmaceuticals in the environment: Naproxen, diclofenac, clofibric acid, and ibuprofen. Aquat. Sci. 65, 342–351. https://doi.org/10.1007/s00027-003-0671-8

Page, S.E., Arnold, W.A., McNeill, K., 2011. Assessing the Contribution of Free Hydroxyl Radical in Organic Matter-Sensitized Photohydroxylation Reactions. Environ. Sci. Technol. 45, 2818–2825. https://doi.org/10.1021/es2000694

Page, S.E., Logan, J.R., Cory, R.M., McNeill, K., 2014. Evidence for dissolved organic matter as the primary source and sink of photochemically produced hydroxyl radical in arctic surface waters. Environ. Sci. Process. Impacts 16, 807–822. https://doi.org/10.1039/C3EM00596H

Page, S.E., Sander, M., Arnold, W.A., McNeill, K., 2012. Hydroxyl Radical Formation upon Oxidation of Reduced Humic Acids by Oxygen in the Dark. Environ. Sci. Technol. 46, 1590–1597. https://doi.org/10.1021/es203836f

Parker, K.M., Mitch, W.A., 2016. Halogen radicals contribute to photooxidation in coastal and estuarine waters. Proc. Natl. Acad. Sci. 113, 5868 LP – 5873. https://doi.org/10.1073/pnas.1602595113

Partanen, S.B., Erickson, P.R., Latch, D.E., Moor, K.J., McNeill, K., 2020. Dissolved Organic Matter Singlet Oxygen Quantum Yields: Evaluation Using Time-Resolved Singlet Oxygen Phosphorescence. Environ. Sci. Technol. 54, 3316–3324. https://doi.org/10.1021/acs.est.9b07246

Paul, A., Hackbarth, S., Vogt, R.D., Röder, B., Burnison, B.K., Steinberg, C.E.W., 2004. Photogeneration of singlet oxygen by humic substances: comparison of humic substances of aquatic and terrestrial origin. Photochem. Photobiol. Sci. 3, 273–280. https://doi.org/10.1039/B312146A

Pavitt, A.S., Bylaska, E.J., Tratnyek, P.G., 2017. Oxidation potentials of phenols and anilines: correlation analysis of electrochemical and theoretical values. Environ. Sci. Process. Impacts 19, 339–349. https://doi.org/10.1039/c6em00694a

Petrie, B., Barden, R., Kasprzyk-Hordern, B., 2015. A review on emerging contaminants in wastewaters and the environment: Current knowledge, understudied areas and recommendations for future monitoring. Water Res. 72, 3–27. https://doi.org/https://doi.org/10.1016/j.watres.2014.08.053

Piechota, E.J., Meyer, G.J., 2019. Introduction to Electron Transfer: Theoretical Foundations and Pedagogical Examples. J. Chem. Educ. 96, 2450–2466. https://doi.org/10.1021/acs.jchemed.9b00489

Pociask-Karteczka, J., 2006. River Hydrology and the North Atlantic Oscillation: A General Review. AMBIO A J. Hum. Environ. 35, 312–314. https://doi.org/10.1579/05-S-114.1

Poulain, L., Mailhot, G., Wong-Wah-Chung, P., Bolte, M., 2003. Photodegradation of chlortoluron sensitised by iron(III) aquacomplexes. J. Photochem. Photobiol. A Chem. 159, 81–88. https://doi.org/https://doi.org/10.1016/S1010-6030(03)00107-2

Premsingh, S., Venkataramanan, N.S., Rajagopal, S., Mirza, S.P., Vairamani, M., Rao, P.S., Velavan, K., 2004. Electron Transfer Reaction of Oxo(salen)chromium(V) Ion with Anilines. Inorg. Chem. 43, 5744–5753. https://doi.org/10.1021/ic049482w

QGIS, 2020. QGIS Geographic Information System. Open Source Geospatial Foundation Project.

Qin, W., Lin, Z., Dong, H., Yuan, X., Qiang, Z., Liu, S., Xia, D., 2020. Kinetic and mechanistic insights into the abatement of clofibric acid by integrated

UV/ozone/peroxydisulfate process: A modeling and theoretical study. Water Res. 186, 116336. https://doi.org/https://doi.org/10.1016/j.watres.2020.116336

Remucal, C.K., 2014. The role of indirect photochemical degradation in the environmental fate of pesticides: a review. Environ. Sci. Process. Impacts 16, 628–653. https://doi.org/10.1039/c3em00549f

Remucal, C.K., McNeill, K., 2011. Photosensitized Amino Acid Degradation in the Presence of Riboflavin and Its Derivatives. Environ. Sci. Technol. 45, 5230–5237. https://doi.org/10.1021/es200411a

Rowland, G.A., Grannas, A.M., 2011. A solid-phase chemical actinometer film for measurement of solar UV penetration into snowpack. Cold Reg. Sci. Technol. 66, 75–83. https://doi.org/https://doi.org/10.1016/j.coldregions.2011.01.009

Ruiz-Villanueva, V., Stoffel, M., Bussi, G., Francés, F., Bréthaut, C., 2015. Climate change impacts on discharges of the Rhone River in Lyon by the end of the twenty-first century: model results and implications. Reg. Environ. Chang. 15, 505–515. https://doi.org/10.1007/s10113-014-0707-8

Saito, F., Tobita, S., Shizuka, H., 1996. Photoionization of aniline in aqueous solution and its photolysis in cyclohexane. J. Chem. Soc. Faraday Trans. 92, 4177–4185. https://doi.org/https://doi.org/10.1039/FT9969204177

Šakić, D., Achrainer, F., Vrček, V., Zipse, H., 2013. The chemical fate of paroxetine metabolites. Dehydration of radicals derived from 4-(4-fluorophenyl)-3-(hydroxymethyl)piperidine. Org. Biomol. Chem. 11, 4232–4239. https://doi.org/10.1039/c3ob40219c

Sanchez-Cruz, P., Santos, A., Diaz, S., Alegría, A.E., 2014. Metal-Independent Reduction of Hydrogen Peroxide by Semiquinones. Chem. Res. Toxicol. 27, 1380–1386. https://doi.org/10.1021/tx500089x

Sandrini, D., Maestri, M., Belser, P., von Zelewsky, A., Balzani, V., 1985. Kinetic parameters for the electron-transfer quenching of the luminescent excited state of ruthenium(II)-polypyridine complexes by aromatic amines in acetonitrile solution. J. Phys. Chem. 89, 3675–3679. https://doi.org/10.1021/j100263a020

Savéant, J.-M., 2014. Concerted Proton-Electron Transfers: Fundamentals and

Recent Developments. Annu. Rev. Anal. Chem. 7, 537–560. https://doi.org/10.1146/annurev-anchem-071213-020315

Schendorf, T.M., Del Vecchio, R., Bianca, M., Blough, N. V, 2019. Combined Effects of pH and Borohydride Reduction on Optical Properties of Humic Substances (HS): A Comparison of Optical Models. Environ. Sci. Technol. 53, 6310–6319. https://doi.org/10.1021/acs.est.9b01516

Schlesinger, W.H., Bernhardt, E.S., 2013. Inland Waters, in: Schlesinger, W.H., Bernhardt, E.S.B.T.-B. (Third E. (Eds.), Biogeochemistry: An Analysis of Global Change. Academic Press, Boston, pp. 275–340. https://doi.org/https://doi.org/10.1016/B978-0-12-385874-0.00008-X

Schmitt, M., Erickson, P.R., McNeill, K., 2017. Triplet-State Dissolved Organic Matter Quantum Yields and Lifetimes from Direct Observation of Aromatic Amine Oxidation. Environ. Sci. Technol. 51, 13151–13160. https://doi.org/10.1021/acs.est.7b03402

Schulze, K., Hunger, M., Döll, P., 2005. Simulating river flow velocity on global scale. Adv. Geosci. 5, 133–136. https://doi.org/10.5194/adgeo-5-133-2005

Schwarzenbach, R.P., Egli, T., Hofstetter, T.B., von Gunten, U., Wehrli, B., 2010. Global Water Pollution and Human Health. Annu. Rev. Environ. Resour. 35, 109–136. https://doi.org/10.1146/annurev-environ-100809-125342

Schwarzenbach, R.P., Escher, B.I., Fenner, K., Hofstetter, T.B., Johnson, C.A., von Gunten, U., Wehrli, B., 2006. The Challenge of Micropollutants in Aquatic Systems. Science (80-.). 313, 1072–1077. https://doi.org/10.1126/science.1127291

Shankar, M. V, Nélieu, S., Kerhoas, L., Einhorn, J., 2008. Natural sunlight NO3-/NO2--induced photo-degradation of phenylurea herbicides in water. Chemosphere 71, 1461–1468. https://doi.org/https://doi.org/10.1016/j.chemosphere.2007.12.003

Sharpless, C.M., 2012. Lifetimes of Triplet Dissolved Natural Organic Matter (DOM) and the Effect of NaBH4 Reduction on Singlet Oxygen Quantum Yields: Implications for DOM Photophysics. Environ. Sci. Technol. 46, 4466–

4473. https://doi.org/10.1021/es300217h

Sharpless, C.M., Blough, N. V, 2014. The importance of charge-transfer interactions in determining chromophoric dissolved organic matter (CDOM) optical and photochemical properties. Environ. Sci. Process. Impacts 16, 654–671. https://doi.org/10.1039/c3em00573a

Silva, E., Mendes, M.P., Ribeiro, L., Cerejeira, M.J., 2012. Exposure assessment of pesticides in a shallow groundwater of the Tagus vulnerable zone (Portugal): a multivariate statistical approach (JCA). Environ. Sci. Pollut. Res. 19, 2667–2680. https://doi.org/10.1007/s11356-012-0761-z

Silverstein, T.P., 2012. Marcus Theory: Thermodynamics CAN Control the Kinetics of Electron Transfer Reactions. J. Chem. Educ. 89, 1159–1167. https://doi.org/10.1021/ed1007712

Solomon, C.T., Jones, S.E., Weidel, B.C., Buffam, I., Fork, M.L., Karlsson, J., Larsen, S., Lennon, J.T., Read, J.S., Sadro, S., Saros, J.E., 2015. Ecosystem Consequences of Changing Inputs of Terrestrial Dissolved Organic Matter to Lakes: Current Knowledge and Future Challenges. Ecosystems 18, 376–389. https://doi.org/10.1007/s10021-015-9848-y

Sommaruga, R., Psenner, R., Schafferer, E., Koinig, K.A., Sommaruga-Wögrath, S., 1999. Dissolved Organic Carbon Concentration and Phytoplankton Biomass in High-Mountain Lakes of the Austrian Alps: Potential Effect of Climatic Warming on UV Underwater Attenuation. Arctic, Antarct. Alp. Res. 31, 247–253. https://doi.org/https://doi.org/10.1080/15230430.1999.12003305

Stenseth, N.C., Ottersen, G., Hurrell, J.W., Mysterud, A., Lima, M., Chan, K., Yoccoz, N.G., Ådlandsvik, B., 2003. Review article. Studying climate effects on ecology through the use of climate indices: the North Atlantic Oscillation, El Niño Southern Oscillation and beyond. Proc. R. Soc. London. Ser. B Biol. Sci. 270, 2087–2096. https://doi.org/10.1098/rspb.2003.2415

Sulzberger, B., Arey, J.S., 2016. Impacts of Polar Changes on the UV-induced Mineralization of Terrigenous Dissolved Organic Matter. Environ. Sci. Technol. 50, 6621–6631. https://doi.org/10.1021/acs.est.5b05994

Sulzberger, B., Durisch-Kaiser, E., 2009. Chemical characterization of dissolved organic matter (DOM): A prerequisite for understanding UV-induced changes of DOM absorption properties and bioavailability. Aquat. Sci. 71, 104–126. https://doi.org/10.1007/s00027-008-8082-5

Sun, L., Qian, J., Blough, N. V, Mopper, K., 2015. Insights into the Photoproduction Sites of Hydroxyl Radicals by Dissolved Organic Matter in Natural Waters. Environ. Sci. Technol. Lett. 2, 352–356. https://doi.org/10.1021/acs.estlett.5b00294

Sur, B., De Laurentiis, E., Minella, M., Maurino, V., Minero, C., Vione, D., 2012. Photochemical transformation of anionic 2-nitro-4-chlorophenol in surface waters: Laboratory and model assessment of the degradation kinetics, and comparison with field data. Sci. Total Environ. 426, 296–303. https://doi.org/https://doi.org/10.1016/j.scitotenv.2012.03.034

Sur, B., Rolle, M., Minero, C., Maurino, V., Vione, D., Brigante, M., Mailhot, G., 2011. Formation of hydroxyl radicals by irradiated 1-nitronaphthalene (1NN): oxidation of hydroxyl ions and water by the 1NN triplet state. Photochem. Photobiol. Sci. 10, 1817–1824. https://doi.org/10.1039/C1PP05216K

Tentscher, P.R., Eustis, S.N., McNeill, K., Arey, J.S., 2013. Aqueous oxidation of sulfonamide antibiotics: Aromatic nucleophilic substitution of an aniline radical cation. Chem. - A Eur. J. 19, 11216–11223. https://doi.org/10.1002/chem.201204005

Timbal, B., Drosdowsky, W., 2013. The relationship between the decline of Southeastern Australian rainfall and the strengthening of the subtropical ridge. Int. J. Climatol. 33, 1021–1034. https://doi.org/10.1002/joc.3492

Timbal, B., Hendon, H., 2011. The role of tropical modes of variability in recent rainfall deficits across the Murray-Darling Basin. Water Resour. Res. 47. https://doi.org/doi:10.1029/2010WR009834

Timko, S.A., Romera-Castillo, C., Jaffé, R., Cooper, W.J., 2014. Photo-reactivity of natural dissolved organic matter from fresh to marine waters in the Florida Everglades, USA. Environ. Sci. Process. Impacts 16, 866–878.

https://doi.org/10.1039/C3EM00591G

Tixier, C., Singer, H.P., Oellers, S., Müller, S.R., 2003. Occurrence and Fate of Carbamazepine, Clofibric Acid, Diclofenac, Ibuprofen, Ketoprofen, and Naproxen in Surface Waters. Environ. Sci. Technol. 37, 1061–1068. https://doi.org/10.1021/es025834r

Topaz, T., Boxall, A., Suari, Y., Egozi, R., Sade, T., Chefetz, B., 2020. Ecological Risk Dynamics of Pharmaceuticals in Micro-Estuary Environments. Environ. Sci. Technol. 54, 11182–11190. https://doi.org/10.1021/acs.est.0c02434

Tran, N.H., Reinhard, M., Gin, K.Y.-H., 2018. Occurrence and fate of emerging contaminants in municipal wastewater treatment plants from different geographical regions-a review. Water Res. 133, 182–207. https://doi.org/https://doi.org/10.1016/j.watres.2017.12.029

Ukkola, A.M., De Kauwe, M.G., Roderick, M.L., Abramowitz, G., Pitman, A.J., 2020. Robust Future Changes in Meteorological Drought in CMIP6 Projections Despite Uncertainty in Precipitation. Geophys. Res. Lett. 46, e2020GL087820. https://doi.org/10.1029/2020GL087820

Ummenhofer, C.C., England, M.H., McIntosh, P.C., Meyers, G.A., Pook, M.J., Risbey, J.S., Gupta, A. Sen, Taschetto, A.S., 2009. What causes southeast Australia's worst droughts? Geophys. Res. Lett. 36. https://doi.org/doi:10.1029/2008GL036801

United Nations Environment Programme, 2019. GEMStat database of the Global Environment Monitoring System for freshwater (GEMS/Water) Programme. [WWW Document]. URL https://gemstat.org/data/statistic-reports/

Vähätalo, A., Xiao, Y., Salonen, K., 2020. Biogenic Fenton reaction – a possible mechanism for the mineralization of organic carbon in fresh waters. Water Res. 116483. https://doi.org/https://doi.org/10.1016/j.watres.2020.116483

Vähätalo, A. V, 2009. Light, Photolytic Reactivity and Chemical Products, in: Likens, G.E.B.T.-E. of I.W. (Ed.), Encyclopedia of Inland Waters. Academic Press, Oxford, pp. 761–773. https://doi.org/https://doi.org/10.1016/B978-012370626-3.00110-1

Vähätalo, A. V, Aarnos, H., Mäntyniemi, S., 2010. Biodegradability continuum and biodegradation kinetics of natural organic matter described by the beta distribution. Biogeochemistry 100, 227–240. https://doi.org/10.1007/s10533-010-9419-4

van Dijk, A.I.J.M., Beck, H.E., Crosbie, R.S., de Jeu, R.A.M., Liu, Y.Y., Podger, G.M., Timbal, B., Viney, N.R., 2013. The Millennium Drought in southeast Australia (2001–2009): Natural and human causes and implications for water resources, ecosystems, economy, and society. Water Resour. Res. 49, 1040–1057. https://doi.org/10.1002/wrcr.20123

Van Loon, A.F., Gleeson, T., Clark, J., Van Dijk, A.I.J.M., Stahl, K., Hannaford, J., Di Baldassarre, G., Teuling, A.J., Tallaksen, L.M., Uijlenhoet, R., Hannah, D.M., Sheffield, J., Svoboda, M., Verbeiren, B., Wagener, T., Rangecroft, S., Wanders, N., Van Lanen, H.A.J., 2016. Drought in the Anthropocene. Nat. Geosci. 9, 89–91. https://doi.org/10.1038/ngeo2646

Varanasi, L., Coscarelli, E., Khaksari, M., Mazzoleni, L.R., Minakata, D., 2018. Transformations of dissolved organic matter induced by UV photolysis, Hydroxyl radicals, chlorine radicals, and sulfate radicals in aqueous-phase UV-Based advanced oxidation processes. Water Res. 135, 22–30. https://doi.org/https://doi.org/10.1016/j.watres.2018.02.015

Vione, D., 2020. A Critical View of the Application of the APEX Software (Aqueous Photochemistry of Environmentally-Occurring Xenobiotics) to Predict Photoreaction Kinetics in Surface Freshwaters. Molecules 25, 9. https://doi.org/https://doi.org/10.3390/molecules25010009

Vione, D., 2018. A model assessment of the role played by the carbonate (CO3−) and dibromide (Br2−) radicals in the photodegradation of glutathione in sunlit fresh- and salt-waters. Chemosphere 209, 401–410. https://doi.org/https://doi.org/10.1016/j.chemosphere.2018.06.066

Vione, D., Carena, L., 2020. The Possible Production of Harmful Intermediates Is the “Dark Side” Of the Environmental Photochemistry of Contaminants (Potentially Adverse Effects, And Many Knowledge Gaps). Environ. Sci.

Technol. 54, 5328–5330. https://doi.org/10.1021/acs.est.0c01049

Vione, D., Das, R., Rubertelli, F., Maurino, V., Minero, C., Barbati, S., Chiron, S., 2010. Modelling the occurrence and reactivity of hydroxyl radicals in surface waters: implications for the fate of selected pesticides. Int. J. Environ. Anal. Chem. 90, 260–275. https://doi.org/10.1080/03067310902894218

Vione, D., Fabbri, D., Minella, M., Canonica, S., 2018. Effects of the antioxidant moieties of dissolved organic matter on triplet-sensitized phototransformation processes: Implications for the photochemical modeling of sulfadiazine. Water Res. 128, 38–48. https://doi.org/10.1016/j.watres.2017.10.020

Vione, D., Falletti, G., Maurino, V., Minero, C., Pelizzetti, E., Malandrino, M., Ajassa, R., Olariu, R.-I., Arsene, C., 2006. Sources and Sinks of Hydroxyl Radicals upon Irradiation of Natural Water Samples. Environ. Sci. Technol. 40, 3775–3781. https://doi.org/10.1021/es052206b

Vione, D., Maddigapu, P.R., De Laurentiis, E., Minella, M., Pazzi, M., Maurino, V., Minero, C., Kouras, S., Richard, C., 2011. Modelling the photochemical fate of ibuprofen in surface waters. Water Res. 45, 6725–6736. https://doi.org/10.1016/j.watres.2011.10.014

Vione, D., Minella, M., Maurino, V., Minero, C., 2014. Indirect Photochemistry in Sunlit Surface Waters: Photoinduced Production of Reactive Transient Species. Chem. Eur. J. 20, 10590–10606. https://doi.org/10.1002/chem.201400413

Vione, D., Scozzaro, A., 2019. Photochemistry of Surface Fresh Waters in the Framework of Climate Change. Environ. Sci. Technol. 53, 7945–7963. https://doi.org/10.1021/acs.est.9b00968

Vogna, D., Marotta, R., Andreozzi, R., Napolitano, A., 2004. Kinetic and chemical assessment of the UV/H2O2 treatment of antiepileptic drug carbamazepine. Chemosphere 54, 497–505. https://doi.org/10.1016/S0045-6535(03)00757-4

Vrček, V., Zipse, H., 2009. Rearrangemements in Piperidine-Derived Nitrogen-Centered Radicals. A Quantum-Chemical Study. J. Org. Chem. 74, 2947–2957. https://doi.org/10.1021/jo900349e

Walpen, N., Schroth, M.H., Sander, M., 2016. Quantification of Phenolic Antioxidant Moieties in Dissolved Organic Matter by Flow-Injection Analysis with Electrochemical Detection. Environ. Sci. Technol. 50, 6423–6432. https://doi.org/10.1021/acs.est.6b01120

Wang, J., Wang, S., 2016. Removal of pharmaceuticals and personal care products (PPCPs) from wastewater: A review. J. Environ. Manage. 182, 620–640. https://doi.org/https://doi.org/10.1016/j.jenvman.2016.07.049

Wang, S., Song, X., Hao, C., Gao, Z., Chen, J., Qiu, J., 2015. Elucidating triplet-sensitized photolysis mechanisms of sulfadiazine and metal ions effects by quantum chemical calculations. Chemosphere 122, 62–69. https://doi.org/10.1016/j.chemosphere.2014.11.007

Wenk, J., Canonica, S., 2012. Phenolic antioxidants inhibit the triplet-induced transformation of anilines and sulfonamide antibiotics in aqueous solution. Environ. Sci. Technol. 46, 5455–5462. https://doi.org/10.1021/es300485u

Wenk, J., Von Gunten, U., Canonica, S., 2011. Effect of Dissolved Organic Matter on the Transformation of Contaminants Induced by Excited Triplet States and the Hydroxyl Radical. Environ. Sci. Technol. 45, 1334–1340. https://doi.org/10.1021/es202028w

Wershaw, R.L., 2004. Evaluation of conceptual models of natural organic matter (humus) from a consideration of the chemical and biochemical processes of humification, Scientific Investigations Report. https://doi.org/10.3133/sir20045121

Westerhoff, P., Mezyk, S.P., Cooper, W.J., Minakata, D., 2007. Electron Pulse Radiolysis Determination of Hydroxyl Radical Rate Constants with Suwannee River Fulvic Acid and Other Dissolved Organic Matter Isolates. Environ. Sci. Technol. 41, 4640–4646. https://doi.org/10.1021/es062529n

Wetzel, R.G., 2001. Limnology: Lake and River Ecosystems, Third. ed. Academic Press. https://doi.org/https://doi.org/10.1016/C2009-0-02112-6

Wilkinson, F., Helman, W.P., Ross, A.B., 1995. Rate Constants for the Decay and Reactions of the Lowest Electronically Excited Singlet State of Molecular

Oxygen in Solution. An Expanded and Revised Compilation. J. Phys. Chem. Ref. Data 24, 663. https://doi.org/https://doi.org/10.1063/1.555965

Willett, K.L., Hites, R.A., 2000. Chemical Actinometry : Using o-Nitrobenzaldehyde to Measure Light Intensity in Photochemical Experiments. J. Chem. Educ. 77, 900–902. https://doi.org/https://doi.org/10.1021/ed077p900

Williams, A.P., Cook, E.R., Smerdon, J.E., Cook, B.I., Abatzoglou, J.T., Bolles, K., Baek, S.H., Badger, A.M., Livneh, B., 2020. Large contribution from anthropogenic warming to an emerging North American megadrought. Science (80-.). 368, 314 LP – 318. https://doi.org/10.1126/science.aaz9600

Winget, P., Weber, E.J., Cramer, C.J., Truhlar, D.G., 2000. Computational electrochemistry: Aqueous one-electron oxidation potentials for substituted anilines. Phys. Chem. Chem. Phys. 2, 1231–1239. https://doi.org/10.1039/a909076b

Wojnárovits, L., Tóth, T., Takács, E., 2020. Rate constants of carbonate radical anion reactions with molecules of environmental interest in aqueous solution : A review. Sci. Total Environ. 717, 137219. https://doi.org/10.1016/j.scitotenv.2020.137219

Xiang, B., Zhu, C., Zhu, L., 2009. Gas-phase absorption cross sections of 2-nitrobenzaldehyde and benzaldehyde in the 285–400nm region, and photolysis of 2-nitrobenzaldehyde vapor at 308 and 351nm. Chem. Phys. Lett. 474, 74–78. https://doi.org/https://doi.org/10.1016/j.cplett.2009.04.056

Xiao, Y., Carena, L., Näsi, M.-T., Vähätalo, A. V, 2020. Superoxide-driven autocatalytic dark production of hydroxyl radicals in the presence of complexes of natural dissolved organic matter and iron. Water Res. 177, 115782. https://doi.org/https://doi.org/10.1016/j.watres.2020.115782

Xie, W., Yuan, S., Tong, M., Ma, S., Liao, W., Zhang, N., Chen, C., 2020. Contaminant Degradation by •OH during Sediment Oxygenation: Dependence on Fe(II) Species. Environ. Sci. Technol. 54, 2975–2984. https://doi.org/10.1021/acs.est.9b04870

Xing, G., Garg, S., Waite, T.D., 2019. Is Superoxide-Mediated Fe(III) Reduction Important in Sunlit Surface Waters? Environ. Sci. Technol. 53, 13179–13190. https://doi.org/10.1021/acs.est.9b04718

Xu, H., Li, Y., Liu, J., Du, H., Du, Y., Su, Y., Jiang, H., 2020. Photogeneration and steady-state concentration of hydroxyl radical in river and lake waters along middle-lower Yangtze region, China. Water Res. 176, 115774. https://doi.org/https://doi.org/10.1016/j.watres.2020.115774

Yan, S., Liu, Y., Lian, L., Li, R., Ma, J., Zhou, H., Song, W., 2019. Photochemical formation of carbonate radical and its reaction with dissolved organic matters. Water Res. 161, 288–296. https://doi.org/10.1016/j.watres.2019.06.002

Yu, F., Yang, C., Zhu, Z., Bai, X., Ma, J., 2019. Adsorption behavior of organic pollutants and metals on micro/nanoplastics in the aquatic environment. Sci. Total Environ. 694, 133643. https://doi.org/https://doi.org/10.1016/j.scitotenv.2019.133643

Zampieri, M., Scoccimarro, E., Gualdi, S., Navarra, A., 2015. Observed shift towards earlier spring discharge in the main Alpine rivers. Sci. Total Environ. 503–504, 222–232. https://doi.org/https://doi.org/10.1016/j.scitotenv.2014.06.036

Zanchettin, D., Traverso, P., Tomasino, M., 2008. Po River discharges: a preliminary analysis of a 200-year time series. Clim. Change 89, 411–433. https://doi.org/10.1007/s10584-008-9395-z

Zeng, Q., Wang, X., Liu, X., Huang, L., Hu, J., Chu, R.K., Tolič, N., Dong, H., 2020. Mutual interactions between reduced Fe-bearing clay minerals and humic acids under dark, oxygenated condition: hydroxyl radical generation and humic acid transformation. Environ. Sci. Technol. https://doi.org/10.1021/acs.est.0c04463

Zeng, T., Arnold, W.A., 2013. Pesticide photolysis in prairie potholes: Probing photosensitized processes. Environ. Sci. Technol. 47, 6735–6745. https://doi.org/10.1021/es3030808

Zhang, T., Hansel, C.M., Voelker, B.M., Lamborg, C.H., 2016. Extensive Dark

Biological Production of Reactive Oxygen Species in Brackish and Freshwater Ponds. Environ. Sci. Technol. 50, 2983–2993. https://doi.org/10.1021/acs.est.5b03906

Zhang, Y., Blough, N. V, 2016. Photoproduction of One-Electron Reducing Intermediates by Chromophoric Dissolved Organic Matter (CDOM): Relation to O2– and H2O2 Photoproduction and CDOM Photooxidation. Environ. Sci. Technol. 50, 11008–11015. https://doi.org/10.1021/acs.est.6b02919

Zhang, Y., Simon, K.A., Andrew, A.A., Del Vecchio, R., Blough, N. V, 2014. Enhanced Photoproduction of Hydrogen Peroxide by Humic Substances in the Presence of Phenol Electron Donors. Environ. Sci. Technol. 48, 12679–12688. https://doi.org/10.1021/es5035798

Zhang, Y., Vecchio, R. Del, Blough, N. V, 2012. Investigating the Mechanism of Hydrogen Peroxide Photoproduction by Humic Substances. Environ. Sci. Technol. 46, 11836–11843. https://doi.org/10.1021/es3029582

Zhang, Y., Wu, Z., Liu, M., He, J., Shi, K., Zhou, Y., Wang, M., Liu, X., 2015. Dissolved oxygen stratification and response to thermal structure and long-term climate change in a large and deep subtropical reservoir (Lake Qiandaohu, China). Water Res. 75, 249–258. https://doi.org/https://doi.org/10.1016/j.watres.2015.02.052

Zhang, Y.N., Zhao, J., Zhou, Y., Qu, J., Chen, J., Li, C., Qin, W., Zhao, Y., Peijnenburg, W.J.G.M., 2019. Combined effects of dissolved organic matter, pH, ionic strength and halides on photodegradation of oxytetracycline in simulated estuarine waters. Environ. Sci. Process. Impacts 21, 155–162. https://doi.org/10.1039/c8em00473k

Zhou, C., Xie, Q., Wang, J., Chen, X., Niu, J., Chen, J., 2020. Effects of dissolved organic matter derived from freshwater and seawater on photodegradation of three antiviral drugs. Environ. Pollut. 258, 113700. https://doi.org/https://doi.org/10.1016/j.envpol.2019.113700

Zhou, H., Yan, S., Lian, L., Song, W., 2019. Triplet-State Photochemistry of Dissolved Organic Matter: Triplet-State Energy Distribution and Surface

Electric Charge Conditions. Environ. Sci. Technol. 53, 2482–2490. https://doi.org/10.1021/acs.est.8b06574

Zhou, L., Ji, Y., Zeng, C., Zhang, Y., Wang, Z., Yang, X., 2013. Aquatic photodegradation of sunscreen agent p-aminobenzoic acid in the presence of dissolved organic matter. Water Res. 47, 153–162. https://doi.org/https://doi.org/10.1016/j.watres.2012.09.045

Zhou, Y., Liu, Miao, Zhou, L., Jang, K.-S., Xu, H., Shi, K., Zhu, G., Liu, Mingliang, Deng, J., Zhang, Y., Spencer, R.G.M., Kothawala, D.N., Jeppesen, E., Wu, F., 2020. Rainstorm events shift the molecular composition and export of dissolved organic matter in a large drinking water reservoir in China: High frequency buoys and field observations. Water Res. 116471. https://doi.org/https://doi.org/10.1016/j.watres.2020.116471

Università degli Studi di Torino

Doctoral School of the University of Torino

PhD Programme in Chemical and Materials Sciences 33rd cycle

The role of dissolved organic matter in surface-water photochemistry: Photoreactions with water contaminants, photoreactivity inhibition, and effects of climate change.

Candidate: **Luca Carena**

Supervisor: Prof. **Davide Vione**

Jury Members:

Prof. **Tina Kosjek**
Jozef Stefan Institute
Department of Environmental Sciences - Jamova 39, Ljubljana, Slovenia

Prof. **Anssi V. Vähätalo**
University of Jyväskylä
Department of Biological and Environmental Science – 40014 Jyväskylä, Finland

Prof. **Marco Minella**
Università degli Studi di Torino
Department of Chemistry – Via P. Giuria 5, 10125 Torino, Italy

Head of the Doctoral School: Prof. Alberto Rizzuti
PhD Programme Coordinator: Prof. Bartolome Civalleri

Torino, 2020